Warwick Manufacturing Group

University of Warwick

Experimental and simulation analysis of novel cooling approaches for automotive lithium-ion batteries

Innovation Report

Submitted in Partial Fulfilment of the Requirements of the Academic Degree:

Doctor of Engineering (International)

Author: Daniel Worwood

Registration number: 1490830

Academic supervisors: Dr. James Marco

Prof. David Greenwood

Industrial supervisor: Dr. Ryan M^{c}Glen (AAVID Thermacore)

20/12/2018

DECLARATION

I hereby declare that all the information contained within this thesis is my own work, unless otherwise stated. Further, I declare that I have fully cited all referenced material that is not original to this work.

Signed:  Date: 20/12/2018

ABSTRACT

Previous research has identified that the ageing rate and performance of lithium-ion cells are negatively influenced by unfavourable cell thermal conditions, specifically, high ambient temperatures and large in-cell temperature gradients. Careful consideration must, therefore, be placed on the design of the battery thermal management system (BTMS) contained within electrified vehicles to ensure that thermal constraints are satisfied whilst avoiding the addition of excessive weight and volume which are detrimental to the overall battery system design.

Common cooling approaches that define the current state of the art BTMS focus on cooling the exterior of the cells. For cylindrical cells, cooling the radial surface is susceptible to the formation of large temperature gradients through the cell material, which is exacerbated as the cells heat generation rate increases. Conversely, for pouch cells, the shorter heat transfer pathway between the cell centre and surface makes internal temperature gradients less problematic. However, common cooling approaches using indirect liquid plates to contact the pouch body suffer from inherent leakage concerns.

Conduction based thermal management methods offer inherent benefits over common indirect liquid cooling solutions as the external cooling location may be positioned further away from the cell, which can reduce the risk of leakage and simplify the overall design. Further, the use of conduction elements that are incorporated directly inside battery cells offer the potential to improve temperature uniformity by increasing the heat transfer to the external surfaces of the battery. To advance the deployment of a conduction based BTMS, this thesis presents and examines the thermal performance of two novel cooling approaches employing advanced conduction methods that tackle the key thermal management issues facing both cylindrical and pouch type lithium ion cells in automotive applications. In the cylindrical cell study, a mathematical model that captures the dominant thermal properties of the cell is created and validated using experimental data. Results from the extensive simulation analysis indicate that the proposed internal cooling strategy can reduce the cell thermal resistance by up to 67.8 ± 1.4% relative to single tab cooling and can emulate the thermal performance of a more complex pack-level double tab cooling approach.

In the pouch cell study, a novel graphite-based fin material with an in-plane thermal conductivity 5 times greater than aluminium is presented for advanced battery cooling in a developed novel BTMS design. The thermal performance of the fin is benchmarked against

conventional copper and aluminium fins in an experimental programme cycling commercially available 53 Ah pouch cells. Results from the rigorous experimental testing and subsequently validated thermal model indicate that under an aggressive electric vehicle duty-cycle, the new fin can reduce the peak cell surface temperature gradient by up to 55% and volume averaged cell temperature rise by 6.3 °C when compared to a comparably sized aluminium fin with the same weight penalty.

The innovative thermal management approaches presented in this thesis offer improved thermal efficiency relative to the current state of the art BTMS reported in the literature, providing important contributions to academia and opportunities for the sponsor company to further the advancement of next generation BTMS.

ACKNOWLEDGEMENTS

Firstly, I would like to thank Dr. James Marco and Prof. David Greenwood for their dedication and expert guidance towards me over the past four years. I would also like to thank Ryan M^{c}Glen for his industrial supervision and for his mentorship during my time at Thermacore. I would like to thank David Mullen (particularly for his help in finding an appropriate clamping method for the test rig) and Kevin Lynn for their support in acquiring the k-core and reference aluminium/copper fin samples necessary for the experimental investigation portion of the research. Further, I would also like to thank Mark Montesano for his expert advice on k-core technology. I would also like to thank everyone else that I had the pleasuring of meeting at my time spent in the UK Thermacore premise, and during my industrial placement at Thermacore USA.

I would like to thank John Palmer for his technical skills and help during the experimental pouch cell testing, particularly for his modification to the air wedge bag that enabled a pressure dial reading. I would like to thank Dr Yue Guo for ensuring that a test chamber was made available for the pouch cell experiment. I express thanks to Quirin Kellner and Elham Hosseinzadeh for their collaborative assistance to the research. I would also like to thank everyone else that I have had the opportunity to work with within the energy storage group at WMG.

I would like to acknowledge that the research presented within this thesis is supported by the Engineering and Physical Science Research Council through the award EP/I01585X/1. The research was undertaken in collaboration with the WMG Centre High Value Manufacturing Catapult (funded by Innovate UK) in collaboration with Thermacore Europe.

Finally, I would like to thank my mother and farther for their love and support and also my fiancé Natasha Lunn, who if not for her, I would not be writing this in the first place!

TABLE OF CONTENTS

TABLE OF FIGURES

APPENDIX TABLE OF FIGURES

TABLE OF TABLES

APPENDIX TABLE OF TABLES

ABBREVIATIONS

Abbreviation	Meaning
EV	Electric vehicle
HEV	Hybrid electric vehicle
PHEV	Plug-in hybrid electric vehicle
xEV	Vehicle containing an electrified powertrain
IEA	International Energy Agency
ESS	Energy Storage System
ICE	Internal combustion engine
BMS	Battery management system
BTMS	Battery thermal management system
USABC	United States Advanced Battery Consortium
APC	Advanced Propulsion Centre
LDV	Light duty vehicle
EOL	End of life
OEM	Original equipment manufacturer
SEI	Solid-electrolyte interface
NREL	National Renewable Energy Laboratory
LMO	Lithium manganese oxide
LTO	Lithium-titanate oxide

NCA	Lithium nickel cobalt aluminium oxide
CFD	Computational fluid dynamics
SOC	Cell state of charge
HVAC	Heating, ventilating and air conditioning
Re	Reynolds number
HPCP	Heat pipe cooling plate
LFP	Lithium-iron phosphate
XFT	Xenon-flash technique
ARC	Accelerating rate calorimetry
ADI	Alternating-direction implicit
OCP	Open-circuit potential
EIS	Electrochemical impedance spectroscopy
NMC	Nickel manganese cobalt oxide chemistry
JLR	Jaguar Land Rover
WLTP	Worldwide harmonized Light vehicle Test Procedures
NEDC	New European Driving Cycle
CNT	Carbon nanotubes
NMC	Nickel manganese cobalt oxide
APG	Annealed pyrolytic graphite
PG	Pyrolytic graphite
CVD	Chemical vapour deposition
TC	Thermocouple
CC-CV	Constant current constant voltage charging procedure
Al	Aluminium
Cu	Copper
MAPE	Mean absolute percentage error
MPE	Maximum percentage error

NOMENCLATURE

Symbol	Meaning	Unit
$k_{z,i}$	Thermal conductivity of material layer 'i' along the z axis	[W.m^{-1}.K^{-1}]
$k_{r,i}$	Thermal conductivity of material layer 'i' along the r axis	[W.m^{-1}.K^{-1}]
A_i	Cross-sectional area of the material layer 'i'	[m^2]
L_i	Length of material layer 'i'	[m]
k_r	Effective thermal conductivity of the cell along the r axis	[W.m^{-1}.K^{-1}]
k_z	Effective thermal conductivity of the cell along the z axis	[W.m^{-1}.K^{-1}]
k_y	Effective thermal conductivity of the cell along the y axis	[W.m^{-1}.K^{-1}]
R_{tc}	Thermal contact resistance	[m^2 K W^{-1}].
ρ	Effective cell density	[kg.m^{-3}]
T	Cell temperature	[K]
r	Radial location	[m]
z	Axial location	[m]
C_p	Effective cell heat capacity	[J.kg^{-1}.K^{-1}]

t	Time	[s]
q'''	Volumetric heat generation rate	[W.m^{-3}]
R_i	Radius of the cell mandrel	[m]
R_0	Radius of the cell	[m]
q''_i	Heat flux at cell surface 'i'	[W.m^{-2}]
h_i	Total heat transfer coefficient at cell surface 'i'	[W.m^{-2}.K^{-1}]
h	Generic heat transfer coefficient	[W.m^{-2}.K^{-1}]
T_i	Temperature at the cell surface 'i'	[K]
T_∞	Temperature of the bulk heat transfer medium	[K]
h_{z0}	Heat transfer coefficient at the bottom tab	[W.m^{-2}.K^{-1}]
h_{zL}	Heat transfer coefficient at the top tab	[W.m^{-2}.K^{-1}]
h_r	Heat transfer coefficient at the outer radial surface	[W.m^{-2}.K^{-1}]
$q''_{i,rad}$	Radiation component of the heat flux from cell surface 'i'	[W.m^{-2}]
ε_i	Emissivity of cell surface 'i'	[-]
σ	Stefan-Boltzmann constant	[W.m^{-2}.K^{-4}]
$h_{rad,i}$	Equivalent radiative heat transfer coefficient	[W.m^{-2}.K^{-1}]
K	Radial mesh resolution parameter	[-]
J	Axial mesh resolution parameter	[-]
$h_{c,i}$	Convective heat transfer coefficient at cell surface 'i'	[W.m^{-2}.K^{-1}]
$T^n_{j,k}$	Temperature location at nodal position j,k at time step n	[K]
$\rho_{j,k}$	Material density at nodal position j,k	[kg.m^{-3}]
$c^p_{j,k}$	Material heat capacity at nodal position j,k	[J.kg^{-1}.K^{-1}]
$k^z_{j,k}$	Material axial thermal conductivity at nodal position j,k	[W.m^{-1}.K^{-1}]
$k^r_{j,k}$	Material perpendicular thermal conductivity at nodal position j,k	[W.m^{-1}.K^{-1}]
dr	Distance between nodes in the perpendicular direction	[m]
dz	Distance between nodes in the axial direction	[m]
dt	Number of time steps	[-]
$q'''^{,n}_{j,k}$	Volumetric heat generation rate at nodal position j,k at time step n	[W.m^{-3}]
Δt	Time step	[s]
r_k	Radial position at node 'k'	[m]
I	Cell current	[A]
V	Cell potential	[V]
$U_{l,avg}$	Average theoretical open-circuit potential for electrochemical reaction l based on the average stoichiometry of the electrode	[V]
q	Battery heat generation rate	[W]
q_{irrev}	Irreversible component of the battery heat generation	[W]
η	Cell overpotential	[V]
η_{ohmic}	Voltage drop arising from the sum of the ohmic drops	[V]
$\eta_{f,pos}$	Polarization voltages from the formation of passive film layers on the positive electrode	[V]

$\eta_{f,neg}$	Polarization voltages from the formation of passive film layers on the negative electrode	[V]
$\eta_{act,pos}$	Voltage drops arising from activation polarisation at the positive electrode	[V]
$\eta_{act,neg}$	Voltage drops arising from activation polarisation at the negative electrode	[V]
η_{con}	Concentration polarisation	[V]
R_{η}	Overpotential/internal resistance of the cell	[Ω]
$\eta_{ch,tr}$	Voltage drops from the charge transfer resistance.	[V]
E_c	Nominal cell capacity	[Ah]
F_p	Propulsion force	[N]
a_c	Vehicle acceleration	[m.s^{-2}]
m	Curb weight of the vehicle	[kg]
f_m	Vehicle mass factor	[-]
F_i	Incline force	[N]
F_r	Rolling force due to the road surface	[N]
F_d	Drag force	[N]
θ	Inclination angle	[radian]
g	Gravitational acceleration constant	[m. s^{-2}]
C_r	Rolling coefficient	[-]
ρ_A	Density of air	[kg.m^{-3}]
C_d	Drag coefficient	[-]
A_f	Frontal area of the vehicle	[m^2]
v_l	Velocity of the vehicle	[m.s^{-1}]
$P_{b,p}$	Battery power for propulsion	[W]
χ	Battery to wheels efficiency	[-]
$P_{b,c}$	Battery charging power	[W]
χ_c	Efficiency of power transfer from regenerative breaking into the battery	[-]
C	Battery C-rate	[hr^{-1}]
P	Battery power profile	[W]
N	Total number of battery cells	[-]
V_c	Nominal voltage of the battery cells	[V]
E_{pack}	Total battery pack capacity	[kWh]
R	Overall thermal resistance	[K.W^{-1}]
T_{max}	Maximum temperature of the battery	[K]
Q_c	Steady-state battery heat generation rate	[W]
R_{cell}	Thermal resistance through the bulk battery cell material	[K.W^{-1}]
T_s	Temperature of the cell surface at the cooling source	[K]
ΔT_{max}	Battery cell maximum temperature gradient	[K]
T_{avg}	Volume averaged cell temperature	[K]
t_w	Thickness of the heat pipe shell wall	[m]
$P_{v,w}$	Vapour pressure of water	[Pa]
Ω	Permissible stress	[Pa]

r_{hp}	Heat pipe radius	[m]
ΔP_c	Capillary pumping pressure	[Pa]
ΔP_l	Total pressure drop for liquid flow in porous wick	[Pa]
ΔP_v	Total vapour flow pressure drop	[Pa]
ΔP_g	Gravitational head pressure drop	[Pa]
σ_s	Surface tension	[N.m^{-1}]
θ_w	Wetting angle	[radian]
r_c	Pore radius	[m]
μ_l	Dynamic liquid viscosity	[kg.m^{-1}.s^{-1}]
l_{eff}	Effective length for fluid flow	[m]
L	Latent heat of heat pipe working fluid	[J.kg^{-1}]
K_p	Permeability of the wick	[m^2]
A	Cross-sectional area	[m^2]
l_e	Length of evaporator	[m]
l_c	Length of condenser	[m]
l_a	Length of adiabatic section	[m]
μ_v	Dynamic vapour viscosity	[kg.m^{-1}.s^{-1}]
ρ_v	Density of vapour	[kg.m^{-3}]
Q	Heat pipe power	[W]
r_v	Radius of vapour space	[m]
φ	Angle between the horizontal plane and the heat pipe	[radian]
R_{hp}	Total heat pipe thermal resistance	[K.W^{-1}]
R_w	Thermal resistance through heat pipe wall	[K.W^{-1}]
R_{wi}	Thermal resistance through wick layer	[K.W^{-1}]
r_{wi}	Radial location at wick layer –heat pipe wall interface	[m]
k_{wi}	Effective thermal conductivity of the wick	[W.m^{-1}.K^{-1}]
k_{hp}	Effective thermal conductivity of the heat pipe	[W.m^{-1}.K^{-1}]
l_s	Height of spreader disc	[m]
k_l	Thermal conductivity of liquid	[W.m^{-1}.K^{-1}]
k_s	Thermal conductivity of solid	[W.m^{-1}.K^{-1}]
ε	Porosity of wick	[-]
l_{hp}	Heat pipe length	[m]
$T_{mid,surf}$	Cell mid-height surface temperature	[K]
f_w	Volume fraction of heat pipe wall layer	[-]
f_{wi}	Volume fraction of heat pipe wick layer	[-]
f_v	Volume fraction of heat pipe vapour core	[-]
Cp_{hp}	Effective heat pipe heat capacity	[J.kg^{-1}.K^{-1}]
Cp_s	Heat capacity of wick particles	[J.kg^{-1}.K^{-1}]
Cp_l	Heat capacity of liquid	[J.kg^{-1}.K^{-1}]
Cp_v	Heat capacity of vapour	[J.kg^{-1}.K^{-1}]
Cp_w	Heat capacity of heat pipe wall	[J.kg^{-1}.K^{-1}]
ρ_{hp}	Effective heat pipe density	[kg.m^{-3}]
ρ_{wall}	Density of heat pipe wall	[kg.m^{-3}]
ρ_s	Density of wick particles	[kg.m^{-3}]

ρ_l	Density of liquid	[kg.m^{-3}]
Q_t	Tab heat generation rate	[W]
R_t	Total tab resistance	[Ω]
$R_{tab,cone}$	Resistance through the tab cone structure	[Ω]
ρ_r	Electrical resistivity of the tab material	[Ω.m]
A	Cross-sectional are of the tab cone	[m^2]
H_{cone}	the height of the tab cone	[m]
A	Cross-sectional area	[m^2]
H_{cell}	Height of the cell body	[m]
$H_{tab,fin}$	Height of the tab fin	[m]
$H_{tab,cone}$	Height of the tab cone	[m]
T_{cone}	Thickness of the tab cone base	[m]
W_{tab}	Width of the tab	[m]
W_{cell}	Width of the cell body	[m]
t_{cell}	Thickness of the cell	[m]
$W_{t,s}$	Spacing between tabs	[m]
$W_{t,e}$	Distance between tab and cell edge	[m]
ρ_r	Electrical resistivity of the tab material	[Ω.m]
ρ_{Al}	Electrical resistivity of aluminium	[Ω.m]
ρ_{Cu}	Electrical resistivity of copper	[Ω.m]
θ	Angle	[radian]
$R_{tab,fin}$	Resistance of the tab fin structure	[Ω]
$R_{t,Cu}$	Total copper tab resistance	[Ω]
$R_{t,Al}$	Total aluminium tab resistance	[Ω]
x_h	Length of the heat transfer pathway	[m]
k	Thermal conductivity	[W.m^{-1}.K^{-1}]
$m_{T_{max}}$	Slope of the line for the T_{max} data	[K.W^{-1}]
$m_{\Delta T_{max}}$	Slope of the line for the ΔT_{max} data	[K.W^{-1}]
m_{Tavg}	Slope of the line for the T_{avg} data	[K.W^{-1}]
H_{Screw}	Height of the protruding screw	[m]
H_{bus}	Height of the busbar block	[m]
H_{offset}	Distance between the base of the fin and the base of the cell	[m]
H_{fin}	Height of the cooling fin	[m]
W_{bus}	Width of the busbar block	[m]
W_{offset}	Distance between the edge of the cell and the edge of the fin	[m]
t_{fin}	Thickness of the cooling fin	[m]
r_{bend}	Bend radius of the fin bend junction	[m]
t_{offset}	Distance between the outer fin bent edge and nearest cell edge	[m]
C_w	Contact length of the bent fin edge onto the cold plate	[m]
t_{screw}	Radius of the screw	[m]
t_{bus}	Thickness of the busbar block	[m]

q_{rev}	Reversible component of the battery heat generation	[W]
h_1	Heat transfer coefficient along the clamped fin edge onto the cold plate	[W.m^{-2}.K^{-1}]
h_2	Heat transfer coefficient on the edges of the fin, exposed tabs and bend radius portion of the fin	[W.m^{-2}.K^{-1}]
h_3	Heat transfer coefficient on the exposed fin body not in contact with the cell surface	[W.m^{-2}.K^{-1}]
h_4	Heat transfer coefficient on the tab busbar blocks and protruding screw	[W.m^{-2}.K^{-1}]
h_5	Heat transfer coefficient on the edges of the cell body	[W.m^{-2}.K^{-1}]
$\Delta T_{max,f}$	Maximum fin surface temperature gradient	[K]
$T_{max,f}$	Maximum fin surface temperature	[K]
$\Delta T_{max,s}$	Maximum cell surface temperature gradient	[K]
W_{clamp}	Length of the embedded fin edge	[m]
W_{edge}	Spacing between the embedded fin edge and the edge of the cell	[m]
t_{Wall}	Thickness of the cooling duct wall	[m]
r_{Chan}	Radius of the cooling duct channel	[m]
ρ_w	Water density	[kg.m^{-3}]
$\vec{v}$	Velocity vector	[m.s^{-1}]
T_w	Water temperature	[K]
V_{chan}	Channel volumetric flowrate	[m^{-3}.s^{-1}]
p	Pressure	[Pa]
I_m	Identity matrix	[-]
F	Body force	[N.m^{-3}]
μ_w	Dynamic viscosity of water	[kg.m^{-1}.s^{-1}]
C_{pw}	Heat capacity of water	[J.kg^{-1}.K^{-1}]
T_w	Water temperature	[K]
$V_{m,p}$	Volume packing metric.	[-]
P	Ideal pump power	[W]
$\Delta T_{av,water}$	Average temperature increase of the exiting water coolant	[K]

1 CHAPTER ONE - INTRODUCTION

1.1 ELECTRFIED AUTOMOTIVE VEHICLE MARKET TRENDS

The use of rechargeable battery technology to provide propulsion power within automotive vehicles can remove the need for liquid based hydrocarbon fuels, thus offering the potential to eliminate tail pipe emissions and reduce local air pollution [1]. The implementation of large scale point source CO_2 reduction methods, such as carbon capture and storage [2] that can be integrated directly within power plants using a fossil fuel feedstock to generate the electrical energy for the battery, may in turn be used as a promising solution to reduce the carbon footprint of electrified transportation vehicles. Power plants using renewable energy sources such as solar [3], wind [4], and tidal [5], may also power electrified vehicles to further lessen CO_2 emissions to the atmosphere.

Due to government initiatives to lower road transportation CO_2 emissions [6] stemming from concerns over climate change and future energy security for the transportation sector, vehicles containing electrified powertrains (xEVs) - such as all-electric vehicles (EVs), hybrid electric vehicles (HEVs) and plug-in hybrid electric vehicles (PHEVs) - are witnessing increased penetration rates into the global automotive market [7]. Specifically, a 2017 report by the International Energy Agency (IEA) [8] estimates that the global stock of EVs and PHEVs may increase from 2 million reported units in 2016 to between 9-20 million units by 2020. Other reports by Goldman Sachs Global Investigation Research also forecast a significant shift in the global automotive powertrain mix towards electrification, where the combined global market share for EVs, PHEVs and HEVs may exceed 30% by 2030 [9].

Many barriers exist that inhibit further adoption of EVs, which include the perceived range anxiety associated with their use, their higher capital expenditure relative to comparable models of pure internal combustion engine (ICE) vehicles and long charging times [1], [10]. The majority of the increased capital cost for EVs arises from the inclusion of the battery pack acting as the energy storage system (ESS) [11]. The battery pack itself typically consists of battery modules (which contain the individual battery cells), the battery management system (BMS), battery thermal management system (BTMS), power electronics and pack housing material [12]. The United States Advanced Battery Consortium (USABC) has outlined that in order for EVs to achieve mass commercialisation by 2020, the price per unit of stored energy (kWh) for the battery pack within EVs should reach USD 125/kWh. However, numerous sources [11], [13]–[15] estimate that the pack price of EVs will fall short of this

target. In particular, a systematic review tracking the decline in manufacturing costs for complete EV battery packs conducted by Nykvist & Nilsson [11] predicts that the USABC targets are not expected to be achieved until 2025 or later by leading automotive EV manufacturers. The UK Advanced Propulsion Centre (APC) forecast a more conservative target of USD 150/kWh for the battery pack cost by 2025 and USD 100/kWh by 2030 for mass commercialisation of EVs, whereby the current battery pack cost is at USD 280/kWh for the year 2017 [16].

Owing to the issues related to EVs, PHEVs and HEVs are also being deployed into the automotive market. Relative to EVs, these vehicles contain much smaller battery packs (in terms of kWh) allowing for smaller capital expenditure. Different to EVs, they incorporate an onboard ICE together with the battery ESS to power the vehicle. This enables HEVs and PHEVs to have longer drive ranges compared to comparably sized EV models whilst being more fuel efficient than pure ICE vehicles [10]. PHEVs differ from HEVs in that the battery energy storage system is sufficiently large (and therefore more costly) to warrant external charging, enabling these variants to sustain an all-electric driving mode, typically between 20-40 miles [17]. However, both HEVs and PHEVs incur greater capital costs than comparable pure ICE vehicles and do not provide zero tail pipe emissions due to their reliance on liquid fuels. IEA predict under their BLUE map scenario (which assumes that governments will work together to achieve a 50% reduction in annual global CO_2 emission levels and a 30% reduction in transport sector CO_2 emissions by 2050 relative to those emitted in 2005) that HEV and PHEV vehicles will remain relevant within the global passenger light duty vehicle (LDV) market for the foreseeable future (up to 2050 and beyond), with a gradual shift towards full electrification. The forecast IEA market split for LDVs based on their technology under the BLUE Map scenario is displayed in Figure 1-1.

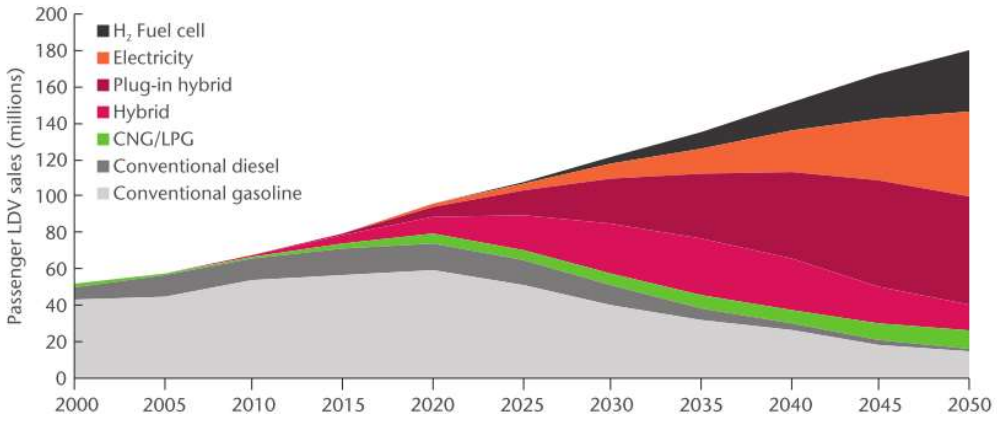

Figure 1-1: IEA forecasts for global annual LDV sales by technology under the BLUE map scenario [7]

1.2 BATTERY TECHNOLOGY FOR ELECTRIFIED AUTOMOTIVE VEHICLES

As the increased existence of EVs, HEVs and PHEVs within the automotive marketplace is of paramount importance to reduce the global reliance on liquid-based fuels, it is necessary to investigate solutions that can accelerate their market penetration.

In addition to the requirements related to the capital cost of battery packs, other parameters important for their uptake include calendar life, cycle life, energy density and power density (both in gravimetric and volumetric terms) [1] and performance [13]. Definitions of these parameters and requirement targets from the USABC and APC are shown in Table 1-1.

Table 1-1: Important battery parameters for ESS

Parameter	Definition	USABC target by 2020 [17], [18]	APC target by 2025 [16]
Calendar life	Usable lifetime of the battery before it reaches its end of life (EOL) threshold - commonly defined as when the battery capacity reaches 80% of its initial value [19].	15 years (EV), 15 years (PHEV).	10 years (EV).
Cycle life	The number of charge and discharge cycles the battery can achieve before it reaches the EOL threshold [19].	1000 cycles (EV).	
Energy density	Amount of energy stored in the battery (on cell or pack level) per unit of volume.	500 $Wh.L^{-1}$ (EV Pack level).	550 $Wh.L^{-1}$ (EV Pack level).
Specific energy density	Amount of energy stored in the battery (on cell or pack level) per unit of mass.	235 $Wh.kg^{-1}$ (EV Pack level).	
Power density	Amount of battery power (on cell or pack level) per unit of volume.	-	-
Specific power density	Amount of battery power (on cell or pack level) per unit of mass.	-	7.5 $kW.kg^{-1}$ (EV Pack level).
Performance	The ability of the battery to meet the vehicle operating requirements under extremes in the ambient temperature e.g. below -20 ℃ and above 40 ℃ [13].	-	-

Owing to their comparatively high energy and power density relative to previous iterations of battery technology such as lead acid and nickel-metal hydride [20], [21], lithium-ion

batteries are an attractive choice for the ESS contained within EVs, PHEVs and HEVs, resulting in their widespread adoption by leading automotive original equipment manufacturers (OEMs) [22]. Figure 1-2 illustrates the advantage offered by lithium-ion technology in providing the necessary combination of high energy and power density required for a compact, lightweight ESS.

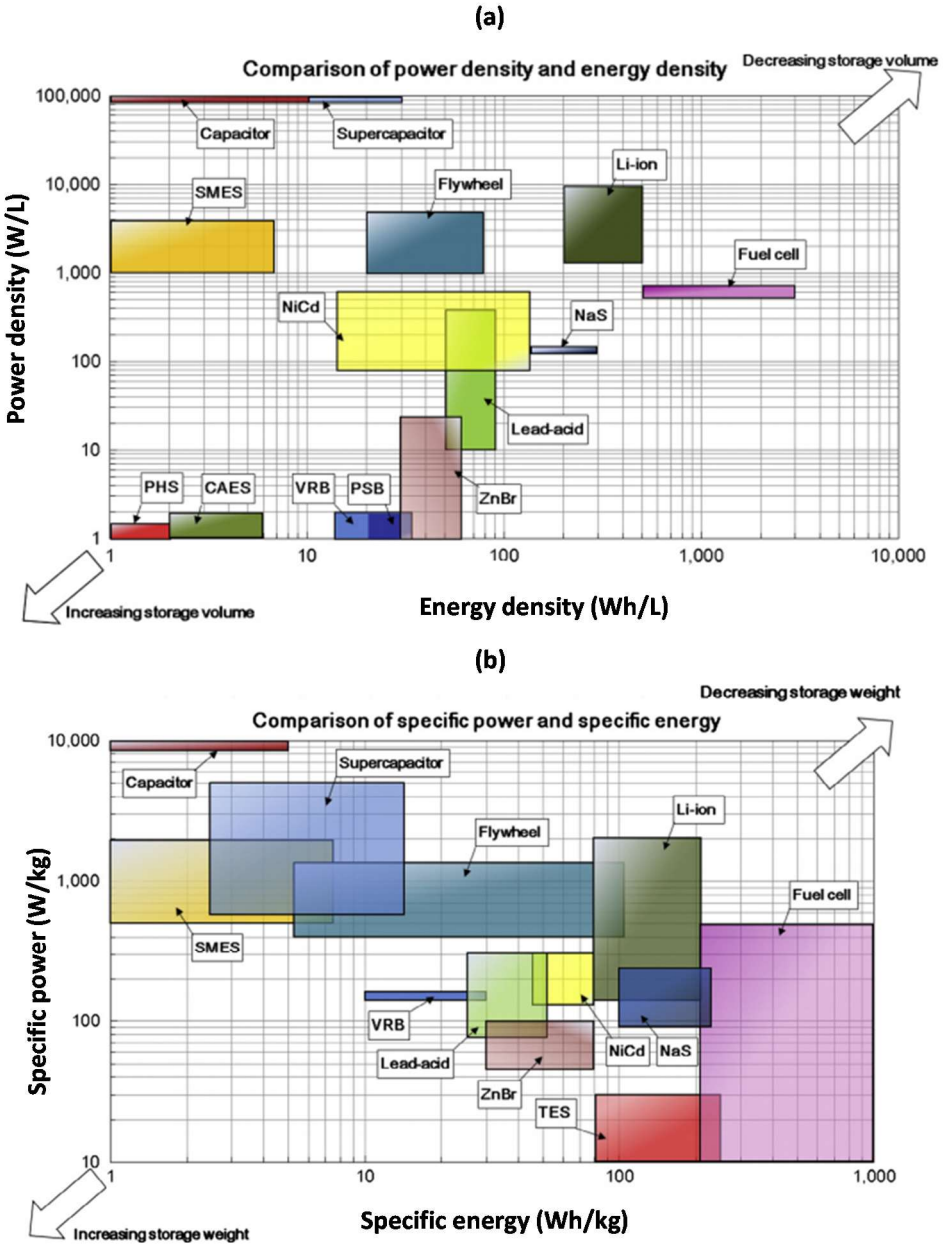

Figure 1-2: Energy and power density comparisons between different ESS technologies extracted from Luo et al. for (a) volumetric level (b) specific/gravimetric level. Abbreviations: pumped hydro storage (PHS), compressed air energy storage (CAES), vanadium redox battery (VRB), zinc-bromine battery (ZnBr), superconducting magnetic energy storage (SMES), thermal energy storage (TES) [20]

Whilst lithium-ion is currently the preferred technology, its theoretical gravimetric energy density of circa 400 $Wh.kg^{-1}$ is still far from the theoretical value offered by gasoline (circa 13,000 $Wh.kg^{-1}$) [23] and practical value (when considering the efficiency of the powertrain) of circa 2000 $Wh.kg^{-1}$ [24]. Due to this limitation, future generations of battery technology such as lithium-sulphur [25] and lithium-air batteries [24] are receiving growing research towards their development.

Lithium-sulphur batteries offer much larger theoretical specific energy densities of circa 2600 $Wh.kg^{-1}$ [25] relative to lithium-ion, and have the potential to be less costly due to the use of cheaper sulphur [26]. However, numerous issues pertain to the use of lithium-sulphur batteries in their current state, which make them unsuitable for use in automotive applications. These include, unacceptable concerns over safety from the formation of lithium dendrites leading to short-circuit events [26], poor capacity retention from heightened self-discharge [27] and short cycling lifespan [25].

Lithium-air batteries offer even larger theoretical specific energy densities of circa 12,000 $Wh.kg^{-1}$ which is comparable to gasoline [24]. Practically, the energy density of the whole battery system is expected to be on the order of 1000 $Wh.kg^{-1}$ [23] which is still over 4 times greater than the 2020 USABC target for EVs using lithium-ion technology. However, as with lithium-sulphur, the technology is still within its infancy whereby further development milestones are required before it can be applied within a vehicle ESS [23]. As such, lithium-ion batteries are expected to be the dominant technology used within automotive ESS for the next several years [28].

1.3 THERMAL RELATED ISSUES FOR LITHIUM-ION BATTERIES

As discussed in Section 1.2, a long calendar life, high cycle life and necessary performance are important requirements for batteries within energy storage systems. Unfortunately, for lithium-ion batteries, these parameters are highly sensitive to the thermal condition of the battery [29].

The performance of lithium-ion batteries is negatively affected at lower temperatures, where whilst chemistry dependent, some studies suggest that the operating temperature should not drop below circa 15 °C to avoid unacceptable reductions in immediate available cell capacity and power output [30], [31]. The poorer performance at lower temperatures is believed to be caused by, but not limited to, reduced rates of the electrochemical charge

transfer reactions occurring at the interface between the battery electrodes and electrolyte, in addition to reduced ion diffusion rates within the porous material that comprise the battery electrodes [32]. Pesaran et al. [31] analysed the temperature effect on the relative capacity of an $LiFePO_4$ type lithium-ion cell, where their results are viewable in Figure 1-3. They observed that operating temperatures below circa 25 ℃ begin to reduce the relative usable capacity of the cell, with a circa 10 % reduction in capacity at 10 ℃ relative to at 25 ℃. Similar reductions in immediate capacity at lower temperatures are also reported by Tourani et al. [30].

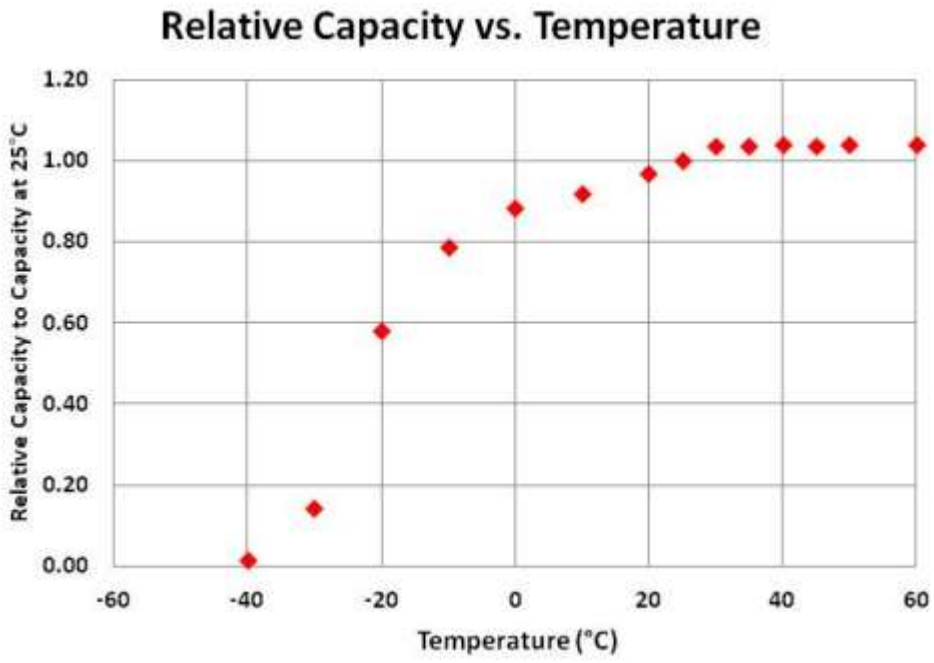

Figure 1-3: Pesaran et al. temperature related relative capacity for an $LiFePO_4$ type lithium-ion cell [31]

Charging at low temperatures is also highly problematic for lithium-ion cells. Specifically, the poor rates of lithium intraparticle mass transfer into the anode structure from the lower temperatures can lead to an accumulation of lithium ions on the anode surface, which in turn can cause the formation of metallic lithium deposits. This mechanism is commonly termed 'lithium plating' [33], [34], where the deposits can irreversibly trap mobile lithium ions and cause an overall irreversible capacity loss and impedance rise for the cell leading to reduced cycle life. Waldmann et al. [35] observed this effect from a post mortem analysis of lithium-ion cells subject to a low temperature charging range of 0 ℃ to -20 ℃, which revealed the presence of white metallic lithium deposits across the anodes. This was not present in their tested cells charged at higher temperatures (25 -70 ℃). They concluded that the rate of capacity loss (ageing) for the cells continually cycled between charging at -20 ℃

followed by a discharge at 25 ℃ was circa 10 times faster than for cells charged at 25 ℃ followed by discharging at -20 ℃, indicating the accelerated ageing was attributed to the low temperature charge portion. Severe safety concerns are also present with the occurrence of lithium plating, where the metallic lithium deposits can form dendrites that may grow to sufficient size to puncture the separator layer, causing an internal cell short circuit [36] and potential subsequent catastrophic thermal runaway event [37].

Whilst higher temperatures are preferable from a performance standpoint, it has been shown that high temperature ageing mechanisms also exist for lithium-ion cells [38]. Specifically, higher temperatures tend to increase the rates of unwanted parasitic side reactions that exist within the cell, mainly from the growing solid-electrolyte interface (SEI) layer which incurs a loss of cyclable lithium leading to increased capacity and power fade losses for the battery [35]. Therefore, it is commonly reported that an optimum battery operating temperature exists for lithium ion-cells between circa 15-35 ℃ that maximises the performance capability whilst minimising the adverse ageing related effects [31], [39]. However, it is noteworthy that others suggest a narrower range of 20±5 [30]. Figure 1-4 summarises the key temperature related effects for lithium-ion batteries when in operation.

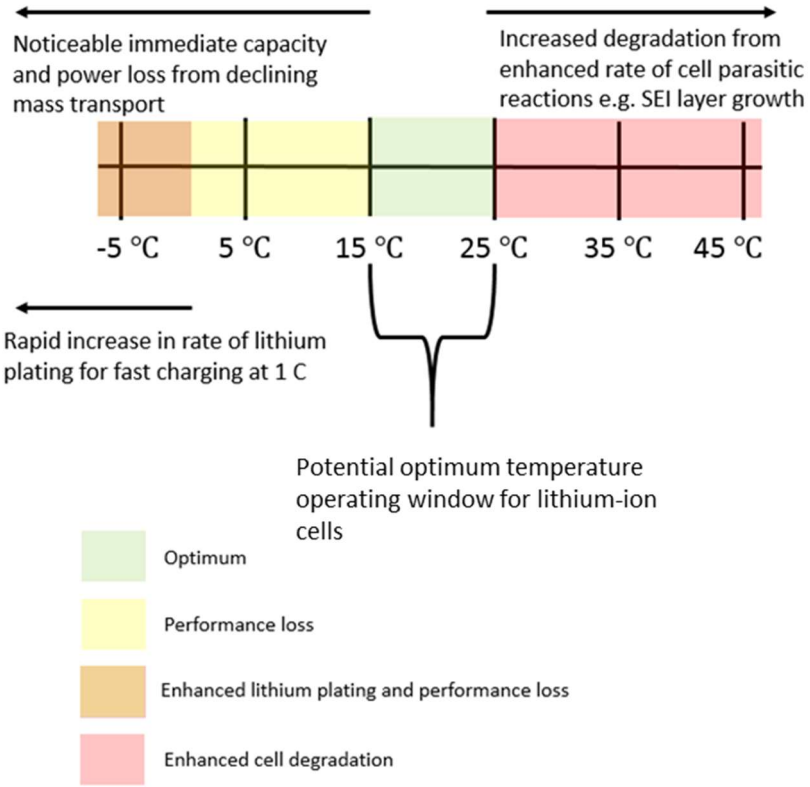

Figure 1-4: Examples of temperature related effects for lithium-ion batteries

Temperature gradients that may form between cells connected in a module, and within the internal layers of individual cells are also of great concern. Yang et al. demonstrated that temperature gradients between cells connected in a parallel string can exacerbate unbalanced discharging, with the ageing rate of the battery increasing linearly as the cell-to-cell temperature gradient increases [40]. On the cell-level, Fleckenstein et al. [41] concluded through simulation that temperature gradients between the cell core and outer surface of cylindrical cells cause inhomogeneities in cell current density, which in turn induces a local state of charge (SOC) imbalance within the cell. Troxler et al. [42] further investigated the effects of in-cell temperature gradients and noticed that the cell performance under a temperature gradient did not perform as if the cell was operating at the volume average temperature, but rather as if at a higher average temperature than the theoretical volume average. This is also consistent with the conclusions from [43]. Owing to this, it is commonly reported [44]–[48] that the magnitude of the gradient both between cells and within individual cells should not exceed circa $5℃$.

Excessive heat accumulation within lithium-ion cells can also cause the onset of a thermal runaway event, with can lead to fire and explosion of the battery pack [49]. Therefore, it is imperative that battery cells are thermally managed during operation to avoid such temperature related issues that can inhibit the uptake of electrified vehicles.

1.4 BATTERY THERMAL MANAGEMENT SYSTEMS

To combat the aforementioned thermal issues associated with lithium-ion batteries, BTMS are usually integrated within automotive battery packs to control the thermal state of the individual battery cells [39].

The design of the BTMS is complex in nature as other parameters such as cell geometry [39], [50], cell chemistry [39] and heat transfer medium choice [51] may affect the rate of heat accumulation within the cells, thus impacting the BTMS design strategy. The BTMS design itself may consist of an arrangement of heat transfer mechanisms that make thermal contact with the individual cells to manage the addition or removal of heat. The implementation of this arrangement, must also be conducive towards attaining compact packing of cells to maximise the pack volumetric energy density, and be of low weight to maximise pack gravimetric energy density [52]. Increased reliability, low design costs [53] and minimal parasitic power [54] (i.e. the power needed to run the BTMS) are other examples of desirable

characteristics for a BTMS to attain. Figure 1-5 summarises some of the key considerations pertaining to the design of the BTMS.

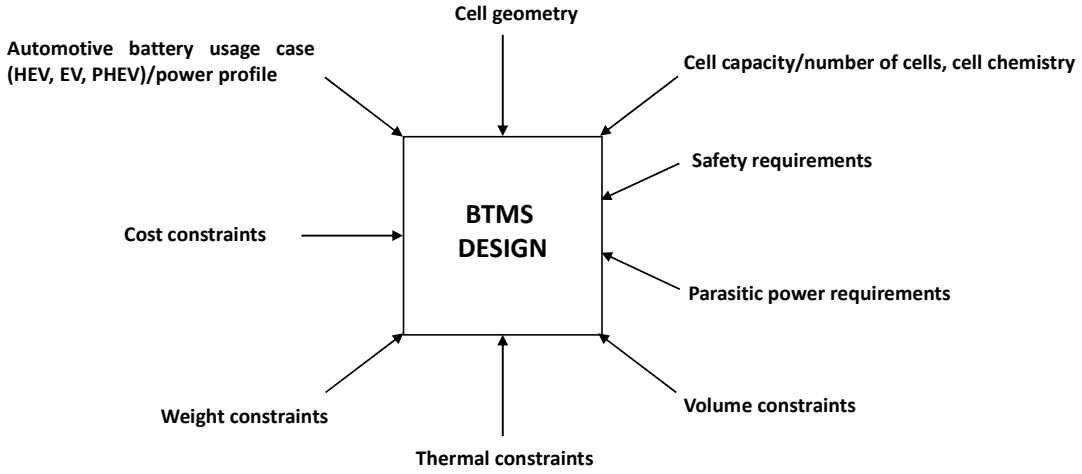

Figure 1-5: Key parameters that affect the design of the battery thermal management design

Due to the complexity involved with balancing the inherent trade-offs between achieving the required thermal control with these conflicting, yet desirable characteristics of the BTMS design (e.g. cost, weight, compactness), a plethora of options for the BTMS design have been reported within the literature and investigated by different commercial organisations and research institutions to date [39], [51].

1.5 SCOPE OF THE THESIS AND ROLE OF THE SPONSOR COMPANY

The primary motivation for research within this International Engineering Doctorate (EngD Int.) is to identify novel design solutions for a BTMS employing new technology underpinned by the capabilities of the industrial sponsor AAVID Thermacore.

The expertise of Thermacore lies within the design and application of thermal management technologies for a variety of commercial markets. However, as of yet, these do not include the electrified powertrain market of which the company is looking to enter. Their current primary markets are: Military and aerospace, Telecom, life sciences and Formula 1 [55].

Examples of key heat transfer technologies offered by Thermacore include two-phase heat transfer devices, such as heat pipes and vapour chambers [56], and advanced solid conduction materials, an example of which is their k-core product line [57]. These advanced devices offer promising possibilities for application within a conduction based BTMS due to

their superior thermal conductance relative to conventional heat transfer materials (such as aluminium).

This thesis will critically review the current offering of BTMS designs reported in the literature to define the current state of the art. This will provide a knowledge foundation to underpin the development of novel next generation BTMS solutions that directly tackles the issues pertaining to the current generation of BTMS.

Upon the identification of limitations with the current generation of BTMS designs, the primary innovative research involves the development of new thermal management techniques (that considers the parameters affecting the BTMS design as shown in Figure 1-5) leveraging Thermacore conduction technology.

Thermal modelling of the BTMS heat transfer physics (both in steady and transient states on the cell-level), cell heat generation modelling, pack-level considerations, experimental test rig design and application are all within the scope of this thesis.

Thermacore act to support the research through the provision of laboratory testing capabilities, technology design, manufacturing capabilities and thermal management expertise.

1.6 ENGD PORTFOLIO STRUCTURE

The individual submissions of the EngD (int.) comprise the main body of research. These Submissions, together with the Personal Profile, academic published papers, MSc modules, industrial placement and Innovation Report constitute the EngD Portfolio. The structure of the EngD Portfolio is presented in Figure 1-6, which displays the key areas of research and the corresponding EngD Submissions where the respective objectives, methodology and results are presented.

Submission 1, Submission 2 and sections of Submission 3 are primarily literature reviews that define the research objectives. Stemming from these research objectives, the main research activities are carried out in the form of related experimental and simulation-based studies. From the literature review and market analysis sections in Submission 1, it is identified that no predominant format of lithium-ion battery currently exists, whereby automotive OEMs are employing both cylindrical and pouch type formats. From Submission 2, it is concluded that due to the differences in geometry between both these battery formats, different

thermal management strategies are required. Resulting from the uncertainty in the market as to which battery format may prevail in the future, two independent but related research streams are pursued to address the thermal management needs pertaining to both cylindrical and pouch type batteries. This approach provides Thermacore with a wider range of opportunities to underpin a future successful BTMS product.

Submission 3 and Submission 4 contain thermal management research for cylindrical type battery cells, whereas Submission 5, Submission 6, and Submission 7 focus on the thermal management design for pouch cells. It is recommended that the Submissions are read in chronological order within each research stream as displayed in Figure 1-6.

The results, conclusions and recommendations for further work from each of the Submissions and research streams are explored further within this Innovation Report. This report draws together in a holistic manner the key areas of innovation resulting from the individual submissions and published academic papers, defining the academic contribution and impact of the Portfolio as a whole.

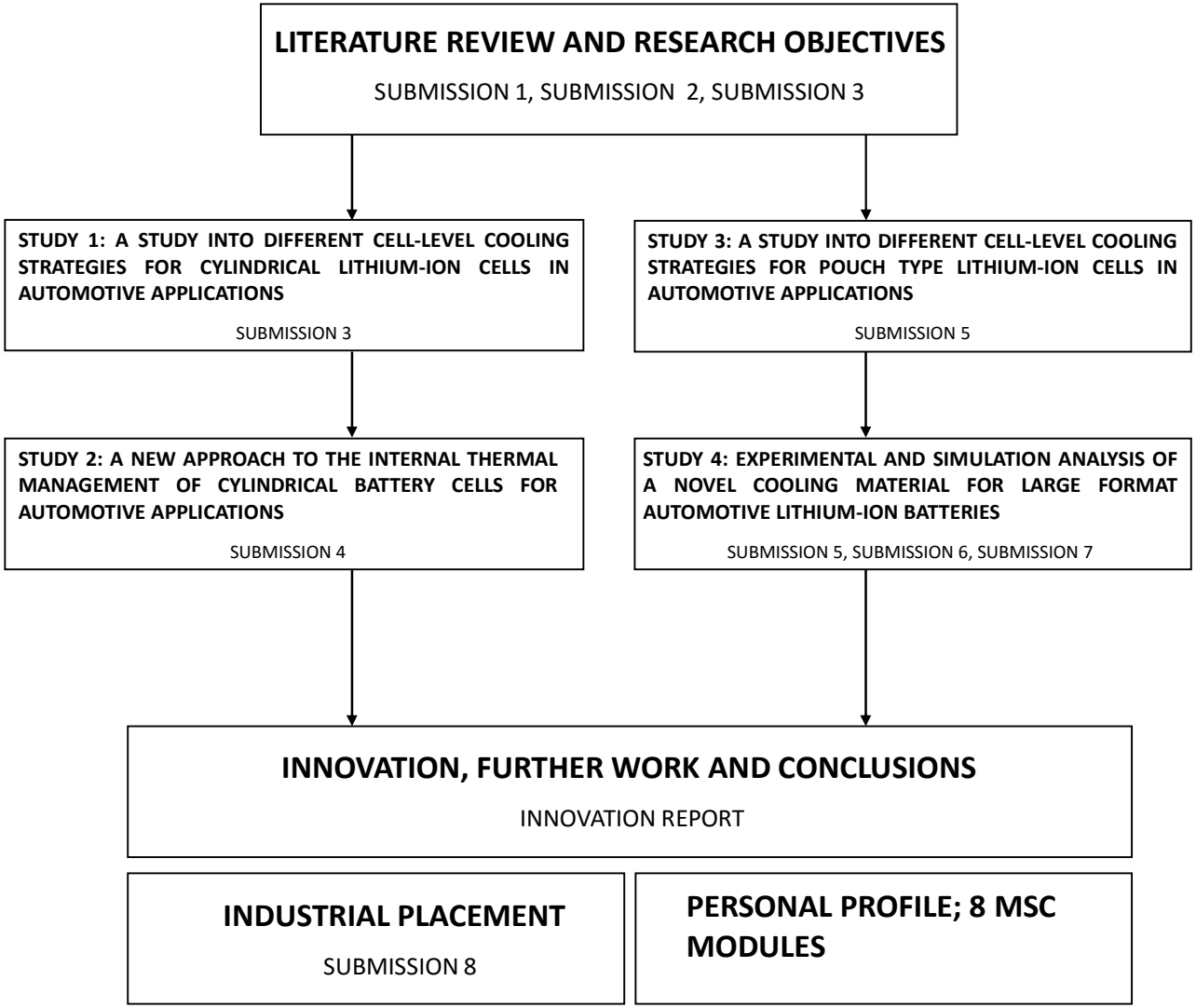

Figure 1-6: Structure of the EngD Portfolio

1.7 INNOVATION REPORT STRUCTURE

The Innovation Report is structured to highlight the key areas of research conducted during the EngD Int., providing the reader of the Portfolio with clarity on how the research has addressed the research objectives and led to the innovation claims. The Innovation Report is structured as follows.

Firstly, Chapter Two contains a critical review of the BTMS designs and strategies present within the literature to define the current state of the art for battery thermal management. The knowledge gaps identified from the literature review defines the research objectives of the thesis, which are also contained Chapter Two.

Chapter Three presents the key areas of novel research related to cylindrical cell thermal management. Here, a 2-dimensional (2-D) thermal model is developed using the governing heat conduction equations and a finite-difference solution method, enabling the creation of a tool to conduct a cell-level cooling analysis. The study assesses the thermal performance of cooling different external surfaces of cylindrical cells, as a function of both cell geometry and cell electrical loading condition (that reflects the realistic usage cases of an EV, PHEV and HEV). The results of the analysis are summarised in thermal design charts, which act to guide readers towards the potential preferred external cooling location for cylindrical cells for a given characteristic steady-state heat generation rate.

Chapter Four presents a novel internal cooling solution developed for cylindrical battery cells. This solution aims to address key limitations of conventional exterior battery surface cooling as highlighted in Chapter Three. Both the developed theoretical modelling procedure, subsequent validation strategy, and further simulation analysis that compares the steady-state and transient thermal performance of the cooling solution against conventional external surface cooling approaches are included.

In Chapter Five, a three-dimensional (3-D) thermal model of a pouch cell that captures both the bulk cell body and external tab heat transfer physics is developed using COMSOL Multiphysics. The model is used to compare the effect of surface cooling intensity and location of cooling on the thermal condition of the cell under steady-state heat generation rates that reflect real life EV and PHEV usage cases. The effect of different tab layouts on the thermal performance of tab cooling the cell is also examined.

Chapter Six contains both an experimental and simulation analysis on a novel graphite-based material for cooling the surface of pouch type batteries. A test rig and experimental programme capable of cycling real 53 Ah pouch cells are developed to test the performance of the cooling material. The experimental analysis quantifies the thermal performance of the new material against conventional copper and aluminium variants, under various electrical loading conditions. These range from standard continuous discharges, to cycles covering moderate PHEV aggressiveness and upwards to extreme performance EV track racing. Further, the extensive simulation study extends the experimental work to assess the potential of the material when employed practically in a novel BTMS design.

In Chapter Seven, a reflective review on the research is contained which identifies the main areas of innovation in terms of its academic contribution and industrial impact, whilst also suggesting areas that merit further research. The overall Conclusions for the thesis are presented in Chapter Eight.

2 CHAPTER TWO - LITERATURE REVIEW

2.1 INTRODUCTION

In this Chapter, a critical review of BTMS designs present within the literature is performed. Its purpose is to identify knowledge gaps that can guide the next generation BTMS design, that in turn defines the research objectives of this thesis.

The critical review of BTMS designs is contained in Section 2.2, where the identified Research Objectives and Conclusions from the literature review are contained in Section 2.3. A brief overview on the predominate formats of battery geometries and components within a battery pack are contained in Appendix A.1 and A.2 respectively.

2.2 BATTERY THERMAL MANAGEMENT DESIGNS

Effectively designed BTMS for an automotive ESS should seek to achieve [52]:

1. Optimum temperature operating window for the battery cells during operation.
2. Inhibit the development of adverse temperatures.
3. Minimise temperature variations within module/pack and through the individual cells.
4. Minimise parasitic cooling/heating power requirement.
5. Lightweight design.
6. Compact design.
7. Minimal cost design.

In this Section, a critical review on BTMS designs within the literature is carried out to identify areas for improvement related to the above parameters.

2.2.1 PASSIVE THERMAL MANAGEMENT

Passive based BTMS options involve those that have very low to zero parasitic power requirements relative to active based systems (discussed in Section 2.2.2), and generally rely on the ambient air to supply the needed heating/cooling. The term passive cooling/heating in the context of this thesis is defined as:

"Cooling/heating that is achieved from heat transfer with the surrounding environment, with no work input being invoked to directly enhance the rate of heat transfer, with the exception of an exhaust fan and/or circulator pump to promote natural cooling".

This definition is inspired by that of Rao [51], and is used to distinguish between a BTMS that uses very low parasitic power to promote natural passive cooling from the environment, to those that rely on built in systems -such as a front fan or compressor unit - that require considerably higher parasitic power loads to achieve the cooling needs.

2.2.1.1 AIR PASSIVE BTMS

One of the simplest forms of passive thermal management control is by using the surrounding ambient air directly. This form of passive thermal management benefits from its simplistic design and is generally of lower cost relative to liquid based systems [39]. However, the poorer heat transfer properties of air relative to liquids (e.g. lower thermal conductivity and heat capacity, as shown in Table 2-1 of Section 2.2.2.2) together with variable supply temperatures and poor flowrate due to lack of an active fan gives limited control over the heat transfer rate for passive systems.

A general passive air cooled system is represented in Figure 2-1, which may or may not include an exhaust fan.

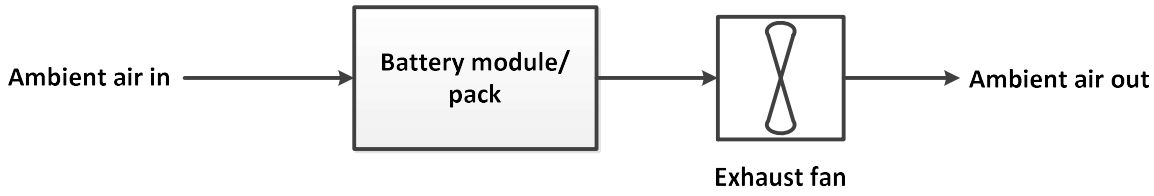

Figure 2-1: Schematic of a typical passive air cooled system for an xEV [51]

An example of a primarily passive air BTMS for an EV similar to that in Figure 2-1 is that used in the Nissan Leaf as seen in Figure 2-2, which has no active cooling solution.

Figure 2-2: Nissan Leaf battery pack [58]

Whilst simple, issues are inherently present with this choice of cooling due to its inability to reliably control the pack operating temperature at optimum levels, as the temperature of the heating/cooling medium is that of the ambient environment. This leaves the pack vulnerable to temperature extremities in the local ambient, raising issues, particularly in hotter climates such as Arizona (average highs of 40 ℃ in August [59]) where many Leaf owners have reportedly experienced permanent range reduction due to enhanced battery degradation [60].

At the opposite scale during winter months, reductions in available drive range have also been reported [61], such as in Canada where the ambient can reach temperatures of -25°C. FleetCarma report the average daily range for the 2012 Nissan Leaf as a function of ambient temperature and is displayed in Figure 2-3. As observed, at -25 °C (-13 °F) the average range reduction is near 75 % when compared to 30 °C (86 °F) ambient temperature. To mitigate these adverse range reductions at these low temperatures, newer models of the Leaf (2013) include a battery warmer that activates at -17 °C to heat the battery to -10°C [62]. Since the addition of an electric heater violates the definition of passive thermal management, solely relying on this method as the BTMS has fallen short of automotive industry expectations for application in such environments.

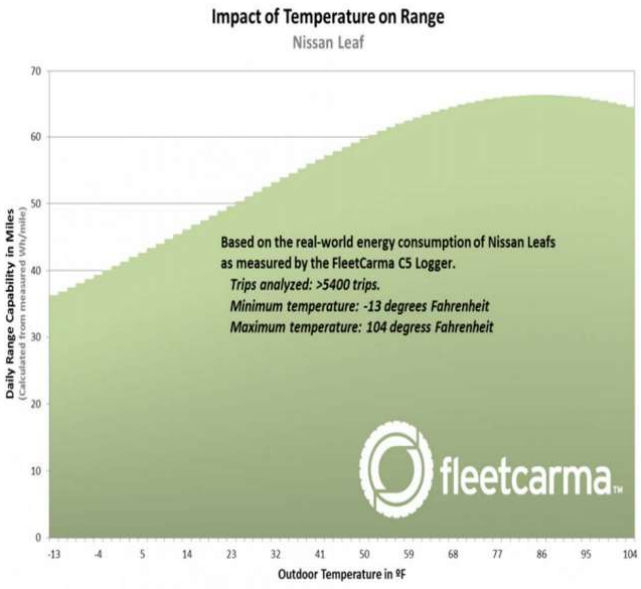

Figure 2-3: FleetCarma data for Nissan Leaf drive range as a function of ambient temperature [31]

2.2.1.2 LIQUID PASSIVE BTMS

Figure 2-4 summarises a typical passive liquid-cooled circuit for a BTMS. The liquid in the primary heat exchanger can be fed either directly onto the cell surface, or indirectly e.g. through a cooling jacket attached to the cells.

As with air passive techniques, the temperature of the liquid in the return line is vulnerable to extremes in the ambient temperature. Although greater heat transfer can usually be achieved with liquid compared to air for a given mass flowrate, issues are embedded within this design due to the limited control offered. The design is also more complex than air, at least in part, due to the need for a secondary heat exchanger and is usually more costly [39].

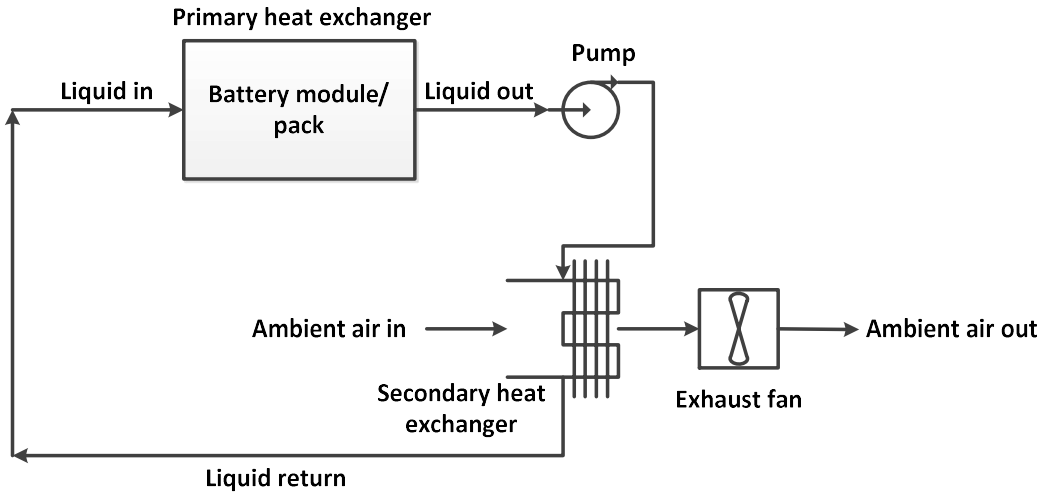

Figure 2-4: Typical liquid passive cooling circuit [51]

2.2.2 ACTIVE THERMAL MANAGEMENT

Under active control, the BTMS can work to improve the heat transfer rate past the reach of passive methods. This may involve the use of additional and/or larger fans/pumps to promote enhanced convective heat transfer, or evaporator and heater cores to control the supply temperature of the heat transfer medium [63]. Working past that which is offered naturally by the ambient requires the input of work, therefore, active BTMS have greater parasitic power requirements than passive and are generally costlier, and less physically compact for the additional and/or larger units required. For example, Pesaran et al. [31] at the National Renewable Energy Laboratory (NREL) demonstrated that engaging the climate-control system for EVs could decrease the available drive range by up to 35 %, and increase the fuel consumption of PHEVs by circa 60 % [31]. Their results for the electric range of a 100 mile EV as a function of climate control method are displayed in Figure 2-5. Given the cost of battery range for supplying conditioned air to the vehicle cabin, it is expected that similar methods to precondition the vehicle battery will also have a large negative impact on battery range.

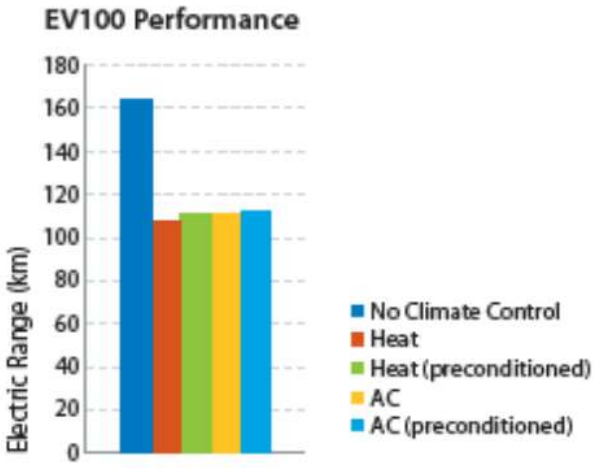

Figure 2-5: EV battery range as a function of climate control method [31]

Gallagher and Nelson estimate the penalty of coupling the battery heat transfer medium to the air-conditioning system to be at a cost of 40 $/KW$_{cooling}$, with an additional penalty for heating requirements of 20 $/KW$_{heating}$ [64]. In the context of this thesis, active cooled systems will be defined as:

"Cooling/heating achieved from methods that directly enhance the heat transfer rate past that offered by the surrounding environment through the direct input of work".

Any passive system can become active with the correct component additions, therefore, active versions exist for each passive method.

2.2.2.1 ACTIVE AIR COOLED BTMS

The general form of an active air cooled BTMS is depicted in Figure 2-6. Here, ambient air is drawn into a blower which specifies the inlet flowrate. The air is then passed into an evaporator/heater which alters the air temperature to match the set point value to be fed into the battery module/pack. Feeding the air directly over the cells in the module provides the cooling/heating requirement. An exhaust fan may be present to facilitate the departure of air from the module, where a portion may recycled back to the blower. The purge/recycle ratio may be altered, together with the inlet flowrate of ambient air, to optimise the inlet temperature of air into the evaporator/heater.

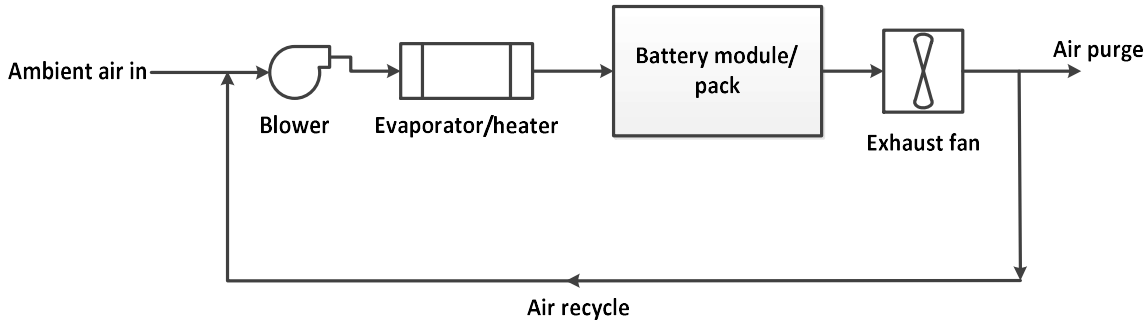

Figure 2-6: General active air cooled BTMS [51]

The method in which air passes over the cells in the module can affect its overall cooling/heating effectiveness. The air can be distributed across the module/pack either in a pure series or pure parallel manner, or a combination of both (series-parallel) [65]. In pure parallel distribution, the air entering the pack is funnelled equally between module compartments, being further distributed equally between rows of cells within the module. Complete parallel distribution may involve each cell receiving the same inlet flowrate and inlet temperature of air e.g. when the air is blown down across each cell. In a parallel-series distribution, the inlet air flows directly through the module without further funnelling. In this manner the air temperature progressively increases along the whole battery pack length, ultimately leaving cells near the pack exit hotter than at the entrance. A pure series cooling arrangement would involve a single string of cells being cooling by a single inlet air stream. The series-parallel arrangement is, therefore, a more practical approach than pure series cooling for vehicles employing a large number of cells (for example the Tesla model S which has greater than circa 400 cells per module [66]), as it avoids having an impractically long

flow path [65]. Figure 2-8 demonstrates an example of series-parallel cooled arrangement involving an aligned bank of cylindrical cells.

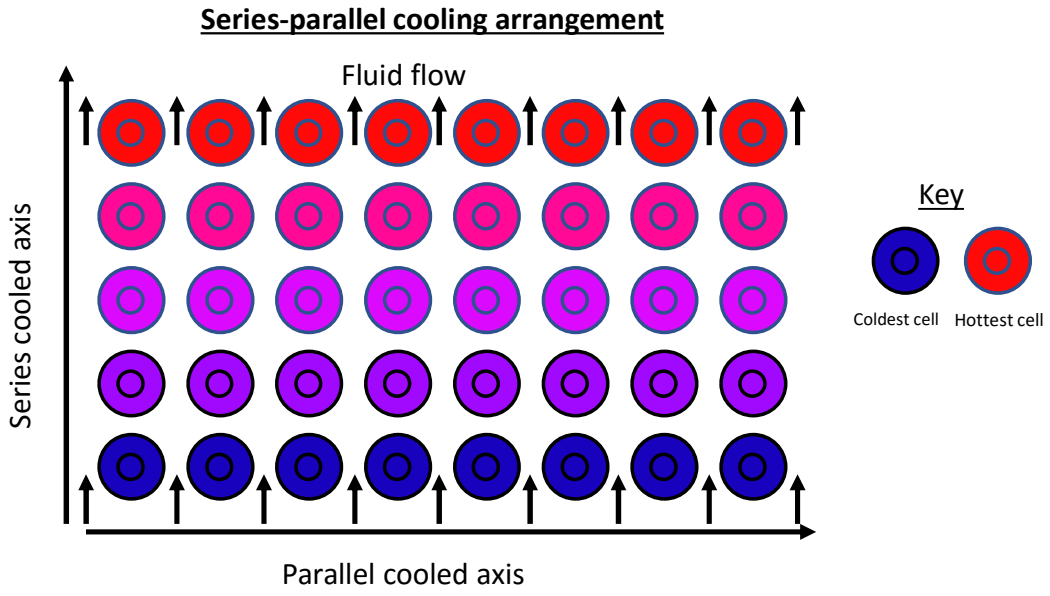

Figure 2-7: Schematic of an aligned bank arrangement of cylindrical cells configured in series-parallel cooling [65]

Pesaran [46] demonstrated that pure parallel cooling for a HEV pack comprising 30 modules could achieve lower maximum temperatures and greater pack temperature uniformity than that obtained with series-parallel cooling. The pack with series-parallel cooling reached a maximum temperature of 58 °C, with maximum pack temperature variation of 18 °C when the inlet air temperature was at 25 °C. Pure parallel distribution of air enabled the peak temperature and temperature difference to fall to 54 °C and 8 °C respectively. His results can be viewed in Figure 2-8. The Toyota Prius is an example of a HEV adopting the pure parallel air cooling technique [46], [67].

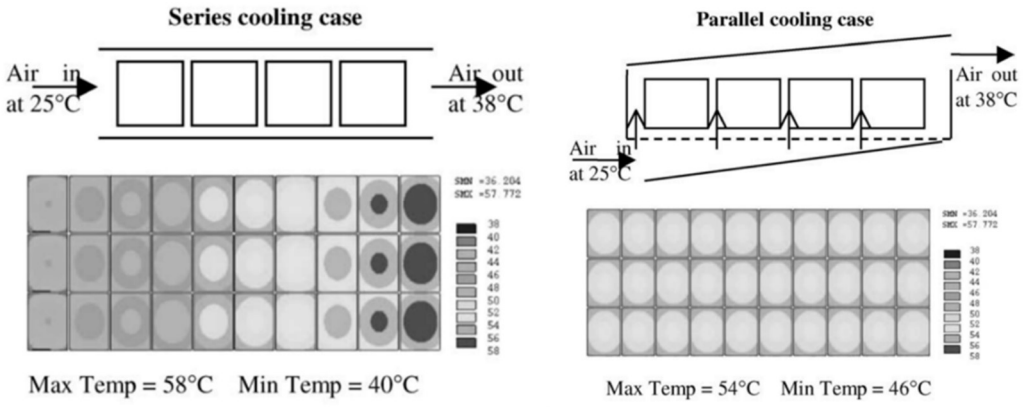

Figure 2-8: Pesaran comparison between series and parallel air distribution cooling [46]

Whilst parallel air cooling is advantageous, it necessitates greater complexity in the design of the air distribution system. Sun et al. [68] analysed the performance of a U-type air flow battery module with a tapered upper air duct for cooling pouch type batteries. Tapering the upper air duct (as shown in Figure 2-9) as opposed to non-tapering enabled greater temperature uniformity across the module. Under US06 driving cycles (high acceleration/aggressive [69]), and with an inlet air flowrate of 0.0283 m^3s^{-1}, the peak temperature variation reduced from 4 ^oC to 1.3 ^oC upon adoption of the tapered design, which also reduced the peak averaged cell temperature from 39 ^oC to 36 ^oC. However, temperature variations up to 2 ^oC over the pouch cell surface remained from the progressive decline in heat transfer rate from the battery cells along the length of the cooling channels. The authors stated that if the thermal conductivity of the battery cell could be increased by 100 %, the variation could near half to 1.2 ^oC.

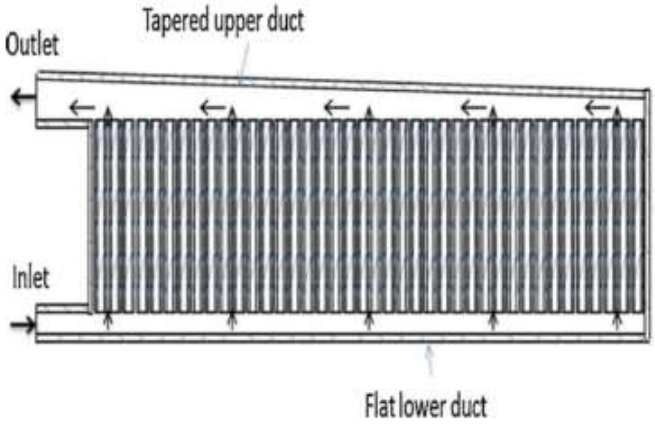

Figure 2-9: Sun et al. upper tapered U-type air flow design [68]

Due to impracticalities in modifying the underlying battery composition to improve thermal conductivity, Sun et al. sought other methods to improve the cell surface temperature uniformity in a following paper [70]. Replacing the base aluminium cooling plate that lined the surface of the pouch cells with a copper plate reduced the surface temperature variation by 0.3 ^oC, owing to the greater thermal conductivity and improved axial heat transfer. A reduction of 0.6 ^oC could be achieved using a thicker aluminium cold plate, however, this reduced the module energy density and increased the peak averaged cell temperature by 0.1 ^oC from the additional thermal resistance. Adding fins into the cooling channel helped lower the thermal resistance, which in turn reduced peak temperature and provided further mechanical stability through resisting the expansion of the pouch cells when electrically loaded. The fins were able to increase the heat transfer rate by 10 %, allowing the peak

temperature to fall by 0.4 °C at a cost of an increased pressure drop by 6 Pa under an air flowrate of 0.0283 $m^3.s^{-1}$. On the module/pack level, Sun et al. also demonstrated that further reductions in temperature variation could be achieved using a modified Z-type air flow design (shown in Figure 2-10). Here, the peak temperature variation between cells was reduced to just 1.1 °C, with a peak averaged cell temperature of 34 °C. Park [71], however, realised that the Z-flow air distribution design may not be applicable in all HEVs due to layout limitations associated with locating the inlet and outlet air passages at opposite ends of the battery module.

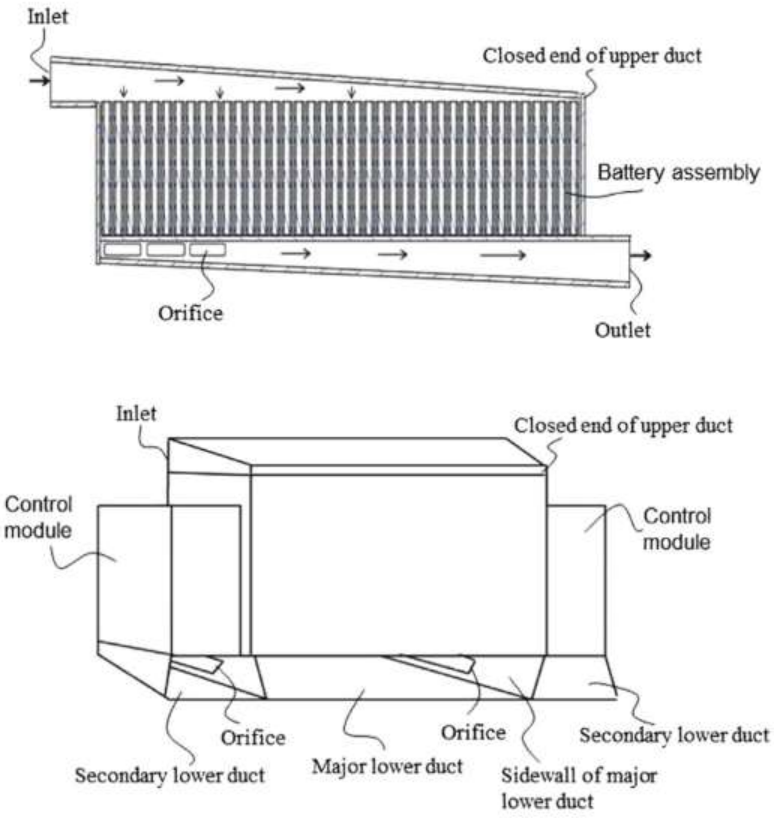

Figure 2-10: Sun et al optimal Z-flow air distribution design [70]

Park and Jung [54] compared the effectiveness of an air cooled system to a liquid cooled system for cooling a simulated HEV battery pack under varying C-rates at steady-state conditions. For the air cooled case, cabin air at 25 °C was actively blown over the cells in the module compartment The modules comprised of 88, 26650 cylindrical format 2.3 Ah $LiFePO_4$ cells arranged in a staggered arrangement, as shown in Figure 2-11.

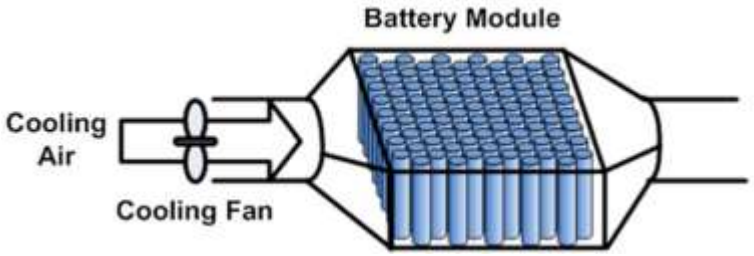

Figure 2-11: Park and Jung series-parallel air cooled module [54]

Upon optimising the aspect ratio of the cells and the inter cell spacing to limit the maximum temperature of the cells within the module to below 60 ^{o}C, whilst also limiting the maximum temperature variation between the coldest and hottest cell in the module to 3^{o}C, a parasitic power requirement of 260 W was required at cell heat generation rates of 5 W per cell ($1.44x10^{5}$ W.m^{-3}, 10.9 C). For the liquid case (which involved direct contact of the cells with mineral oil), a much smaller parasitic cooling requirement of 28 W was required for the same thermal constraints. Increasing the heat generation rate to 7 W per cell ($2.02x10^{5}$ W.m^{-3}, 12.9 C) necessitated 909 W of parasitic power using air and 445 W for liquid. This highlighted the inability of air to efficiently cool the module at higher cell heat generation rates. However, at lower levels of cell heat generation (3 W per cell, $0.869x10^{5}$ W.m^{-3}, 8.4 C), air cooling could achieve more acceptable parasitic power requirements of 29 W. Although still higher than liquid, they concluded that the air case option could be more advantageous for gentler drive cycles, due to the more simplistic design and lower weight compared to liquid which required a secondary air-liquid heat exchanger.

Fan et al. [72] also analysed the effect of gap spacing and cooling distribution technique on peak temperature and temperature uniformity, in this case for 8, 15 Ah prismatic lithium manganese oxide (LMO) cells in an active air cooled PHEV module. The time-averaged cell heat generation rates within the cells were measured with an isothermal calorimeter, with a value of $0.280x10^{5}$ W.m^{-3}.

In their design, air is drawn through the cooling channel spaces between prismatic cells in the module. Similar to the conclusions form Park and Jung for cooling cylindrical cells, they observed from their 3-D simulations that smaller gap spacing favoured a reduction in peak temperature, but a worsening in temperature uniformity for a set air flowrate. Increasing the flowrate of the fan for a set cell spacing reduced peak temperature, but again worsened temperature uniformity. Comparing one sided cooling to cooling on both sides, they found that using one side cooling lead to larger peak temperatures. However, the temperature

uniformity and module compactness improved (shown in Figure 2-12). Their results highlight the conflicting nature between achieving both a lower peak cell operating temperature together with minimising the temperature variation through the cells and between cells in a module, particularly with air as the heat transfer medium.

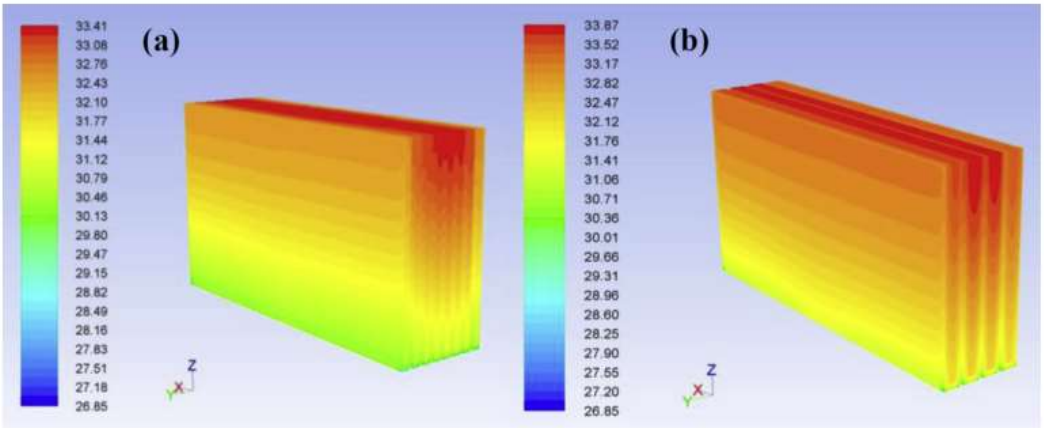

Figure 2-12: Fan et al. temperature profile results after 600 s of a 1.3XUS06 drive cycle (values in ^{o}C) for 8 active air cooled prismatic cells in a module with fan output of 0.00567 $m^3.s^{-1}$ and 27^{o}C inlet air temperature for (a) cooling on each side of the cell with a channel gap of 3 mm (b) 2 cells sandwiched together giving cooling on only one side of each cell with a channel gap of 3 mm [72]

Mohammadian and Zhang [73] found that the temperature uniformity across the surface of prismatic lithium-ion cells (15 Ah, LMO) could be increased via the addition of a pin-fin heat sink. This heat sink constitutes a solid conductive sheet with metallic pins inserted on its surface to increase the heat transfer area. The sink was designed such that the pin-fin height increased along the axial length of the battery, stabilising the heat transfer rate by offsetting the reduction in temperature driving force between the rising air coolant temperature and plate with an increase in heat transfer area. Their design is shown in Figure 2-13.

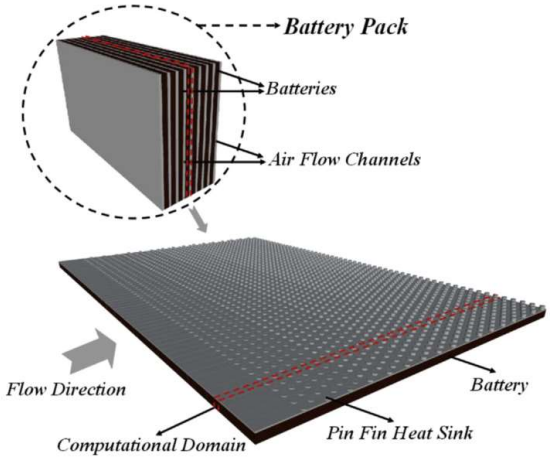

Figure 2-13: Conceptual pin-fin heat sink design from Mohammadian and Zhang [73]

At an inlet air temperate of 25 ^{o}C and flow velocity of 0.2 m.s^{-1}, the maximum temperature variation in the battery and peak temperature decreased by 9.9% and 7.0% respectively with the plate-fin heat sink, as opposed to the plate without fins when discharging at 2 C for 600 s.

Giuliano et al [74] demonstrated that active air cooling could be a viable option for cooling large format 50 Ah lithium-titanate oxide (LTO) pouch cells under high C-rates (4 C) with heat generation at 40 W per cell (0.464x10^{5} W.m^{-3}). In their design (shown in Figure 2-14), air was actively blown through cooling channels between cells in which each cell surface was lined with an aluminium sheet (1.27 mm in thickness). Porous aluminium foam (20 pores per inch, 8% dense) was inserted in the cooling channel to increase the heat transfer area.

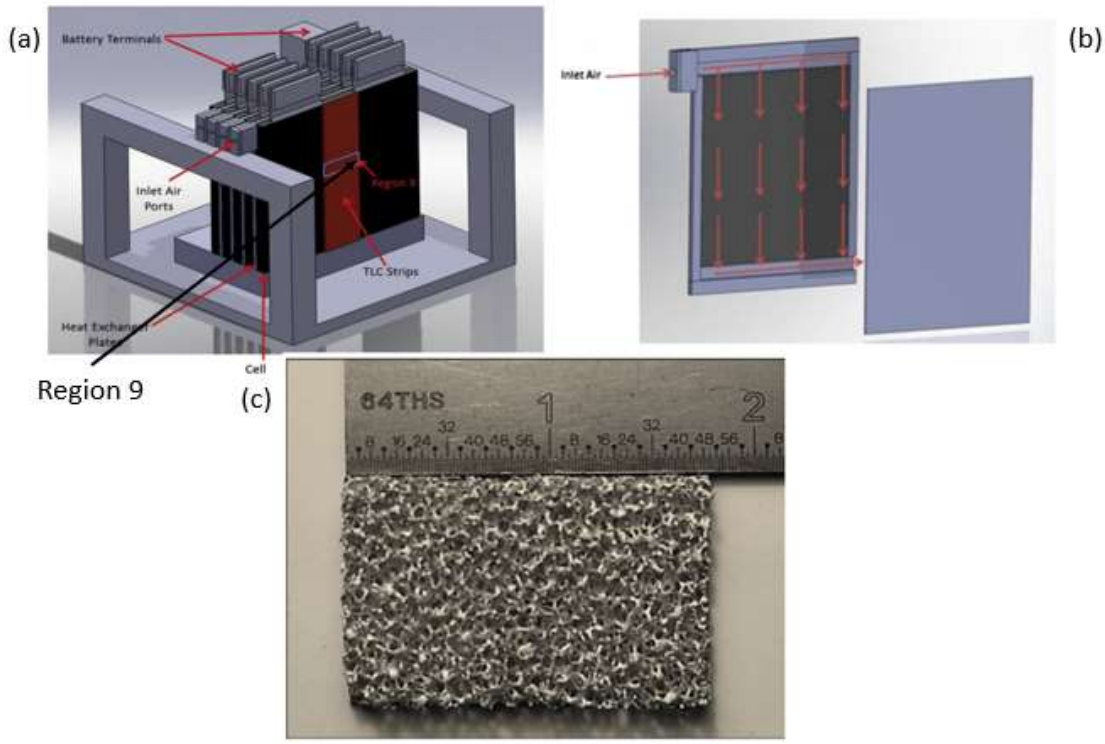

Figure 2-14: Giuliano et al. pouch cell air cooled design (a) stack design (b) air flow passageway (b) porous aluminium foam for insertion into air cooling channels [74]

With an inlet air temperature and flowrate of 22 ^{o}C and 0.0011 m^{3}.s^{-1} per channel respectively, the surface temperature of the cell measured through thermochromic liquid crystal thermography at region 9 (as depicted in Figure 2-14) reached a maximum temperature of 35 ^{o}C after 70 minutes of continuous charge-discharge cycling at 4 C. This required a parasitic fan power of 5.69 W per channel. Decreasing the flowrate of air to 0.0008 m^{3}.s^{1} per channel resulted in a greater increase in exit air temperature, which increased the

maximum cell surface temperature to 37 °C after cycling at 4 C. The fan power decreased to 2.76 W per channel. The authors concluded that the design could limit the maximum surface temperature of the battery to 50 °C, when using inlet ambient air temperatures as high as 40 °C at 0.0011 $m^3.s^{-1}$ channel flowrate. However, they did not report the axial variation in temperature across the surface of the pouch cell. In addition, their specific design is not expected to be practical for real use due to the large cell-to-cell spacing required (and therefore poor volumetric energy density), which exceeds 7 mm between adjacent cell surfaces.

Other air distribution techniques include reciprocating flow. Here the direction of air flow is periodically varied to redistribute the heat and promote thinning of the thermal boundary layer. Mahamud and Park [75] demonstrated that the reciprocating flow distribution technique could reduce the maximum time averaged cell temperature, and peak time averaged cell temperature variation relative to normal series-parallel cooling. Their design is presented in Figure 2-15.

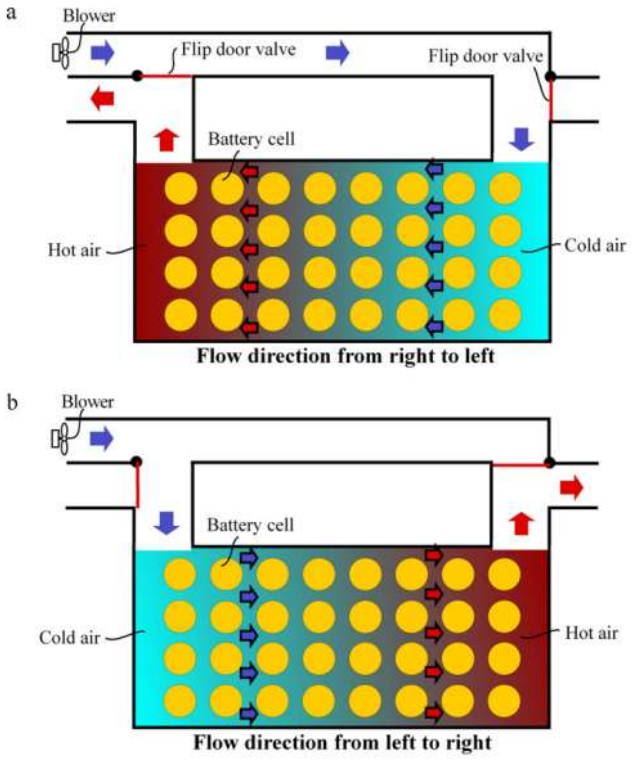

Figure 2-15: Mahamud and Park reciprocating flow distribution technique with altering direction of flow from right to left(a) and left to right (b) [75]

Specifically, for periods of 120 s between flow reversal (with inlet air temperatures of 20 °C, 0.0042 $m^3.s^1$ flowrate and constant cell discharge of 7 C) their computational fluid dynamics

(CFD) model predicated a drop in peak time averaged cell temperature from 29.6 °C to 28.1 °C, with a significant reduction in time averaged maximum temperature variation from 5.5 °C to 1.5 °C upon adopting the reciprocating flow technique. However, the authors stated that these small reciprocating periods on the order of 120 s would not be desirable for practical application, possibly due to the greater parasitic losses incurred from the more frequent flow reversal and higher pressure drop. This presents issues with its application in high heat generating situations, as shorter flow reversal periods would be required for set air flowrates than in a lower heat generating scenario to limit the cell-to-cell temperature variation to its required value. Increasing the air flowrate could extend the length of the reciprocating period, but this does not resolve issues with air series-parallel cooling at high levels of heat generation (mainly inordinate parasitic losses from greater volumetric flowrates [54]). The design is also more complex compared to general air series-parallel cooling due to the inclusion of the reciprocating flow mechanism.

2.2.2.2 ACTIVE LIQUID COOLED BTMS

In active liquid cooled circuits, additional and/or larger pumps may be present relative to the passive system to increases the rate of heat transfer. Actively controlling the inlet temperature of the liquid cooling medium may involve further auxiliary heaters and/or evaporator cores to heat/cool the circulating liquid in the primary cooling loop. A general active cooled liquid circuit is depicted in Figure 2-16.

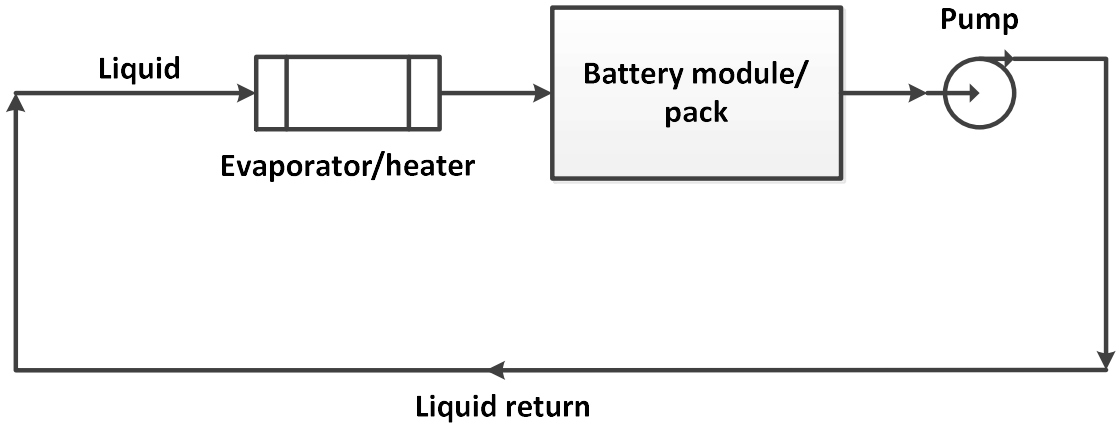

Figure 2-16: General active liquid cooled BTMS

Similar to passive cooling, the liquid may be passed directly or indirectly through tubing/cooling jackets to make contact with the battery cells [76]. Direct cooling usually involves submerging the cells with non-conductive mineral oil, which has the advantage of providing cooling on all exterior surfaces of the cells, therefore, utilising more heat transfer

area [77]. However, as shown by Kim and Pesaran [78] the larger kinematic viscosity to density ratio of mineral oil (with reference to Table 2-1) results in it incurring circa 25 times more parasitic pumping power than water-glycol for the same mass flowrate and hydraulic channel dimeter (under laminar flow conditions and neglecting other pressure drop losses from the duct and tubing design). The lower thermal conductivity and heat capacity of mineral oil relative to water glycol also result in it having a reduced heat transfer efficiency. This is reflected in the results of Chen et al., who demonstrated through simulation that indirect plate cooling pouch cells with a water glycol mixture offered greater control over the cell temperature rise than mineral oil for a given mass flowrate [79]. However, as further highlighted by Kim and Pesaran [78], care must be taken with indirect cooling methods to ensure that the added thermal resistance between the cell surface and heat transfer medium does not offset the heat transfer benefit from using conductive fluids. The risk of leakage may also be greater in these systems that use electrically conductive heat transfer mediums [79] given the potential to create a cell short circuit event [80].

Table 2-1: Properties of typical heat transfer mediums used in automotive battery cooling [78]

Property	Air	Mineral oil	Water-glycol
Density [kg.m^{-3}]	1.225	924.1	1069
Heat capacity [J.kg^{-1}.K^{-1}]	1006	1900	3323
Thermal conductivity [W.m^{-1}.K^{-1}]	0.0242	0.13	0.3892
Kinematic viscosity [m^2.s^{-1}]	1.46×10^{-5}	5.60×10^{-5}	2.58×10^{-6}

An example of an indirect active cooled BTMS currently used in the automotive industry is that of the Tesla Model S. The 85 kWh version of the Tesla Model S contains 16 modules, with each module containing 444 cells connected in an 6S74P configuration [66]. Each module is further connected in series to provide a nominal pack voltage of circa 355 V. The complete Tesla Model S battery pack arrangement can be viewed in Figure 2-17.

Figure 2-17: Tesla Model S battery pack arrangement [81]

Different from the Nissan Leaf, Tesla employ an indirect liquid cooling approach to cool their 7104 cylindrical 18650 cells [66]. This is achieved through contacting a flexible cooling jacket along a portion of the outer radial surface of the cells [82]. This cooling jacket is represented by the yellow material depicted in Figure 2-18.

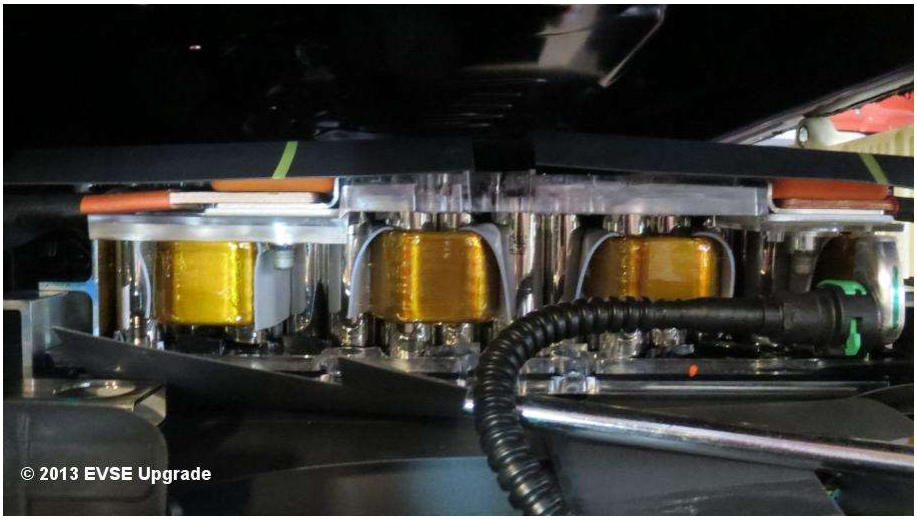

Figure 2-18: Tesla Model S cooling jacket [81]

The hollow cooling jacket contains the liquid coolant. The overall cooling for the battery module involves the coupling of individual cooling jackets in both a series and parallel arrangement as shown in Figure 2-19.

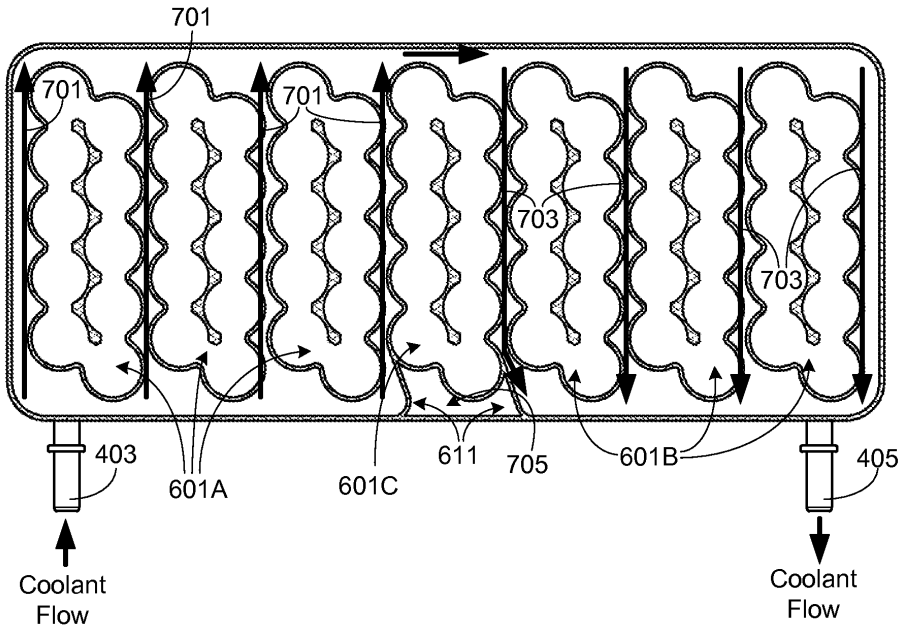

Figure 2-19: Indirect liquid cooling arrangement for the Tesla Model S battery module [82]

As seen in Figure 2-19, the cells are asymmetrically cooled and thus rely on the metallic casing of the cell to conduct the heat from the opposing side towards the cooling source. The design does not utilise full contact with the cell surface, and therefore may only be practical for an EV use case where the cell heat generation rate is low to warrant the reduced heat transfer capability.

Other examples of indirect liquid cooling are those used in the in the first and second and generation of the Chevrolet Volt PHEV. The battery pack configuration for the second generation of the Volt is displayed below in Figure 2-20.

Figure 2-20: Second generation Chevrolet Volt battery pack design [83]

The battery pack consists of 192 pouch cells connected in a 96S2P connection providing a nominal pack capacity of 18.4 kWh and a nominal pack voltage of 360 V [83]. The second and first generation Volt batteries utilise an indirect liquid cooled fin plate to cool the surfaces of the cells as shown in Figure 2-21 [84]. Whilst this method of parallel indirect liquid cooling may be effective, issues are raised with the numerous leakages sources, as each cooling plate represents a minimum of two sources for potential leakage when connected to the primary liquid channel that funnels the liquid into and out of the cooling fin [65].

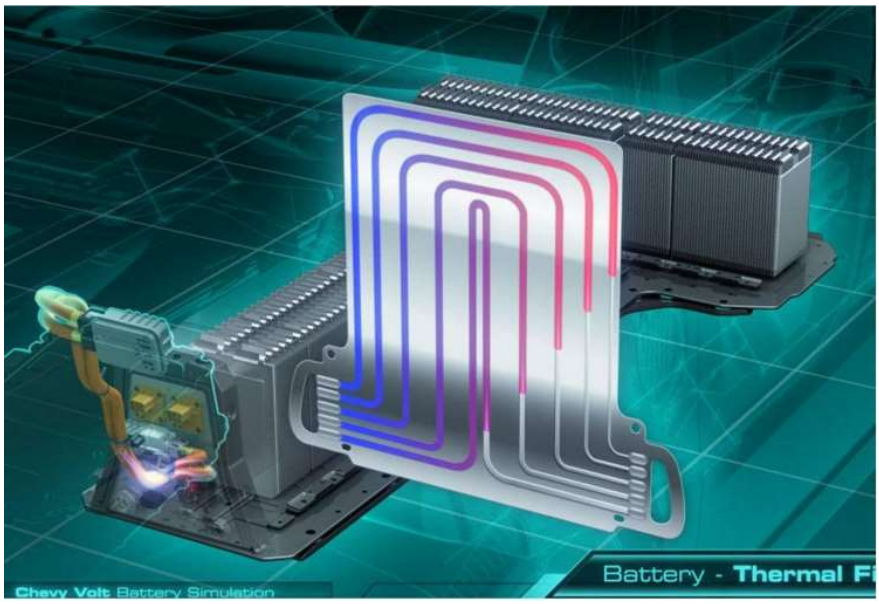

Figure 2-21: Second generation Chevrolet Volt indirect liquid cooling fin [84]

Similar options for indirect liquid cooling with water have been investigated by Huo et al. [85], who analysed the effectiveness of attaching mini-channel cold plates to the surfaces of pouch batteries (7 Ah, $LiFePO_4$ cathode chemistry). Their simulated mini-channel cold plate comprised of an aluminium plate with cooling channels carved through its axial length (depicted in Figure 2-22). Through numerical simulations, the authors examined the effect of channel number, direction of flow through the channels and mass flowrate on the maximum temperature difference across the battery surface and its peak temperature. Increasing the channel number from 2 to 6 reduced the peak temperature from 63.4 ^{o}C to 58.4 ^{o}C following complete 5 C discharge with an inlet water temperature of 25 ^{o}C and channel flowrate of $5x10^{-6}$ $kg.s^{-1}$. Though the temperature difference was slightly worsened with the 6 channel arrangement at the end of discharge compared to that using a lower numbers of channels, the lower cell temperature from the greater overall heat transfer rate was deemed more beneficial, and thus taken forward for their further analysis.

Figure 2-22 shows the effect of differing permutations of flow direction along each of the 6 channels in their design on the axial temperature variation across the cold plate. Here, the location of the pouch tabs is at the left of the cold plate, between the 1st and 2nd and 5th and 6th cooling channels. Feeding cooling liquid from the tab side provided the greatest temperature uniformity and lowest peak cell temperature, due to the greater temperature driving force between the liquid inlet and hotter cell tabs. The authors concluded that Design 1 gave both the lowest peak temperature and temperature variation relative to their other designs, where at the end of the 5 C discharge with a flowrate of $5x10^{-4}$ $kg.s^{-1}$ per channel at 25 °C, the maximum battery temperature reached 30.5 °C with a maximum temperature variation across the battery surface of 4.8°C.

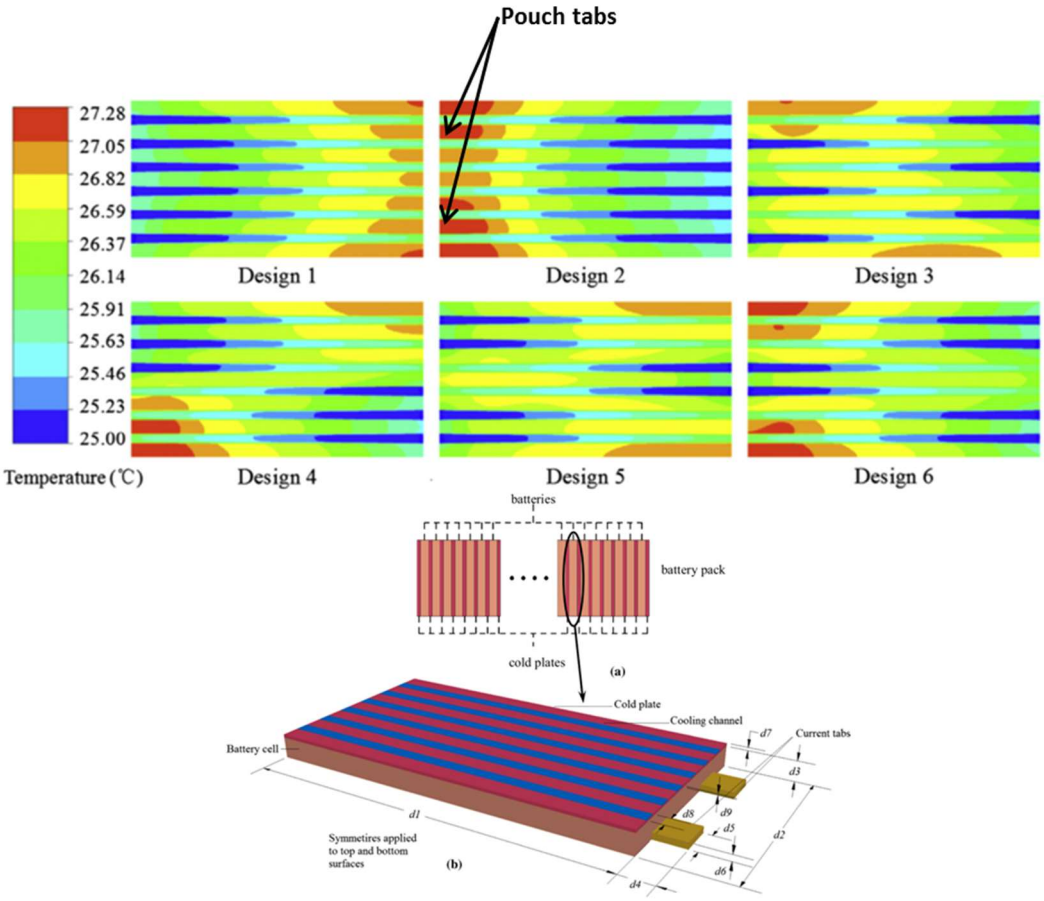

Figure 2-22: Huo et al. axial temperature distribution across the cold plate, for various permutations of flow direction, at the end of a 5 C discharge with an inlet liquid temperature of 25 °C and flowrate of $5x10^{-4}$ $kg.s^{-1}$ [85]

Zhao and Rao [86] investigated the cooling performance of a micro channel liquid cooled cold plate for cooling and array of 42110 cylindrical 10 Ah $LiFePO_4$ cells. Their design, as depicted in Figure 2-23, involves the distribution of liquid through a cold plate that funnels the liquid through micro channels contained in a jacket. The jacket encapsulates each

individual cell, where the flow of liquid through the channels cools the cell from the radial surface. During a 5 C discharge, their cooling design could not limit the maximum battery temperature difference to below 5 °C, either by altering the number of cooling channels, cooling channel size, or mass flowrate through each channel. This highlights the limitations of reducing the temperature gradient through cooling cylindrical cells at the radial surface, which is a result of the poor radial (or cross-plane) thermal conductivity of circa 0.20 $W.m^{-1}.k^{-1}$[87], [88], combined with the long heat transfer pathway between the cell core and outer radial surface. This creates a large thermal resistance for heat transfer through the cell material. As with the Tesla case, such designs of radial surface cooling (particularly for cells with a large diameter) may be incapable of controlling the internal cell temperature gradient below the 5 °C limit under higher C-rates. Radial surface cooling may, therefore, prove particularly problematic for HEV and PHEV usage conditions, where the average cell C-rate during operation is likely larger than for EVs, which is depicted in Table A 2 of Appendix A.4.

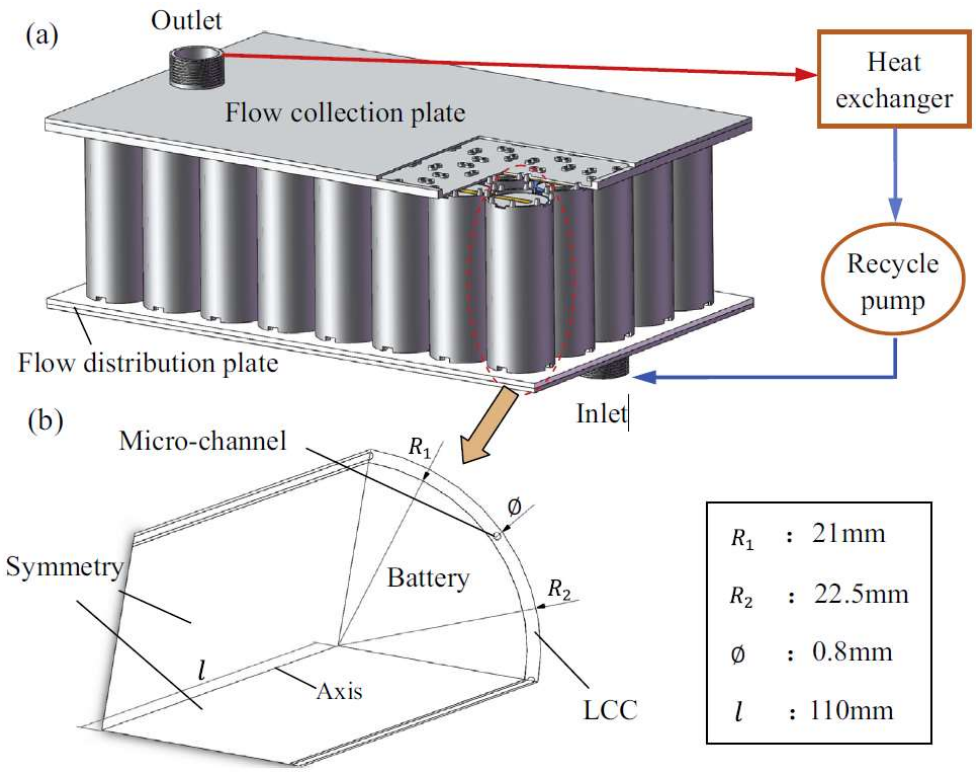

Figure 2-23: Zhao and Rao design of liquid cooled cold plate with incorporated micro channels for cooling the radial surface of cylindrical cells [86]

Other developing methods of indirect liquid cooling involve placing conductive sheets between the battery cells (commonly termed fin cooling or extended surface cooling), where the heat from the cell surface is transferred to an external location which further dissipates the heat [79]. These approaches have the advantage of simplifying the duct and tubing

arrangement, given that the fluid is not passed across the large bodies of all the individual cells. Fewer manifold connections and/or seals may, therefore, be present relative to mini-channel cold plates that reduces the leakage risk. In addition, the external liquid cooled location may also be positioned in a safer area away from the cell compartment, to further improve the overall safety of the battery pack [89]. Basu et al. [89] presented a novel extended surface BTMS design for cylindrical cells (18650 type with a graphite anode and lithium nickel cobalt aluminium oxide (NCA) cathode) using aluminium conduction elements to transfer heat conducted from the cells to two side cold plates. Their design is shown in Figure 2-24.

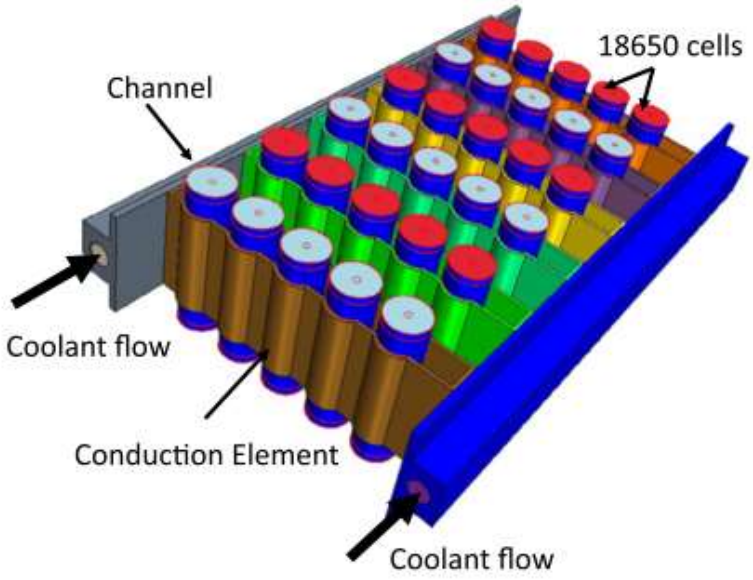

Figure 2-24: Basu et al. conduction based BTMS for cylindrical cells [89]

From their simulations, they concluded that the design could efficiently limit the maximum cell temperature rise across a string of 5 cells to within circa 7 ℃ at the end of a 2.7 C discharge, whilst operating with low liquid velocities in the side cold plates (0.01 $m.s^{-1}$). Hosseinzadeh et al. [50], however, concluded that placing aluminium fins between large format pouch cells may be a poor thermal management choice under more aggressive heat generation conditions (3 C and 5 C). Specifically, for a simulated 40 Ah pouch cell at the end of a 3 C discharge subject to single edge aluminium fin cooling, an extreme volumetric temperature gradient of 22.9 ℃ was predicted through the cell. Increasing the fin thickness from 1.5 mm to 5 mm could lower the gradient to 11.9℃, but may be impractical due to the added weight and volume penalty. Chen et al. [79] further demonstrated that single edge fin cooling large format batteries with aluminium fins may add excessive weight to the cell

(39%), relative to mini-channel cold plate cooling (7%) for a fixed volume penalty. Evidently, there is scope within the literature to improve the thermal efficiency of fin cooling when applied to large format batteries.

2.2.3 DIRECT REFRIGERATION AND BOILING HEAT TRANSFER

Refrigeration cooling of battery cells may be achieved through coupling a battery cooling evaporator plate to the existing refrigerant loop used for the heating, ventilating and air conditioning (HVAC) system, which provides cabin climate control. The overall cooling circuit schematic design for such a system is presented by Huber and Kuhn [53], and is viewable in Figure 2-25.

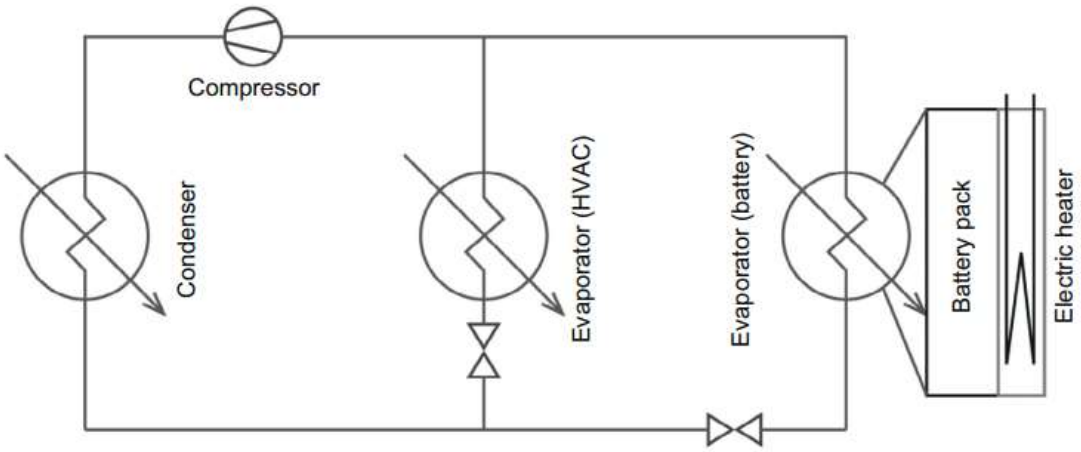

Figure 2-25: Refrigerant loop for battery pack cooling [53]

Huber and Kuhn highlight that the direct refrigeration cooling approach (using an evaporator plate for cooling battery cells) can increase the compactness of the cooling system, and reduce weight compared to a liquid cooled system. This is since additional secondary coolant loops are not required, thus removing the need for additional components (e.g. an air-liquid heat exchanger, chiller and coolant loop) [53]. In addition, since refrigeration involves boiling heat transfer, higher convective heat transfer can be obtained than with liquid convection [90]. This has the potential to provide lower peak temperatures and greater temperature uniformity, due to the constant temperature evaporation process. However, the coupling of the battery cooling system to the same refrigeration loop as the HVAC system can raise control issues, since the thermal loads of the battery cooling system and HVAC system are now interlinked.

An example of a direct refrigeration method for a BTMS is that used in the BMW i3 and BMW i8.The 22 kWh BMW i3 battery pack consists of 8 battery modules connected in series, with

each battery module containing 12 prismatic cells (also connected in series) to give a nominal pack voltage of 360 V [91].

Cooling the battery modules is achieved through placing the modules onto a base rack of cooling tubes (as depicted in Figure 2-26) whereby refrigerant is passed through the coolant tubes providing the cooling through direct expansion of the refrigerant. The images from Figure 2-26 and Figure 2-27 have been acquired from a video by Munro & Associates, INC. in [92].

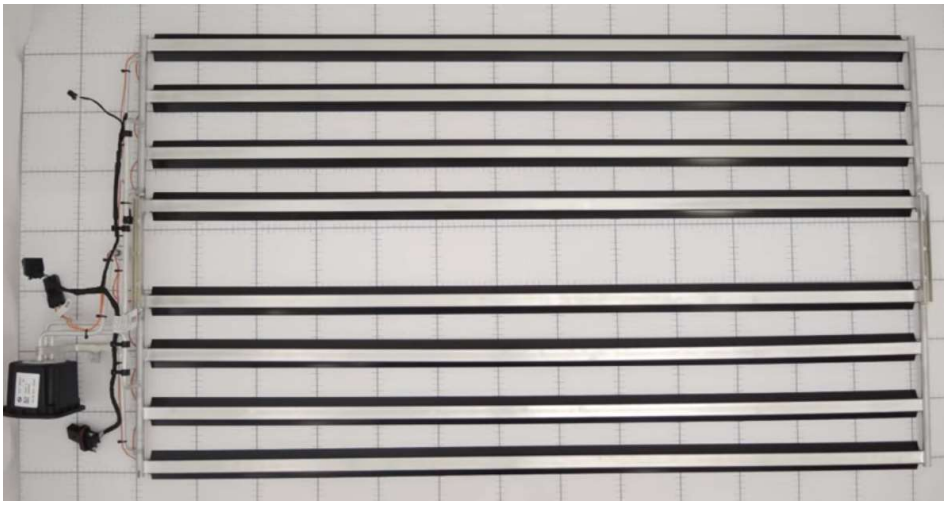

Figure 2-26: BMW i3 base refrigerant coolant tubes [92]

Figure 2-27: BMW i3 battery module [92]

Extended surfaces or fins may be connected to the sides of the cells and the bottom cold plate to increase the overall heat transfer area, allowing heat to also be extracted from the wide surfaces of the cells as well as their base. An example of a method using extended surfaces/fin cooling connected to a bottom base plate is represented schematically in Figure

2-28. Here, metallic fins act to conduct all the heat received from the battery surfaces towards the cold plate, which is further cooled by direct refrigeration [93]. It is noteworthy that the fin ends may also be cooled with an air or liquid heat transfer medium for an air or liquid based BTMS.

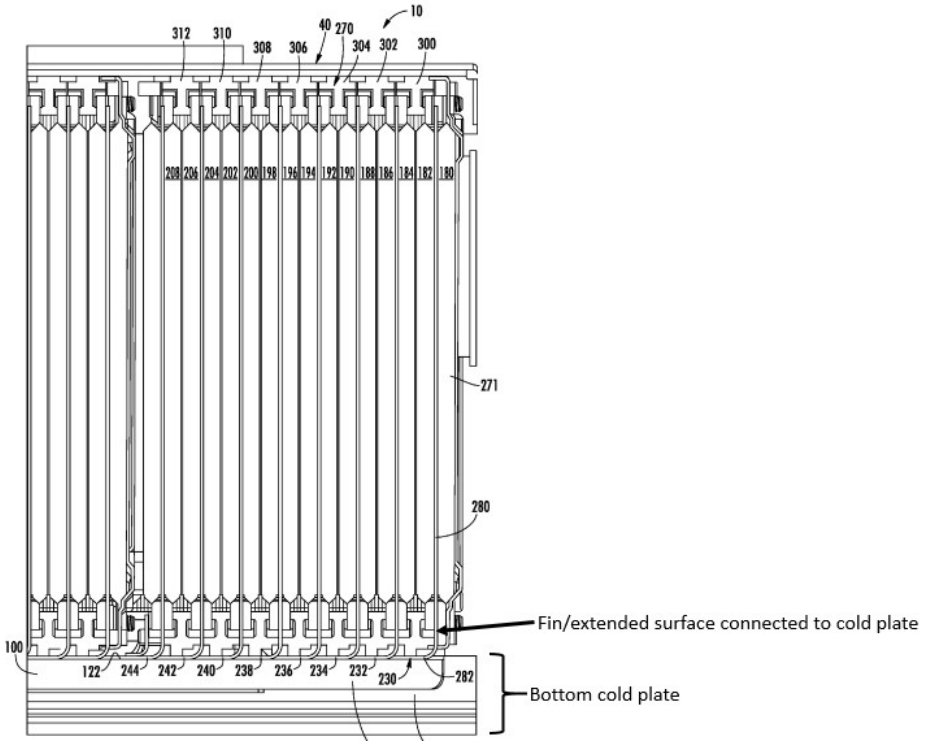

Figure 2-28: Adapted from LG Chem patent on refrigeration cooling with cold plate and extended surfaces/fins [93]

As discussed in Section 2.2.2.2, the heat transfer effectiveness of this method heavily relies on the thermal properties of the fin material, which must have sufficient thermal conductance and or/thickness to provide an acceptable thermal resistance to satisfy the BTMS thermal constraints.

Other examples of utilising boiling heat transfer for cooling battery cells have been conducted by Gils et al. [94], who investigated the efficiency of utilising a dielectric fluid (Novec 7000) with a low boiling temperature for cooling a low capacity cylindrical cell (1 Ah). They found that without boiling, submerging the cell in the liquid provided greater heat transfer through natural convection of the fluid than compared to air due to the greater thermal conductivity. At atmospheric pressure, the dielectric Novec 7000 fluid, however, boiled at 34 ^{o}C, which was induced by repeated cycling of the cell at 5 C. Upon boiling, the latent heat of vaporisation was able to eliminate the temperature difference across the outer surface of the cell due to the constant temperature process, operating in similar principles

to a phase changed material (PCM). The authors noted that the pressure within the battery module could dictate the boiling temperature of Novec 7000. At 0.05 atm underpressure, the boiling initiated at lower temperatures, whereas at 0.05 atm overpressure boiling could be supressed. Control over the pressure within the module could therefore dictate the onset of boiling and degree of boiling, providing greater control over the heat transfer rate than a wax based PCM which has its melting temperature fixed by the material properties. However, the high density of Novec 7000 (circa 1400 $Kg.m^{-3}$) makes it heavier than conventional paraffin wax (circa 900 $kg.m^{-3}$) [39], and may thus incur a larger weight penalty than PCM depending on the amount of fluid required. It is expected that the majority of the parasitic requirements needed for this design will be in attaining the required overpressure and/or underpressure within the module compartment.

2.2.4 PHASE CHANGE MATERIAL (PCM) PASSIVE AND ACTIVE BTMS

An alternative to conventional air and liquid BTMS has emerged in the form of utilising PCM [95]–[99]. These materials work by providing a large thermal capacity, where upon melting, large quantities of heat can be absorbed during the constant temperature phase change process.

Sabbah et al. [97] demonstrated that passive cooling obtained by the use of PCM could be comparable, and even surpass active air cooling at high C-rates (6.67 C). In their model, they compared the cooling effectiveness of actively blowing air between the interstitial spaces of an in-line arrangement of 18650 type cylindrical 1.5 Ah cells (20 cells giving 0.111 kWh per module), to that of filling the space with PCM. At 6.67 C and 25 ^{o}C ambient temperature, the PCM (graphite/PCM-composite) controlled the cell temperature to 43 ^{o}C after 450 s, which was comparable to active cooling using air (shown in Figure 2-29 (a)) that required 0.071 W of fan power). At a higher ambient temperature of 45 ^{o}C under the same C-rate, upon reaching approximately 52^{o}C the melting of the PCM maintained the volume averaged temperature of the cell below 55^{o}C (Figure 2-29 (b)), which could not be achieved by active air cooling. The authors stated that an inordinate amount of fan power would be required using active air cooling to achieve similar temperatures as the PCM under these conditions. The PCM also achieved superior temperature uniformity across the pack than the air cooled case, with a near zero temperature variation between cells of 0.1 ^{o}C using the PCM as opposed to the much higher value of 4.2^{o}C for the air case at 25 ^{o}C ambient temperature and flow Reynolds number (Re) of 631. However, their results only include the value of the volume averaged cell temperature, and not the exact peak cell temperature that is present

within the core of the cell, giving no information on the overall cell volumetric temperature gradient.

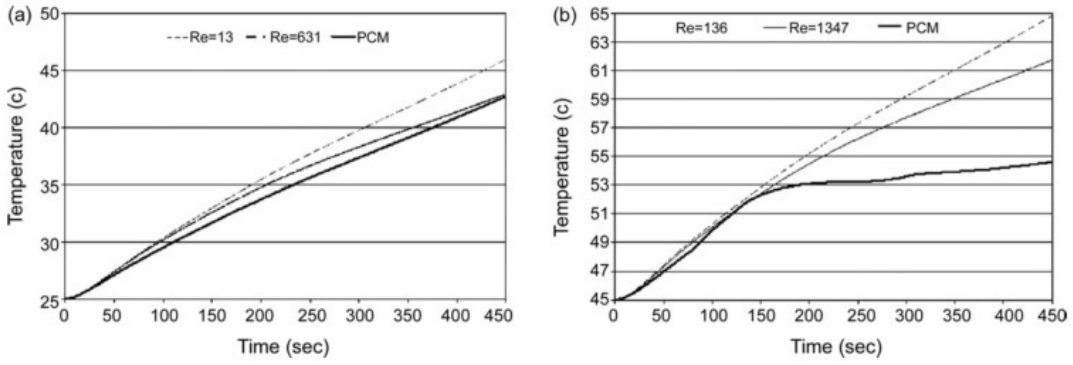

Figure 2-29: Sabbah et al. volume averaged temeprature comparison between PCM cooling and air cooling with different channel reynolds numbers at 6.67 C discharge for (a) 25 °C ambient (b) 45 °C ambient [97]

Whilst promising, concerns over the use of PCM based BTMS solutions have arisen, particularly for application in HEVs where the battery is continually cycled at high rates posing issues for prolonged thermal management [47]. In these cases, the low heat transfer capability of natural air convection may be insufficient to recuperate the PCM latent heat, giving only finite thermal control up until the whole PCM mass melts. Attempts to address these issues have involved coupling the PCM with an active cooled air system as discussed by Ling et al. [98]. The authors showed that this coupled system enabled the PCM to recover sufficient quantities of latent heat to allow thermal control across more cycles than the pure passive PCM relying solely on natural convective heat transfer. However, this method requires care such that the presence of active air flow does not also induce a temperature gradient across the cells.

Other issues associated with the use of PCM include the low thermal conductivity of waxes (circa 0.12-0.25 $W.m^{-1}.K^{-1`}$ for paraffin wax [51]), although these can be increased through the addition of additives such as expanded graphite [100]. Increased weight (high density), non-uniform melting across the pack, and issues over leakage with harnessing the liquidised PCM in the correct location also present challenges for PCM based BTMS [39], [101].

2.2.5 HEAT PIPE PASSIVE AND ACTIVE BTMS

With their high effective thermal conductance, heat pipes can transport large quantities of heat over long distances with minimal thermal resistance relative to that of conventional solid conductors e.g. solid copper [56].

Different varieties of heat pipe exist, including variable conductance, flat and cylindrical [56]. Each contain a wick structure (usually comprised of a sintered metal material) that lines the length of the outer wall, as depicted in Figure 2-30 .

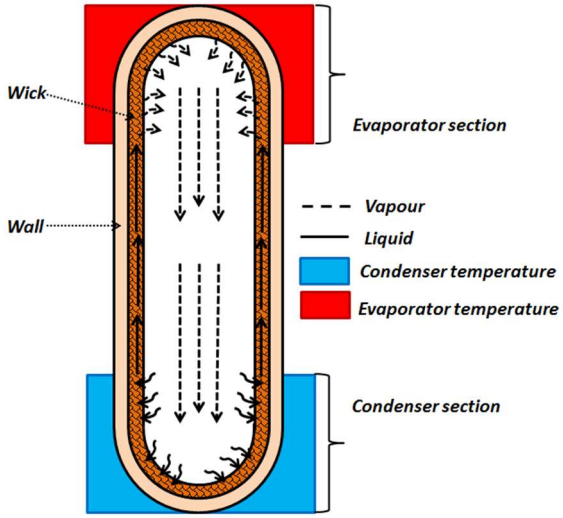

Figure 2-30: Operating principles of typical cylindrical heat pipe

A heat transfer fluid is contained within the pipe under vacuum, where the degree of evacuation dictates its vaporisation temperature. In the evaporator section, heat is transferred through the pipe wall into the wick structure causing the interstitial fluid to vaporise. The latent heat of vaporisation allows large quantities of heat to be absorbed with minimal temperature rise of the working fluid. The pressure gradient created from vaporisation channels the vapour through the heat pipe mandrel towards the condenser section, where the latent heat of condensation is absorbed by the condenser. The condensed liquid is then pumped back towards the evaporator section via capillary forces created in the wick structure. The wick structure distinguishes a heat pipe from a thermosyhpon, with the heat pipe being able to transport liquid against gravitational forces [56].

As heat pipes require no moving parts, or any input work to operate, they are considered as passive devices. However, the heat pipes function only to transport heat with lower thermal resistance; therefore, the method in which the heat is removed at the location for heat transfer (e.g. the condenser end) may be passive or active based. The following accounts of heat pipe use for BTMS will, therefore, include both active and passive methods of removing heat from the condenser sections of the heat pipe.

Wu et al. [102] demonstrated that inserting a heat pipe into two annular aluminium fins attached to the wall of cylindrical cells (12 Ah cylindrical cell 44 mm diameter, 110 mm long)

dramatically reduced the cell surface temperature. At the end of a 0.83 C discharge, the measured surface temperature with only the annular fins attached reached 45 ^{o}C under natural convection with air at 15 ^{o}C. Inserting the copper heat pipe into the fins reduced the temperature to 38 ^{o}C. Whilst both methods of cooling gave a near uniform temperature across the outer cell surface, large temperature gradients of up to 20 ^{o}C were simulated to remain between the battery centre and surface due to the poor radial thermal conductivity of the battery material. Using forced convection of air over the condenser ends of the heat pipe (which were attached to metallic fins) further reduced the surface temperature to circa 30 ℃ whilst maintaining the uniform temperature gradient across the outer cell surface. However, direct air blown across the complete cell surface attached to the aluminium fin without the heat pipe gave a lower temperature of circa 26 ℃, albeit at the cost of inducing a surface temperature gradient of 3.5 ℃. This highlights that the benefit of the heat pipe, in this instance, is in its ability to conduct heat to a potentially more preferable location for external cooling (at the cost of adding a thermal resistance leading to slightly higher surface temperatures), rather than requiring air to be blown directly across the cells themselves.

Tran et al.[103] investigated the effectiveness of using flat heat pipes for cooling battery modules designed for HEVs. Flat and induction heaters were used to simulate the nominal and transient heat flux through the side of the battery module, which comprised 14 cylindrical cells (7 Ah 38 mm diameter, 142 mm length) within a resin matrix. Under natural convection, the copper heat sink with fins reached a maximum temperature of 46 ^{o}C at the heat sink-heater interface, when an imposed heat flux of 0.115 W.cm^{-2} was applied from the flat heater. Attaching the flat heat pipe with thermal grease to the base of the heat sink reduced the thermal resistance and lowered the maximum temperature to 38 ^{o}C for the same conditions. Under forced convection of air at 0.2 m.s^{-1} over the fins, the heat pipe again outperformed the copper heat sink without the heat pipe, effectively reducing the thermal resistance of the heat sink by 20%. No significant change in performance was observed between horizontal and vertical orientations of the heat pipe, however, slight decreases in performance were seen upon inclination to 20^{o} above horizontal, where the maximum temperature increased by 2 ^{o}C. The heat pipe also minimised the amplitude of temperature fluctuations during transient heat flux due to a lower overall thermal resistance, with larger fluctuations observed with the lone copper heat sink, indicating its reduced effectiveness in limiting the peak temperature rise within the battery pack.

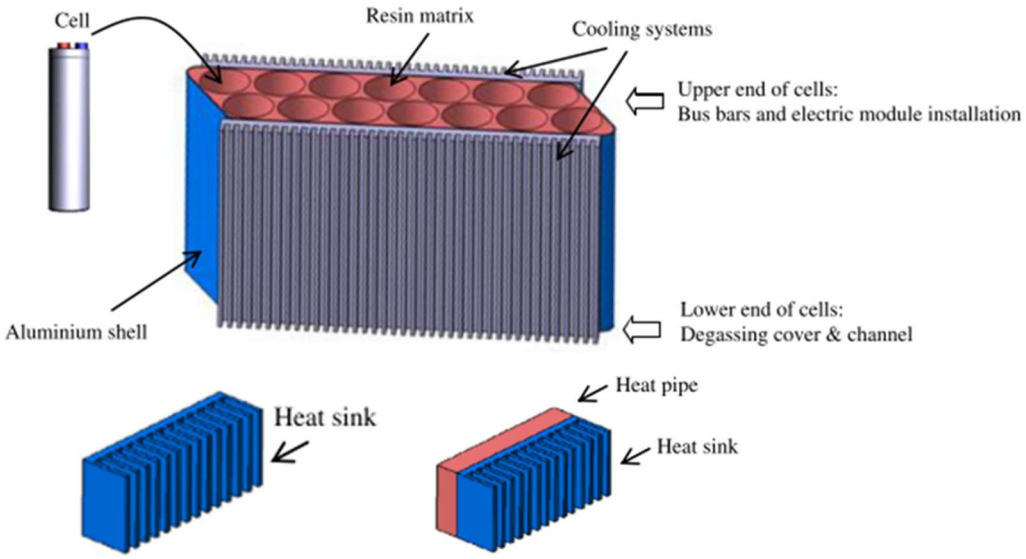

Figure 2-31: Cooling design as presented by Tran et al. [103]

Rao et al.[104] evenly distributed 4 cylindrical copper heat pipes (5mm diameter, 18 mm length) with flat evaporator sections across the surface of a restive heater using thermal silica as the interface material. The condenser sections of the heat pipes were immersed in a thermostat bath, maintained at a temperature of 25 ^{o}C. The schematic of their experimental set-up, displaying the 4 heat pipes, battery and thermostat bath can be viewed in Figure 2-32.

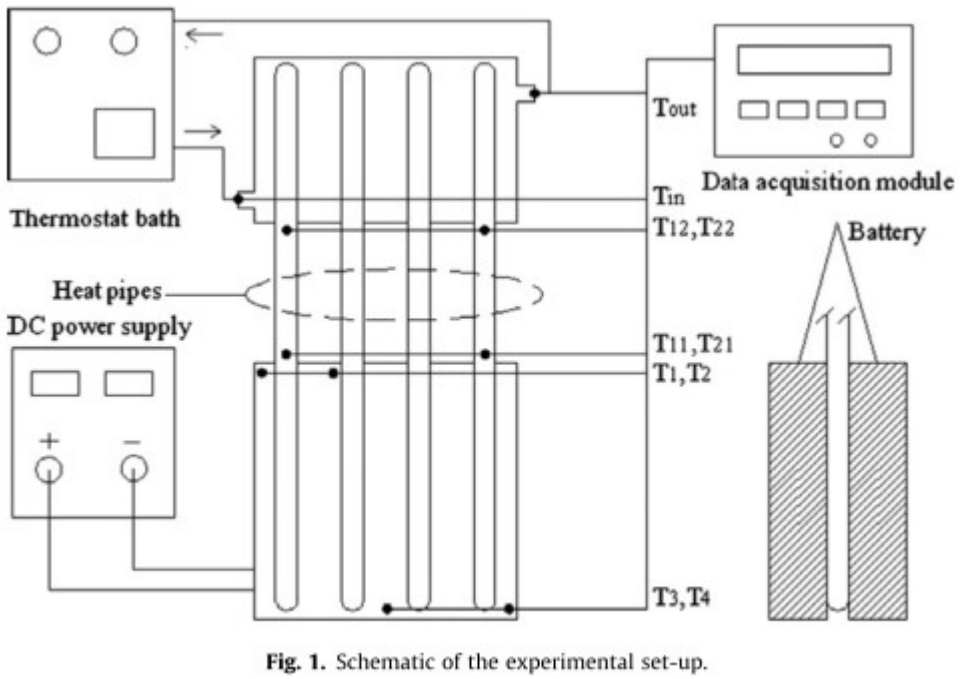

Figure 2-32: Rao et al. heat pipe experimental set-up [104]

Upon reaching steady-state at 30 W input power, the maximum surface temperature of the heater reached 36 °C, with a maximum temperature difference slightly under 5 °C across the surface of the heater. Increasing the power input to 50 W increased the maximum temperature to 42 °C, with a maximum temperature difference of 8 °C. Varying the orientation of the heat pipe away from vertical worsened the temperature uniformity, with the maximum temperature difference exceeding 5 °C at 30 W input power. This is believed to be due to the lower power capability of the heat pipe when the return of liquid to the evaporator section is not aided fully by gravity. The temperature gradient within the heater was not reported.

Following from Tran et al, Zhao et al. [48] extended the use of the flat heat pipes to cooling pouch type batteries (3 Ah and 8 Ah). Three aluminium flat heat pipes with a grooved wick structure were used to cool four pouch cells, with each heat pipe sandwiched between two cells. Five cooling methods were examined for cooling the condenser ends, which included natural convection, horizontal and vertical fan cooling, immersion in a water bath and horizontal spray cooling. These arrangements are depicted in Figure 2-33.

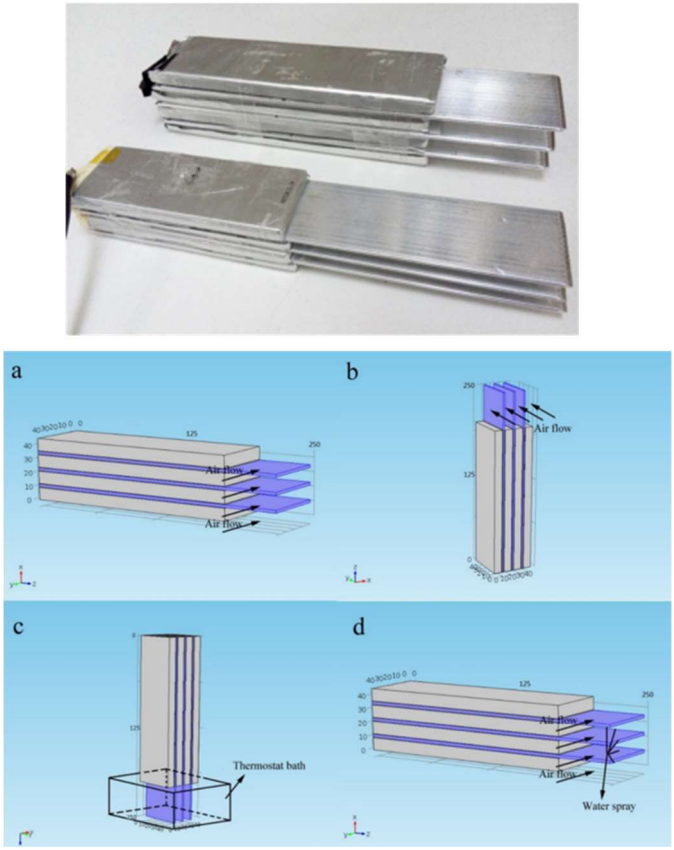

Figure 2-33: Zhao et al. flat heat pipe cooling design (a) horizontal fan (b) vertical fan (c) water bath (d) spray cooling [48]

The temperatures at various points across the cell stack (as depicted in Figure 2-34) were measured using K-type thermocouples, where the cross-plane temperature differences across the stack (T_6-T_3) and across the surface of the centre battery (T_a-T_e) could be obtained.

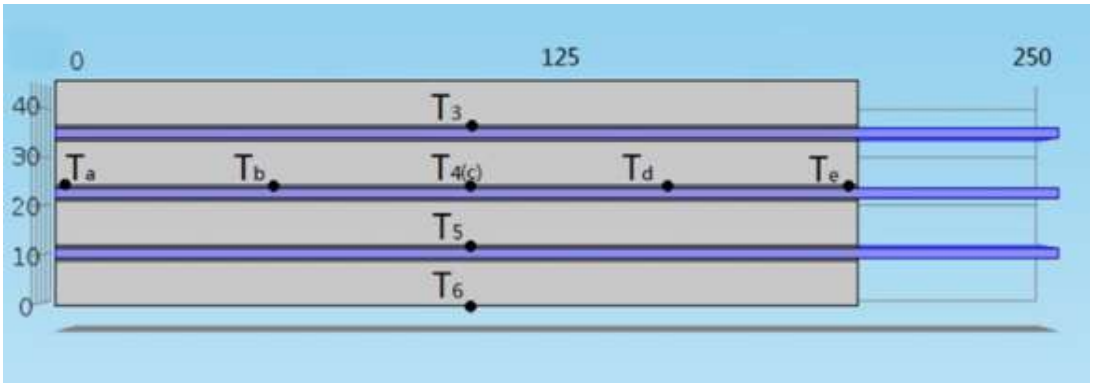

Figure 2-34: Locations of the K-type thermocouple measurements from Zhao et al. [48]

Following complete 3 C discharge of the 3 Ah cells, the maximum temperature of the battery pack reached 41.1°C under natural convection at room temperature (25 °C), a 7.7 °C decline from 48.8 °C without the heat pipes. The maximum temperature difference across the battery stack also dropped from 6.8 °C to 2.9 °C, with the centre cell surface temperature difference ($T_a - T_e$) dropping from 2.1 °C to 0.8 °C with the heat pipes in place. Using forced convection of air to cool the heat pipe ends in both horizontal and vertical orientations reduced the peak temperature further to 31.8 °C. The temperature uniformity also improved, with the maximum temperature difference across the stack dropping to 2.2 °C and across the centre cell to 0.7 °C. Submerging the condenser ends in a water bath at a constant temperature of 25 °C proved less effective than forced convection of air, with the peak battery temperature reaching 38.2 °C. This poor performance was attributed to bubble formation at the condenser ends reducing the local heat transfer coefficient [48]. The use of active convective liquid heat transfer and/or a defoamer was suggested to remove the bubbles. Spray cooling provided the greatest temperature uniformity on both the stack and cell-level. The maximum stack temperature gradient reduced to just 1.2 °C, with the centre cell surface temperature gradient reducing to 0.5 °C with spray cooling. No variation in heat pipe performance was observed between vertical and horizontal orientations, which was attributed to the thin design and internal wick-structure providing a large capillary force.

Ye et al. [45] sought to improve the heat transfer from flat heat pipes (which were wedged in between large format, 10 Ah prismatic cells) by extending the surface area of the condenser section. The overall structure termed the 'heat pipe cooling plate' (HPCP),

included a rectangular evaporator section with cylindrical condenser ends, continuing the wick structure into the condenser section, as seen in Figure 2-35 (b).

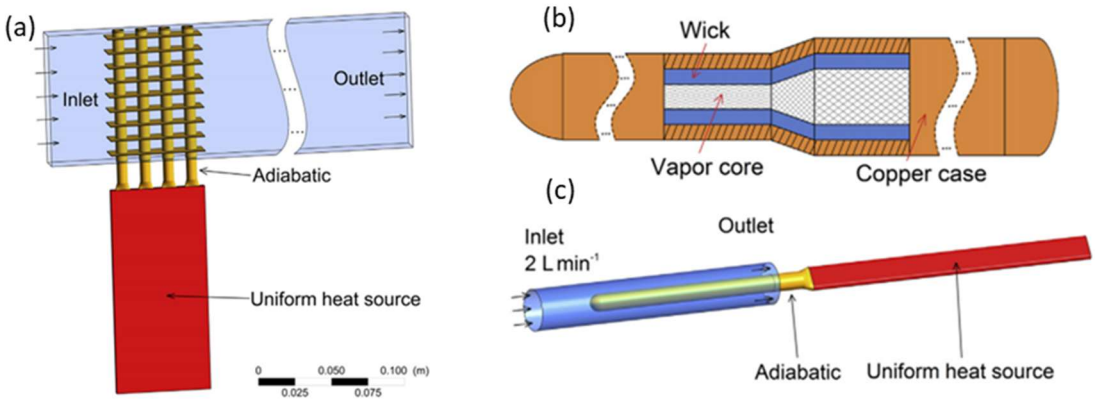

Figure 2-35: Ye et al heat pipe cooling plate (HPCP) design with (a) HPCP with added copper fins on the condenser section (b) HCPC internal structure (c) condenser section cooling method without copper fins [45]

The authors compared the effect of different cooling approaches on the temperature uniformity and peak temperature of the HPCP. Increasing the number of heat pipes in the structure reduced peak temperatures within the HPCP. However, larger temperature variations were present across the HPCP. Presumably, this was due to the increased rate of the water temperature change, driven by the greater heat rejection from the additional heat pipes, leading to a reduction in local heat transfer coefficient upon progression along the cooling channel [45]. Installing copper fins (as depicted in Figure 2-35 (a)), and two copper heat spreaders soldered to the 4 heat pipes attached to the battery wall via thermal paste and compression helped reduce the peak temperature. This also improved the temperature uniformity of the HPCP. At 8 C charge (which corresponded to an average cell heat generation rate of 54.4 W (3.993×10^5 $W.m^{-3}$)), in which the heat generation was measured using an accelerated rate calorimeter, the temperature difference across the HPCP was calculated to fall from 5.3 °C to 1.2 °C upon the addition of the copper heat spreaders. However, such additions are expected to incur great weight to this particular BTMS design due to the use of solid copper.

Using air as the channel cooling medium could maintain the maximum battery temperature below 40 °C following a 5 C charge (1.861×10^5 $W.m^{-3}$ cell volumetric heat generation), achievable with the enhanced heat transfer from the fins. However, due to the poor heat capacity of air (1005 $J.kg^{-1}.K^{-1}$ for air compared to 4182 $J.kg^{-1}.K^{-1}$ for water at 20 °C), a temperature rise of 0.9 °C was observed for the air exit temperature after passing one HPCP. Upon scale up to the module level, this temperature increase would accumulate, leading to

potentially large module-level temperature variations with such a series flow distribution method. Therefore, the authors concluded that air cooling would likely be infeasible using the series cooling approach, and recommended the use of heat transfer mediums with greater heat capacities, such as mists or pure liquids.

Overall, heat pipes have shown versatility in the thermal management of lithium-ion cells. Rapid conduction allows heat to be transferred to areas where increases in surface area can be readily achieved with minimal thermal resistance, improving the effectiveness of natural or active convection. The internal wick structure can enable heat pipes to operate against gravity, however, care must be taken in the design of the wick structure to ensure that the power capabilities of the heat pipe can be achieved. The variety of shapes and custom sizes of heat pipes also allows for non-intrusive methods of heat extraction/provision, preserving compactness within battery modules. However, it is expected that the method in which heat is removed from the condenser ends will require careful consideration as to not add excessive weight to the BTMS (for example the case of Ye at al. that examines the use of copper fins attached to the heat pipe ends, which may be impractical from a gravimetric energy density standpoint).

2.2.6 INTERNAL CELL COOLING TECHNIQUES

Externally cooling the surface of lithium-ion cells can offer limited control over the peak temperature that exists in the internals of the cell. In addition, cells which are cooled externally on a surface that is perpendicular to the layers within the cell (i.e. on the radial surface for cylindrical cells or the front and back faces of pouch/prismatic cells) can be susceptible to large internal temperature gradients. This is due to the poor effective cross-plane thermal conductivity (circa 0.20 $W.m^{-1}K^{-1}$) of lithium-ion cells, which can be near two orders of magnitude smaller than the overall effective axial thermal conductivity of the cell (circa 30 $W.m^{-1}K^{-1}$) [87], [88]. Indeed, Wu et al. [102] noticed that the simulated radial temperature gradient through a 40110 type cylindrical lithium-ion battery cell could reach near 20 ℃ at the end of a 10 A constant current discharge, with the axial temperature gradient across the cell surface reaching only a maximum of 2.5 ℃ under natural convective cooling of the cell surfaces with air. Song and Evans [105] also observed this effect for cooling a stack of prismatic cells. Cooling the ends of the stack lead to an increase in the temperature gradient across the stack due to the low cross-plane thermal conductivity of the stack. However, cooling the top and bottom of the stack effectively removed the majority of the

temperature gradient, due to the increased thermal conductivity along the axial plane of the stack.

The inability to remove heat from the core of the cell can be particularly problematic for cylindrical cells. This is since the heat transfer pathway between the cell core and external surface is typically longer than for comparable pouch cells, by circa: 44% for a common 18650 cell relative to a 10 mm thick pouch cell which can be cooled externally on both sides. Therefore, larger perpendicular gradients may be present within these formats. In light of these issues, a few researches [106], [107] have investigated methods that can extract heat directly from within cylindrical cells, thus reducing the heat transfer pathway between the hotter regions of the cell and the cooling source to reduce the internal temperature gradients through the cell.

Sievers et al. [106] (through simulations) investigated the effectiveness of cooling cylindrical cells (33.6 mm diameter, 142.8 mm length and with a nominal capacity of 7.5 Ah) through incorporating an internal cooling channel that traverses the mandrel of the cell. Their conceptual cell cooling design is depicted in Figure 2-36.

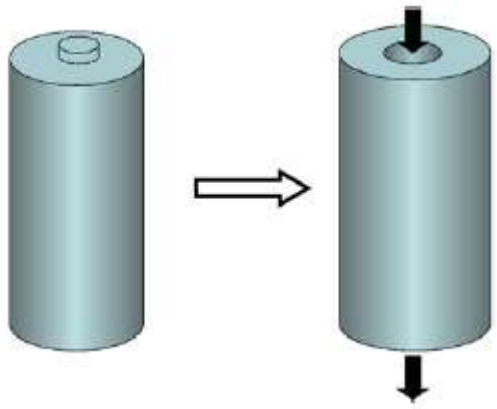

Figure 2-36: Sievers et al. internal cooling tube design for cylindrical battery cells [106]

In their design, dielectric silicon heat transfer oil (Syltherm 800) was modelled to pass through the cell mandrel and alongside the outer radial surface and tabs of the cell at a velocity of 1.4 $m.s^{-1}$. Their simulated results for the temperature profile through the cell for varying diameters of the internal cooling channel are shown in Figure 2-37.

For a constant internal tube diameter, increasing the velocity of liquid from 0.8 $m.s^{-1}$ to 1.4 $m.s^{-1}$ was observed to give only a small reduction in the peak cell temperature, signifying that the dominant thermal resistance present to heat transfer was from conduction through the material of the cell, rather than from axial convection through the cell mandrel. Altering the

geometry of the cell through increasing the diameter of the internal cooling channel gave the largest reduction in cell temperature, but at an ever increasing cost of decreasing energy density.

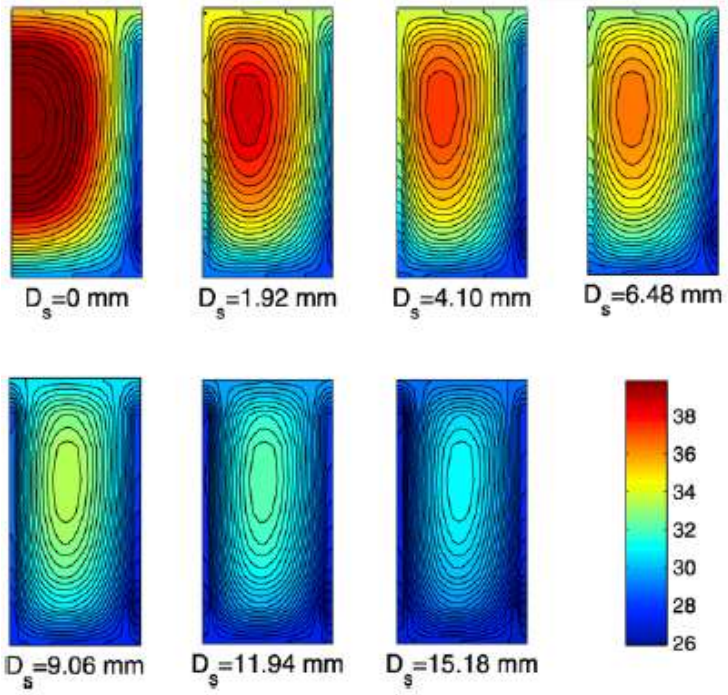

Figure 2-37: Sievers et al. results for the temperature distribution through a cylindrical cell, subject to cooling with dielectric silicone oil passed through the cell core and across the outer radial surface at an inlet velocity of 1.4 m.s^{-1}, for varying diameters of the internal cooling tube [106]

The authors stated that the maximum internal cell diameter should not exceed 18.9 mm (56 % the value of the overall cell outer diameter of 33.6 mm) in order to retain a plausible cell geometry. Their results for the variation in maximum and minimum cell temperature against internal tube diameter, and for different inlet velocities of cooling fluid are show in in Figure 2-38.

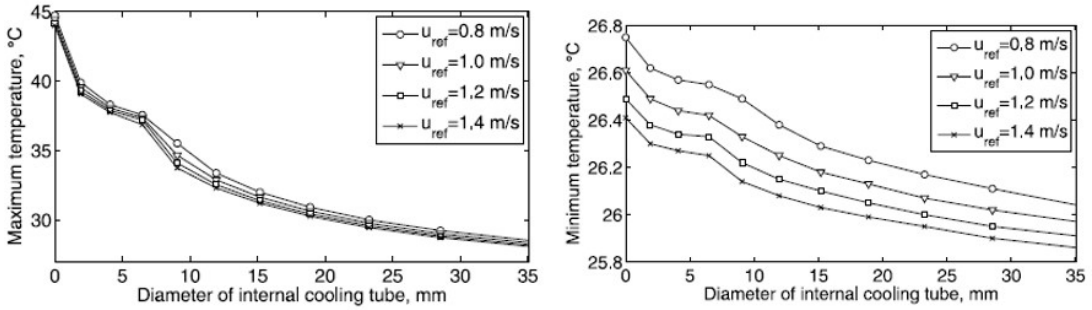

Figure 2-38: Sievers et al. simulation results for maximum (left) and minimum (right) cell temperature as a function of coolant flowrate and internal tube diameter size [106]

Sievers et al. also assessed the performance of substituting the internal cooling channel with a solid rod of copper or aluminium to conduct the heat axially out from the cell core. Through their simulations, they noted that for tube/rod diameters in excess of 5 mm, the copper bar could achieve greater cooling than with air as the cooling fluid through the internal tube. In the case of an aluminium rod, a much larger tube diameter in excess of 10 mm was required to exceed the performance of air cooling, due to the reduced axial thermal conductivity (240 $W.m^{-1}.K^{-1}$) compared to copper (395 $W.m^{-1}.K^{-1}$.) [106]. However, the copper bar could not reach the performance of liquid cooling with dielectric oil for any rod/tube diameter size.

Shah et al. [107] extended the concept of internal cooling via the insertion of a heat pipe into the mandrel of an experimental cylindrical cell, where the condenser end protruded from the bottom tab. Under natural convection on the cell external radial surface, with forced convection on the heat pipe condenser end, the temperature of the cell core was reduced by 20 ℃ with the heat pipe when the cell heat generation rate was 1.62 W. Similar to the Sievers et al. solution, this method enabled the hot spot to shift from the core nearer to the outer surface of the cell, reducing both the magnitude of the temperature gradient and hot spot. However, the inclusion of both a bottom cooling channel in addition to accommodating air flow/circulation across the large heat transfer area offered at the outer radial surface of the cells likely reduces the gravimetric energy density potential of the complete pack design. This is since an increased or considered inter-cell spacing is required to accommodate cooling channels/air flow circulation between cells, which may also increase pack-level complexity from targeting cooling at multiple locations. In addition, Shah et al. observed that no appreciable benefit of the heat pipe was observed upon its replacement with a solid copper bar, signifying the superior heat transfer potential offered by the heat pipe with this design is not realised. Evidently, there exists scope within the literature to improve upon the implementation of core cooling for cylindrical format battery cells.

2.3 CONCLUSION

The literature review presented highlights that initial approaches for automotive battery thermal management have relied on passive cooling with the ambient (for example in the Nissan Leaf), whereby some HEV models utilised active air cooling (e.g. the early models of the Toyota Prius). However, as the thermal issues associated with the inadequate temperature control have become more apparent, an increasing number of OEMs such as Tesla [82] and Chevrolet [83] have opted for indirect liquid cooling in their respective models of EVs and PHEVs to utilise the improved heat transfer potential.

Many of the strategies within the current state of the art for battery cooling employ external surface cooling. Table A 1 contained within Appendix A.3 summarises the BTMS performance for the majority of the analysed designs contained within the literature review. For cylindrical cells, either cooling jackets or direct submersion within mineral oil have been used. Other more developing methods have involved attaching heat pipes to the battery outer radial surface. These strategies can improve the surface temperature gradient and reduce the thermal resistance between the cell surface and heat transfer medium. Whilst these strategies can reduce the volume averaged temperature rise of the cell, they fail to rectify issues associated with the development of hot spots located within the cell core, which is a limitation of the poor radial thermal conductivity of lithium-ion cells. Shah et al. demonstrated that these issues are exasperated for thicker cells [87] (which are usually favoured for EV use where thicker electrodes are employed to increase the energy density) and for HEV and PHEV applications where the average C-rate profile is larger (therefore resulting in greater heat accumulation within the cell). Therefore, there is a clear need that future generations of BTMS should seek to further develop internal cooling strategies, and/or further investigate tab cooling approaches (of which there is a limited research base) that utilise the more thermally conductive axial pathways present within the cell to reduce the core temperature.

For pouch and prismatic cells, mini-channel cold plate designs are common and offer effective heat transfer removal from the pouch front and back surfaces. However, these designs require heat transfer fluid to be routed across the large bodies of all the individual cells which necessitates numerous manifold connections and/or seals to be present. Ultimately, this provides greater locations for leakage, and therefore increases the risk of an undesirable cell short circuit when using electrically conductive heat transfer mediums.

Alternative solutions to mini-channel cold plate cooling involve using conductive metal sheets attached to the pouch cells (also known as fin cooling, further examples of which are included in [79]). These extended surfaces act to conduct heat from the cell surface to an external location, which is in turn further cooled. Positioning the external cooling source in a safer area away from the cell compartment to reduce the leakage risk is a benefit of these approaches [65]. However, these designs incur an added thermal resistance relative to mini-channel cold plate designs, therefore, there is scope to improve their performance from the use of higher conductive materials than relative to conventional aluminium which is commonly employed [50], [79].

The use of heat pipes and/or advanced solid conductors with increased thermal conductivity has proven effective in developing BTMS designs. These devices can lower the thermal resistance for heat transfer between the cell surface and heat transfer medium, which as shown by Tran et al. [103], can reduce the parasitic cooling requirement of the system from enabling lower coolant flowrates for a set cooling requirement (relative to the case without the heat pipe addition). However, care must be taken to ensure that the heat pipe system does not incur excessive weight that can compromise the benefit of a reduced thermal resistance. There is scope within the literature to improve upon the application of heat pipes, particularly for core cooling cylindrical cells, of which current methods as in [107] have not fully utilised the potential offered by the heat pipe relative to using regular solid copper conductors.

Also highlighted from the literature review is that many of the thermal management studies focus on the thermal performance of a design for a set heat generation condition, that is usually reflective of an EV, HEV or PHEV electrical loading condition. However, given that the cooling location on the cell together with the internal heat generation rate affects the internal temperature gradient (due to the anisotropic nature of the battery thermal conductivity [88]), it is unclear and not properly defined as to what the exact heat generation limit is that satisfies the recommended thermal constraints with regard to the targeted external cooling location.

The identified Research Questions and Objectives stemming from the literature review are as follows, where a summary of the identified Research Questions and Research Objectives (agreed with the sponsoring company) for the thesis are contained within Table 2-2. Here, the location within the Innovation Report that contains the research stemming from the Research Objective is included, together with the Submission number in which the research is initially studied. References for where the work has been published in the scientific literature are also contained within Table 2-2.

2.3.1 RESEARCH QUESTION 1 - HOW DOES THE CELL ELECTRICAL LOADING CONDITION INFLUENCE THE REQUIRED CELL-LEVEL THERMAL MANAGEMENT STRATEGY FOR CYLINDRICAL CELLS?

From the literature review, it is observed that a knowledge gap exists for lack of a clear strategy on the cylindrical cell-level cooling choice, that considers both volume averaged temperature and internal temperature gradient constraints, as a function of the cell heat generation rate. It is, therefore, unclear whether internal cooling, tab cooling or surface

cooling strategies are preferable and/or required for batteries subject to either EV, PHEV or HEV driving conditions.

2.3.2 RESEARCH QUESTION 2 - HOW CAN INTERNAL HEAT PIPE COOLING OPTIONS FOR CYLINDRICAL CELLS BE IMPROVED?

The research from Shah et al. [107] demonstrated the thermal benefits of placing solid conductors or heat pipes within the core of cylindrical cells. However, their approach and other investigated approaches on internal core cooling to do not address the limitations of the poor perpendicular heat transfer through the cell, therefore relying on radial surface cooling to accompany cooling at the core. This can complicate the overall thermal management design from accommodating cooling at multiple surfaces. Therefore, identifying methods that improve the heat transfer from the cell material into the core cooling device is beneficial for the development of more efficient BTMS.

2.3.3 RESEARCH QUESTION 3 - HOW DOES THE CELL ELECTRICAL LOADING CONDITION INFLUENCE THE REQUIRED CELL-LEVEL THERMAL MANAGEMENT STRATEGY FOR POUCH CELLS?

It is unclear, within the literature, as to when cooling both sides of the pouch cell is required to satisfy volume average temperature and temperature gradient constraints through the cell for realistic automotive use cases. Cooling a single side may improve the ESS energy density, however, the longer heat transfer pathway between the cell hot spot and cooled surface from single side cooling may result in inadequate thermal control for particular usage cases. In addition, research by Hunt et al. [108] has highlighted that tab cooling pouch cells may be preferred in some instances over surface cooling. This is due to the direction of the temperature gradient being along all the layers within the cell (for tab cooling), as opposed to between layers in the cell (for surface cooling), which in their study was shown to reduce the cell ageing rate as all the layers within the cell aged more uniformly under tab cooling. However, the smaller heat transfer area present at the tabs may result in overall larger temperatures for the cell when subject to tab cooling. Therefore, there is scope to conduct pouch cell-level thermal modelling to explore the effect of the chosen cooling approach and the internal heat generation rate on the cell thermal performance.

2.3.4 RESEARCH QUESTION 4 - HOW CAN INDIRECT LIQUID COOLED METHODS EMPLOYING CONDUCTIVE FINS BE IMPROVED?

As discussed in the literature review, fin or extended surface indirect cooling approaches may offer the benefit of a simpler pack-level manifold distribution system that improves the inherent safety of liquid cooled BTMS. However, as demonstrated in the literature [50], [79], the added thermal resistance incurred when using conventional aluminium fin materials has resulted in underwhelming performance relative to mini-channel cold plate cooling designs.

2.3.5 RESEARCH OBJECTIVE 1 – CONDUCT A CYLINDRICAL CELL-LEVEL THERMAL MODELLING STUDY TO ANALYSE THE CELL THERMAL RESPONSE TO VARIATIONS IN THE TARGETED EXTERNAL COOLING LOCATION, TARGETED EXTERNAL COOLING INTENSITY AND INTERNAL HEAT GENERATION RATE

The development of cell-level thermal models will provide a tool to conduct a thermal analysis on the cell thermal response when subject to electrical loading conditions representative of EV, PHEV and HEV usage cases. Alteration of the external boundary conditions will enable different cooling options to be simulated. Identification of preferable cell-level thermal management strategies for heat generation rates reflective of the different automotive use cases will provide insight into which class of xEV will benefit the most from a more involved thermal management strategy.

2.3.6 RESEARCH OBJECTIVE 2 – INVESTIGATE METHODS THAT IMPROVE THE THERMAL PERFORMANCE OF HEAT PIPE CORE COOLING FOR CYLINDRICAL CELLS

Heat pipes have shown promise in developing BTMS and are a core product of the industrial sponsor Thermacore. Given the need to alleviate the development of internal temperature gradients within cylindrical cells, techniques that improve the effectiveness of internal heat pipe cooling offer promising solutions for use in next generation BTMS.

2.3.7 RESEARCH OBJECTIVE 3 – CONDUCT A POUCH CELL-LEVEL THERMAL MODELLING STUDY TO ANALYSE THE CELL THERMAL RESPONSE TO VARIATIONS IN THE TARGETED EXTERNAL COOLING LOCATION, TARGETED EXTERNAL COOLING INTENSITY AND INTERNAL HEAT GENERATION RATE

Similar to the cylindrical cell study, pouch cell-level thermal modelling will aid to identify the heat generation limits under which different surface and tab cooling approaches can satisfy

the thermal constraints imposed on the cell. This will guide the choice of cell-level cooling strategies that are appropriate for different types of automotive use (e.g commercial EV, PHEV and high performance EVs).

2.3.8 RESEARCH OBJECTIVE 4– IDENTIFY AND ASSESS THE THERMAL PERFORMANCE OF A NEW FIN MATERIAL FOR AN INDIRECT LIQUID COOLED BTMS

It is envisaged that fin materials employed within the next generation BTMS will require greater thermal conductivity relative to conventional aluminium fins, to enable superior thermal performance for the same volume penalty, or similar thermal performance at a reduced volume penalty. In addition, the new fin will require similar or lower densities than aluminium to ensure that excessive weight is not added to the BTMS that can compromise its gravimetric energy density. As Thermacore specialise in the development of advanced solid conduction materials, there is a clear case for pursuing this avenue of research.

Table 2-2: Research Questions and Research Objectives of the thesis

Research Question	Research Objective	Chapter in Innovation Report	Studied in submission(s)	Relevant published research
1). How does the cell electrical loading condition influence the required cell-level thermal management strategy for cylindrical cells?	1). Conduct a cylindrical cell-level thermal modelling study to analyse the cell thermal response to variations in the targeted external cooling location, targeted external cooling intensity and internal heat generation rate.	Three	3	Reference: *D. Worwood, R. Algoo, R. McGlen, J. Marco, and D. Greenwood, "A study into different cell-level cooling strategies for cylindrical lithium-ion cells in automotive applications," Int. J. Powertrains, vol. 7, pp. 199–266, 2018.*[109].
2). How can internal heat pipe cooling options for cylindrical cells be improved?	2). Investigate methods that improve the thermal performance of heat pipe core cooling for cylindrical cells.	Four	4	Reference: *D. Worwood et al., "A new approach to the internal thermal management of cylindrical battery cells for automotive applications," J. Power Sources, vol. 346, pp. 151–166, 2017.*[110].
3). How does the cell electrical loading condition influence the required cell-level thermal management strategy for pouch cells?	3). Conduct a pouch cell-level thermal modelling study to analyse the cell thermal response to variations in the targeted external cooling location, targeted external cooling intensity and internal heat generation rate.	Five	5	Reference: *D. Worwood et al., "Thermal analysis of a lithium-ion pouch cell under aggressive automotive duty cycles with minimal cooling," in IET Conference Publications, 2016, no. CP691.* [111].
4). How can indirect liquid cooled methods employing conductive fins be improved?	4). Identify and assess the thermal performance of a new fin material for an indirect liquid cooled BTMS.	Six	5,6,7,8	Manuscript titled 'Experimental and simulation analysis of a novel cooling material for large format automotive lithium-ion batteries' submitted and (at the time of writing) under review in the Journal of Energy Conversion and Management.

3 CHAPTER THREE - A STUDY INTO DIFFERENT CELL-LEVEL COOLING STRATEGIES FOR CYLINDRICAL LITHIUM-ION CELLS IN AUTOMOTIVE APPLICATIONS

3.1 INTRODUCTION

This Chapter seeks to address Research Objective 1, by analysing the cooling performance of both radial and tab cooling methods for cylindrical cells when subject to a wide range of electrical loading conditions. These conditions reflect aggressive yet realistic use cases for a representative EV, PHEV and HEV. This facilitates the decision into the potential preferred cell-level thermal management strategy for a given application that minimises the detrimental thermal related effects on the cell.

This Chapter is structured as follows. Section 3.2 investigates suitable cell-level thermal modelling approaches for lithium-ion cells, where the modelling approach adopted that is capable of conducting a transient thermal analysis is discussed in Section 3.3. In Section 3.4, battery heat generation estimation techniques are explored for use as an input into the thermal model. The accuracy of the developed thermal model is compared against experimental temperature measurements from 18650 cylindrical cells subject to two different current profiles, which are contained in Section 3.5.2. In Section 3.6 and Section 3.7, vehicle models that consider realistic duty cycles reflective of real world driving conditions for an EV, PHEV and HEV respectively are developed to produce current profiles as inputs into the thermal model. In Section 3.8, a cooling study analysis is performed to further assess the steady-state and transient thermal performance of different exterior surface cooling methods under the analysed EV, PHEV and HEV duty cycles. A sensitivity analysis on the effect of the cell anisotropic thermal conductivity parameters on the outputted cell thermal response is included in Section 3.9. Recommendations for Further Work and Conclusions from this study are discussed in Section 3.10 and Section 3.11 respectively.

3.2 CELL-LEVEL THERMAL MODELLING

3.2.1 MODELLING APPROACHES

Within the literature, two common approaches have been employed for the thermal modelling of lithium-ion cells. These are: homogenous bulk layer thermal models and discrete thermal models [112].

In homogenous bulk layer models, the internal active material of the cell contents (which includes the cell electrode assemblies) are treated as one homogenous material displaying effective physical properties. A schematic of the individual layers that comprise an electrode assembly are shown in Figure 3-1.

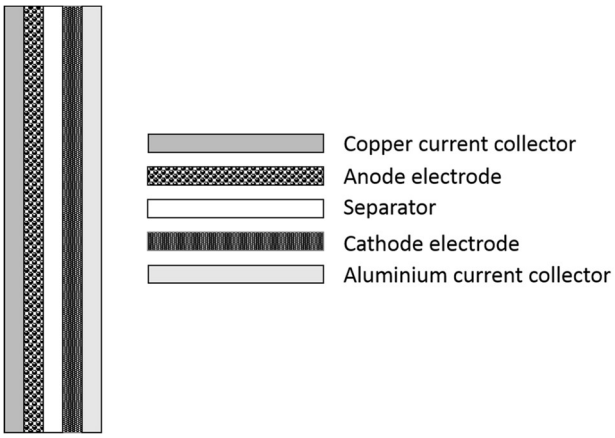

Figure 3-1: Electrode assembly of a lithium-ion cell

For discrete thermal models, each individual layer of the electrode assembly is included, therefore, no simplification of the internal contents is applied. Capron et al. [116] conducted a thermal study comparing the accuracy of a discrete and homogenous thermal modelling approach, in which the metallic housing of the cell was treated as a separate distinct layer in both thermal models. In their study, the thermal response of a large format (60 mm in dimeter,159 mm in height) 18 Ah lithium-iron phosphate (LFP) cylindrical cell was analysed by recording the mid-height outer surface temperature under different discharge and charging rates (between 1 C -5 C for discharge and 1 C-4 C for charge). Upon comparison of the experimental data with the outputs of the models, they observed that both modelling approaches gave good agreement to the experimental surface data, with a maximum root mean squared error of 1.5 ℃. They concluded that due to the faster computational time and high accuracy, the use of the homogenous thermal model was appropriate for cell-level thermal modelling of cylindrical cells both in both 1-dimensional (1-D) and 2-D studies. However, they noted that the discrete modelling approach may provide a more realistic representation of the temperature distribution through the cell.

Chen et al. [113] also performed a comparative analysis between discrete and homogenous thermal modelling. In their modelling approach, they treated the battery cell as having three distinct regions, these being a core layer comprising the cell active material, a surrounding electrolyte contact layer and the metallic housing material. A schematic of a battery cell displaying these regions is shown in Figure 3-2. They reported that simplifying the core layer

as homogenous using effective physical properties gave a small deviation in results between treating the core region as fully discrete. Specifically, the homogenous core layer assumption gave a deviation of -0.04% for the maximum cell temperature, a +3.75% deviation for the minimum cell temperature and a -0.29 % deviation for the averaged cell temperature relative to the discrete model at the end of a 3 C discharge for a large-scale 185.3 Ah rectangular battery, subject to forced exterior convective cooling at 100 $W.m^{-2}.K^{-1}$. The deviations were smaller during natural convective cooling when the heat transfer from the cell was less. Due to the homogenous assumption, the computational time was reported to be circa 660 times faster than the discrete model, where the authors noted that the discrete model may not be practical due to its computational inefficiency. Chen at al. also argued the importance of considering the outer electrolyte contact layer and metallic housing within the thermal model. From their simulation, they observed that thicker contact layers favoured a reduction in cell temperature under natural convection due to the added heat capacity, however, an opposite trend was observed under forced convection where the added thermal resistance presented by the contact layer resulted in an increase in cell temperature.

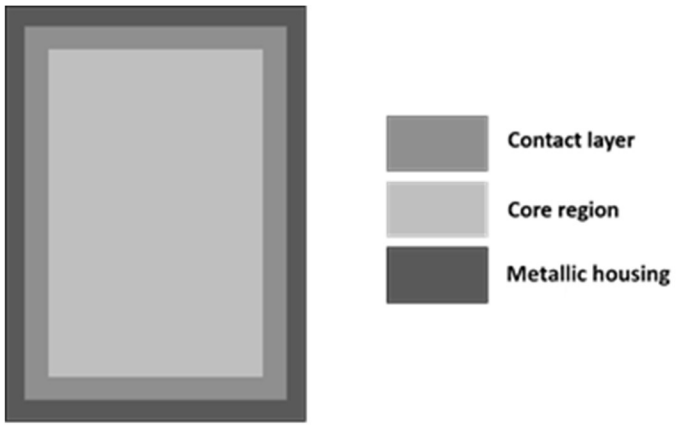

Figure 3-2: Schematic of a battery cell with a core region, outer electrolyte contact layer and metallic housing layer

Different to Chen at al. and Capron et al., Drake et al.[88] and Shah et al. [87] took a more simplified approach to homogenous thermal modelling, where they treated the complete cell structure as homogenous, rather than separating the internal core region from the metallic housing and/or electrolyte contact layer. Drake et al. suggested that the accuracy of such homogenous thermal modelling relies on the accurate characterisation of the effective battery thermal properties. Therefore, it is expected that neglecting or including the presence of the battery metallic housing and/or electrolyte contact layer will require careful consideration to the method of determining the effective thermal properties of the battery.

3.2.2 BATTERY THERMAL PARAMETERS

Many values for the thermal conductivity of lithium-ion cells have been reported in the literature (see Table 3-2), and vary considerably depending on whether the anisotropic nature of the battery composite is included. In general, the lumped perpendicular thermal conductivity of lithium-ion cells is considerably lower than the lumped in plane thermal conductivity, due to the large number of thermal interfaces between the electrode, current collector and insulating separator layers [113].

The properties and thicknesses of general battery components have been reported by Chen et al. [113] and are displayed in Table 3-1. The properties of the porous separator and electrode layers are measured following soaking to saturation with liquid electrolyte, therefore maximising the value of the effective thermal conductivity relative to a dry measurement.

Table 3-1: Physical properties of common battery materials [113]

Material	Density (kg m^{-3})	Heat Capacity (J kg^{-1} K^{-1})	Thermal conductivity (W m^{-1} K^{-1})	Thickness (µm)
Graphite electrode	1347.3	1437.4	1.04	140 (core region)
LiCoO2 electrode	2328.5	1269.2	1.58	116 (core region)
Al foil	2702.0	903.0	238.0	20 (core region)
Cu foil	8933.0	385.0	398.0	14 (core region)
Separator	1009.0	1978.2	0.33	35 (core region)
Liquid electrolyte	1130.0	2055.1	0.60	500 (contact layer)
S.S. AISI-304 (Metallic housing)	7900	477	14.6	700 (Metallic housing)

A schematic of the layered material structure within a lithium-ion cell displaying the anisotropic thermal conductivity is displayed in Figure 3-3. Here, $k_{z,i}$ is the thermal conductivity of material layer 'i' along the z axis [$W.m^{-1}.K^{-1}$], $k_{r,i}$ the thermal conductivity of material layer 'i' along the r axis [$W.m^{-1}.K^{-1}$], A_i the cross-sectional area of the material layer 'i' [m^2] and L_i the length of material layer 'i' [m].

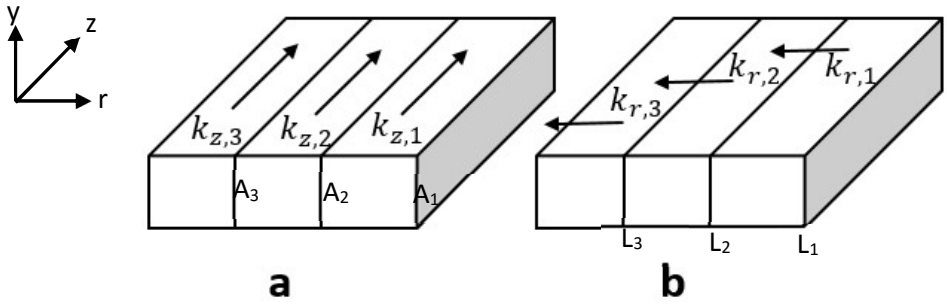

Figure 3-3: Anisotropic thermal conductivity in a composite material (a) along the z and y axis (parallel) (b) along the r axis (series or cross-plane) [113]

Along the z and y axis (layers in parallel) the effective theoretical lumped thermal conductivity of the composite can be calculated by [113]:

$$k_z = k_y = \frac{\sum_i A_i k_{z,i}}{\sum_i A_i} = \frac{\sum_i A_i k_{y,i}}{\sum_i A_i} \quad (1)$$

Along the r axis, in which heat is transferred between the layers in series, the effective theoretical thermal conductivity is expressed by [113]:

$$k_r = \frac{\sum_i L_i}{\sum_i \left(\frac{L_i}{k_i}\right)} \quad (2)$$

Chen et al. utilised these expressions to characterise the thermal conductivity properties of the homogenous core region, as depicted in Figure 3-2, arriving at a value of 1.035 $W.m^{-1}.K^{-1}$ for the cross-plane thermal conductivity and 24.840 $W.m^{-1}.K^{-1}$ for the axial thermal conductivity. However, one critique of this theoretical method for modelling the cross-plane thermal conductivity is that it neglects thermal contact resistances that are present between the battery composite layers [88], [114], which have been shown to have a negative effect on the heat transfer rate within the cell [115].

In an effort to include the presence of contact resistances, Drake et al. [88] developed a method to experimentally measure the effective thermal conductivity of a complete battery structure, such that the contact resistances existing throughout the whole cell are implicitly

included in the effective conductivity values. In their paper, they determined the effective thermal conductivity of the whole battery in both the perpendicular and axial/in-plane directions through an experimental approach involving subjecting the cell to a constant heat flux (once at the outer surface and once at the cell tab) imposed by a Kapton heater under vacuum. The measured surface temperature as a function of time was then imputed into their 1-D transient analytical model to back calculate the effective thermal conductivity of the cell in each direction. They report a value of 0.20±0.01 W m^{-1} K^{-1} for k_r and 30.4±1.5 W m^{-1} K^{-1} for k_z for an 18650 cell with $LiFePO_4$ cathode chemistry. Drake et al. state that due to the inclusion of contact resistances, their value for the perpendicular thermal conductivity is expected to be more accurate than other values reported by Maleki et al. [116], who measure (using a xenon-flash technique (XFT)) a value of 3.39 W m^{-1} k^{-1} for a single electrode assembly (i.e. the structure as viewed in Figure 3-1), and that of Chen et al. using the theoretical calculation procedure.

Other measurements for thermal properties of lithium-ion cells have been conducted by Barsoukov et al. [117], specifically for determining the perpendicular cell conductivity together with the cell heat capacity of a sample of 18650 cells from different manufacturers, using a thermal impedance spectroscopy approach, together with an equivalent circuit thermal model. For the effective perpendicular thermal conductivity of the electrode stack, they arrived at a fitted value of 1.4 W m^{-1} K^{-1} for the Panasonic cell.

Ye et al. proposed an alteration to Equation (2) that includes the effect of thermal contact resistances as an additional term in the denominator [114]. Their schematic that highlights the location for the contact resistances between the layers in the electrode assembly is included in Figure 3-4. The modified equation for the effective cross-plane thermal conductivity is given by:

$$k_r = \frac{\sum_i L_i}{\sum_i \left(\frac{L_i}{k_i}\right) + \sum_i R_{tc}} \tag{3}$$

Where R_{tc} is the thermal contact resistance [m^2 K W^{-1}].

Exact values for R_{tc} are difficult to calculate and require experimental methods. Ponnappan et al.[118] conducted experimental measurements on a common battery electrode stack under various temperatures and pressures to determine the effect on the overall thermal

contact resistance of the stack. They concluded that temperature effects had only a small effect on the contact resistance within the stack, and that the degree of electrolyte saturation had a significate effect on the contact resistance, whereby increasing the electrolyte saturation decreased the contact resistance.

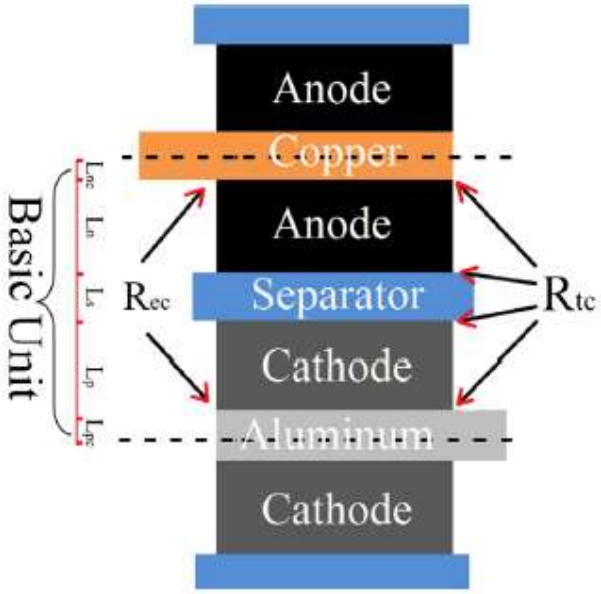

Figure 3-4: Schematic of the presence of thermal contact resistances (R_{tc}) within an electrode assembly, as presented by Ye et al. [114]

They stated that the wet electrode stack resistance was up to 2.5 times lower than that of the dry stack, with pressure effects on the contact resistance for the wet stack being negligible compared to the dry stack. Overall, the measured contact resistances for the electrode stack was found to vary between 0.0001 -0.0009 m^2 K W^{-1} under pressures and temperatures ranging from 1 bar to 17 bar and -15 to 95 °C. Upper values for a dry electrode stack were at 0.0009 $m^2.K.W^{-1}$ and 0.0004 $m^2.K.W^{-1}$ for a wet electrode stack at 1.75 bar 20°C. Using this contact resistance for the wet stack it is possible to determine an amended effective thermal conductivity from the data of Chen et al. that includes the effect of the contact resistance for the core region electrode stack. Using Equation (3) and data in Table 3-1, the amended value is 0.456 $W.m^{-1}.K^{-1}$ which is under half the theoretical value. Other parameters such as thickness of layers within the cell may contributed to the discrepancy between the reported experimental values of 0.20 W $m^{-1}.K^{-1}$ for a complete cell from Ye et al. and Drake et al. Using the reported layer material layer thicknesses from Ye et al. [114] for a cylindrical cell, the calculated cross plane value with 0.0004 $m^2.K.W^{-1}$ contact resistance is.0.270 $W.m^{-1}.K^{-1}$. Back calculating the thermal contact resistance with their reported value

for cross-plane thermal conductivity of 0.20 W m^{-1} K^{-1} gives a value of 0.0006 m^2.K.W^{-1}, which is within the reported rage of Ponnappan et al.

Vishwakarma et al. [115] also report experimentally determined contact resistance for electrode assembly samples acquired from commercial 26650 type lithium-ion cells. In their testing, they reported a total contact resistance across the electrode assembly of 0.000951 m^2.K.W^{-1}, which is consistent with the values of Ponnappan et al. This contact resistance resulted in an effective perpendicular thermal conductivity value of 0.24 W.m^{-1}.K^{-1}, which is significantly less than the calculated theoretical value of 1.76 W.m^{-1}.K^{-1} that ignored the contact resistance. For their electrode assembly samples, they observed that the large majority (88%) of the contact resistance (0.000840 m^2.K.W^{-1}) was due poor to poor adhesion between the cathode and separator. They proposed that chemically modifying the surface of the cathode structure and applying plasma treatment to the separator layer could dramatically reduce the contact resistance at the cathode-separator interface, through improving the adhesion. Specifically, applying both cathode and separator treatment measures was reported to increase the effective perpendicular conductivity of the electrode assembly to 0.76 W.m^{-1}.K^{-1}.

Vertiz et al. [119] conducted heat capacity and thermal conductivity measurements on a 14 Ah pouch type cell using an accelerating rate calorimetry (ARC) technique to measure the effective cell heat capacity and the C177-97-ASTM technique (described in [120]) for the thermal conductivity measurement. They noted that the measured value for the cell heat capacity varied little by varying the cell SOC, with a difference of less than 1% between measurements carried out at 0% SOC and 100% SOC. The measured value at 50% SOC for the cell heat capacity was reported as 1114 J.kg^{-1}.K^{-1}. They calculated the theoretical value for the cell thermal conductivity in the cross-plane direction using Equation (2) as 1.01 W.m^{-1}.K^{-1}, which gave a significant difference when compared to the C177-97-ASTM experimental measurements carried out at different levels of cell SOC. For their reference case measurement at 50 % SOC, the measured value was 0.284 W.m^{-1}.K^{-1}. However, at 100 % SOC, the value decreased by 16.23 % to 0.238 W.m^{-1}.K^{-1}. A similar decrease of 17.22 % was observed at 0 % SOC relative to the 50 % SOC reference value indicating that noticeable changes in effective cross-plane thermal conductivity are observed within the extremes of cell SOC. At 10 % SOC, the measured value was 7.41 % less (0.264 W.m^{-1}.K^{-1}) than the reference value indicating a much smaller deviation outside of the deep discharge region. For an inert cell free of electrolyte, the measured value was reported as 0.175 W.m^{-1}.K^{-1},

38.69 % less than the reference cell with electrolyte at 50% SOC. They highlighted the importance of the electrolyte effect on reducing the thermal contact resistance present between the layers through filling in air voids with liquid electrolyte, which has a thermal conductivity ranging between 0.45 -0.60 $W.m^{-1}.K^{-1}$ [119] compared to the much lower value of air at 0.024 $W.m^{-1}.K^{-1}$.

Table 3-2 summarises the values reported in the literature review for the anisotropic thermal conductivity and heat capacity of lithium-ion cells.

Table 3-2: Summary of key physical properties for lithium-ion batteries

Heat capacity [J kg^{-1} k^{-1}]	Cross-plane thermal conductivity [W m^{-1} K^{-1}]	In-plane thermal conductivity [W m^{-1} K^{-1}]	Technique	Reference and comments
1117	0.284	-	ARC technique for heat capacity measurement at 50 % cell SOC. Cross-plane thermal conductivity measured through C177-97-ASTM technique at 50 % cell SOC.	Pouch cell, 14 Ah $LiFePO_4$. Vertiz et al. [119]. Electrolyte filled cell.
-	0.175	-	As above.	Pouch cell, 14 Ah $LiFePO_4$ et al. [119]. 'Dry' cell without electrolyte.
1720±86	0.20±0.01	30.4±1.5	Adiabatic constant heat flux with Kapton heater. Measurements input into 1-D transient model in both r and z directions to determine the thermal properties. Properties effective for whole cell.	18650 $LiFePO_4$ cell. Drake et al. [88].
1650±80	0.15±0.01	32±1.6	As above.	26650 $LiFePO_4$ cell. Drake et al.[88]
1280	3.40	28.05	Xenon-flash technique and analytical model. Values effective for 1 repetition of sub cell components.	18650 $LiPF_6$ battery components. Maleki et al.[116].
-	1.035	24.84	Calculated from Equation (1) and (2).	Prismatic. Chen et al.[113].
-	1.039	32.84	Calculated from Equation (1) an (2) using data from Table 3-1.	Generic battery material properties. Values for core region of battery cell (neglecting contact layer and metallic housing effects).

1900	1.4	-	Thermal impedance spectroscopy together with analytical model fitting. Heat capacity for complete cell, thermal conductivity for electrode stack.	Panasonic 18650. Barsoukov et al.[117].
-	0.20	-	Measured. Technique not reported.	26650 $LiFePO_4$ cell. Ye et al. [121].
-	0.456	-	Calculated from Equation (3) and data from Table 3-1 for the core region using measured thermal contact resistance of 0.0004 $m^2K\ W^{-1}$ reported by Ponnappan et al. [118].	Value for the core region of the battery cell (neglecting contact layer and metallic housing effects).
	0.270	-	Calculated from Equation (3) and data from Ye et al [114] for cylindrical cell material layer thicknesses. Thermal contact resistance value of 0.0004 $m^2K\ W^{-1}$ reported by Ponnappan et al. [118].	Value for the core region of the battery cell (neglecting contact layer and metallic housing effects).
1390	0.35	28.9-35.1	Thermography and 1-D heat transfer equations.	Two test pouch cells, 14.5 and 10 Ah. Capacity. Bazinski et al. [122].
-	0.24	-	Determination of thermal contact resistance.	26650 electrode assembly samples. Vishwakarma et al. [115].

3.3 BATTERY THERMAL MODEL

3.3.1 THERMAL MODEL DEVELOPMENT

Due to their high solution efficiency and proven accuracy, a homogenous thermal modelling approach is chosen to model the heat transfer for the cylindrical cell model. The complete cell (active material, electrolyte contact layer and metallic housing) is treated as one homogenous material displaying effective anisotropic thermal conductivity, heat capacity and density, therefore, capturing the dominant thermal properties of the cell. The presence of a separate electrolyte contact layer and metallic housing layer are not included, which is in line with the approach taken by Drake et al. [88] and Shah et al. [87]. This enables the use of thermal conductivity values determined from experiments performed on complete cell samples, as the full range of contact resistances existing within a complete cell structure are inherently included in its value. This is not the case for experiments performed on isolated electrode assembly samples [88].

To satisfy Research Objective 1, consideration of both the axial and radial heat transfer modes within the cell is required. This enables an analysis to be performed on the thermal performance of the cell when subject to conventional cooling options involving tab cooling, radial cooling and combinations of tab and radial cooling. Therefore, the use of a 1-D spatial thermal model is insufficient and the development of a 2-D model is necessary. Further, as automotive duty cycles are highly dynamic in nature, consideration of the transient heat transfer must also be included to be representative of real world usage. Therefore, the model must also include the transient component.

The transient heat conduction equation for the cell material is given by:

$$\rho C_p \frac{\partial T}{\partial t} = q''' + \frac{1}{r}\frac{\partial}{\partial r}\left(k_r r \frac{\partial T}{\partial r}\right) + \frac{\partial}{\partial z}\left(k_z \frac{\partial T}{\partial z}\right) \quad (4)$$

Where ρ is the effective cell density [kg.m^{-3}], T the local cell temperature [K], r the radial location [m], z the axial location [m], C_p the effective cell heat capacity [J.kg^{-1}.K^{-1}], t the time [s], q''' the volumetric heat generation rate [W.m^{-3}], k_r the effective radial thermal conductivity and k_z the effective axial thermal conductivity [W.m^{-1}.K^{-1}].

Equation (4) assumes azimuthal symmetry (i.e. the temperature variation along the angular coordinate is neglected) such that the temperature profile through the cross-section of the cylindrical cell can be represented by a 2-D plane. For radial cooling strategies, this assumption requires that the complete radial surface of the cell is cooled equally. A schematic of the cell 2-D plane is shown in Figure 3-5 (a). Here, R_i is the radius of the cell mandrel [m], R_0 the radius of the cell [m], z = 0 the location at the bottom tab of the cell [m] and z=L the location at the top cell tab.

The boundary conditions considered in the model include Newton's law of cooling, which is specified at the exterior surfaces z=0, z=L and r=R_o. At r=R_i there exists an insulation condition due to symmetry within the cell. Newton's law of cooling is expressed as [123] :

$$q''_i = h_i(T_i - T_\infty) \quad (5)$$

Where q''_i is the heat flux at cell surface 'i' (e.g. bottom tab, top tab, outer radial surface) [W.m^{-2}], h_i the total heat transfer coefficient at cell surface 'i' [W.m^{-2}.K^{-1}], T_i the temperature at the cell surface 'i' [K] and T_∞ the temperature of the bulk heat transfer medium [K]. With reference to Figure 3-5 (a), h_{z0}, h_{zL}, and h_r represent the heat transfer coefficient at the bottom tab, top tab and outer radial surface respectively [W.m^{-2}.K^{-1}]. The volumetric heat

generation rate is assumed uniform throughout the cell material, as outlined in [124] for time dependent heat transfer cell-level modelling.

Whilst radiation heat transfer is not always accounted for in cell-level thermal modelling of battery cells, for example it is neglected in [72], [87], [103], its effect can be included from the use of the Stefan-Boltzmann Law via [123]:

$$q''_{i,rad} = \varepsilon_i \sigma \left(T_i^4 - T_\infty^4\right) \quad (6)$$

Where $q''_{i,rad}$ is the radiation component of the heat flux from cell surface 'i', ε_i the emissivity of cell surface 'i' and σ the Stefan-Boltzmann constant [W.m^{-2}.K^{-4}]. From Equation (6), an equivalent radiative heat transfer coefficient ($h_{rad,i}$ [W.m^{-2}.K^{-1}]) can be derived to characterise the component of cooling from radiation heat transfer. This is given by:

$$q''_{i,rad} = \varepsilon_i \sigma \left(T_i^4 - T_\infty^4\right) = h_{rad,i}(T_i - T_\infty) \quad (7)$$

As outlined by Hatchard et al. [125], Equation (7) can be simplified through the use of a Taylor series expansion for values of $\Delta T \leq 25$ ℃ (where $\Delta T = T_i - T_\infty$) and for ambient temperatures below circa 50℃. Under these circumstances, the temperature dependence on the cell surface for the $h_{rad,i}$ value can be removed at a peak error penalty of approximately 10%, with the error declining as the ΔT value is reduced below 25 ℃. The approximation for $h_{rad,i}$is given as [125]:

$$h_{rad,i} = 4\sigma\varepsilon T_\infty^3 \quad (8)$$

The total heat transfer coefficient h can be defined as the addition of both the convective and radiative heat transfer coefficient terms [125]:

$$h_i = h_{c,i} + h_{rad,i} \quad (9)$$

Where $h_{c,i}$ is the convective heat transfer coefficient at cell surface 'i'. Therefore, the effect of radiation can be included readily in this manner. This simplification of the radiation heat transfer component is expected to be a justifiable approximation for thermal modelling of battery cells given that the ambient temperature is unlikely to increase past 50 ℃, where a greater than 25 ℃ difference between the cell surface and surrounding air is also unlikely in an actively cooled BTMS.

3.3.2 THERMAL MODEL SOLUTION PROCEDURE

Equation (4) can be solved analytically through the procedure as described by Shah et al. [124]. However, to explore the effect of adding internal components within the cell to investigate the potential of internal core cooling methods in later studies, spatial dependence on the material properties is required. As such, a finite differencing method [126] is chosen to solve Equation (4) which can more readily accommodate alterations in spatial dependence.

One common method that has proved effective for solving the heat conduction equation in 2-D coordinates is the alternating-direction implicit (ADI) finite difference method [126], [127] [105]. This technique discretises the heat conduction equation, producing two ADI equations which are solved using tri-diagonal matrices. As such, this is a more computationally efficient method whilst maintaining the unconditional stability of the solution with regards to the chosen time step size Δt, than compared to implicit methods which require a more computationally intensive iterative solution approach [127], [128].

The solution grid for the ADI method is shown in Figure 3-5 (b). Here, the nodal points represent the temperature values at the corresponding grid points to be solved by the solution procedure. In this instance, a uniform grid spacing is chosen for simplicity, however, non-uniform grids can also be implemented [126]. The total number of grid points in the r direction is given by K+1, where K represents a mesh resolution parameter to define the size of the mesh in the r direction. Similarly, J+1 represents the total gird points in the z direction, with J representing a mesh resolution parameter to define the mesh size in the z direction.

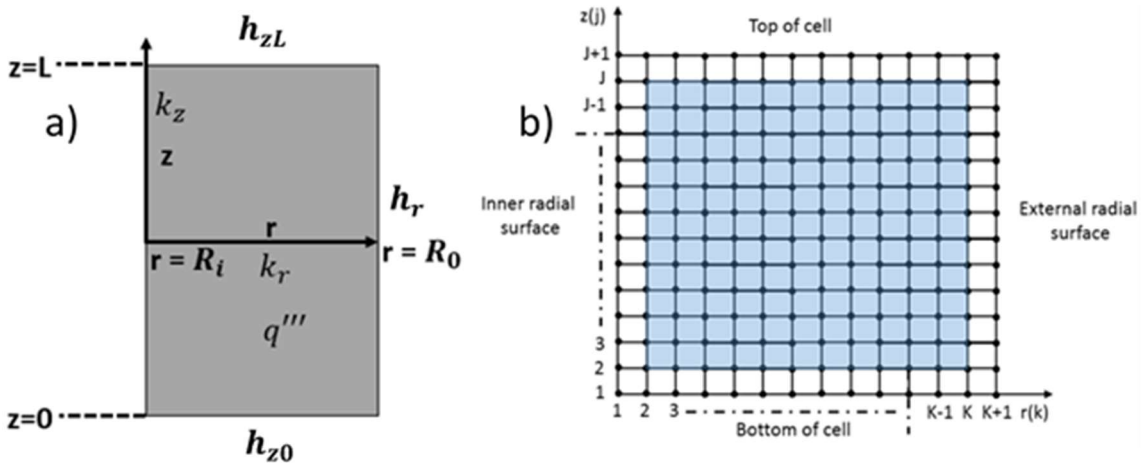

Figure 3-5: (a) Schematic of bulk layer thermal model (b) solution grid for finite difference method

The general discretised form of the heat conduction equation in 2-D form for polar coordinates where the thermal properties of the material may vary based on spatial location is given below by the following ADI equations. These equations are valid for grid points between j=2:J and k=2:K as represented by the shaded area in Figure 3-5 (b). The ADI equations in each direction are:

z direction:

$$\frac{T_{j,k}^{n+\frac{1}{2}} - T_{j,k}^{n}}{\left(\frac{\Delta t}{2}\right)} = \frac{1}{\rho_{j,k} c_{j,k}^{p} dz^2}\left(k^{z}_{j+\frac{1}{2},k}\left(T_{j+1,k}^{n+\frac{1}{2}} - T_{j,k}^{n+\frac{1}{2}}\right) - k^{z}_{j-\frac{1}{2},k}\left(T_{j,k}^{n+\frac{1}{2}} - T_{j-1,k}^{n+\frac{1}{2}}\right)\right) + \frac{1}{\rho_{j,k} c_{j,k}^{p} dr^2}\left(\frac{r_{k+\frac{1}{2}} k^{r}_{j,k+\frac{1}{2}}}{r_k}\left(T_{j,k+1}^{n} - T_{j,k}^{n}\right) - \frac{r_{k-\frac{1}{2}} k^{r}_{j,k-\frac{1}{2}}}{r_k}\left(T_{j,k}^{n} - T_{j,k-1}^{n}\right)\right) + \frac{q'''^{,n}_{j,k}}{\rho_{j,k} c_{j,k}^{p}} \tag{10}$$

r direction:

$$\frac{T_{j,k}^{n+1} - T_{j,k}^{n+\frac{1}{2}}}{\left(\frac{\Delta t}{2}\right)} = \frac{1}{\rho_{j,k} c_{j,k}^{p} dz^2}\left(k^{z}_{j+\frac{1}{2},k}\left(T_{j+1,k}^{n+\frac{1}{2}} - T_{j,k}^{n+\frac{1}{2}}\right) - k^{z}_{j-\frac{1}{2},k}\left(T_{j,k}^{n+\frac{1}{2}} - T_{j-1,k}^{n+\frac{1}{2}}\right)\right) + \frac{1}{\rho_{j,k} c_{j,k}^{p} dr^2}\left(\frac{r_{k+\frac{1}{2}} k^{r}_{j,k+\frac{1}{2}}}{r_k}\left(T_{j,k+1}^{n+1} - T_{j,k}^{n+1}\right) - \frac{r_{k-\frac{1}{2}} k^{r}_{j,k-\frac{1}{2}}}{r_k}\left(T_{j,k}^{n+1} - T_{j,k-1}^{n+1}\right)\right) + \frac{q'''^{,n+\frac{1}{2}}_{j,k}}{\rho_{j,k} c_{j,k}^{p}} \tag{11}$$

Where dz is the distance between nodes in the z direction [m] and dr the distance between nodes in the r direction [m]. The superscripts for the temperature and heat generation parameters refer to the time step n, where n indicates an 'nth' time step. For the thermal conductivity material properties, the superscripts represent the direction in which the thermal conductivity is defined (i.e. z for axial and r for radial). The subscripts for the properties refer to its location with the solution grid as defined by the spatial parameters j and k. Here, potential spatial variations of the material properties (as would occur for a composite material) are included through use of the harmonic mean value for the thermal

conductivity as described by Patankar [126]. Use of the harmonic mean value (defined as the number of elements divided by the sum of the individual element reciprocals), as opposed to a linear interpolation between two grid points enables the interface thermal conductivity to physically capture steep changes in thermal conductivity gradients between two materials more accurately, and is hence recommend for use in modelling composite materials [126], [129]. The harmonic mean values for the interface thermal conductivities are given as:

$$k^z_{j+\frac{1}{2},k} = \left(\frac{2k^z_{j,k}k^z_{j+1,k}}{k^z_{j,k} + k^z_{j+1,k}}\right) \tag{12}$$

$$k^z_{j-\frac{1}{2},k} = \left(\frac{2k^z_{j,k}k^z_{j-1,k}}{k^z_{j,k} + k^z_{j-1,k}}\right) \tag{13}$$

$$k^r_{j,k+\frac{1}{2}} = \left(\frac{2k^r_{j,k}k^r_{j,k+1}}{k^r_{j,k} + k^r_{j,k+1}}\right) \tag{14}$$

$$k^r_{j,k-\frac{1}{2}} = \left(\frac{2k^r_{j,k}k^r_{j,k-1}}{k^r_{j,k} + k^r_{j,k-1}}\right) \tag{15}$$

For polar coordinates the r terms in Eq. (10) and (11) are discretised as [128] :

$$r_k = R_i + dr \times k \tag{16}$$

$$r_{k+\frac{1}{2}} = R_i + dr(k + 0.5) \tag{17}$$

$$r_{k-\frac{1}{2}} = R_i + dr(k - 0.5) \tag{18}$$

The source term at the time interval n+$\frac{1}{2}$ is given as a liner interpolation between the value for the source term at time interval n+1 and time interval n:

$$q'''^{,n+\frac{1}{2}}_{j,k} = \frac{1}{2}\left(q'''^{,n}_{j,k} + q'''^{,n+1}_{j,k}\right) \tag{19}$$

The Newton's law of cooling boundary conditions for each external surface of the cell are:

For the top of the cell:

$$-k_z \frac{dT}{dz}_{z=L} = h_{zL}(T_{z=L} - T_\infty) \tag{20}$$

With the discretisation:

$$-k_{J+1,k}^{z}\frac{\left(T_{J-1,k}^{n+1}-4T_{J,k}^{n+1}+3T_{J+1,k}^{n+1}\right)}{2dz}=h_{zL}\left(T_{J+1,k}^{n+1}-T_{\infty}^{n+1}\right) \quad (21)$$

For the bottom of the cell:

$$k_z\frac{dT}{dz}_{z=0}=h_{z0}(T_{z=0}-T_{\infty}) \quad (22)$$

With the discretisation:

$$k_{1,k}^{z}\frac{\left(-3T_{1,k}^{n+1}+4T_{2,k}^{n+1}-T_{3,k}^{n+1}\right)}{2dz}=h_{zL}\left(T_{1,k}^{n+1}-T_{\infty}^{n+1}\right) \quad (23)$$

For the external radial surface:

$$-k_r\frac{dT}{dr}_{r=R}=h_r(T_{r=R}-T_{\infty}) \quad (24)$$

With the discretisation:

$$-k_{j,K+1}^{r}\frac{\left(T_{j,K-1}^{n+1}-4T_{j,K}^{n+1}+3T_{j,K+1}^{n+1}\right)}{2dr}=h_r\left(T_{j,K+1}^{n+1}-T_{\infty}^{n+1}\right) \quad (25)$$

For the inner radial surface at r=R_i the insulation condition is applied due to symmetry:

$$k_r\frac{dT}{dz}_{r=0}=0 \quad (26)$$

With the discretisation:

$$k_{j,1}^{r}\frac{\left(-3T_{j,1}^{n+1}+4T_{j,2}^{n+1}-T_{j,3}^{n+1}\right)}{2dr}=0 \quad (27)$$

Using the above equations, the temperatures at each node and each time step can be solved using a commercially available computational package. For this research Matlab is used.

3.4 BATTERY HEAT GENERATION

For the purpose of this study, an experimental approach is taken to characterise the battery heat generation rather than through the development and use of electrochemical models. An example of such electrochemical modelling approaches can be found in [130]. These approaches require knowledge of numerous battery parameters such as electrode particle size, lithium-ion diffusivity, and can incur additional computational resources when coupling

the electrochemical model to the thermal model. As such, many researchers [119], [131]–[134] have turned towards experimental methods to calculate the battery heat generation rate.

Bandhauer et al. conducted a critical review on the thermal issues present in lithium ion batteries and concluded that the Bernardi et al.[135] expression for battery heat generation is the most commonly employed for automotive battery thermal modelling, partially due to its ease of application [29].

The Bernardi et al. equation for the battery heat generation rate, that neglects contributions from enthalpy-mixing and phase change terms, and considers only the enthalpy of reaction is [135]:

$$q = \left(\sum_{l} IU_{l,avg} - IV\right) - \sum_{l} I\left(T\frac{dU_{l,avg}}{dT}\right) \tag{28}$$

Where I the current through the cell [A], V the cell potential [V], $U_{l,avg}$ the average theoretical open-circuit potential (OCP) for electrochemical reaction l based on the average stoichiometry of the electrode [V], and q the battery cell heat generation rate [W].

The first term in Equation (28) $\left(\sum_l IU_{l,avg} - IV\right)$ represents the irreversible heat generation arising from the cell overpotential. The second term $(\sum_l I\left(T\frac{dU_{l,avg}}{dT}\right))$ is the reversible heat caused by changes in Gibbs free energy of the battery contents [135]. Neglecting the heat of mixing within battery systems is usually acceptable when the electrode particle size is sufficiently small, which as noted by Bandhauer et al., is generally the case for commercial lithium-ion batteries [29].

The irreversible component of heat generation (q_{irrev}) can be expressed in terms of the battery overpotential which is:

$$q_{irrev} = \left(\sum_{l} IU_{l,avg} - IV\right) = I\left(\sum_{l} U_{l,avg} - V\right) = I\eta \tag{29}$$

Where η is the cell overpotential [V] and q_{irrev} the total irreversible heat generation rate [W].

From Ohms law, q_{irrev} is often expressed in terms of the cell 'overpotential resistance' or 'internal resistance' as indicated in the research by Onda et al. [131] and Viswanathan et al. [136]:

$$q_{irrev} = I\eta = I^2 R_\eta \tag{30}$$

Where R_η is the overpotential/internal resistance of the cell [Ω].

The cell overpotential is comprised of several voltage drops, and has been cited for lithium-ion batteries to comprise of [137]:

$$\eta = \eta_{ohmic} + \eta_{f,pos} + \eta_{f,neg} + \eta_{act,pos} + \eta_{act,neg} + \eta_{con} \tag{31}$$

Here, η_{ohmic} is the voltage drop arising from the sum of the ohmic drops due to the resistivity of the different layers in the battery material, e.g. from the separator layer, electrolyte layer, through the electrodes and from contact resistances present between layers [138].Terms 2 and 3 ($\eta_{f,pos}$, $\eta_{f,neg}$) are the polarization voltages arising due to the formation of passive film layers on the positive electrode ($\eta_{f,pos}$) and negative electrode ($\eta_{f,neg}$). Terms 4 and 5 are the voltage drops arising from activation polarisation at the positive electrode ($\eta_{act,pos}$) and negative electrode ($\eta_{act,neg}$) respectively. These are caused due to the charge-transfer reaction at the electrode electrolyte film layer interface [137]. The concentration polarisation (η_{con}) is due to mass transfer limitations within the cell (e.g. diffusion of ions through electrolyte and in particles). Pilatowicz et al. noted that there is currently no significant evidence to prove the presence of a passive layer on the positive cathode electrode and negative anode during discharge, therefore, $\eta_{f,pos}$ and $\eta_{f,neg}$ can be neglected for some chemistry types [137]. Due to this simplification, others [138] express the cell overpotential simply as the sum of the ohmic, concentration polarisation and charge transfer polarisation voltage drops :

$$\eta = \eta_{ohmic} + \eta_{ch,tr} + \eta_{con} \tag{32}$$

Where the activation polarisation voltage from the negative and positive electrode are grouped into a single term $\eta_{ch,tr}$, which represents the associated drops from the charge transfer resistance.

Various experimental methods have been used to determine the value for the overpotential resistance, which include V-I characterisation, evaluation of the difference between cell OCP

(U) and operating voltage (V), intermittent discharge/charge pulse methods, and through measurements using electrochemical impedance spectroscopy (EIS). The methods for these experimental techniques can be found in [131], [133], [139] and more in-depth discussion for the intermittent pulse-discharge technique in [138].

Vertiz et al.[119] concluded from their research that the current pulse method for the calculation of the overpotential resistance was the most suitable technique due its ability to include the dependence of SOC, temperature, and current rate by ease in varying the test condition. They also witnessed greater inaccuracy in the EIS method for calculating the internal resistance value to determine the irreversible heat generation rate.

In this study, the reversible component of the battery heat generation is neglected, where only irreversible components are considered. The portion of the irreversible heat generation relative to reversible heat has been shown to increase under electrical duty cycles which display higher C-rate pulses (or higher constant C-rates in the case of static charge or discharge) [136]. Specifically, Schuster et al. [132] report that for a 40 Ah pouch cell with nickel manganese cobalt oxide chemistry (NMC), the measured proportion of the reversible heating effect to the total heat generation rate was 37% at 0.125 C discharge, but only 7% at 1 C discharge. Higher contributions have, however, been reported by Xiao and Choe [130] for a 15.7 Ah LMO pouch cell, where the reversible heating effect was approximately 12% the total heat generation rate for a 1 C discharge.

3.5 BATTERY THERMAL MODEL VALIDATION

3.5.1 COMPARISON TO LITERATURE

Two methods are carried out to validate the finite difference thermal model. The first method involves comparing the model outputs to those from Shah et al., who report steady-state temperature results for a cylindrical cell using a similar effective bulk model solved analytically, which is validated against experimental data [87]. A comparison to this paper is made due to the same assumptions that underpin both modelling approaches. To achieve this, the cell geometry and material properties from their work are inputted into the model and the steady-state temperature contours compared to their reported results.

The model input parameters from Shah et al. are summarised in Table 3-3, together with the boundary condition values for the heat transfer coefficient. A mesh resolution analysis is first conducted to assess the effect of the mesh resolution parameters J, K and time step

parameter dt (i.e. dt is the number of time steps) on the maximum cell temperature rise. The results of the mesh resolution analysis are shown in Figure 3-6, where a time period of 10,000 s is chosen to ensure that the solution reaches steady-state. The mesh analysis is performed using the data from Table 3-3 as the thermal model inputs for the case where hr = 10 W $m^{-2}k^{-1}$.

Table 3-3:Literature thermal model parameters used in the literature comparison [87], [88]

Cell geometry	Cell thermal conductivity [$W.m^{-1}.K^{-1}$]		Cell density [$kg.m^{-3}$]	Cell heat capacity [$J.kg^{-1}.K^{-1}$]	Total heat transfer coefficient [$W.m^{-2}.K^{-1}$]			Volumetric heat generation [$W.m^{-3}$]
	Radial	Axial			Top of cell	Bottom of cell	External radial surface	
26650, 0 mm mandrel	0.20	30	2285	1605	100	100	10-1500	1.7386e+05

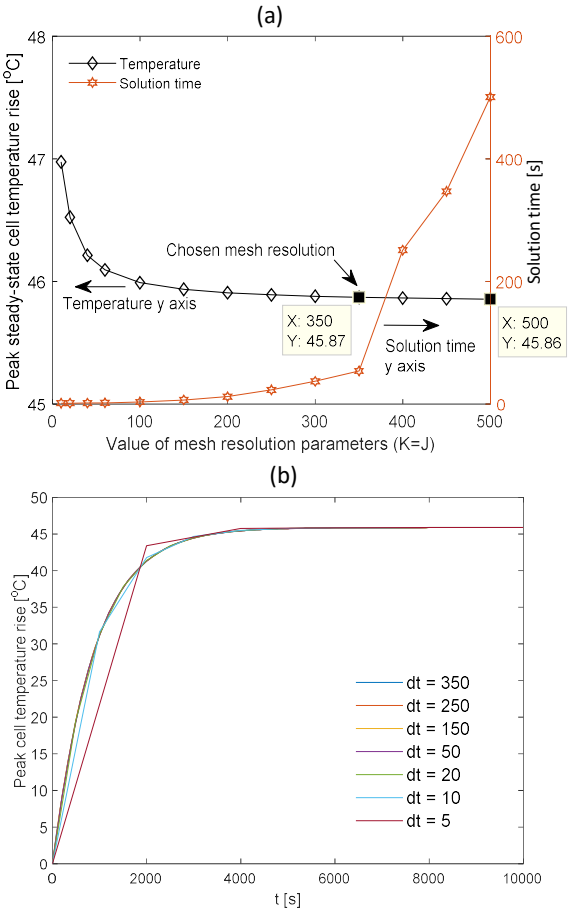

Figure 3-6: Mesh resolution analysis for the 26650 cell using the model inputs from Table 3-3 with hr = 10 W $m^{-2}k^{-1}$ for (a) spatial mesh resolution parameters J and K with dt =350 (b) number of times steps dt with J=K=350

Figure 3-6 (a) (where dt = 350) demonstrates that values for the peak steady-state cell temperature converge for equal mesh resolution parameters (where J=K) past circa 300. The effect of the computational solution time is also shown, which shows that the solution time begins to increase significantly past values of J=K=350. Given that the difference between the outputted temperatures is very small (0.01 ℃) between J=K=350 and J=K=500, and that the solution takes only 54 s for J=K=350 but 501 s for J=K=500, the value of 350 is chosen to define the mesh size (which is considered the optimal trade-off between accuracy and solution time efficiency).

Figure 3-6 (b) outlines the effect of dt on the outputted cell temperature. As seen, the steady-state solution maintains high accuracy even for very low values of dt (dt =5), highlighting the benefit of the ADI solution approach with regard to the unconditional stability for the chosen time step size. However, as seen from the full temperature profile, the temperature transients are not captured correctly for low values of dt. Values larger than dt=50 demonstrate a negligible effect on the outputted cell temperature profile in this instance.

The results from Shah et al. are displayed in Figure 3-7, where the results from the finite difference model (displayed in the same order as the subplots in Figure 3-7) using these same parameters are summarised in Figure 3-8.

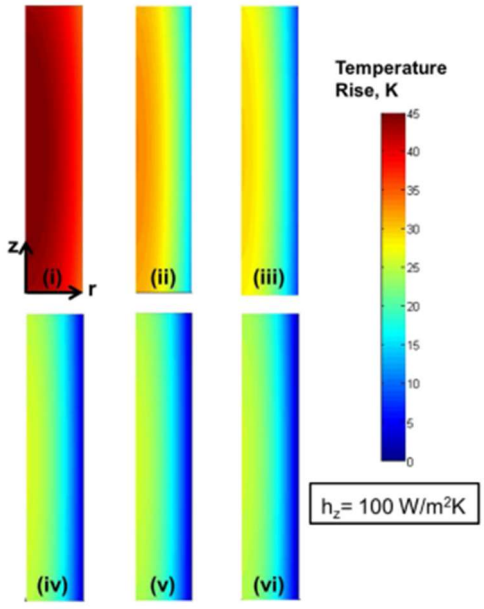

Figure 3-7: Steady-state simulated temperature profile results by Shah et al. for a 26650 cell subject to 1.7386 x10^5 Wm^{-3} of uniform internal volumetric heat generation with k_r =0.20 W m^{-1}k^{-1}, k_z = 30 W m^{-1}k^{-1}for (i) hr = 10 W m^{-2}k^{-1} (ii) hr = 50 W m^{-2}k^{-1} (iii) hr = 100 W m^{-2}k^{-1}(iv) hr = 500 W m^{-2}k^{-1} (v) hr = 1000 W m^{-2}k^{-1} (vi) hr = 1500 W m^{-2}k^{-1} [87]

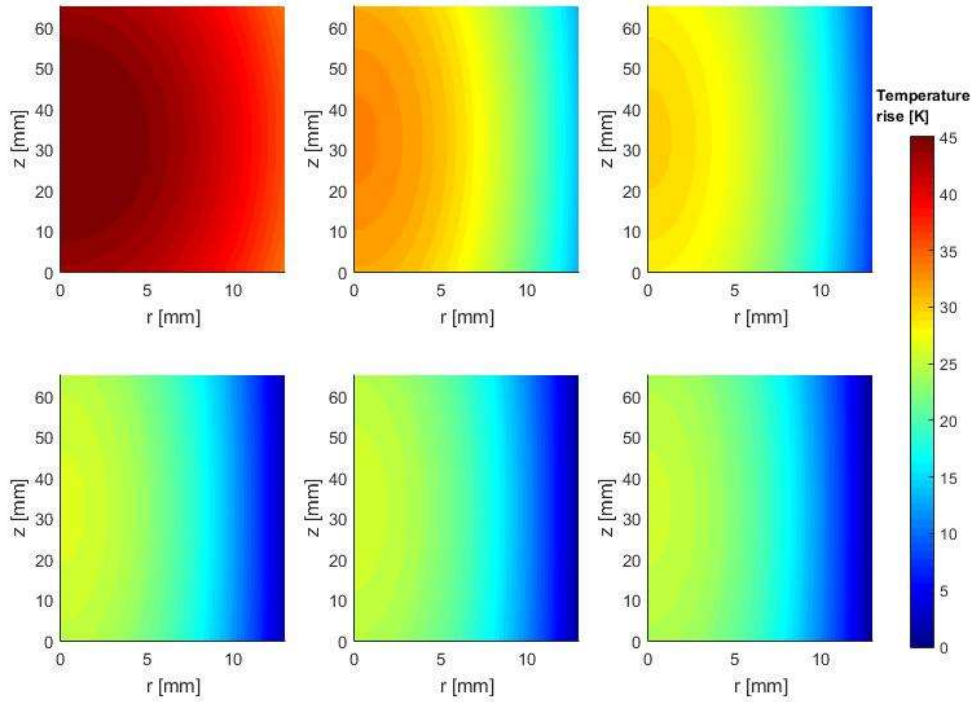

Figure 3-8: Steady-state temperature results from the finite difference thermal model using the same parameters as Shah et al. (images shown in the same order as in Figure 3-7)

Here the ambient and initial temperature of the cell are set as 0 ℃ to present the temperature contours in terms of a generic temperature rise, which is consistent with the approach by Shah et al.

Through visual inspection of the temperature contours (Figure 3-7 & Figure 3-8) together with the through thickness temperature variation (shown in Figure 3-9) between the finite difference model and the results of Shah et al., it is observed that the model provides the same steady-state results indicating the finite difference method has been implemented correctly.

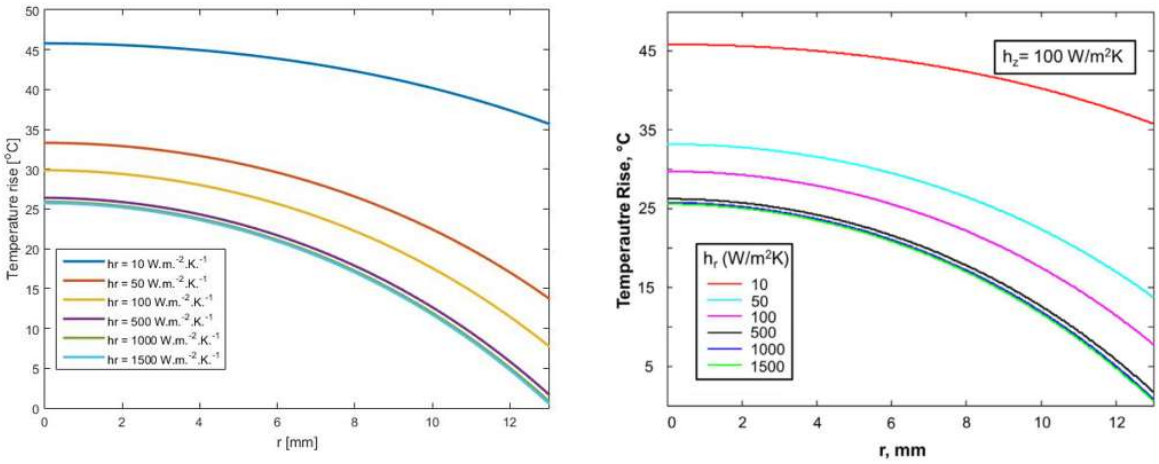

Figure 3-9: Through thickness temperature profile using Table 3-3 input parameters for (left) finite difference thermal model used in this study (right) Shah et al. analytical model results as presented in [87]

3.5.2 EXPERIMENTAL VALIDATION

To test the accuracy of the model under a transient scenario, the model outputs are compared against experimental temperature measurements obtained from new 18650 energy cells (with a graphite anode and NCA cathode chemistry) with a nominal capacity rating of 3.1 Ah subject to two test electrical loading conditions. The experimental results are provided through collaboration with Jaguar Land Rover (JLR) UK.

In the experimental testing, the cells are placed in a climate chamber that circulates air at 25 ^{o}C. Thermocouples (K-type) are placed at the top, bottom and mid-height exterior surfaces of the cells facing outward from the module. Insulating polystyrene sheets are placed around the module to limit the convective effects created by the climate chamber air circulation. Figure 3-10 shows the positioning of the temperature monitored cells, and an example of the location of the thermocouples as indicated by the yellow stars. Only temperature monitored cells are shown (labelled 1-5). The 19 cells within the module are connected in parallel during testing.

Figure 3-10: Temperature monitored cells within a 19 cell module

The physical thermal parameters for the 18650 cell used in the thermal model are viewable in Table 3-9 (in Section 3.8).The value for the effective cell density is calculated given the weight of the cell (40 g) and the known volume of the cell material (here a 3 mm cell mandrel size has been assumed based on images from [140], such that the void mandrel volume is not included in the effective cell volume). The value for the cell effective heat capacity is given by the cell manufacturer. Values to define the cell effective perpendicular thermal conductivity are chosen based off values that implicitly include the contribution of thermal contact resistance present between layers in the electrode assembly, which as shown in Section 3.2.2, typically give rise to values in the region of 0.15-0.28 $W.m^{-1}.K^{-1}$, near a magnitude lower than measured values for isolated electrode assembly samples [116]. The axial thermal conductivity value is taken as that reported by Drake et al. [88] which is determined from experimental measurements and similar to values reported elsewhere for the effective axial thermal conductivity of lithium-ion batteries [122]. The R_η value of the cell is measured experimentally (also provide by JLR) as a function of the cell SOC using the pulse method technique as described in [138] with a 10 s pulse duration performed at 25 °C. The provided values for R_η determined from the current pulse method are viewable in Figure 3-11. The fitted polynomial from Figure 3-11 is used within the thermal model to determine the internal resistance of the cell as a function of SOC. The model is simplified to ignore the temperature dependence on the internal resistance for this level of modelling fidelity. This is expected to be a reasonable assumption for the cell initial condition when at 25 ℃, as it is shown in a number of studies that the internal resistance decline, and therefore the change in cell heat generation rate, is less dependent on temperature at temperatures exceeding 25 ℃ [119], [141]. However, if the model were to be applied for cell temperatures below 25 ℃, larger changes in the internal resistance are expected as the cell self-heats which may warrant the use of a temperature dependent term for the internal resistance. Adaptation of the model for use in such lower temperatures is, therefore, a scope for further work.

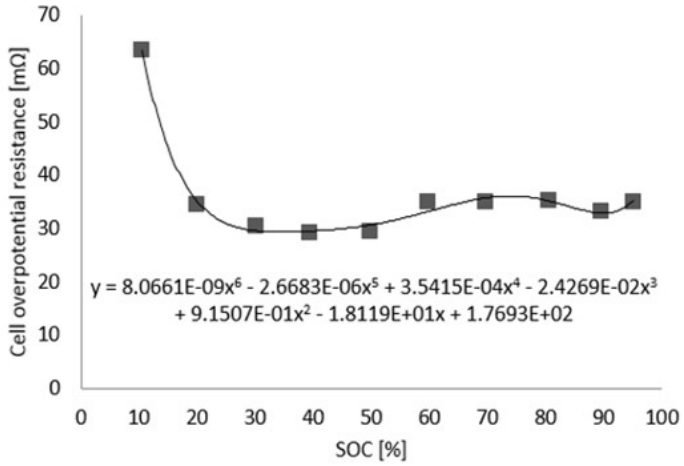

Figure 3-11: Cell overpotential resistance as a function of SOC at 25 ℃

The electrical loading profiles considered are a complete 1 C discharge (from 100-0% SOC) and a test duty cycle starting at 100% SOC. This enables the accuracy of the model to be tested under both dynamic and static current conditions. The C-rate profile of the test cycle (whereby the current profile can be extract by dividing the C-rate profile by the nominal cell capacity (3.1Ah)) is shown in Figure 3-12.

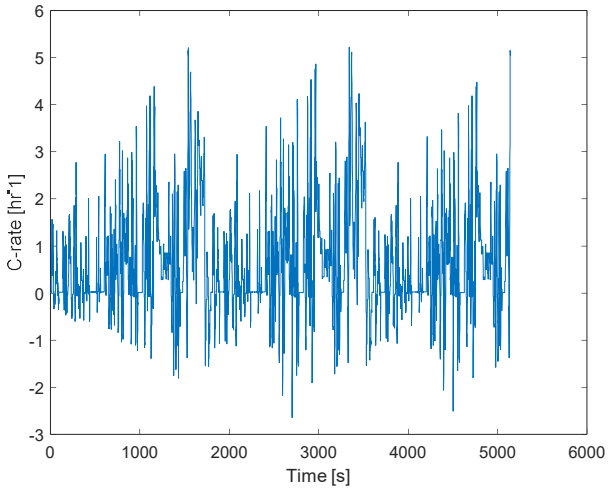

Figure 3-12: Cell C-rate profile for the test drive cycle

Comparison results between the thermal model outputs and the experimental cell mid-height surface temperature measurements for Cell 1, Cell 3 and Cell 5 (where the cell positions are shown in Figure 3-10) for both the 1 C discharge and drive cycle tests are shown in Figure 3-13. The convective coefficient values employed at the radial and bottom tab surface are 6 $W.m^{-1}.K^{-1}$ (within the region of natural convection with air across a cylinder [123]). The suggested higher value of 10 W m^{-2} K^{-1} from Shah et al. [87], [124] is set at the top

tab which is more exposed to air circulation effect from the climate chamber. Mesh resolution parameters of J=K=350 are chosen in the finite difference model, where a time step of 1 s is chosen to coincide with the resolution of the test drive cycle.

As seen in Figure 3-13, the experimental mid height surface data for both Cell 1 and Cell 5 are similar, as shown by the overlay of the temperature curves. However, it is observed that Cell 3 exhibits a slight positive temperature offset relative to the other cells. This is assumed to be due to the additional neighbouring effect from adjacent cells, as Cell 3 is surrounded by four cells, whereas the edge cells Cell 1 and Cell 5 are only surrounded by two and three cells respectively. The additional heat rejection from the additional adjacent cells may, therefore, contribute to the higher temperature of Cell 3. To reduce the potential neighbouring effect, the accuracy of the model is compared against the temperature data obtained from the edge cell, Cell 1 (which is in close agreement with the data obtained from Cell 5).

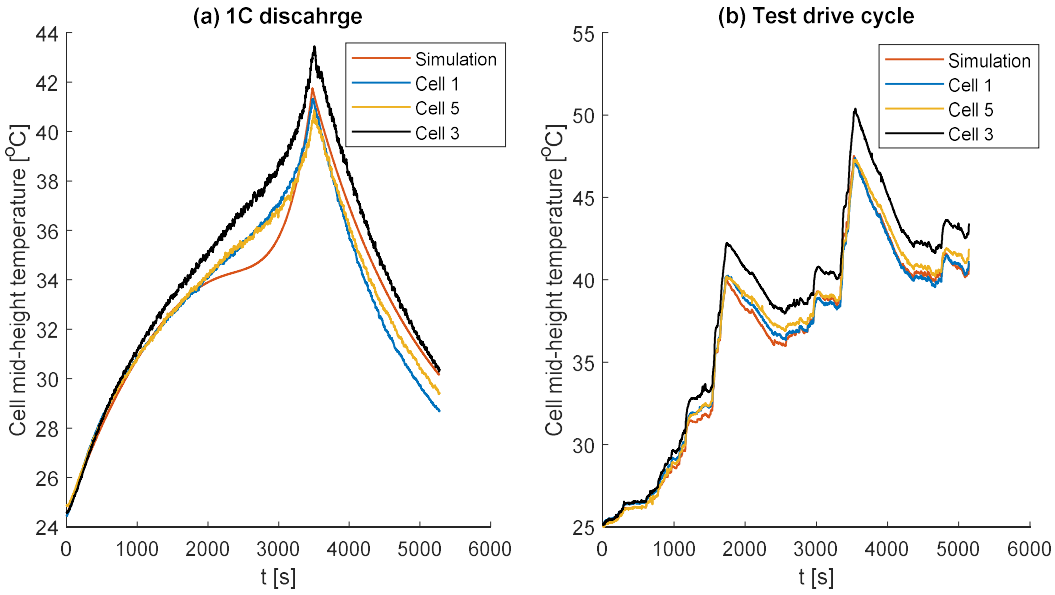

Figure 3-13: Mid-height outer cell surface temperature (a) constant 1 C discharge (b) test drive cycle

Relative to the data from Cell 1, the model provides good agreement with the experimental measurement for both test cases, with a peak error of 5.3% for the 1 C discharge and 2.4% for the test drive cycle. The use of the R_η polynomial has been used for the 1 C discharge, given that the deep SOC discharge results in a large increase in R_η. The cell SOC evolution is estimated through the use of Coulomb counting and is given via:

$$SOC^{n+1} = SOC^{n} - \frac{I\Delta t}{3600(E_c)} \times 100 \quad (33)$$

Where 'n' refers to the time step number, I the cell current [A] (with positive values indicating discharge and negative values indicating charge), and E_c the nominal cell capacity [Ah], which for these cells is 3.1 Ah.

As shown in Figure 3-13 (a), the model slightly under predicts the temperature within the low SOC range <17% where the large increase in R_η begins. This discrepancy may be a result of neglecting the entropic heating effect, which can, in some instances, be greater than 10% of the value of the irreversible heat term between 0-20% SOC depending on the chemistry type at 1 C discharge [136]. Including the effect of entropy is a scope for further work and is discussed further in Section 3.10. For the test drive cycle, the cell SOC does not drop below 17%, and therefore avoids the region of large resistance increase and potentially higher contributions from entropy heating. Given that R_η varies little between 100-17% SOC, a nominal value of 32 mΩ is used in the thermal model for the test drive cycle case. Through avoiding the lower SOC region, the error arising from extrapolation of the polynomial curve to calculate R_η at SOC levels below 10% is avoided. This may explain why the overall observed experimental error is less for the test drive cycle case.

Further comparisons of the model between experimental temperature data obtained from other cell types are conducted in Chapter Four, which is also shown to provide strong agreement between the thermal model and experimental data.

3.6 EV AND PHEV VEHICLE MODEL

To derive battery current profiles (used as an input into the thermal model) that are realistic of real world driving conditions, a 1-D, backward-facing, lumped parameter vehicle model as described in [142], [143] is utilised for the EV and PHEV study. This type of model assumes that the battery supplies the complete power to propel the vehicle, which in addition to EVs, is also appropriate for PHEVs that are operating in charge-depletion or electric only drive mode [144]. The total propulsion force of the vehicle is expressed as [143]:

$$F_p = mf_m a_c + F_i + F_r + F_d \quad (34)$$

Where F_p is the propulsion force [N], a_c the vehicle acceleration [m.s^{-2}], m the curb weight of the vehicle [kg], f_m the mass factor for the vehicle (which accounts for the influence of

the rotating inertias), F_i the force resulting from gradients (incline force) [N], F_r the rolling force due to the road surface [N], and F_d the drag force [N].

The incline force is expressed as:

$$F_i = mg \sin\theta \tag{35}$$

Where g is the gravitational acceleration constant [m. s^{-2}] and θ the inclination angle [rad]. The rolling force F_r is given as:

$$F_r = mgC_r \cos\theta \tag{36}$$

Here, C_r is the rolling coefficient and is related to the condition of the road surface and vehicle tyre material. The drag force assuming zero wind speed is given as:

$$F_d = \frac{1}{2}\rho_A C_d A_f {v_l}^2$$

Where ρ_A is the density of the surrounding air [kg.m^{-3}], C_d the drag coefficient, A_f the frontal area of the vehicle [m^2], and v_l the velocity of the vehicle [m.s^{-1}].

The total power required from the battery to propel the vehicle is given by [142]:

$$P_{b,p} = \frac{F_p v_l}{\chi} = \frac{\left(mf_m a_c + mg\sin\theta + mgC_r\cos\theta + \frac{1}{2}\rho_A C_d A_f {v_l}^2\right) v_l}{\chi} \tag{37}$$

Where $P_{b,p}$ is the battery power for propulsion [W] and χ the efficiency factor which accounts for losses from the inverter, battery and motor (also known as the efficiency of battery to wheels [142]).

For instances where the vehicle propulsion force is negative, the battery can recuperate a portion of the waste energy in the form of regenerative breaking. In this case, the charging power on the battery can be expressed via [142]:

$$P_{b,c} = \frac{F_p {v_l}_p}{\chi} = \left(mf_m a_c + mg\sin\theta + mgC_r\cos\theta + \frac{1}{2}\rho_A C_d A_f {v_l}^2\right) v_l \times \chi_c \tag{38}$$

Where $P_{b,c}$ is the charging power [W] and χ_c the efficiency of power transfer from regenerative breaking into the battery.

The C-rate profile of an individual battery cell can be calculated via:

$$C = \frac{\left(\frac{P}{V_c N}\right)}{E_c} \tag{39}$$

Where C is the battery C-rate [hr^{-1}], V_c the nominal voltage of the battery cells [V], N the total number of battery cells in the battery pack, and P the power profile for the battery. The term $\frac{P}{V_c N}$ is the current through each individual battery cell.

The vehicle properties of a commercial EV and PHEV are used, specifically the 16 kWh Chevrolet Volt [145] and Tesla Model S [146] respectively. These vehicle parameters are deemed to be representative and are shown in Table 3-4. The battery type and chemistry considered for these vehicles are those used for the validation of the thermal model: 18650 type 3.1 Ah cells with a graphite anode and NCA cathode, which are deemed appropriate for use as high energy automotive EV and PHEV batteries (supported by the data provided in Figure A. 6 of Appendix A.5). The number of cells required for each battery pack is calculated from the nominal cell voltage, the nominal cell capacity and the total battery pack capacity (E_{pack}) [kWh].

Table 3-4: Example EV, PHEV vehicle and battery parameters used in the vehicle model

	Curb weight + 80 kg driver [kg]	Frontal area [m^2]	C_d [-]	Cell type [-]	V_c [V]	N [-]	E_c [Ah]	E_{pack} [kWh]
Example EV	2188 [146]	2.33 [147]	0.24 [147]	18650	3.7	7104	3.1	81
Example PHEV	1801[148]	2.20 [147]	0.28 [147]	18650	3.7	1395	3.1	16

Values for the battery to wheels efficiency, efficiency of power transfer from breaking into the battery, rolling coefficient, mass factor and inclination angle are contained in Table 3-5. The values chosen for the efficiency factors and rolling coefficient for an asphalt surface are taken from Peterson et al. [142]. The mass factor value for a typical vehicle is given in [143]. The inclination angle is considered zero for this analysis to represent a complete horizontal surface.

Table 3-5: Efficiency factors, mass factor, rolling coefficient and inclination angle values used in the vehicle model

χ	χ_c	f_m	C_r	θ
[-]	[-]	[-]	[-]	[rad]
0.8 [142]	0.4 [142]	1.05 [143]	0.011 [142]	0

To account for other power requirements aside from vehicle propulsion, such as cabin climate control, lighting etc., a constant positive load of 0.8 kW is added to both Equation (37) and Equation (38) as outlined in [142].

3.6.1 EV AND PHEV DUTY CYCLES

A sample of representative real-world drive cycles are displayed in Figure 3-14, which track the speed of the vehicle with time. These include the US06 drive cycle [69], the Worldwide harmonized Light vehicle Test Procedures (WLTP) Class 3 drive cycle for high power vehicles with a power-to-mass ratio >34 (in which the power of the vehicle is in kW and vehicle mass in metric tonnes) [149], the New European Driving Cycle (NEDC) [150] and the Artemis (Assessment and Reliability of Transport Emissions Models and inventory Systems) cycles [150]. For this analysis, it is desirable to identify a duty cycle that is the most aggressive yet realistic usage condition for which the BTMS for an EV and PHEV may be designed against. Designing a BTMS against a drive cycle that is too gentle may result in inadequate thermal control during its use by the customer, whereas designing against a condition that is overly aggressive and not realistic may result in an overdesigned BTMS that incurs extra cost, weight, volume etc.

For the EV and PHEV analysis, the cells chosen are tailored towards high energy. Table A 3 in Appendix A.5 summarises the appropriate continuous C-rate and pulse C-rate capability of different lithium-ion chemistries, where the NCA chemistry employed in EV and PHEV vehicles is suitable for pulses up to circa 5 C. Therefore, the cell C-rate should not exceed circa 5 C during a duty cycle to remain realistic for the cells chosen in the analysis. The outputted C-rate profiles obtained from the vehicle model for each duty cycle are shown in Figure 3-15 and Figure 3-16 for the EV and PHEV cases respectively. Here, a positive C-rate denotes discharge and a negative C-rate denotes charging.

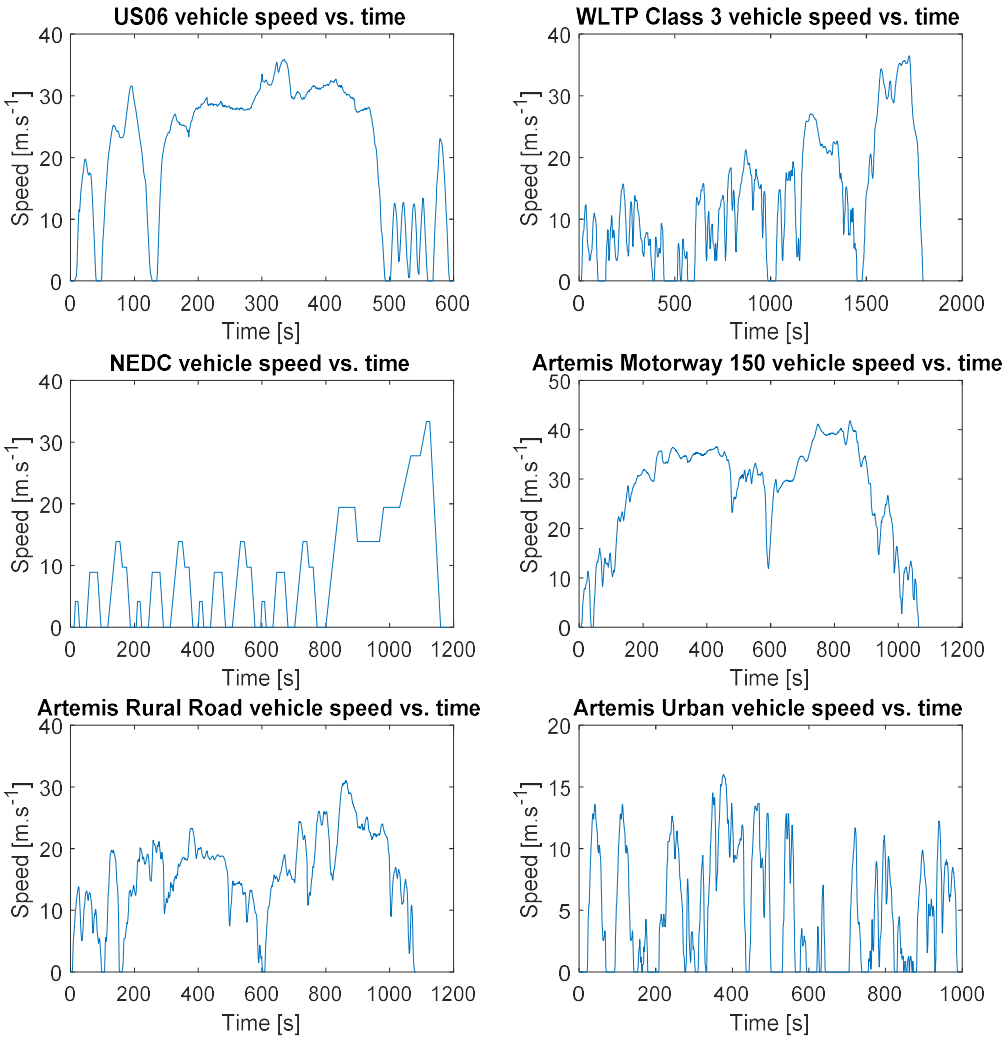

Figure 3-14: Analysed vehicle drive cycles

From Figure 3-15 for the EV case, it is observed that the US06 and Artemis Motorway 150 cycles provide the most aggressive driving scenarios owing to the higher time averaged absolute C-rates. The least aggressive cycles are the NEDC and Artemis Urban. Table 3-6 summarises the values for the peak battery power, peak C-rate, time averaged absolute C-rate, and the average heat generation rate across the cycle calculated from Equation (30) and use of the nominal resistance value of 32 mΩ. As observed, the peak C-rates are within the recommended 5 C discharge pulse limit of the cell. The maximum battery power of 152 kW during the US06 cycle is also within the ability of the Tesla Model S electric machine, which has a peak motor power of 310 kW [146].

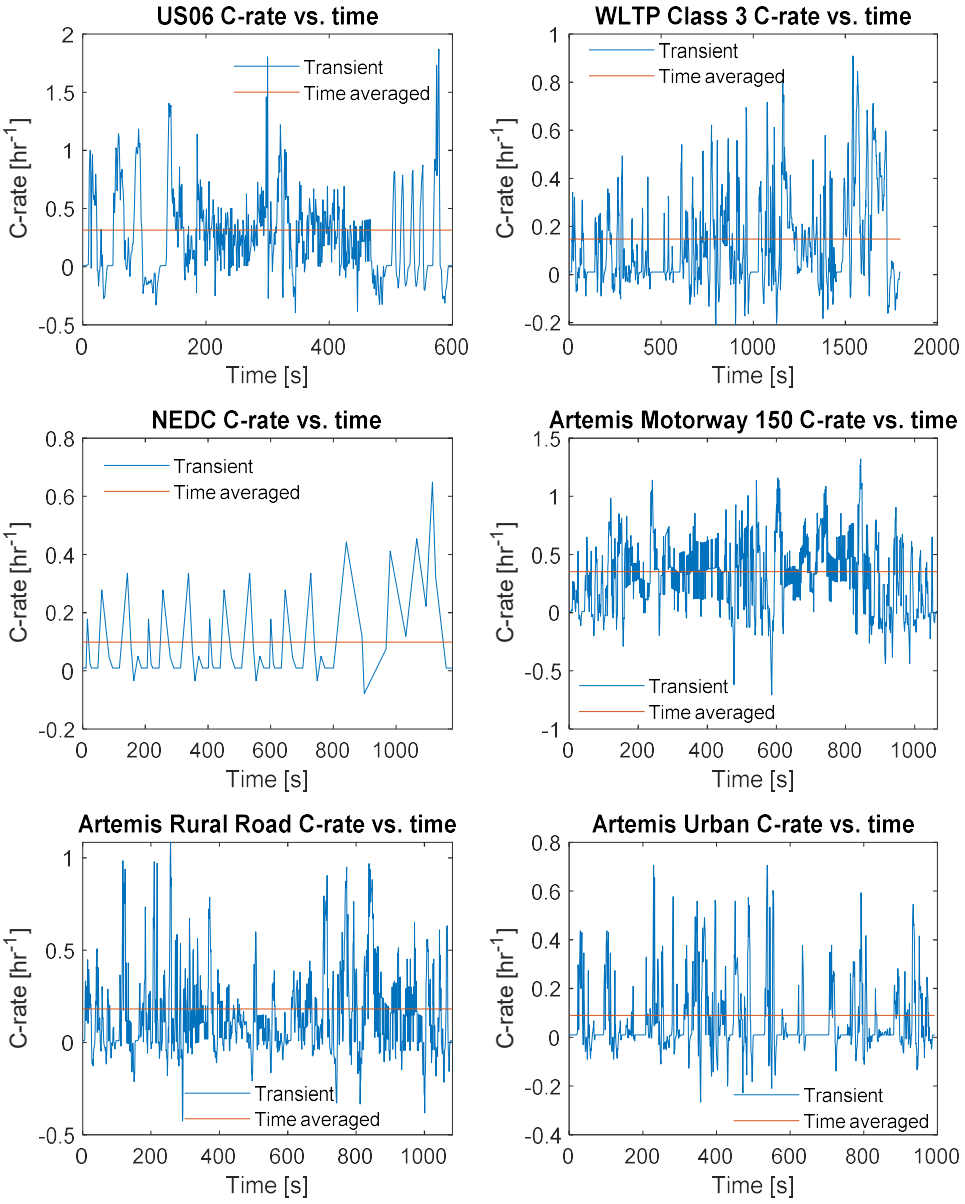

Figure 3-15: EV C-rate profiles (C-rate time average is taken over the absolute C-rate values)

Similar observations are observed for the PHEV case, where the US06 and Artemis Motorway 150 cycles are the most aggressive. However, as seen in Figure 3-16 and Table 3-6, both cycles lead to peak C-rates in excess of 5 C which may be unrealistic for this this cell type and PHEV vehicle operating in all electric drive mode. The most aggressive realistic driving scenarios in this case may, therefore, be the Artemis Rural Road and WLTP Class 3 cycles, whereby the Artemis rural road provides the larger peak C-rate of 4.6 C which is within the performance envelope of this cell type.

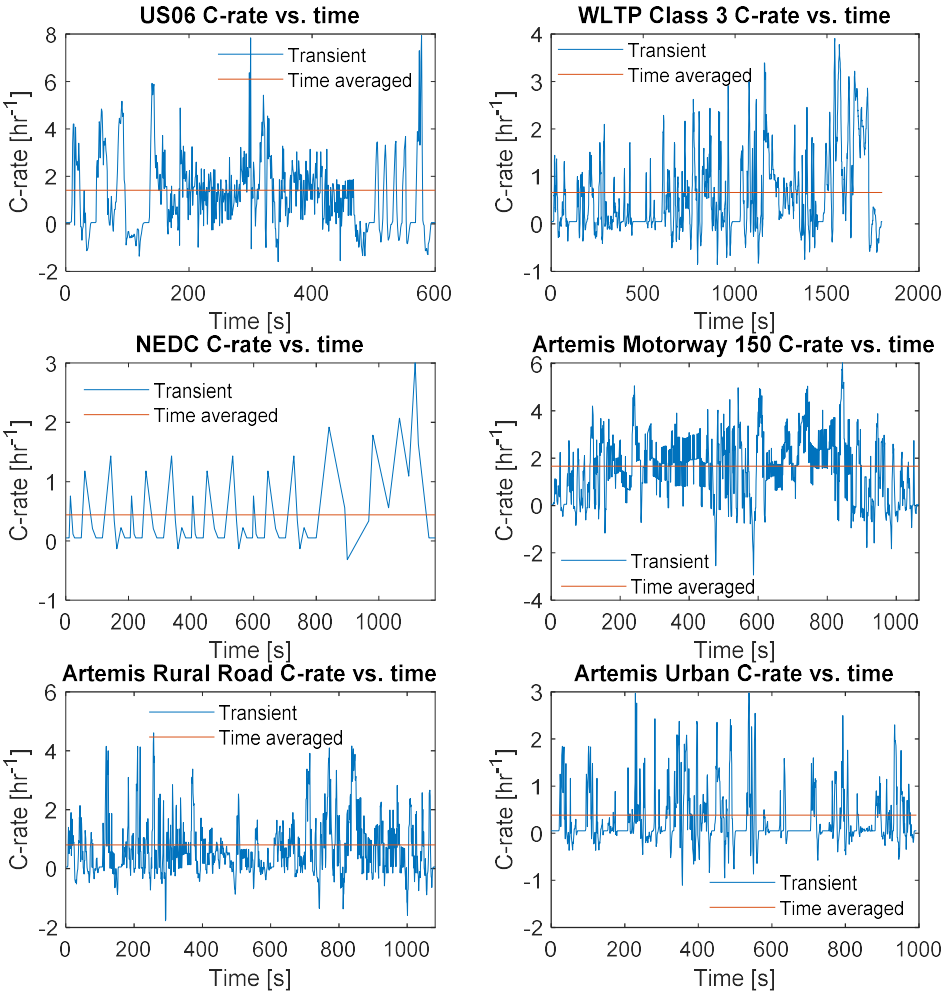

Figure 3-16: PHEV C-rate profiles (C-rate time average is taken over the absolute C-rate values)

For the thermal analysis, only the Artemis Rural Road and WLTP Class 3 cycles will, therefore, be considered for the PHEV case. This is since the US06 and Artemis Motorway 150 are outside the limits of the cell capability. The NEDC and Artemis Urban cycles are also not considered as they are not as aggressive as the WLTP Class 3 and Artemis Urban Road cycles. For the EV case, the US06 cycle is considered as it is the most aggressive case out of the six cycles and satisfies the limits of the cell. However, as the averaged heat generation for the EV US06 cycle is small relative to the PHEV cycles, a 40 minute 1 C charge (from 20% to 87% SOC) is also considered for the EV as a potential worst case scenario for the BTMS. The 1 C charge provides a heat generation rate of 0.308 W using the nominal cell resistance of 32 mΩ, which is circa 5 times greater than the time averaged heat generation across the US06 cycle.

Table 3-6: Summary of the peak battery power, C-rates and average heat generation for the PHEV and EV driving scenarios using 18650 type cylindrical cells

Drive cycle	Model output	EV	PHEV
US06	Peak C-rate [hr^{-1}]	1.870	7.931
	Absolute C-rate average [hr^{-1}]	0.315	1.421
	Peak power [kW]	152.4	126.9
	Average cell heat generation [W]	0.0606	1.179
WLTP Class 3	Peak C-rate [hr^{-1}]	0.909	3.907
	Absolute C-rate average [hr^{-1}]	0.147	0.662
	Peak power [kW]	74.09	62.51
	Average cell heat generation [W]	0.0157	0.316
NEDC	Peak C-rate [hr^{-1}]	0.649	3.002
	Absolute C-rate average [hr^{-1}]	0.0985	0.438
	Peak power [kW]	52.89	48.04
	Average cell heat generation [W]	0.00882	0.175
Artemis Motorway 150	Peak C-rate [hr^{-1}]	1.32	6.021
	Absolute C-rate average [hr^{-1}]	0.351	1.662
	Peak power [kW]	107.6	96.35
	Average cell heat generation [W]	0.0586	1.276
Artemis Rural Road	Peak C-rate [hr^{-1}]	1.084	4.607
	Absolute C-rate average [hr^{-1}]	0.182	0.799
	Peak power [kW]	88.35	73.72
	Average cell heat generation [W]	0.0224	0.422
Artemis Urban	Peak C-rate [hr^{-1}]	0.706	2.979
	Absolute C-rate average [hr^{-1}]	0.0894	0.382
	Peak power [kW]	57.55	47.67
	Average cell heat generation [W]	0.00762	0.137

3.7 HEV DUTY CYCLE

The HEV cycle (based on 4 loops of the US06 drive cycle, is obtained through a simulation with the IPG CarMaker software, which has been provided through collaboration with another member of the Warwick Manufacturing Group (WMG) research team. In this simulation, a medium sized parallel hybrid vehicle is modelled for the HEV that represents a commercially available 5 door premium saloon. The HEV cycle considers 4 loops of the US06 drive cycle. Table 3-7 presents the vehicle parameters used. A full derivation of the model is contained within [151] and will therefore not be repeated here.

The battery control is specified such that the SOC window is constrained to between 70% and 20% SOC. The target SOC of the battery during operation is set to 50%, so as to avoid the limits of deep discharge and deep charge. The initial SOC of the battery at the beginning of the simulation is set to 70%. Electric driving is enabled above an SOC of 50% up to a speed limit of 100 $km.h^{-1}$. Assistance through the electric motor is enabled at an SOC above 25% and becomes active if the vehicle torque demand exceeds either the maximum or optimum

combustion engine torque. This vehicle model is used in conjunction with the speed-time trace of the US06 driving cycle (which is looped 4 times) to determine the HEV battery duty profile.

Table 3-7: Vehicle parameters used in IPG CarMaker simulation

Parameter	HEV
Powertrain	Parallel hybrid
Vehicle Body	Rigid body
Vehicle mass [kg]	1925
Height of centre of gravity [m]	0.6
Wheelbase [m]	2.97
Frontal Area [m^2]	2.38
Drag coefficient [-]	0.3
Electric machine peak power [kW]	40
Electric machine peak torque [N.m]	125
ICE performance [N.m]	400 @ 3500 rpm

A high power 32113 format (32 mm diameter, 113 mm length) cylindrical cell with a nominal capacity of 4.5 Ah is used in the vehicle model (similar to that used in the BMW Active Hybrid 5 [152]) which is produced by A123 Systems and uses a LFP cathode chemistry [152], [153].The nominal internal resistance of the cell is cited as being 4 mΩ [154], with C-rate pulse capabilities in excess of 35 C [153], [154]. The determined C-rate profile for the HEV case using the IPG CarMaker software is shown in Figure 3-17. The average heat generation rate calculated across the duration of the electrical loading condition, given the nominal internal resistance value of 4 mΩ, is 5.828 W.

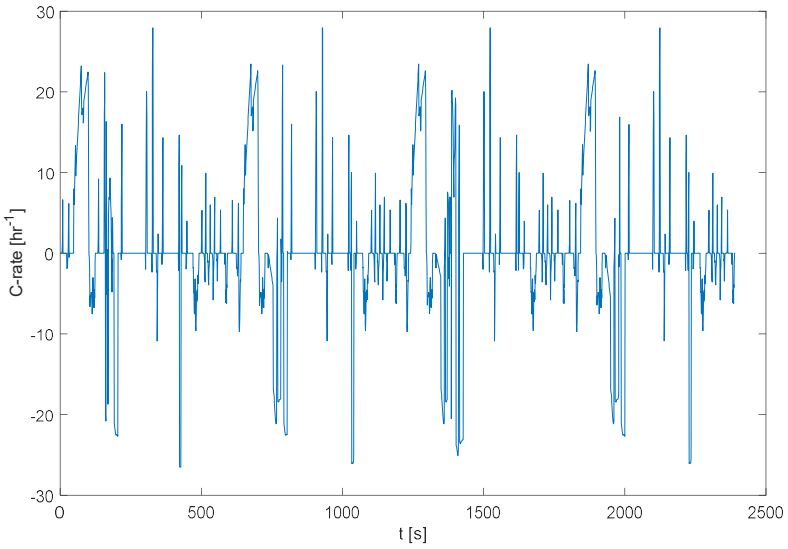

Figure 3-17: HEV 4 loop US06 C-rate profile

3.8 COOLING STUDY ANALYSIS

In this section, the effectiveness of five conventional cell-level cooling strategies are analysed when subject to the EV, PHEV and HEV electrical loading conditions. The five main exterior cooling possibilities for cylindrical cells are:

a. Radial surface cooling
b. Single tab cooling
c. Single tab cooling + radial cooling
d. Both tab cooling
e. Both tab and radial cooling (all sides)

A schematic representation of each of these cooling approaches can be viewable in Figure 3-18. Here, the insulated boundaries where no heat transfer occurs are represented by the dashed rectangles, with the cell material by the homogenous grey larger rectangles. Where there is no insulation, convective cooling exists which is represented by the presence of a convective heat transfer coefficient (h_{z0}, h_{zl} and h_r for the bottom tab, top tab and outer radial surface respectively [W.m^{-2}.K^{-1}]). It is noted that schematic b) and c) in Figure 3-18 may also be expressed as top tab, and top tab and radial cooling respectively, in which bottom tab cooling has been shown in this instance.

The first two cases a) and b) represent typical cooling choices, with a form of radial cooling being employed in the current model of the Tesla Model S [66]. The last three represent a

more involved cooling approach which targets cooling at multiple exterior surfaces of the cell. Such approaches are expected to require a more complicated cooling design, achieved either through direct submersion of the cell with a dielectric heat transfer medium (potential for case e)) or through a cooling jacket/discrete tubing that encompasses more than one surface for the cell. All approaches utilise only exterior cell cooling and do not cool at the cell core, which is representative of the current approach for battery thermal management [39].

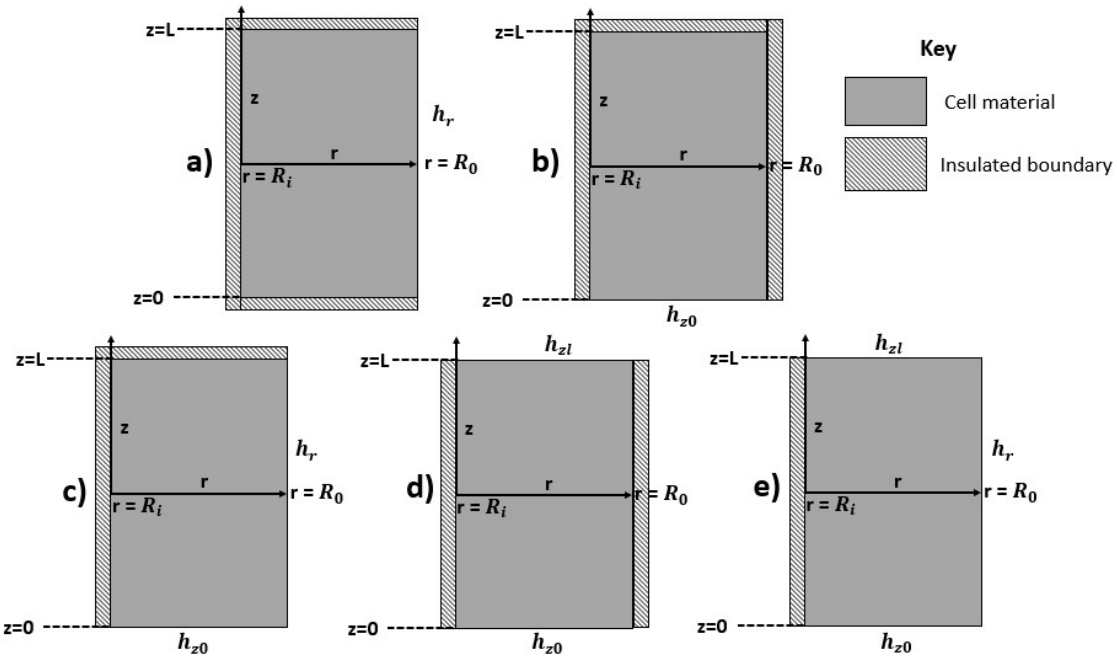

Figure 3-18: Schematic of different approaches for externally cooling cylindrical battery cells (a) radial cooling (b) bottom tab cooling (c) bottom tab and radial cooling (d) both tab cooling (e) both tab and radial cooling/all sides cooling

The heat generation profiles obtained from the vehicle duty cycles and nominal cell resistances from Table 3-9 for the case study simulation are shown in Figure 3-19. Both the full transient profile and the time averaged value for the heat generation rate across the profile are shown. Values for the time averaged heat generation rate for each of the analysed electrical loading conditions are summarised in Table 3-8.

Table 3-8: Time averaged heat generation rate values for each electrical loading condition considered in the case study analysis

Case study scenario	Time averaged heat generation rate [W]
HEV US06 (32113 cell)	5.828
PHEV Artemis Rural Road (18650 cell)	0.422
PHEV WLTP Class 3 (18650 cell)	0.316
EV 1 C fast charge (18650 cell)	0.308
EV US06 (18650 cell)	0.0606

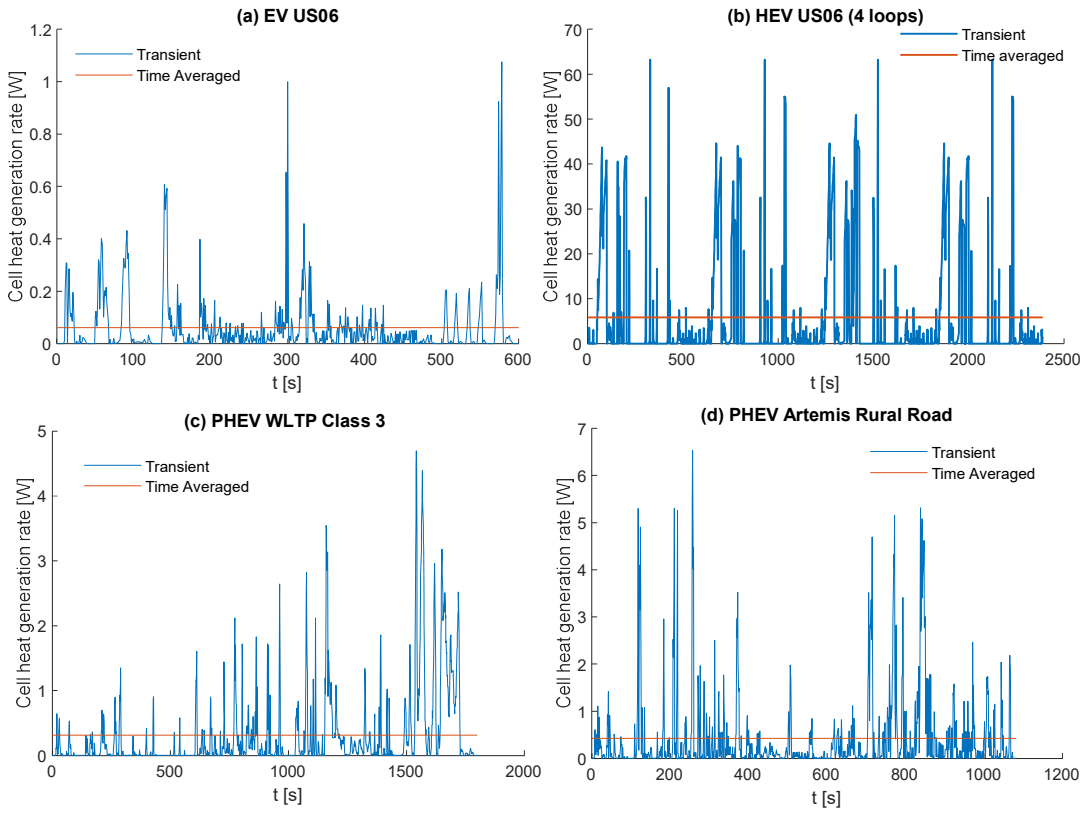

Figure 3-19: Cell heat generation rate profiles for the simulation cooling study analysis (a) EV US06 (b) HEV US06 (c) PHEV WLTP Class 3 (d) PHEV Artemis Rural Road

The cell properties used in the thermal model for both the 18650 and 32113 cell are summarised in Table 3-9.

Table 3-9:Physical properties of battery cells used in simulation

Cell format	k_z [W.m^{-1}.K^{-1}]	k_r [W.m^{-1}.K^{-1}]	C_p [J.kg^{-1}.K^{-1}]	Cell mass [g]	ρ [kg.m^{-3}]	mandrel size [mm]	Nominal cell capacity [Ah]	Nominal R_η [mΩ]
18650	30 [88]	0.25 [107]	1015	40	2418	3 [140]	3.1	32
32113	30	0.25	1020 [155]	205 [153]	2276	3	4.5	4

3.8.1 STEADY-STATE THERMAL ANALYSIS

The thermal resistance concept [123] is employed to rank the effectiveness of the cooling approaches as a function of cooling degree (i.e. 'h' value) applied at the associated cooling boundary surface(s). Thermal management strategies that are of an overall lower thermal resistance (R [K.W^{-1}]) can more effectively supply or remove heat into/out of the cell. For a transient analysis, a lower R value is indicative of a system which can more readily dampen out temperature oscillations [78], and would therefore be preferable for use within a system

with large current fluctuations, e.g. in an HEV cell. The overall thermal resistance constant for heat transfer between the cell hot spot and bulk heat transfer medium is defined as:

$$R = \frac{(T_{max} - T_{\infty})}{Q_c} \tag{40}$$

Where T_{max} is the cell hot spot temperature [K] and Q_c the steady state cell heat generation rate [W]. The thermal model is used to calculate T_{max} and R evaluated from Equation (40).

The results of the R value as a function of h and cooling strategy are displayed in Figure 3-20 (a) - (b) for the 18650 and 32113 cells. The number of h value data points used is shown in the curve for double tab cooling as an example. For cases where more than one surface is cooled, the same value of h is applied at each individual surface. Contact resistance between the cell surface and external cooling mechanism is not considered in this study, which is in-line with the assumptions of previous studies [156].

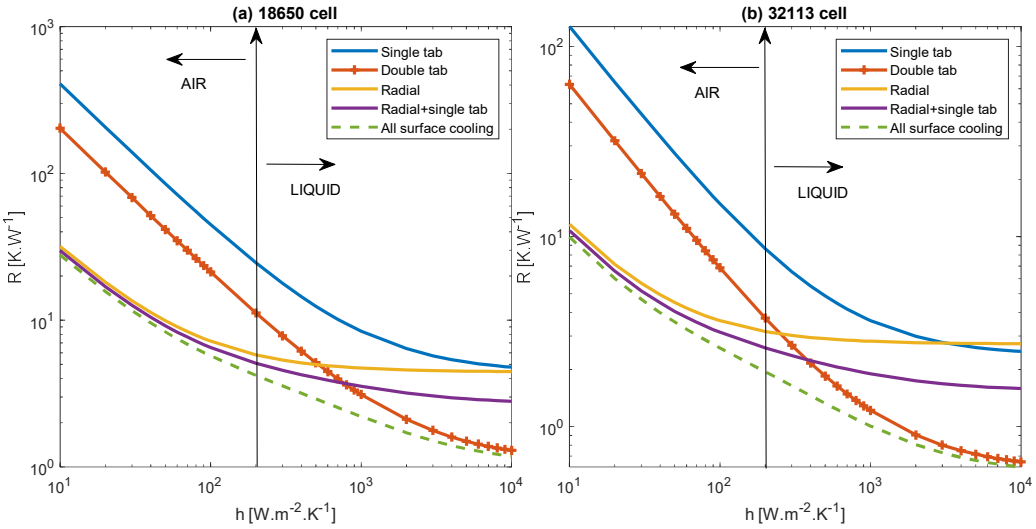

Figure 3-20: Overall thermal resistance as a function of convective heat transfer coefficient and cell-level thermal management strategy for (a) 18650 cell (b) 32113 cell

For singular surface cooled cases, Figure 3-20 highlights that for a given steady-state heat generation rate, radial cooling offers lower R values than singular tab cooling for the 18650 cell for the whole range of h values. For the 32113 cell, the R value of singular tab cooling decreases below radial cooling at h values past 3229 $W.m^{-2}.K^{-1}$. This demonstrates the increased effectiveness of tab cooling for the 32113 cell over the 18650 cell, due to its increased aspect ratio (cell diameter divided by height), whereby a larger surface area for heat transfer is present at the tabs. Also observed for both cells is that tab cooling strategies are primarily limited by the convective component of the overall thermal resistance,

whereby sole radial cooled strategies begin to experience a flattening of the resistance curve past h values of circa 500 $W.m^{-2}.K^{-1}$ for the 18650 cell and 300 $W.m^{-2}.K^{-1}$ for the 32113 cell. This indicates that the cell material thermal resistance begins to limit the overall heat transfer rate under these circumstances, which is a combination of the poor perpendicular effective cell thermal conductivity in the radial direction together with the larger heat transfer area present at the outer radial surface. For tab cooling strategies, the combination of an improved axial thermal conductivity (which is circa two orders of magnitude larger than the radial thermal conductivity component) and lower heat transfer area present at the tab increases the h value range in which axial convective components of the overall thermal resistance limit the heat transfer rate. This is reflected in the levelling of the tab cooling resistance curves at much higher h values. Radial cooling strategies are, therefore, more susceptible to the limitation of the cell thermal conductivity, whereas tab cooling strategies present a greater heat flux issue to the BTMS.

For the 1-D heat transfer cases (radial, singular tab & double tab cooling), the cell material component of the resistance, R_{cell}, can be expressed as a constant by:

$$R_{cell} = \frac{(T_{max} - T_s)}{Q_c} \tag{41}$$

Where T_s is the temperature of the cell surface at the cooling source $[K]$. Knowledge of R_{cell} is useful as T_s is also the minimum cell temperature, therefore, R_{cell} can be used to calculate the magnitude of the cell temperature gradient (ΔT_{max}) for a given value of Q_c. The calculated values for R_{cell} using the thermal model and Equation (41) for the 1-D heat transfer cases are shown in Table 3-10. For the 18650 cell, it is observed that the cell material thermal resistance for radial cooling is near identical to that of singular tab cooling, which implies that the value of the temperature gradient will be near the same in both instances. However, as the direction of the temperature gradient is axial along all the material layers within the cell for tab cooling rather than perpendicular across the layers with radial cooling, it is expected that a reduced ageing rate will occur for the tab cooled method [108], provided that the volume averaged cell temperatures are similar.

The value for the average convective heat transfer coefficient (h) across a body surface is related to the average Nusselt number (which is a function of both the Reynolds number and Prandtl number), fluid thermal conductivity and the characteristic length or hydraulic diameter of the cooling duct/channel [123]. As the value of h is directly related to the fluid

properties of the heat transfer medium, the cooling requirements of the BTMS may dictate whether an air or liquid based BTMS is required. An upper limit for the h value achieved with an air BTMS may be in the region of h = 200 $W.m^{-2}.K^{-1}$ [157], which would correspond to a situation where cross-flow of air exists over the cell to promote turbulence. An example of such a series-parallel type BTMS design is in [54]. However, as stated in [54], this system would consume a much greater amount of parasitic power to operate relative to a liquid cooled system due to the larger volumetric flowrates and hence higher pressure drop incurred by the air system [78]. Smaller mass flowrates to reduce parasitic power would be penalised through incurring a greater pack-level temperature gradient due to the inferior heat capacity of air. As such, such a high h value may not be practical to achieve with air cooling in a large sized EV battery with a long flow path. The potential upper limit of 200 $W.m^{-2}.K^{-1}$ achievable in an air cooled BTMS is highlighted in Figure 3-20, whereby higher values of h indicate the need for a liquid heat transfer medium.

Table 3-10: Steady state cell material thermal resistance and limiting heat generation rate to maintain ΔT_{max}=5°C as a function of cooling strategy and cell type

Cooling strategy	Cell material thermal resistance (R_{cell}) [$K.W^{-1}$]		Limiting steady state heat generation rate for ΔT_{max}=5°C [W]	
	18650 cell	32113 cell	18650 cell	32113 cell
Radial	4.44	2.71	1.13	1.85
Single tab	4.38	2.36	1.14	2.12
Double tab	1.09	0.59	4.59	8.47

Parallel type designs where air is blown axially through channels over the outer cell surface may benefit from improved pack level temperature uniformity [46] but suffer from a reduced h value relative to the cross-flow design. For a parallel type system with a channel hydraulic diameter of 2.2 mm, Kim and Pesaran [78] report an h value of 60 $W.m^{-2}.K^{-1}$, which from Figure 3-20 would result in an R value of 9.01 $K.W^{-1}$ for the 18650 cell and 4.21 $K.W^{-1}$ for the 32113 cell. To achieve the same R value, singular tab cooling would require an h value of 875 $W.m^{-2}.K^{-1}$ and 680 $W.m^{-2}.K^{-1}$ respectively for the 18650 and 32113 cell, which would position it in the region of a water glycol system [78].

As R_{cell} is near identical for singular tab and radial cooling for the 18650 cell, the single tab cooling method requires an h value circa 15 times greater than the radial cooled case to

achieve the same R value. Tab cooling methods alone are thus ineffective with an air based BTMS and should only be considered when a liquid or evaporative [158] heat transfer pack-level strategy is required e.g. for packs that necessitate a large cooling power [53]. It is important to note that these heat transfer medium choices would require the use of an indirect thermal management approach, thus incurring additional thermal resistances between the base of the tab and the cooling/evaporator plate which is not modelled here. To ensure that the tab cooling method remains effective, care must be taken to minimise these resistances when implementing the external heat transfer mechanism.

Figure 3-21 displays the relationship between the steady-state 18650 cell thermal performance, targeted external cooling location and heat generation rate for the case of an air heat transfer medium and liquid heat transfer medium. A value of 50 $W.m^{-2}.K^{-1}$ is chosen to reflect the air cooled system and a value of 750 $W.m^{-2}.K^{-1}$ to reflect the liquid cooled system, which is representative of the cooling configuration employed by Kim and Pesaran for a typical parallel type flow system [78]. The heat transfer medium temperature is set as a constant with a value of 25 °C.

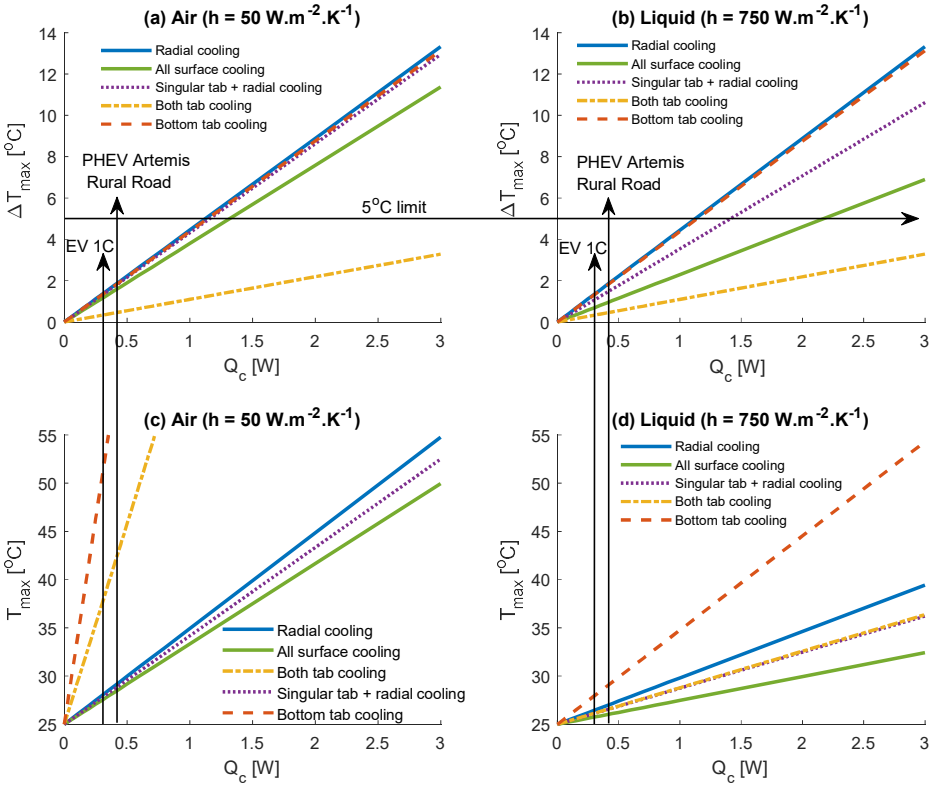

Figure 3-21: Relationship between key 18650 cell thermal conditions and internal heat generation rate as a function of the cooling strategy with (a) ΔT_{max} at h = 50 $W.m^{-2}.K^{-1}$(b) ΔT_{max} at h = 750 $W.m^{-2}.K^{-1}$ (c) T_{max} at h = 50 $W.m^{-2}.K^{-1}$(d) T_{max} at h = 750 $W.m^{-2}.K^{-1}$

The values of the time averaged heat generation rate representative of the drive cycle scenarios from Table 3-8 are displayed by the vertical arrows, which reflect potential realistic limits for the cell operation for both the simulated EV and PHEV. The horizontal arrow represents the 5 °C threshold for ΔT_{max}, which has been considered by many researchers [40], [44], [104] to be a design constraint for the thermal management system to avoid excessive battery degradation rates.

Employing air as the heat transfer medium is suitable for both limiting heat generation cases in limiting ΔT_{max} below 5 °C. For radial and singular tab cooling, ΔT_{max} remains unaltered upon increasing the convection rate to represent forced liquid cooling given the constant cell material thermal resistance. During a transient analysis, increasing the degree of cooling at a given target surface will result in steady state occurring sooner, thus the rise in ΔT_{max} upon initiation of the cooling may be greater for the liquid system relative to the air system. This consideration is important if the characteristic time averaged heat generation values for the given electrical loading condition result in steady-state ΔT_{max} values exceeding 5 °C, as the threshold may be surpassed during the duration of the use scenario.

Whilst tab cooling strategies with air may be suitable in providing acceptable values for ΔT_{max}, Figure 3-21 (c) highlights that the much higher convective thermal resistance at the tabs results in the formation of high hot spot temperatures within the cell. For the EV 1 C charge case, T_{max} approaches 50 °C, whereby for the PHEV case T_{max} exceeds 55 °C. Radial cooling with air enables T_{max} to remain at circa 30 °C, which is acceptable given that this is only a 5 °C rise in temperature relative to that of the bulk heat transfer medium. Upon increasing the convective coefficient to 750 $W.m^{-2}.K^{-1}$, singular tab cooling provides a similar value for T_{max} as with air cooling for the radial case, which reaffirms the need for liquid cooling when employing a tab cooled strategy.

The benefits of cooling multiple surfaces of the cell with air are minimal within the PHEV heat generation region. Targeting additional surfaces of the cell will likely complicate the design of the duct system, thus increasing the complexity of the complete pack design for minimal thermal gain. Therefore, this analysis suggest that air cooling for these applications should likely aim to solely target the complete radial surface.

The steady-state thermal results for the 32113 cell are displayed in Figure 3-22. The higher limit from the HEV time averaged heat generation rate renders cooling strategies that target only a singular surface of the cell ineffective for achieving a limit on ΔT_{max} to $\leq$5 °C. Double

tab cooling is the only strategy that enables ΔT_{max} to remain below 5 °C at the HEV US06 limit. In addition, whilst cooling all surfaces of the cell results in the lowest hot spot temperature, the introduction of a radial cooling component worsens the temperature gradient relative to double tab cooling. The 2-D heat transfer within the cell from combining tab cooling with radial cooling initiates the formation of complex multidirectional temperature gradients within the cell, and given that the temperature gradients are not completely axial, it is expected that such a gradient will induce an increased ageing rate relative to if the same magnitude of gradient were completely axial [108]. Double tab cooling with liquid may, therefore, be the most appropriate choice in terms of cell-level thermal performance.

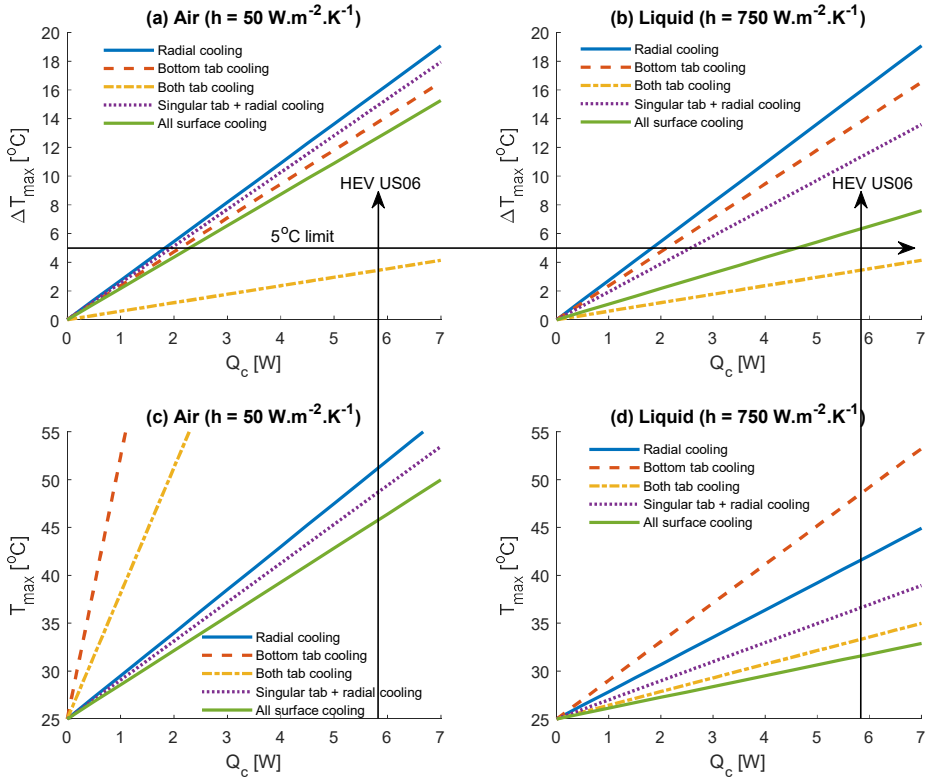

Figure 3-22: Relationship between key 32113 cell thermal conditions and internal heat generation rate as a function of cooling strategy with (a) ΔT_{max} at h = 50 W.m^{-2}.K^{-1}(b) ΔT_{max} at h = 750 W.m^{-2}.K^{-1} (c) T_{max} at h = 50 W.m^{-2}.K^{-1}(d) T_{max} at h = 750 W.m^{-2}.K^{-1}

Radial cooling with liquid can further reduce the hot spot temperature of the cell relative to using air, however, the temperature gradient through the cell becomes increasingly problematic when subject to higher rates of heat generation. At the HEV US06 heat generation limit, liquid radial cooling limits T_{max} to below 45 °C, however, ΔT_{max} reaches 16 °C leading to potentially severe conditions within the cell due to the implied accelerated

electrochemical related ageing effects [41]. Radial cooling with liquid may, therefore, be an inappropriate choice for both the 18650 and 32113 cell, as lower heat generation conditions where ΔT_{max} remains below the 5°C threshold could be satisfied with air cooling or singular liquid tab cooling, whereas higher heat generation conditions begin to become limited by the value of ΔT_{max},which is governed by the thermal resistance within the cell material and not the choice of heat transfer medium. Recommendations for the design of such radial cooled liquid systems as presented in [86] may therefore be misleading, particularly as their thermal modelling does not account for the thermal anisotropy present within the cell nor the inclusion of contact resistances between cell layers.

The thermal contours through the cell for the HEV US06 heat generation rate case and liquid cooled heat transfer medium are displayed in Figure 3-23, highlighting the nature of the internal temperature gradients for each cooling strategy.

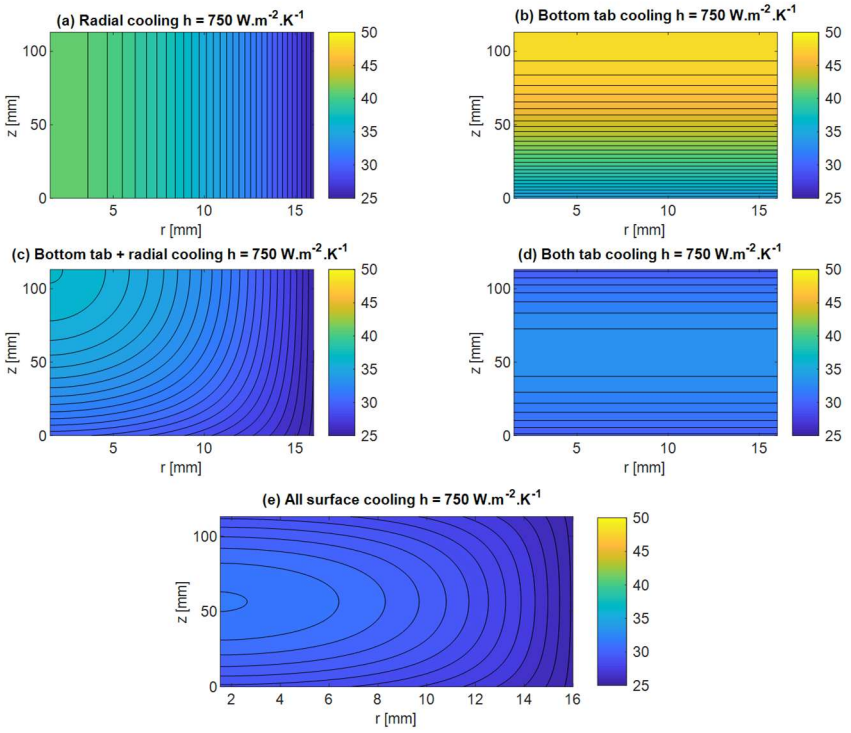

Figure 3-23: Steady state temperature contours for the 32113 type cell with 5.828 *W heat generation rate for different external cooling strategies (colorbar units in* °C*)*

Cooling all surfaces of the cell (Figure 3-23 (e)) with an equal h value at each surface results in the formation of a hot spot at the core of the cell. For sole radial cooling (Figure 3-23 (a)), the hot spot occurs along the axial length at the cell core. One advantage of sole tab cooling (Figure 3-23 (b)) is that the cell hot spot forms at the uncooled tab, therefore, temperature

monitoring sensors may be placed at the more accessible outer surface rather than at the core with radial cooling. This has the potential to improve the reliability of the BTMS as estimations of the internal hot spot temperature may no longer be required.

3.8.2 TRANSIENT THERMAL ANALYSIS

In this section, the full transient electrical loading profiles are input into the thermal model to track the transient temperature evolution of both simulated cells subject to their respective electrical loading conditions. The transient analysis captures all of the thermal data, rather than using simplified heat generation averages and considers the evolution of the cycle under its full usage duration.

Thermal results for the EV model subject to 4 loops of the US06 cycle, together with a 40 minute 1 C charge (from 20% to 87 % SOC) are shown in Figure 3-24. Here, the volume averaged cell temperature rise T_{avg} is also included (shown in Figure 3-24 (c)). The estimated SOC profiles for each of the transient duty cycles are shown in Figure 3-25.

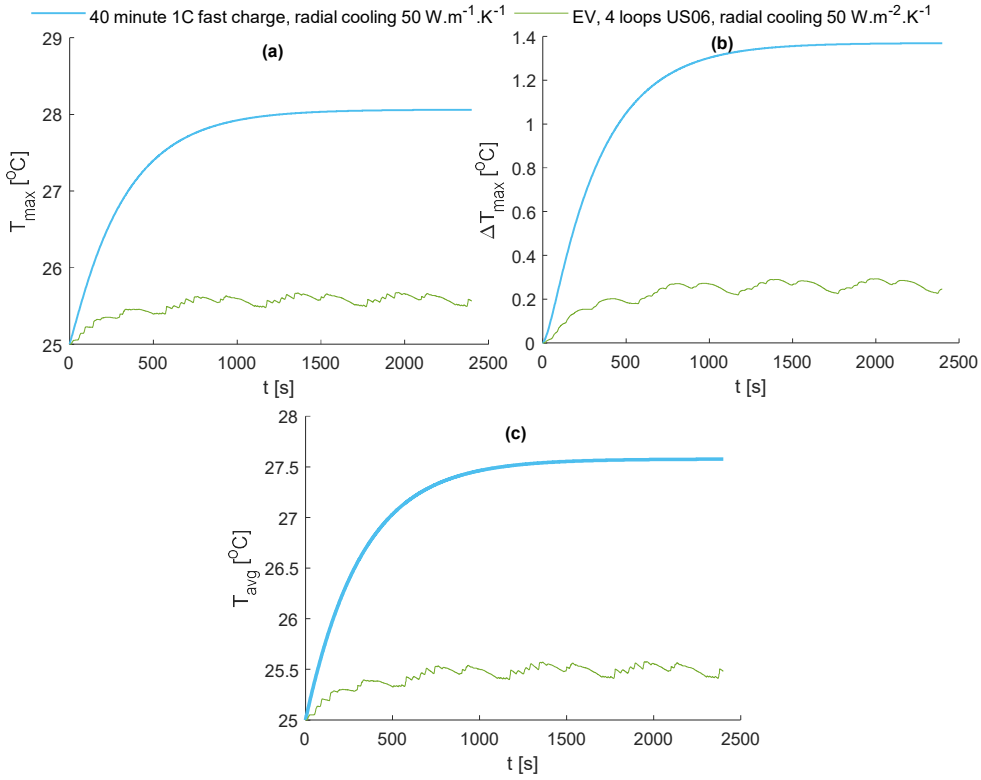

Figure 3-24: EV thermal model results for the 18650 type cell subject to radial air cooling boundary condition with (a) T_{max} evolution (b) ΔT_{max} evolution (c) T_{avg} evolution

Owing to the small time averaged cell heat generation rate across the US06 cycle of 0.0606 W (as a result of the large pack size (81 kWh)), Figure 3-24 demonstrates that there is a small

thermal effect on the cell. There is little fluctuation from the steady-state analysis using the time averaged heat generation rate owing to the low cell C-rates experienced, whereby a quasi steady-state condition is achieved. For both electrical loading conditions, a basic radial air cooling approach is still sufficient to limit ΔT_{max} to below 1.5 °C. The small thermal effect on the cell may explain why Tesla is able to employ a cooling mechanism that utilises a much lower heat transfer surface area by only contacting a portion of the outer radial surface in their Model S EV (see Figure 2-19 in Chapter Two).

Transient thermal results for the PHEV electrical loading conditions can be viewed in Figure 3-26 for the Artemis Rural Road Cycle and Figure 3-27 for the WLTP Class 3 cycle. Each drive cycle is looped back-to-back 3 times to provide full quasi steady-state temperature profiles. Moderate forced convection of air with h = 50 $W.m^{-2}.K^{-1}$, as with the steady-state analysis, again provides almost identical temperature performance as singular tab cooling with liquid at h = 750 $W.m^{-2}.K^{-1}$. The final estimated SOC of the cell after the 3 loops of the Artemis Rural Road cycle is 39.7% (shown in Figure 3-25 (b)).

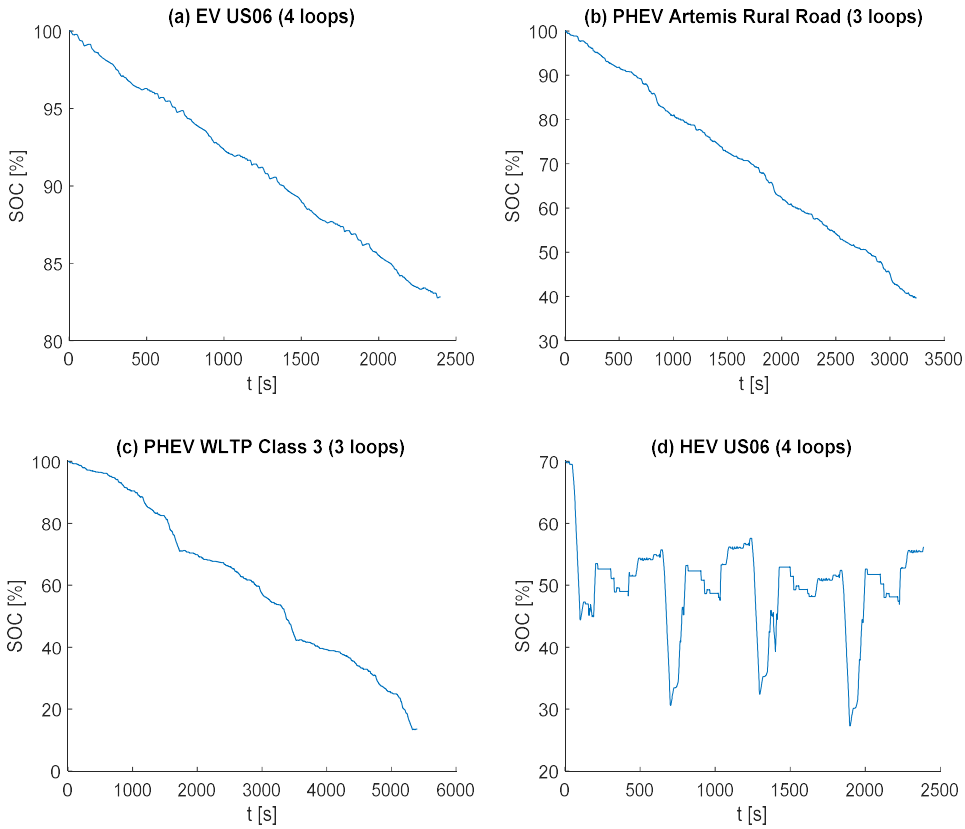

Figure 3-25: Estimated cell SOC during the duty cycles for (a) EV US06 (4 loops) (b) PHEV Artemis Rural Road (3 loops) (c) PHEV WLTP Class 3 (3 loops) (d) HEV US06 (4 loops)

For a PHEV, the typical SOC range may vary from 100-30%, where after 30% SOC the vehicle may disengage the EV drive mode and operate in a charge sustaining mode as discussed in [144]. Therefore, looping the Artemis Rural Road cycle 3 times may be considered a potentially realistic driving condition for the vehicle. For the WLTP Class 3 cycle, the final SOC is 13.6%, indicating that 3 complete loops of the WLTP cycle may potentially be an unrealistic condition for the vehicle.

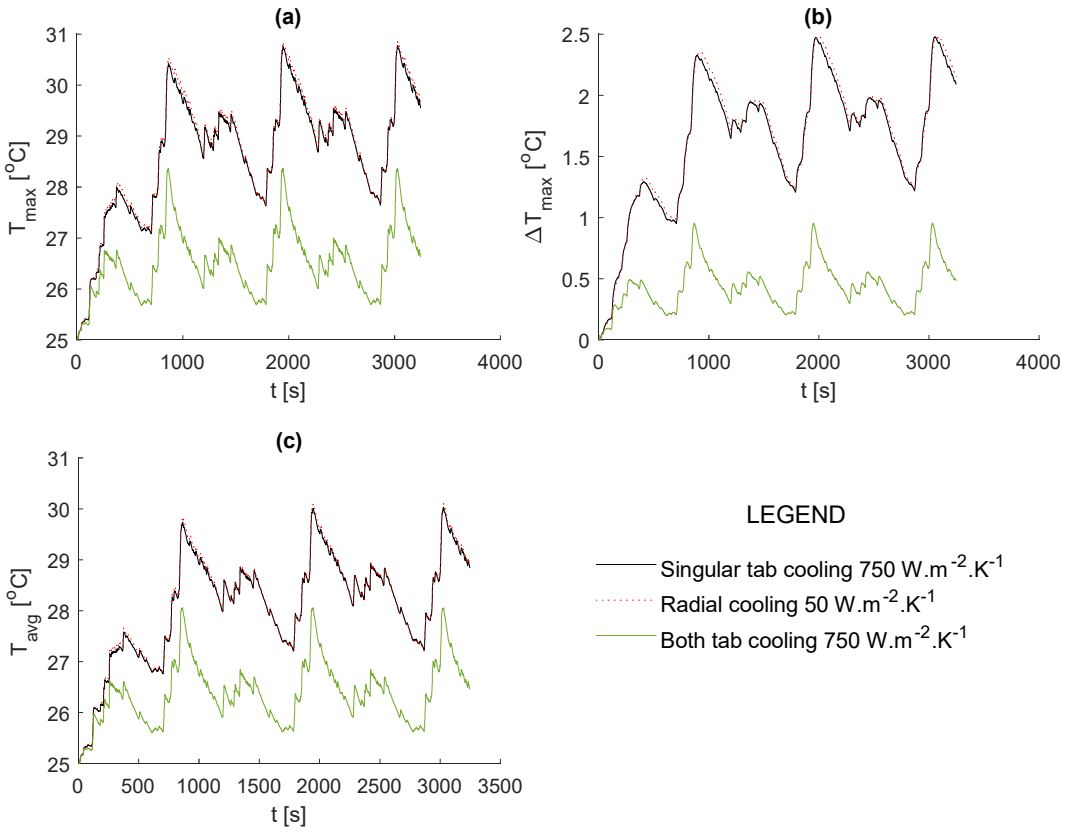

Figure 3-26: PHEV thermal model results for 18650 type cell for 3 loops of Artemis Rural Road cycle with (a) T_{max} evolution (b) ΔT_{max} evolution (c) T_{avg} evolution

Figure 3-26 (a) and Figure 3-27 (a) highlight that the peaks in ΔT_{max} during the transient cycle are higher than that predicted by the steady state analysis using the time averaged heat generation value. This is a result of the higher C-rates experienced during the cycle when compared to that in the EV case. However, ΔT_{max} (Figure 3-26 (b) and Figure 3-27 (b)) does not exceed 5 ℃ for all cooling options considered, whereby both radial air and liquid tab cooling offer acceptable thermal performance. Double tab cooling is the only option that offers a significant reduction in cell temperature gradient, together with effectively limiting the amplitude of peak temperature transients.

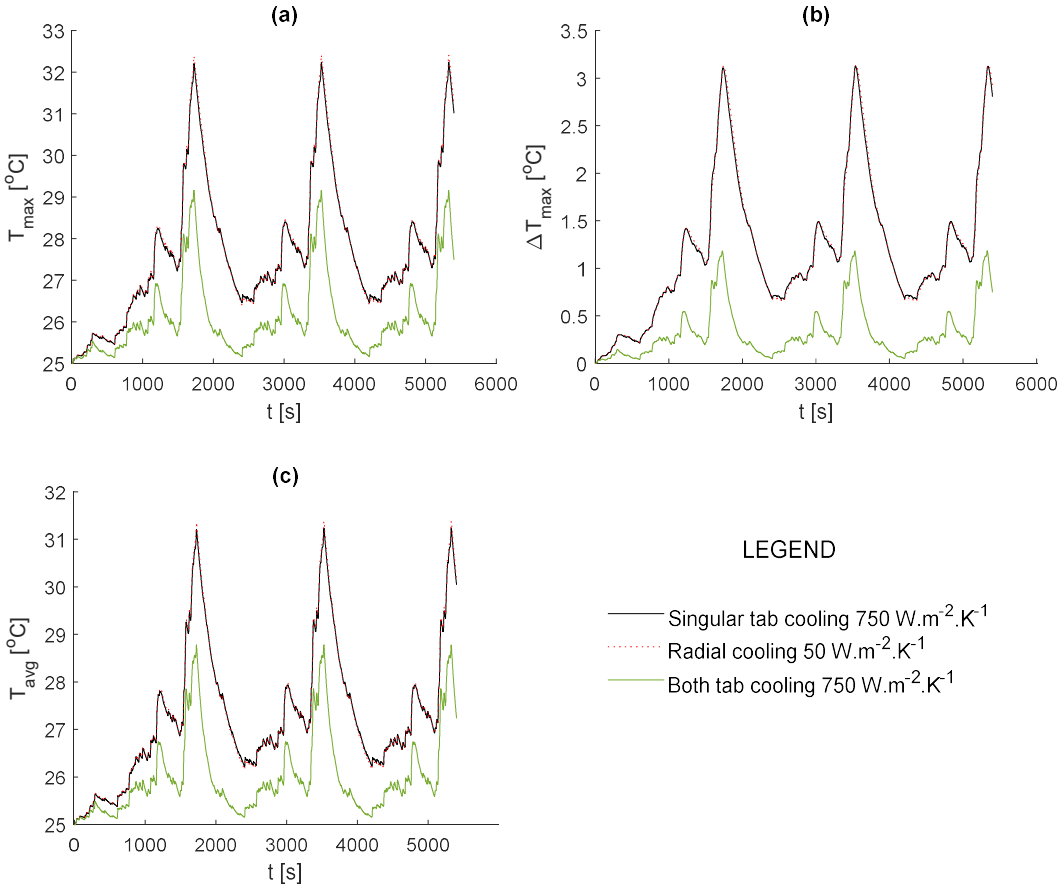

Figure 3-27: PHEV thermal model results for 18650 type cell for 3 loops of WLTP Class 3 cycle with (a) T_{max} evolution (b) ΔT_{max} evolution (c) T_{avg} evolution

Transient thermal results for the HEV case subject to 4 loops of the US06 cycle are shown in Figure 3-28. For radial cooling with air and singular tab cooling with liquid, ΔT_{max} and T_{max} exceed 15 ℃ and 50 ℃ respectively during the 4 loops of the US06 HEV cycle. Introducing liquid radial cooling together with singular tab cooling offers a large reduction in both the value of T_{max} and T_{avg} by more than 10℃ at the hottest point (t = 1428 s), relative to sole liquid radial cooling. However, this strategy still fails to limit the peak value of ΔT_{max} to below 15 ℃, and actually results in larger transient peaks in ΔT_{max} of up to 18. ℃. The greatest dampening effect on the value of ΔT_{max} is again observed with double tab cooling with liquid, enabling the peak value to remain at 6 ℃.

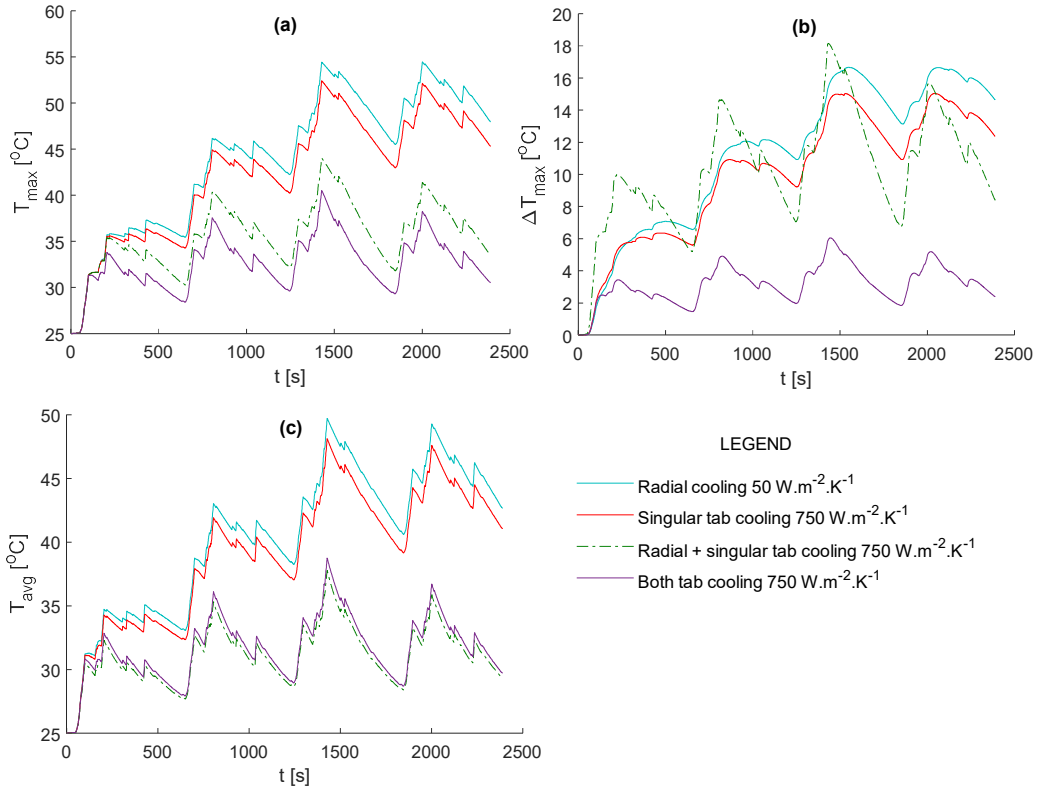

Figure 3-28: HEV thermal model results for the 32113 type cell for 4 loops of the US06 cycle with (a) T_{max} evolution (b) ΔT_{max} evolution (c) T_{avg} evolution

3.8.3 COMPARISON BETWEEN THE TIME AVERAGED AND TRANSIENT HEAT GENEARATION THERMAL OUTPUTS

The steady-state charts contained within Section 3.8.1 offer an insight into the thermal performance differences between the cell-level external cooling strategies. In addition, when using the time averaged heat generation rate of the cycle, the steady-state charts provide an initial indication into the potential thermal performance of the cooling method prior to running the full transient model. However, the steady-state results using the time averaged heat generation rate will lead to an underestimation of the peak thermal outputs experienced during the cycle use scenario. Therefore, it is beneficial to compare the differences between running the time averaged heat generation rate for use in the steady-state charts to that obtained with the more involved full transient thermal model.

Figure 3-29 displays the comparison between the thermal model outputs using the full transient heat generation profile and the static time averaged heat generation rate for the HEV cycle subject to single tab cooling at h = 750 $W.m^{-1}.K^{-1}$. Here, it is apparent that full steady-state is not reached with the time averaged input, although it is approached due to the levelling of the temperature curves.

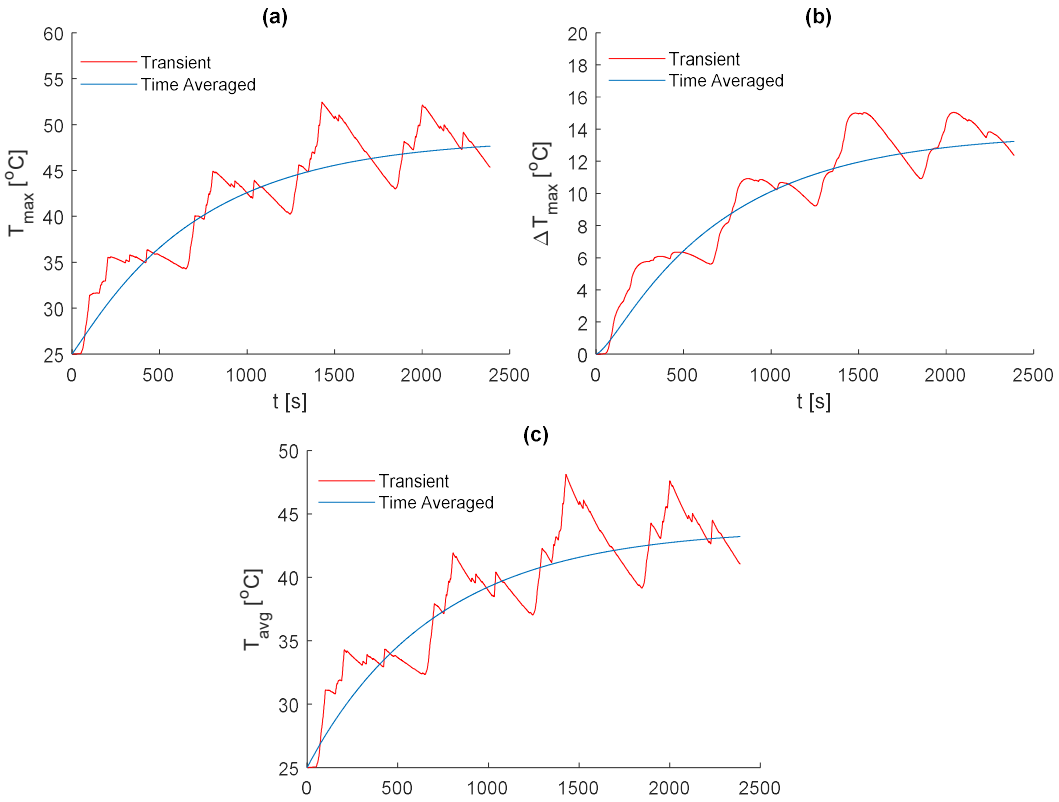

Figure 3-29: Comparison between the thermal model outputs using the static time averaged heat generation rate and full heat generation rate profile for single tab cooling with h = 750 W.m^{-1}.K^{-1} for the HEV cycle with (a) T_{max} evolution (b) ΔT_{max} evolution (c) T_{avg} evolution

Table 3-11 summarises the differences between the thermal outputs of the transient and stead-state model using the time averaged heat generation rate. For the HEV cycle, the steady-state model leads to a T_{max} value of 48.5 °C, whereas the peak temperature transient is 52.42 °C which is an underestimation of circa 4 °C. A similar difference is observed for the T_{avg} values. For the ΔT_{max} values, the steady -state approximation with time averaged heat generation underestimates the peak ΔT_{max} transient by circa 1.5 °C.

Similar comparisons for the PHEV cases are viewable in Figure 3-30 for the Artemis Rural Road (3 loops) and Figure 3-31 for the WLTP Class 3 cycle (3 loops). For the Artemis Rural Road case, steady-state is achieved for the time averaged heat generation model, where an understimation of crica 2 °C is observed for the T_{max} and T_{avg} values relative to their peak transient values. For ΔT_{max}, the difference is lower at less than 1 °C. For the WLTP Class 3 cycle, the difference between the two models is larger wherby T_{max} and T_{avg} are underestimated by circa 4 °C and ΔT_{max} by circa 2 °C, likely owing to the greater amplitude of the temperature spikes experienced when running the full transient model.

Table 3-11: Comparison between the thermal metrics from using the time averaged static heat generation and full transient heat generation profile

Duty Cycle	Using time averaged heat generation rate			Using full transient profile		
	Steady-state value of thermal parameter			Peak value of thermal parameter		
	T_{max} [°C]	T_{avg} [°C]	ΔT_{max} [°C]	T_{max} [°C]	T_{avg} [°C]	ΔT_{max} [°C]
HEV US06 (4 LOOPS)	48.49	43.88	13.76	52.43	48.12	15.03
PHEV Artemis Rural Road (3 loops)	29.12	28.50	1.85	30.77	30.03	2.48
PHEV WLTP Class 3 (3 loops)	28.09	27.62	1.38	32.24	31.23	3.13

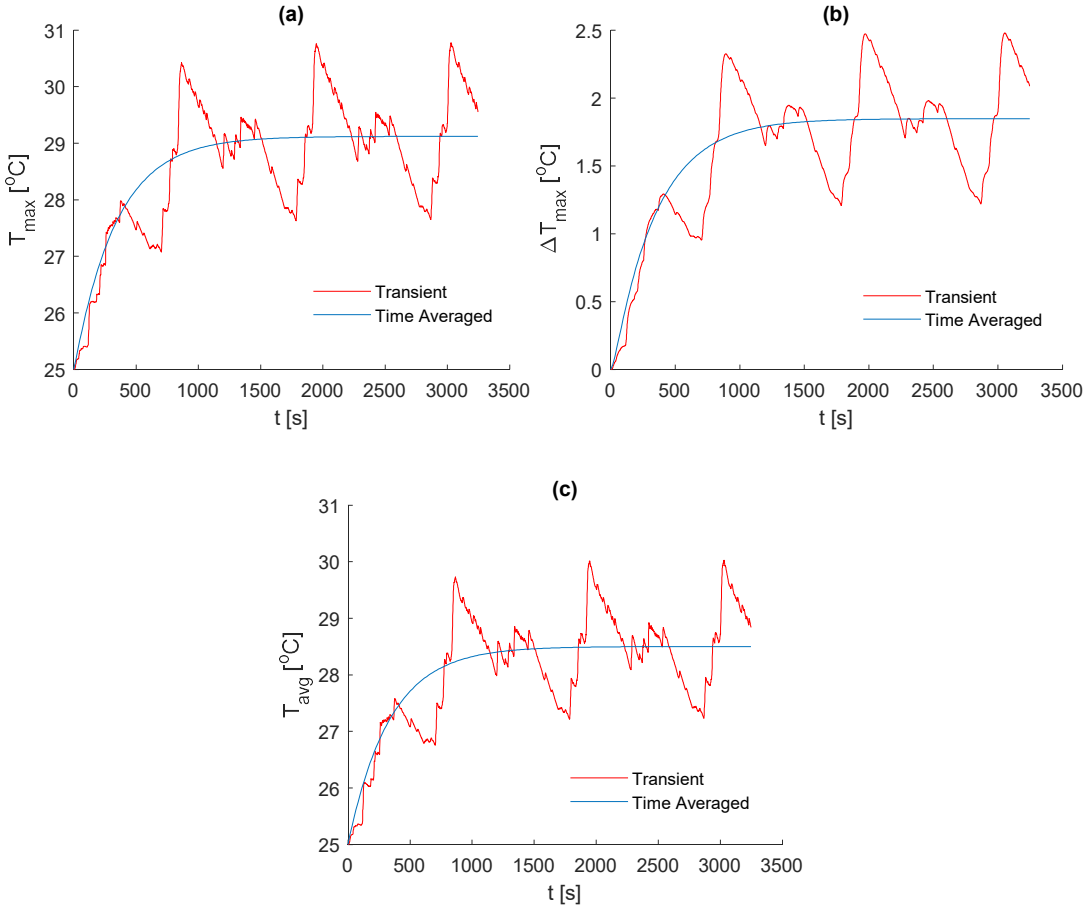

Figure 3-30: Comparison between the thermal model outputs using the static time averaged heat generation rate and full heat generation rate profile for single tab cooling with h = 750 W.m^{-1}.K^{-1}for 3 loops of the PHEV Artemis Rural Road cycle with (a) T_{max} evolution (b) ΔT_{max} evolution (c) T_{avg} evolution

Overall, provided the duty cycle under analysis is looped multiple times to enable a quasi steady-state condition, the use of the time averaged heat generation rate and steady-state charts contained in Section 3.8.1 provide a reasonable indication into the average thermal performance of the cycle relative to running the full transient thermal model. However, care must be taken when using the charts for time averaged heat generation rates that lead to ΔT_{max} values approaching 5°C, as the transient spikes will likely exceed this value.

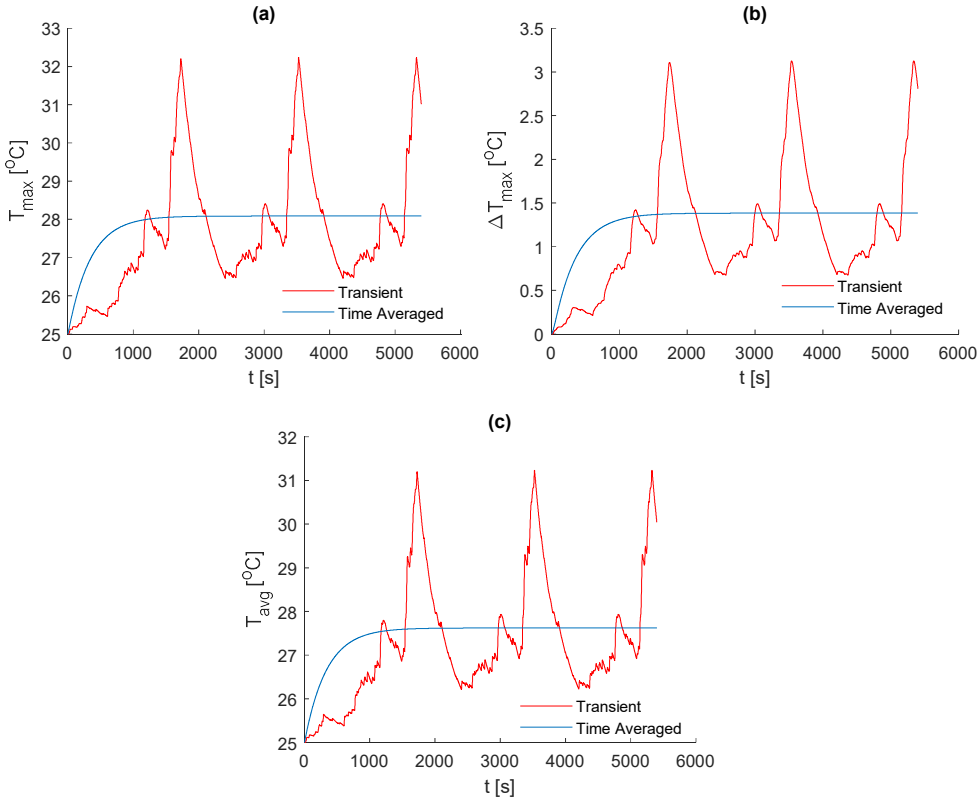

Figure 3-31: Comparison between the thermal model outputs using the static time averaged heat generation rate and full heat generation rate profile for single tab cooling with h = 750 W.m^{-1}.K^{-1}for 3 loops of the PHEV WLTP Class 3 cycle with (a) T_{max} evolution (b) ΔT_{max} evolution (c) T_{avg} evolution

3.9 CELL THERMAL CONDUCTIVITY SENSITIVITY ANALYSIS

The thermal analysis uses average values for the effective cell thermal conductivity, which are obtained from the literature review analysis for lithium-ion cell thermal properties in Section 3.2.2. Given that these values have not been measured for either the 18650 type or 32113 type cells in this particular thermal analysis, a sensitivity study is performed to investigate the effect of thermal conductivity on cell thermal performance for radial and tab cooling.

From Section 3.2.2, Vertiz et al. [119] report a low end value of 0.175 $W.m^{-1}.K^{-1}$ for the perpendicular thermal conductivity in a 'dry' pouch cell. Without electrolyte, the thermal contact resistance present between layers is higher since the gap thermal conductance is lowered from the presence of low conductivity air/gases within the voids formed from contact of the material asperities. For a cell saturated with electrolyte, the measured thermal conductivity from Vertiz et al. increased to 0.284 $W.m^{-1}.K^{-1}$ [119], further highlighting the importance of the electrolyte in increasing the thermal conductivity. Drake et al. [88] report a lower value (experimental) of 0.15 $W.m^{-1}.K^{-1}$ for a 26650 cylindrical cell, and is one of the lowest values reported in literature. This value is therefore chosen to represent a potential lower bound for the perpendicular thermal conductivity in the sensitivity study. Values as high as 0.4 $W.m^{-1}.K^{-1}$ have been reported by Fleckenstein et al. [41] for the effective perpendicular thermal conductivity of the cell spiral roll material in a 32113 cell, but this neglects the presence of the outer casing and electrolyte contact layer. A value of 0.50 $W.m^{-1}.K^{-1}$ is chosen as the upper bound in the sensitivity analysis to see the effect of such a high perpendicular thermal conductivity for the cell.

The results for the perpendicular thermal conductivity sensitivity study are shown in Figure 3-32, which has been conducted for the HEV case study with radial only cooling at 50 $W.m^{-2}.K^{-1}$. As seen, increasing the perpendicular thermal conductivity results in a marked reduction in ΔT_{max} together with an overall decrease in T_{avg}. This is attributed to the lower thermal resistance through the cell material as the cell thermal conductivity is increased. Specifically, increasing the thermal conductivity from 0.15 $W.m^{-1}.K^{-1}$ by 66.7 % to 0.25 $W.m^{-1}.K^{-1}$ results in the peak temperature difference decreasing from 25.04 ℃ to 16.66 ℃ (33.5 % decrease). Given these results, effort should thus be made to ensure that the cell internals are sufficiently saturated with fluid electrolyte to maximise the perpendicular thermal conductivity if a radial cooling strategy is sought for. However, given that ΔT_{max} still approaches circa 10 ℃ during the 4th cycle of the US06, with T_{max} approaching 49℃, the choice of radial air cooling with the upper limit for perpendicular thermal conductivity remains inferior to double tab liquid cooling.

For the axial thermal conductivity sensitivity analysis, a deviation of 10 $W.m^{-1}.K^{-1}$ around the value of 30 $W.m^{-1}.K^{-1}$ reported by Drake et al. [88] is specified. In addition, the effects of substituting the conventional graphite anodes of lithium-ion cells to axially orientated carbon nanotubes (CNT) with an axial thermal conductivity of 300 $W.m^{-1}.K^{-1}$ as mentioned in [106] is investigated. Using a value of 300 $W.m^{-1}.K^{-1}$ in replace of 1.04 $W.m^{-1}.K^{-1}$ for conventional

graphite anodes, together with the material properties and layer thicknesses of of common battery materials contained in Table 3-1 in Section 3.2.2 together with Equation (1) , the theoretical effective cell axial thermal conductivity with CNT is calculated as 162 W.m^{-1}.K^{-1}.

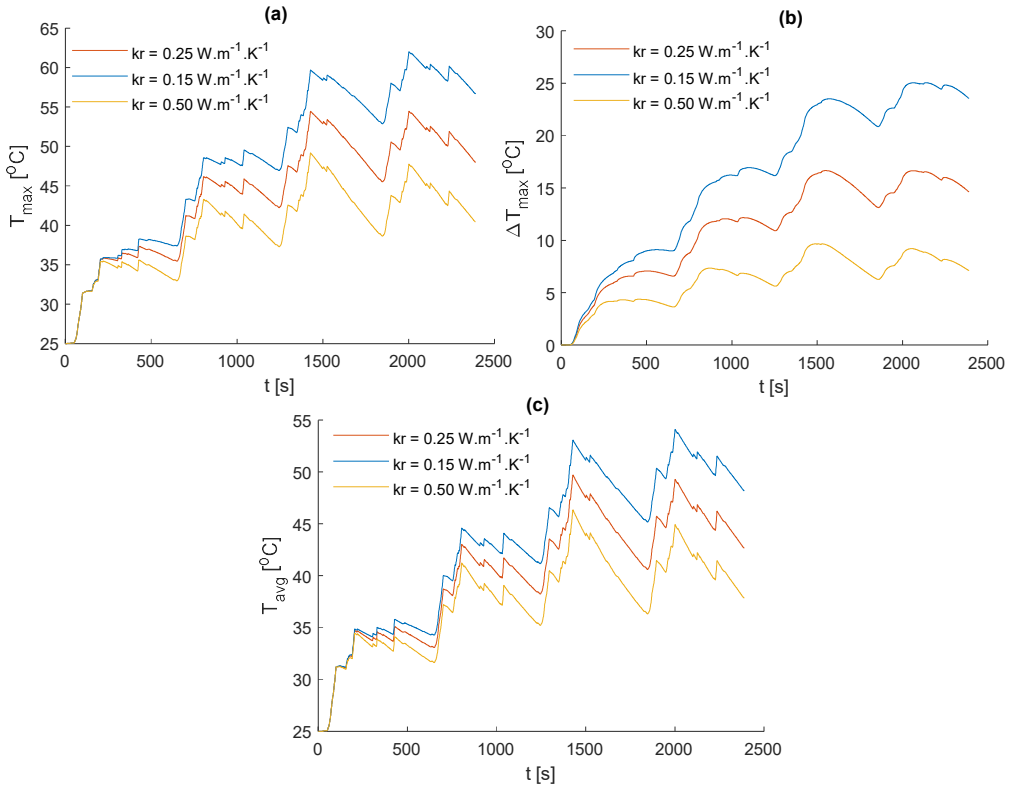

Figure 3-32: Perpendicular thermal conductivity sensitivity study for the 32113 cell subject to HEV duty cycle with radial cooling (50 W.m^{-2}.K^{-1}) for (a) T_{max} evolution (b) ΔT_{max} evolution (c) T_{avg} evolution

Figure 3-33 displays the effect of cell axial thermal conductivity on the thermal performance of the HEV cell subject to bottom tab cooling (750 W.m^{-2}.K^{-1}). From 20 W.m^{-1}.K^{-1} to 30 W.m^{-1}.K^{-1}, ΔT_{max} along the course of the transient analysis is reduced from 20.74 ℃ to 15.03 ℃ (27.5% decrease). Further increasing the thermal conductivity from 30 W.m^{-1}.K^{-1} to 40 W.m^{-1}.K^{-1} offers a lower percentage reduction in ΔT_{max} of 19.3 %. With the CNT and singular tab cooling, the maximum temperature gradient through the cell is 3.8 ℃, less than for the case of double tab cooling. Therefore, provided that issues with CNT for use as anodes in lithium ion-cells can be overcome (such as poorer volumetric capacity relative to conventional graphite anodes [159]), it has the potential to be a particularly attractive thermal management strategy when coupled with tab cooling.

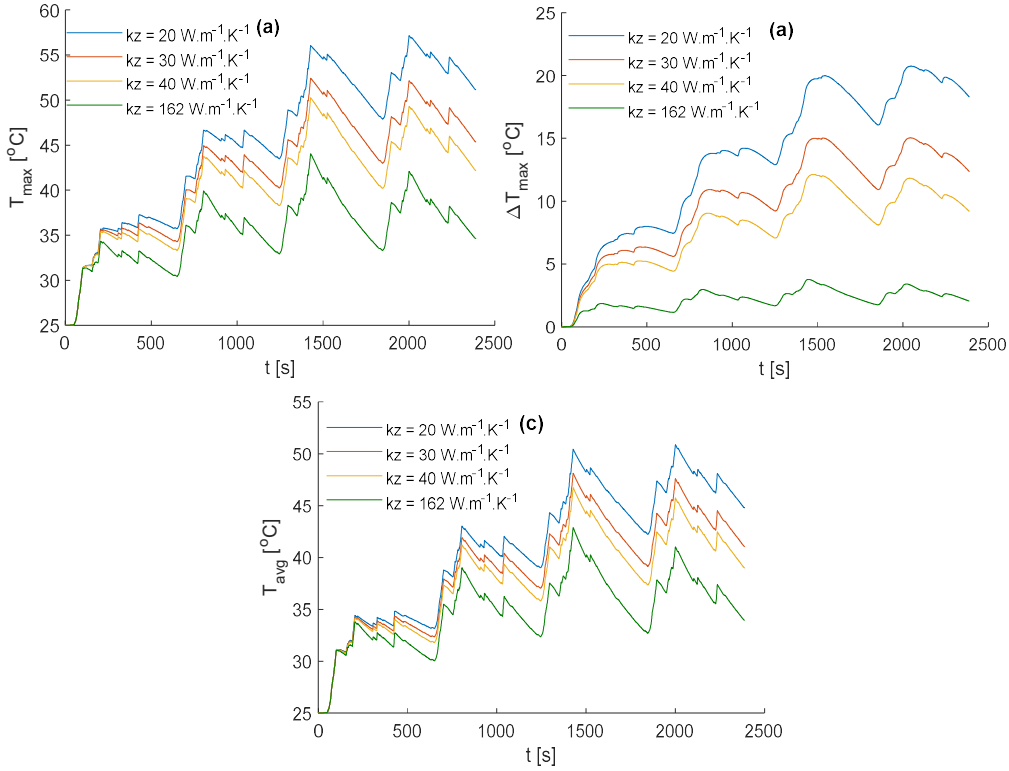

Figure 3-33: Axial thermal conductivity sensitivity study for 32113 cell subject to HEV duty cycle with bottom tab cooling (750 W.m^{-2}.K^{-1}) for (a) T_{max} evolution (b) ΔT_{max} evolution (c) T_{avg} evolution

3.10 FURTHER WORK

Given the limitations of conventional cooling strategies (radial and tab cooling) in thermally managing the cell under high heat generation conditions, additional thermal studies should seek to incorporate heat transfer mechanisms that can directly enhance the heat transport through the internal of the cell. Such mechanisms may avoid the need for double tab cooling, which may overcomplicate the design of the pack-level thermal management strategy given that cooling must be applied at both ends of the cell.

Including the effect of entropy and temperature dependence within the heat generation estimation is also a scope for further work to increase the fidelity of the thermal model.

3.11 CONCLUSION

To address Research Objective 1, the following conclusions are drawn on the cell-level thermal management options for cylindrical cells under different automotive duty cycles.

Results from the steady-state thermal analysis indicate that radial cooling 18650 type energy cells with either air or liquid is effective in limiting ΔT_{max} to below 5 ºC when subject to

constant heat generation rates of up to 1.1 W. This value covers the range of time averaged heat generation values considered for the aggressive EV and PHEV duty cycles, whereby the limiting value for a realistic aggressive application was identified as 0.42 W for the Artemis rural road PHEV cycle. For these conditions, it is likely that internal core cooling is not required due to the adequate thermal performance of singular tab and/or radial cooling.

Singular tab cooling with liquid results in a similar thermal performance as radial cooling with air, with the difference that the internal cell hot spot is moved from the core of the cell towards the opposite tab that is not cooled. Combining air cooling at the tabs in addition to the radial surface offers little benefit within the steady-state limit of PHEV time averaged heat generation. Therefore, the additional complexity involved with targeting air cooling at multiple cell surfaces is not justified. For battery packs designed with a liquid heat transfer medium, singular tab cooling is expected to be the preferred choice over radial cooling provided that the convective heat transfer rate is with the region of 750 $W.m^{-2}.K^{-1}$, given the more preferable direction of the thermal gradient that is similar in magnitude.

For 32113 type power cells, radial and singular tab cooling can limit ΔT_{max} to below 5 ºC up to a steady-state heat generation rate of 1.8 W and 2.1 W respectively. This is far below the limit for the time averaged value of 5.8 W across four loops of the US06 HEV cycle. In order to avoid excessive cell degradation rates under these conditions, the results of the thermal modelling suggest that double tab cooling with a liquid heat transfer medium is required. If cooling at a single surface is desired, methods to reduce the thermal resistance within the cell, such as through internal cooling, should be sought.

Comparison between the steady-state thermal results using the time averaged cycle heat generation rate and full transient thermal model did not identify any appreciable differences that would alter the choice of cooling strategy, provided the transient model reaches a quasi steady-state (e.g., by looping the drive cycle of interest multiple times). The difference between the two models becomes larger during cycles with greater fluctuations in the C-rate (e.g. for the HEV and PHEV cases) where transient temperature spikes are larger. However, the steady-state model is within circa 4 ºC of the highest peak temperature transient predicted for all cooling cases and analysed electrical loading conditions. The steady-sate thermal charts contained within this Chapter, therefore, provide useful initial design guidelines for facilitating the cylindrical cell-level thermal management choice for a given characteristic time averaged drive cycle heat generation rate.

4 CHAPTER FOUR - A NEW APPROACH TO THE INTERNAL THERMAL MANAGEMENT OF CYLINDRICAL BATTERY CELLS FOR AUTOMOTIVE APPLICATIONS

4.1 INTRODUCTION

The research from Chapter Three has identified that conventional cooling approaches that target either a singular tab or outer surface of common format cylindrical lithium-ion battery cells suffer from a high cell thermal resistance, which is a limitation of the cell format and material properties. Therefore, BTMS designs that focus on such external cooling approaches are inherently limited in their ability to inhibit the formation of large in-cell temperature gradients and high hot spot temperatures (which are known to accelerate ageing and further reduce performance) under aggressive electrical loading conditions. Specifically, high power 32113 cells subject to a realistic HEV cycle and duty cycles that exceed a time averaged heat generation rate of circa 1.1 W for 18650 type cells were identified as cases that particularly suffer from poor thermal conditions.

To overcome these limitations, it is envisaged that the next generation of BTMS for cylindrical cells will need to employ methods that can reduce the thermal resistance for heat transfer within the cell. As discussed in Chapter Two, a few studies within the literature have examined the possibility of employing core cooling within cylindrical cells, specifically the research by Sievers et al. [106] and Shah et al. [107].However, the effectiveness of both these strategies relies on the presence of an external cooling mechanism to exist at multiple surfaces of the cell, which in the case of Shah et al. is the protruding heat pipe condenser section in addition to at the external radial surface. The inclusion of both a bottom cooling channel in addition to accommodating air flow/circulation across the large heat transfer area offered at the outer radial surface of the cells reduces the volumetric energy density potential of the complete pack design, as increased inter-cell spacing consideration to accommodate cooling channels/air flow circulation between cells is needed. Another disadvantage of the heat pipe method in [107] is that no appreciable benefit of the heat pipe was observed upon its replacement with a solid copper bar, signifying the superior heat transfer potential offered by the heat pipe with this design is not realised.

In this Chapter, a new approach to internal thermal management of cylindrical battery cells is introduced to significantly enhance the thermal performance of a singular tab cooled

approach, thus alleviating any pack-level complications associated with targeting cooling at multiple surfaces of the cell. Improving the effectiveness of core cooling in this manner acts to address Research Objective 2 (with reference to Table 2-2). The modelling procedure and description of the cooling strategy is discussed in Section 4.2, while an additional validation study comparing the finite difference model to experimental data from other samples of 18650 cells is discussed in Section 4.4. A cooling study analysis that ranks the effectiveness of the internal cooling strategy against conventional tab cooling and outer surface cooling approaches, subject to the same aggressive electrical loading conditions, is conducted in Section 4.5. Further work and Conclusions are presented in Section 4.6 and Section 4.7 respectively.

4.2 INTERNAL COOLING APPROACH

The newly proposed internal cooling method involves placing a heat pipe (a core product of the sponsor company) inside the mandrel of the battery cell, whereby both the condenser and evaporator ends of the heat pipe are embedded within an aluminium heat spreader disc. This formed heat conduction network is termed the 'heat pipe system', where this method of core cooling seeks to improve upon the Shah et al. method via the inclusions of the heat spreader discs that utilise the more efficient axial heat conduction pathways present within the cell. The top spreader disc in contact with the heat pipe evaporator acts to conduct heat through the top of the cell spiral roll (i.e. all the layers of the cell) into the heat pipe. The spreader disc in contact with the condenser end of the heat pipe acts to dissipate heat from the heat pipe across the base of the bottom tab which is actively cooled. A schematic of the conceptual design is shown in Figure 4-1.

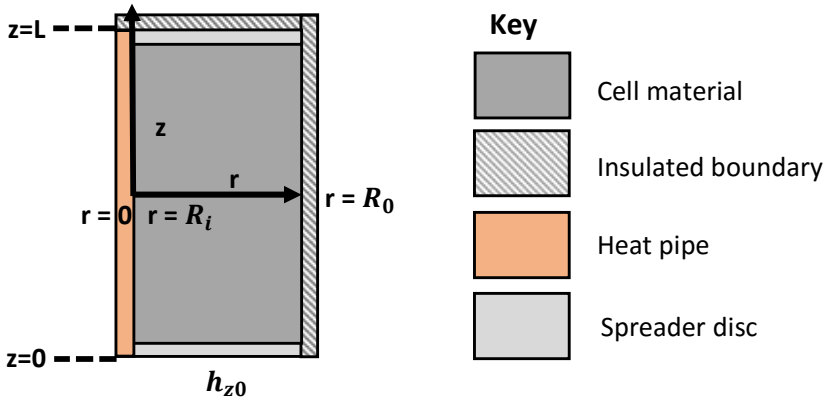

Figure 4-1: Schematic of the internal heat pipe system cooling design

4.3 HEAT PIPE THERMAL MODELLING

The baseline finite-difference model developed in Chapter Three is utilised again in this section of the thesis, where the following modifications are applied to incorporate the heat pipe system. Instead of specifying an insulation condition at r=R_i, a heat pipe is modelled in place of the mandrel. In addition, the capability of the model to incorporate spatial variations of the material properties is utilised to include the heat pipe system within the cell. This modelling approach assumes that the heat pipe behaves as a solid conductor which has an effective density, heat capacity and thermal conductivity [56], [160]. These modelling simplifications employed for the heat pipe model have been used previously in related research [107], [160].

The thermal properties of the heat pipe used in the model are estimated through considering the design strategy of the heat pipe as outlined in [56]. The operating range of the heat pipe is chosen to identify a suitable working fluid. Given that lithium-ion cells prefer an operating range between 20 –25℃, water is chosen as the working fluid.

For the wick structure, a sintered copper wick is chosen with a pore size and permeability of 9×10^{-6} m and 1.74×10^{-12} m^2 respectively [56]. The thickness of the copper outer heat pipe wall is determined to withstand a 200 ℃ bonding temperature to the spreader discs, whereby the thickness is calculated using the thin cylinder formula:

$$t_w = \frac{P_{v,w} r_{hp}}{\Omega} \tag{42}$$

Where t_w is the thickness of the copper shell, [m], r_{hp} the radius of the heat pipe [m], $P_{v,w}$ the vapour pressure of water at 200 ℃ [Pa] and Ω the permissible stress of annealed copper at 200 ℃ which is taken as 18.5 $MN.m^{-2}$ from [161]. For a 6 mm diameter heat pipe, t_w is calculated as 0.3 mm. For simplicity, this thickness is taken as constant and used for smaller heat pipe diameters used in the simulation study. The size of the vapour space is taken as a design variable which sets the remaining wick layer thickness, thus dictating the power capability of the heat pipe. For correct operation of the heat pipe, the capillary pumping pressure must be equal to or greater than the sum of the pressure drops present in the heat pipe and is given by [56]:

$$\Delta P_c = \Delta P_l + \Delta P_v + \Delta P_g \tag{43}$$

Where ΔP_c is the capillary pumping pressure [Pa], ΔP_l the pressure drop for liquid flow in the porous wick material from condenser to evaporator [Pa], ΔP_v the pressure drop of the

vapour flow from evaporator to condenser [Pa] and ΔP_g the gravitational head pressure drop [Pa].

The capillary pumping pressure is expressed as:

$$\Delta P_c = \frac{2\sigma_s cos\theta_w}{r_c} \tag{44}$$

Where r_c is the pore radius [m], σ_s the surface tension [N.m^{-1}] and θ_w the wetting angle [radian]. It is assumed that perfect wetting exists such that $\theta = 0$. The pressure drop for liquid flow through the porous wick is given by:

$$\Delta P_l = \frac{\mu_l l_{eff} Q}{L\rho_l K_p A} \tag{45}$$

Where μ_l is the dynamic liquid viscosity [kg.m^{-1}.s^{-1}], Q the heat pipe power [W], L the latent heat of the working fluid [J.kg^{-1}], ρ_l the density of the liquid [kg.m^{-3}], K_p the permeability of the wick [m^2], A the cross-sectional area of the wick [m^2] and l_{eff} the effective length for fluid flow [m]. Assuming that the mass change per unit length across the evaporator and condenser regions is linear, then l_{eff} can be expressed as:

$$l_{eff} = \frac{l_e + l_c}{2} + l_a \tag{46}$$

Where l_e, l_c and l_a are the lengths of the evaporator, condenser and adiabatic section respectively. Assuming laminar flow of vapour and complete pressure recovery in the condenser, then ΔP_v is given by [162]:

$$\Delta P_v = \frac{8\mu_v Q l_{eff}}{\rho_v L\pi r_v^4} \tag{47}$$

Where μ_v is the dynamic vapour viscosity [kg.m^{-1}.s^{-1}], ρ_v the density of the vapour [kg.m^{-3}] and r_v the radius of the vapour space [m]. The pressure drop associated with the gravitational head is given by:

$$\Delta P_g = \rho_l g l_{eff} sin\varphi \tag{48}$$

Where g is the gravitational acceleration [m.s^{-2}] and φ the angle between the horizontal plane and the heat pipe [radian].

The maximum power of the heat pipe is determined through substituting the above expressions into Equation (43) and solving for Q.

It is assumed that the thermal resistance for heat transfer through the vapour core is very small relative to other resistance terms, therefore, the overall heat pipe thermal resistance network [162] is simplified giving an expression for the total heat pipe thermal resistance (R_{hp}) as:

$$R_{hp} = 2(R_w + R_{wi}) \tag{49}$$

Where R_w is the thermal resistance through the copper wall and R_{wi} the thermal resistance through the wick layer [K.W^{-1}]. The contact resistance between the heat pipe and cell material interfaces is neglected.

With reference to Figure 4-1**,** the area of the condenser and evaporator sections are assumed to be those solely in contact with the spreader disc for determining l_{eff} and R_{hp}. The adiabatic section is taken as the remaining length of the heat pipe which passes through the cell mandrel. This relies on the assumption that the heat flux into the heat pipe from the cell material is very small relative to that from the heat flux at the aluminium spreader discs - heat pipe interface. The validity of this assumption is tested further, through an extensive simulation study, discussed within Section 4.5.1.

The copper wall and wick thermal resistances are expressed as [162] :

$$R_w = \frac{ln(r_{hp}/r_{wi})}{2\pi k_w l_s} \tag{50}$$

$$R_{wi} = \frac{ln(r_{wi}/r_v)}{2\pi k_{wi} l_s} \tag{51}$$

Where r_{wi} the radial location where the wick layer meets the copper wall [m], k_c the thermal conductivity of the wall material (copper) [W.m^{-1}.K^{-1}], k_{wi} the effective thermal conductivity of the wick [W.m^{-1}.K^{-1}] and l_s the height of the aluminium spreader discs which is set as 2 mm.

For heterogeneous copper sintered wicks, the Maxwell relation [163] is used to determine k_{wi} which is given by:

$$k_{wi} = k_c \left[\frac{2 + k_l/k_s - 2\varepsilon(1 - k_l/k_s)}{2 + k_l/k_s + \varepsilon(1 - k_l/k_s)}\right] \tag{52}$$

Where k_l and k_s are the thermal conductivity of the liquid water and solid particles (copper) respectively [W.m^{-1}.K^{-1}], and ε the porosity of the wick which is given as 0.52 based on the reported permeability and pore radius results of the sintered wick sample from [56].

The overall heat pipe thermal conductivity is calculated from the expression for R_{hp}, assuming that it acts as a solid conductor given by:

$$R_{hp} = \frac{l_{hp}}{k_{hp}\pi r_{hp}^2} \tag{53}$$

Where l_{hp} is the length of the heat pipe [m] and k_{hp} the overall effective heat pipe thermal conductivity [W.m^{-1}.K^{-1}].

4.4 FURTHER VALIDATION OF THE BATTERY THERMAL MODEL

The accuracy of the baseline thermal model has been tested against experimental data previously in Section 3.5.2 of Chapter Three. However, given that the experimental test conditions are not ideal for cell-level validation as neighbouring effects between cells in the test model may be present, a further validation comparison is conducted. In this validation study (where through collaboration the experimental data and testing has been provided and performed by another researcher within WMG) 4 new unaged 18650 type cells with a graphite anode NCA cathode are used. The nominal capacity of the test cells is 2.9 Ah. The 4 cells are placed horizontally on the top tray within a climate chamber that circulates air to maintain its set point ambient temperature. A thermocouple is placed at the outer surface of each cell at its mid height. Figure 4-2 displays the test setup adopted prior to attachment of the thermocouples. Each of the 4 cells are subject to two separate electrical loading profiles, each performed at a different ambient temperature to further test the model accuracy under different scenarios. The electrical loading profiles for both tests are shown in Figure 4-3 (b), where a negative current denotes discharge and a positive current charging in this instance.

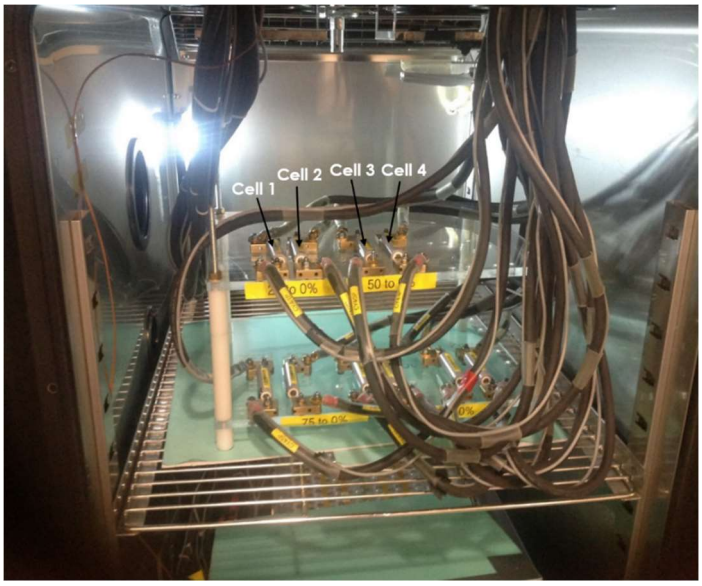

Figure 4-2: Experimental test setup for validation of baseline thermal model

The physical properties for the 18650 cell used in this analysis are displayed in *Table 4-1*. Given that a moderate degree of air circulation is present within the climate chamber and that the cells are fully exposed to its circulatory effect, an h value of 25 $W.m^{-2}.K^{-1}$ [164] is assumed at both the tabs and exterior surface of the cell in the thermal model. The properties of the mandrel in the thermal model are set with a thermal conductivity of 2e-10 $W.m^{-1}.K^{-1}$ to provide the desired insulating condition. The spreader disc thickness is set as 0 mm.

The current pulse method [138] with a pulse length of 10 s has been applied at 4 SOC locations for the cell (20%, 50%, 80% and 95%) at both 25 ℃ and 10 ℃ to determine the overpotential resistance at these SOC levels. The average results over the 4 cells are shown in Figure 4-3 (a), whereby Equation (33) is used to estimate the SOC profile for each current input. Given that the cell resistance data points for <20% and >95% SOC were unavailable, the fitted polynomial is used to extrapolate the resistance values within these SOC regions for calculating the cell heat generation in the thermal model [109]. This is highlighted by the presence of vertical dashed lines in the simulation/experimental results comparison curves in Figure 4-3 (e) & (f), where between the lines the polynomial is interpolated between the data points.

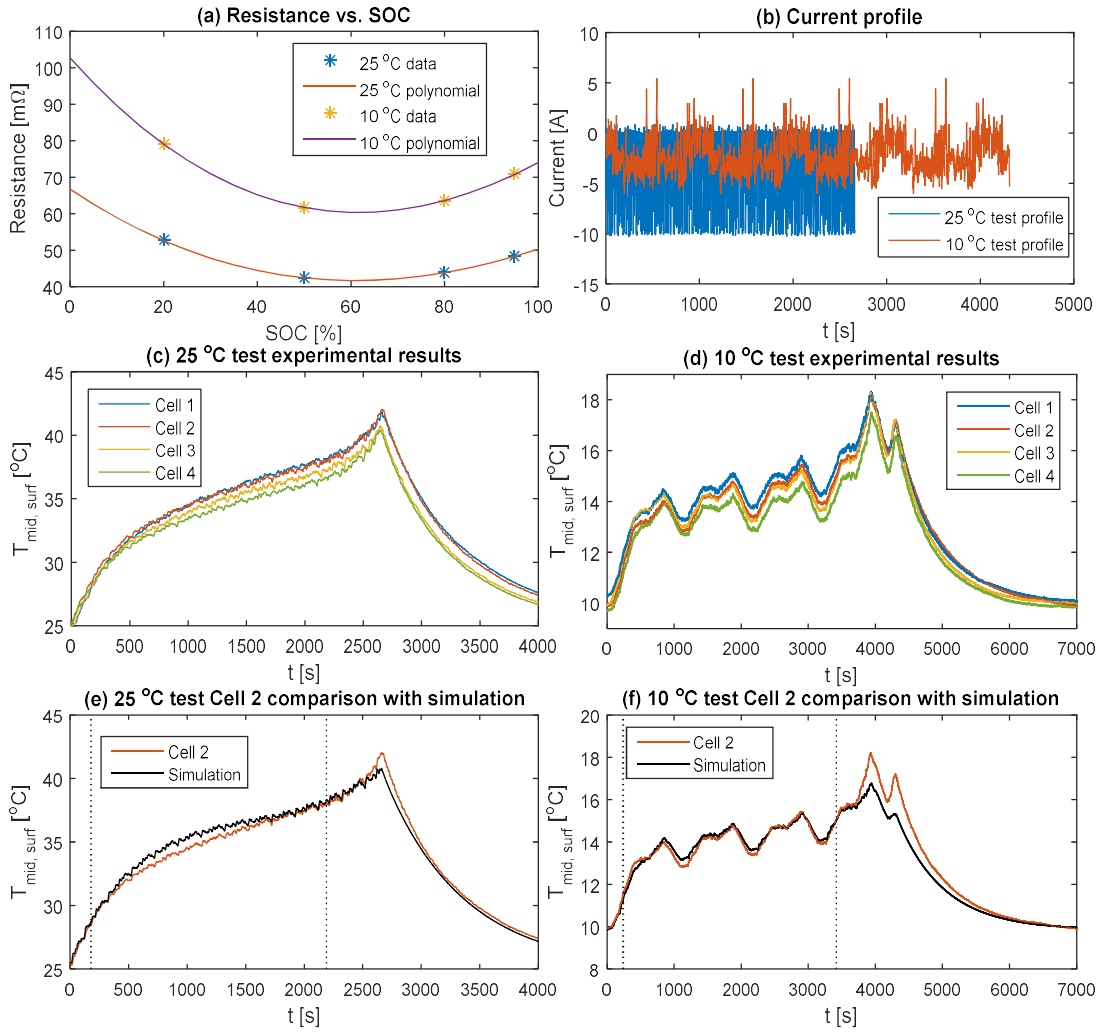

Figure 4-3: (a) overpotential resistance from current pulse method (b) cell current profiles for 25 °C and 10 °C test (c) 25 °C test experimental results (d) 10 °C test experimental results (e) comparison between test Cell 2 and simulation for the 25 °C test (f) comparison between test Cell 2 and simulation for the 10 °C test

The mid-height surface temperature ($T_{mid,surf}$) results for the test cells are viewable in Figure 4-3 (c) -(d). The slight discrepancy in temperature between the cells are believed to be due to the increasing air convection occurring on the cells nearer the right of the chamber (in closer proximity to the air circulation inlet) leading to additional cooling. As a result of the variable heat transfer conditions experienced by the cells, validation of the thermal model is compared to the readings of Cell 2, which appears to be more representative of the static h value of 25 $W.m^{-2}.K^{-1}$ used in the thermal model. Figure 4-3 (e) -(f) highlight that there is good agreement between the baseline thermal model and $T_{mid,surf}$ data from Cell 2 for both test cases. The highest discrepancy occurs for the lower temperature test and corresponding drive cycle in the deep discharge region (20% <SOC), as seen to the right of the dashed vertical line in Figure 4-3 (f). This is assumed to be due to the heightened error associated with the polynomial extrapolation. The model gives a peak error of 11.3% which occurs for the 10 °C test, with a mean absolute error of 1.94% across the whole 10 °C test. Between the

vertical lines bounded by resistance data points, the peak error and mean absolute error reduces to 3.15% and 1.11 % respectively for the 10 ℃ test.

4.5 COOLING STUDY ANALYSIS

In this section, the thermal performance of the 18650 and 32113 cell formats with the internal heat-pipe system are investigated using the thermal model when subject to two aggressive duty cycles. Thermal performance is compared against the conventional exterior cooling strategies discussed previously in Chapter Three. For the heat pipe cooled method, the calculated heat pipe physical properties and properties of the aluminium spreader disc material are input at the grid locations where these objects exist.

First, a steady-state analysis is conducted to investigate the cell material and overall thermal resistance for the cell with the heat pipe system. An analysis into the effect of thermal conductivity of the heat pipe/solid conductor material on the cell thermal performance is also investigated. A full transient analysis using the full duty cycle profiles is undertaken to quantify the effect of the cooling strategy choice on the magnitude of the temperature profiles. The thermal properties used for the cells considered in the simulation study are viewable in Table 4-1. In all instances, the initial cell temperature and temperature of the bulk heat transfer medium (T_∞) are set at 25 ℃.

Table 4-1: Physical properties of battery cells used in this study

Cell format	k_z [W.m^{-1}.K^{-1}]	k_r [W.m^{-1}.K^{-1}]	C_p [J.kg^{-1}.K^{-1}]	Cell mass [g]	ρ [kg.m^{-3}]	Reference mandrel size [mm]	Nominal cell capacity [Ah]
18650	30 [88]	0.25 [107]	1280 [116]	47	2923	3 [140]	2.9
32113	30	0.25	1020 [155]	205 [153]	2276	3	4.5

For the 32113 cell analysis, the HEV US06 (4 loop) profile as described in Chapter Three is employed as the electrical loading condition. For the 18650 cell, an aggressive performance EV cycle is used that is representative of track racing conditions. The cycle has been provided by another researcher within WMG, whereby the methodology behind the construction of the cycle is viewable in [165]. In short, the race cycle is derived from a database of battery power demand duty cycles that are generated again using the IPG CarMaker software. The software simulates the race circuits, electric vehicle and the driver. The track models of 11 recognised race circuits are created using the process described in [166]. The vehicle

parameters used in the IPG CarMaker simulation for the performance EV are viewable in Table 4-2.

The C-rate and calculated heat generation profiles for the performance EV cycle are shown in Figure 4-4, together with the estimated SOC profile calculated from Equation (33) with the cell nominal capacity of 2.9 Ah . The polynomial resistance profile at 25 ℃ is used to estimate the heat generation rate as a function of cell SOC given that the SOC enters the deep discharge region where large increases in R_η are observed.

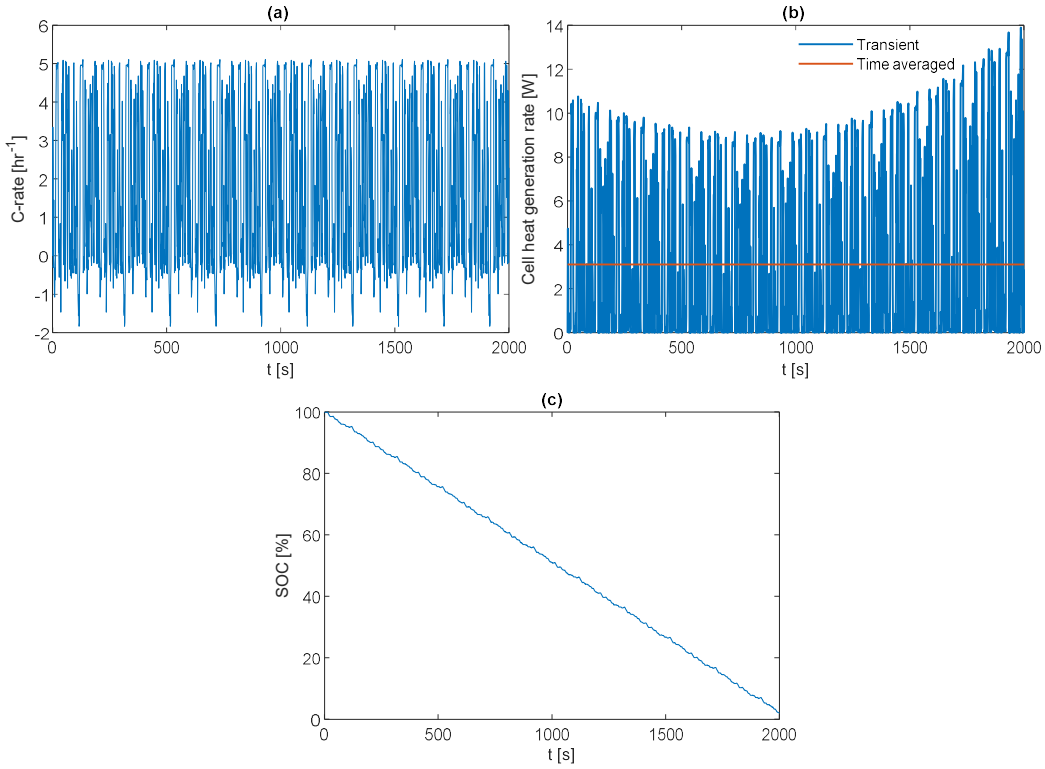

Figure 4-4: (a) EV performance cycle C-rate profile (b) Calculated EV performance cycle heat generation profile (c) Estimated EV performance cycle SOC profile

Table 4-2: Vehicle parameters used in IPG CarMaker simulation

Parameter	Performance EV
Powertrain	Electric
Vehicle Body	Rigid body
Vehicle mass [kg]	1564
Height of centre of gravity [m]	0.5
Wheelbase [m]	2.67
Frontal Area [m2]	2.0
Drag coefficient	0.3
Electric machine peak power [kW]	300
Electric machine peak torque [Nm]	850
0 - 200 km/h [s]	12.4
Top Speed [km/h]	300

4.5.1 STEADY-STATE THERMAL ANALYSIS

The layer dimensions of the heat pipe which dictate the value for k_{hp} are specified to meet the requirement for the heat pipe power Q. This requirement is set based on the time averaged heat generation values for both cell types. From Figure 4-4 (b) and Figure 3-19 (b), this is 3.11 W for the EV cycle and 5.83 W for the HEV cycle respectively. Given that all the heat generated by the cell will not transmit into the heat pipe, the Q value for the 32113 cell is set as the maximum value obtainable with a 4 mm heat pipe (given the chosen wick material) which is 4.32 W. For the 18650 cell, the maximum Q value is set using a 3 mm heat pipe which is 3.60 W. Values are determined using water fluid properties from [56] at the lowest heat pipe operating temperature of 25 ℃ to give the worst case. The 3 mm heat pipe is not deemed suitable for the 32113 cell given that the maximum obtainable Q is only 2.03 W (due to the longer length of the heat pipe).

The determined values for R_{hp}, k_{hp} and the occupied volume fractions of each heat pipe layer relative to the overall heat pipe volume are shown in Table 4-3. Here, f_w ,$f_{wi}$and f_v are the volume fractions of the copper wall, wick layer and vapour core layer respectively. The calculated values for k_{hp} range from circa 8000 – 19,000 W.m^{-1}.K^{-1} and are comparable to similar analytical computed results reported in [162].

Table 4-3: Heat pipe design properties for set Q of 3.60 W for 18650 cell and 4.32 W for 32113 cell

Cell type	Heat pipe size [mm]	R_{hp} [K.W^{-1}]	k_{hp} [W.m^{-1}.K^{-1}]	f_w [-]	f_{wi} [-]	f_v [-]
18650 cell	3 mm heat pipe	1.016	9.611×10^3	0.360	0.529	0.111
	4 mm heat pipe	0.313	17.527×10^3	0.278	0.270	0.452
	6 mm heat pipe	0.127	19.169×10^3	0.190	0.120	0.690
	8 mm heat pipe	0.075	18.316×10^3	0.144	0.068	0.788
32113 Cell	3 mm heat pipe	-	-	-	-	-
	4 mm heat pipe	1.132	8.225×10^3	0.278	0.626	0.096
	6 mm heat pipe	0.242	17.072×10^3	0.190	0.255	0.555
	8 mm heat pipe	0.128	18.176×10^3	0.144	0.143	0.713

The results of the steady-state overall thermal resistance values as a function of h and cooling strategy are displayed in Figure 4-5 (a) and Figure 4-5 (b) for the 18650 and 32113 cell respectively, whereby conventional exterior cooling strategies are included for reference. All cooling options involving a heat pipe or solid conductor include both the top and bottom 2 mm aluminium heat spreader disc, where the thickness of the heat spreader disc kept as a constant.

For the 18650 cell, the introduction of the 3 mm heat pipe system effectively lowers R_{cell}, prolonging the region in which R is dominated by convective components of the resistance relative to single tab cooling without the heat pipe system. This is observed by the delayed levelling of the resistance curves with the heat pipe system additions. Past h values of circa 1300 W.m^{-2}.K^{-1}, the 3 mm heat pipe system offers lower R values than radial cooling, whereas without the heat pipe system, singular tab cooling results in larger R values than radial cooling even when the h value is 10,000 W.m^{-2}.K^{-1}.

Upon transition towards the larger 32113 cell, the R values for the 4 mm heat pipe system are lower than radial cooling for h values in excess of 670 W.m^{-1}.K^{-1}, which again highlights the increase in thermal performance when adopting a tab cooling approach for a cell of this aspect ratio over radial cooling relative to the 18650 cell.

Figure 4-5 (c)- (d) outline the impact of the effective thermal conductivity of the solid conductor on the R value. Increasing the thermal conductivity value prolongs the region in which R has a linear dependence with h on the log-log scale, signifying a lower R_{cell} value. For a convective coefficient value of 3000 W.m^{-2}.K^{-1} (representing moderate liquid cooling with water [157], [158]) for the 32113 cell, the overall thermal resistance decreases by 14.0% upon addition of a solid copper bar (k=398 W.m^{-1}.K^{-1}) connected to the discs relative to single tab cooling without these additions. With a k_{hp}value of 8225 W.m^{-1}.K^{-1} to simulate the heat pipe, R decreases by 49.1 %. The much greater reduction in R clearly highlights the benefit of utilising a heat pipe over a simpler copper rod solution. For the 18650 cell at h = 3000 W.m^{-1}.K^{-1}, the R value decreases by 20.3 % with the copper rod and 51.5 % with the 3 mm heat pipe with k_{hp} of 9611 W.m^{-1}.K^{-1}.

The calculated values of R_{cell} for the heat pipe cases are show in Table 4-4. With the heat pipe system, the heat transfer is multidimensional, therefore, T_s (which is the temperature at the interface between the bottom spreader disc and bulk cell material) is not uniform. In this instance, the average temperature for T_s across the interface is taken from the thermal model and using Equation (41) used to calculate R_{cell} at logarithmic h value increments between 500 – 100,000 W.m^{-2}.K^{-1}. The average value of R_{cell} over this range is taken and given to represent the constant value of R_{cell}.

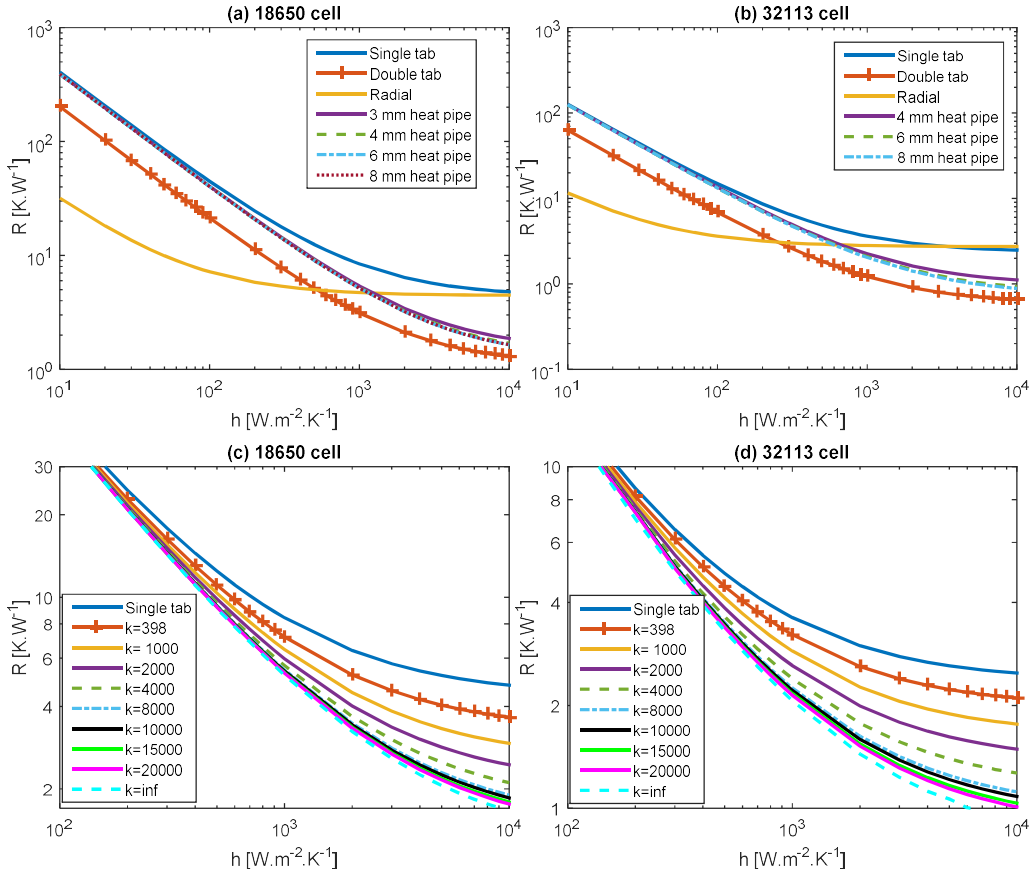

Figure 4-5: Overall thermal resistance as a function of convective heat transfer coefficient and cell-level thermal management strategy for (a) 18650 cell (b) 32113 cell, and effect of thermal conductivity on the mandrel material connected to 2 mm spreader discs for (c) 18650 cell 3 mm mandrel (d) 32113 cell 4 mm mandrel

Table 4-4: Steady-state cell material thermal resistance as a function of cooling strategy and cell type

Cooling strategy	Cell material thermal resistance (R_{cell}) [K.W-1]	
	18650 cell	32113 cell
Radial	4.44	2.71
Single tab	4.38	2.36
Double tab	1.09	0.59
3 mm heat pipe	1.41±0.06	-
4 mm heat pipe	1.25±0.05	0.95±0.06
6 mm heat pipe	1.21±0.04	0.77±0.06
8 mm heat pipe	-	0.73±0.06
Cooling strategy	Cell material thermal resistance percentage decrease relative to single tab cooling [%]	
	18650 cell	32113 cell
3 mm heat pipe	67.8±1.4	-
4 mm heat pipe	71.5±1.1	59.7±2.5
6 mm heat pipe	72.4±0.9	67.4±2.5
8 mm heat pipe	-	69.1±2.5

Table 4-4 highlights the degree of reduction in R_{cell} from the introduction of the heat pipe and spreader discs relative to single tab cooling without these additions. The error associated with R_{cell} values used to estimate ΔT_{max} for the heat pipe cases when compared to the

direct ΔT_{max} calculation from the thermal model is included. For the 18650 cell, a 3 mm heat pipe offers a 67.8±1.4% reduction in R_{cell} approaching the lower resistance offered by double tab cooling. Increasing the diameter of the heat pipe in the heat pipe system further past 3 mm offers only a small reduction in R_{cell} by circa 5%. For the 32113 cell, increasing the heat pipe diameter from 6 mm to 8 mm results in a diminishing reduction in R_{cell} relative to the reduction achieved from 4 mm to 6 mm.

The relationship between the reduction in cell energy density and increase in cell mass (relative to the reference cells without the heat pipe and spreader disc additions) as a function of heat pipe diameter are shown in Figure 4-6. The effective density of the heat pipe used to determine the effective heat pipe weight is calculated from the sum of the density properties of each material layer, given its fraction of occupation within the heat pipe [160]. This is expressed by:

$$\rho_{hp} = f_w\rho_{wall} + f_{wi}(1-\varepsilon)\rho_s + f_{wi}\varepsilon\rho_l + f_v\rho_v \quad (54)$$

Where ρ_{hp}, ρ_{wall}, ρ_s, ρ_l and ρ_v are the density of the heat pipe, wall (copper), solid wick particles (copper), liquid water and saturated steam respectively [kg.m^{-3}].

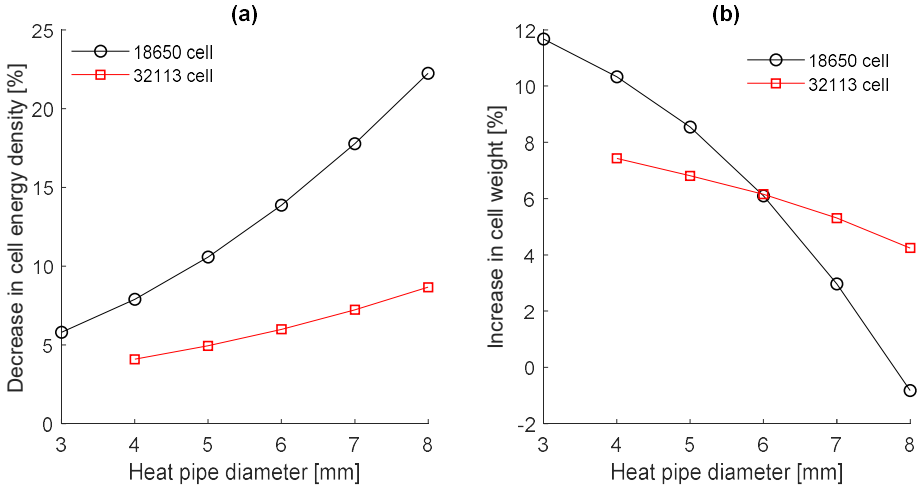

Figure 4-6: Effect of the heat pipe diameter (designed to achieve a power capability if 3.60 W for the 18650 cell and 4.32 for the 32113 cell) on (a) cell energy density (b) cell weight

From Figure 4-6 (a), for the 18650 cell with the referenced sized mandrel, the addition of the heat pipe system decreases the cell energy density by 5.8%. Increasing the diameter further to 4 mm decrease the energy density by 7.9%. However, as seen in Figure 4-6 (b), larger heat pipe diameters result in a decreasing mas increase for the cell. For the 3 mm heat pipe, the mass increase is 11.7%, however, this penalty is reduced to 10.3% for the 4 mm heat pipe. This is a result of the declining effective density of the heat pipe as the vapour core fraction

increases with larger heat pipes, where the heavier wick layer thickness is reduced to match the same heat pipe power requirement (the calculated values for the heat pipe density as a function of heat pipe diameter are shown in Table A 5 of Appendix A.6). For very large heat pipe diameters of 8 mm, the effective heat pipe density reaches a stage where it is lower than the cell material effective density, which results in a slight decrease in overall cell weight. Similar observations are seen for the 32113 cell, where there is a trade-off between a less energy dense design and a lighter weight cell design with increasing the heat pipe diameter. Ultimately, the exact choice of heat pipe diameter may depend on the mass and volume constraints imposed on the BTMS design. For the remainder of this study, the 3 mm heat pipe and 6 mm heat pipe are considered for the 18650 and 32113 cell respectively.

Steady state temperature contours throughout the 18650 cell subject to the time averaged heat generation rate of 3.11 W for the performance EV cycle are shown in Figure 4-7. An h value of 60 $W.m^{-2}.K^{-1}$ is chosen for the radial cooled case to reflect an air cooled parallel design, and 875 $W.m^{-2}.K^{-1}$ for the tab cooled cases (with and without the heat pipe system) to reflect water-glycol cooling as discussed in Section 3.8.1 of Chapter Three.

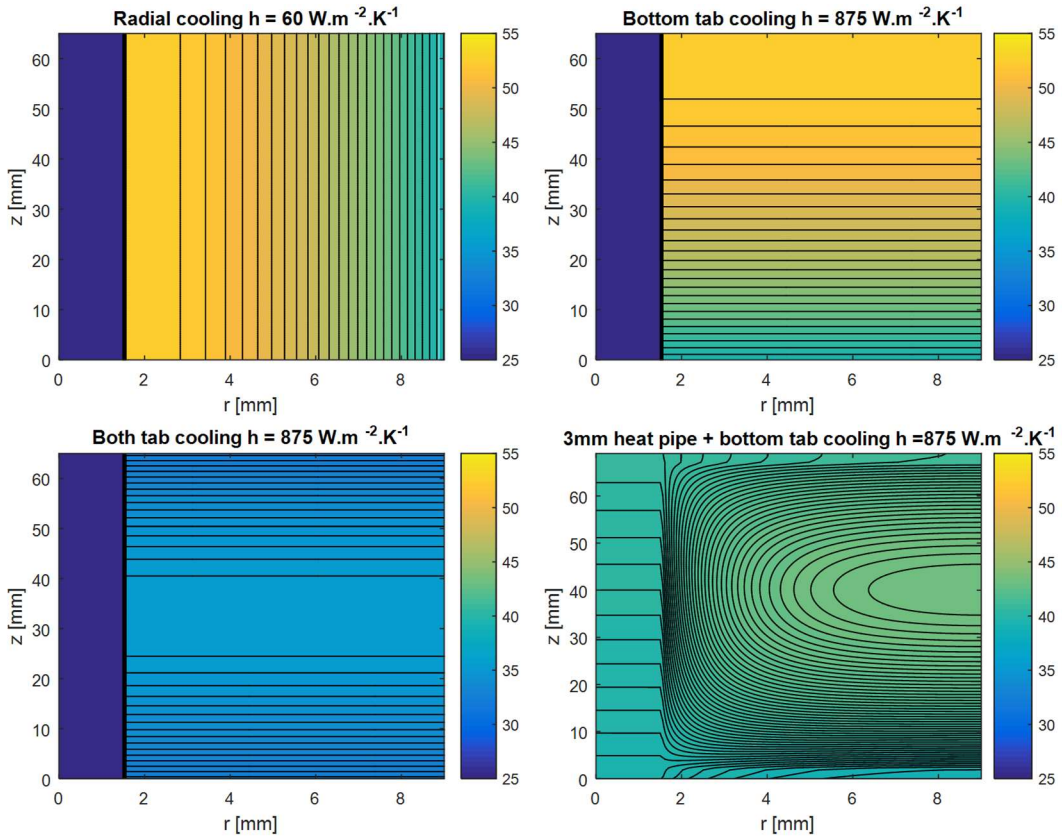

Figure 4-7: Steady state temperature contours through the 18650 EV cell as a function of thermal management strategy with a time averaged cell heat generation rate of 3.11 W (colorbar scale in °C)

Figure 4-7 visualises the effectiveness of the spreader discs and heat pipe in isothermalising the internal temperature gradients within the cell. Relative to radial cooling, the cell hot spot is shifted towards the outer surface slightly above the cell mid height. As with conventional tab cooling, this enables the hot spot of the cell to be monitored at an accessible outer surface and is desirable from a control standpoint as estimations of the core temperature are not necessary. The total amount of heat entering the heat pipe, given the negative heat flux along its axial length at the heat pipe cell interface and heat pipe spreader disc interface is 1.52 W. Of this, the majority of the total heat (1.24 W) enters the heat pipe across the top spreader disc interface with the remaining 0.28 W entering across the heat pipe-cell material interface. This highlights the importance of the top spreader disc, as it acts as the dominant mechanism in transporting heat from the cell into the heat pipe. This may explain why the results in [107] did not show much benefit from transitioning from a solid copper rod to a heat pipe in cooling the core of the cell, as the poor perpendicular heat transfer pathway effectively hinders the supply of heat into the rod/heat pipe relative to its axial conduction. The much smaller heat of 0.28 W also supports the assumption used in the heat pipe effective length calculation (Equation (46)) that the heat pipe evaporator section lies at the heat pipe-spreader disc interface, with the remaining contact area between the cell and heat pipe being relatively adiabatic.

There still exists a more unfavourable perpendicular gradient between the layers of the cell with the heat pipe system. The effects of such a complex gradient on the overall cell degradation are not fully understood and would require further investigation (see Section 4.6). Nevertheless, the magnitude of ΔT_{max} with the heat pipe is reduced by a factor of approximately 3 relative to both single tab and radial cooling. A summary of ΔT_{max}, T_{max} and T_{avg} values for each cooling strategy is shown in Table 4-5.

Table 4-5: Summary of cell thermal performance results from the steady state analysis using time averaged drive cycle heat generation

Cell type	Strategy	T_{max} [°C]	ΔT_{max} [°C]	T_{vol} [°C]	h [W.m^{-2}.K^{-1}]
18650 cell	Radial	52.83	13.68	47.99	60
	Bottom tab	52.98	13.62	48.40	875
	Double tab	35.59	3.41	34.45	875
	3 mm heat pipe	43.46	4.52	41.87	875
32113 cell	Radial	49.39	15.81	43.82	60
	Bottom tab	49.40	13.70	44.79	680
	Double tab	33.78	3.43	32.63	680
	6 mm heat pipe	40.35	4.86	38.68	680

The results for the 32113 cell are also presented when subject to the time averaged heat generation rate of 5.83 W, where a value of 680 W.m^{-2}.K^{-1} is chosen to reflect liquid cooling in this instance. The total heat input into the 6 mm heat pipe is 2.99 W. All heat pipe properties used are those displayed in Table 4-3.

4.5.2 TRANSIENT THERMAL ANALYSIS

A transient thermal analysis of the thermal performance of the cells for each corresponding aggressive duty cycle case is shown in Figure 4-8 for the 32113 cell and Figure 4-9 for the 18650 cell. The effective heat capacity is calculated following the same procedure used to calculate the effective density, and is given by [160]:

$$Cp_{hp} = f_w Cp_w + f_{wi}(1-\varepsilon)Cp_s + f_{wi}\varepsilon Cp_l + f_v Cp_v \quad (55)$$

Where Cp_{hp}, Cp_w, Cp_s, Cp_l and Cp_v are the heat capacity of the heat pipe, wall (copper), solid wick particles (copper), liquid water and saturated steam respectively [J.kg^{-1}.K^{-1}]. Given that the fluid properties used to calculate Cp_{hp} and ρ_{hp} are a function of temperature and change as the heat pipe warms/cools, the average of the 3 calculated values at 25 ℃, 40 ℃ and 60 ℃ is taken. This is a justifiable simplification given that the deviation in the values calculated for Cp_{hp} and ρ_{hp} at 25 ℃ and 60 ℃ is 0.6% for the 3 mm heat pipe. The calculated values for the heat pipe density and heat capacity used in the transient thermal analysis are shown in Table 4-6.

Table 4-6: Calculated values for the effective heat capacity and density of the heat pipe modelled in the transient thermal analysis

Heat pipe type	Cp_{hp} [J.kg^{-1}.K^{-1}]	ρ_{hp} [kg.m^{-3}]
18650 cell, 3 mm heat pipe	1595	5773
32113 cell, 6 mm heat pipe	1793	3692

More aggressive values for h are chosen in this analysis, which for air cooling is 100 W.m^{-2}.K^{-1} e.g. to reflect a narrower channel hydraulic diameter for parallel cooling (at the cost of greater pressure drop and parasitic fan power requirement) and 3000 W.m^{-2}.K^{-1} for more aggressive liquid cooling. These values are comparable to those employed in [157]. For double tab cooling, the h value is halved at the tabs. This is used to demonstrate that the heat pipe design has the potential to reach that of double tab cooling provided that the higher heat flux at the bottom tab can be addressed.

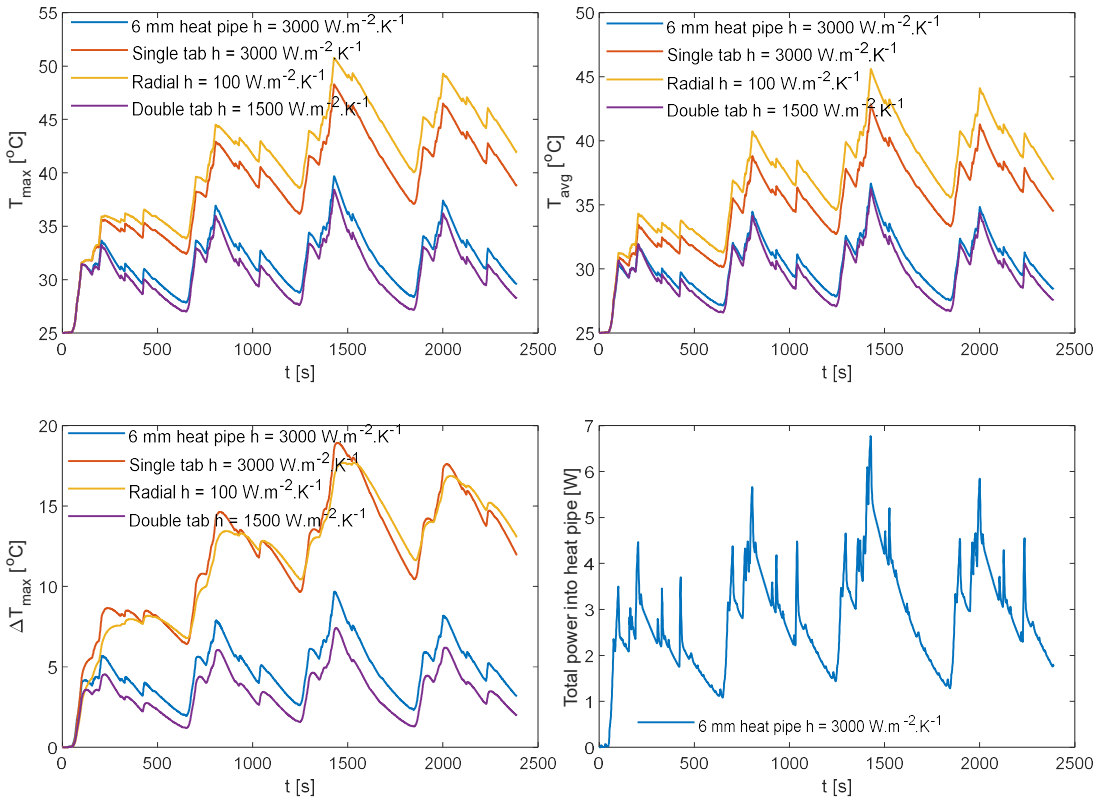

Figure 4-8: Transient thermal performance of the 32113 HEV cell as a function of cooling strategy with (a) T_{max} evolution (b) ΔT_{max} evolution (c) T_{avg} evolution

From Figure 4-8, it is observed that with the 6 mm heat pipe and 2 mm thick spreader discs, the heat pipe system offers comparable thermal performance to that of double tab cooling. For the double tab cooled case, T_{max} peaks at 38.4 ℃ with a ΔT_{max} value of 7.4 ℃, where with the heat pipe system in place the corresponding values for T_{max} and ΔT_{max} are 39.7℃ and 9.7 ℃ respectively. The transient total power load on the heat pipe is also shown. As the peak power load reaches 6.8 W, the 6 mm heat pipe properties from Table 4-3 are not acceptable given that Q exceeds 4.3 W. Therefore, a thicker wick layer has been chosen to achieve a higher design Q value of 7.0 W at 25 ℃ with a corresponding k_{hp} value of 9861 W.m^{-1}.K^{-1}. This the values for Cp_{hp} and ρ_{hp} in Table 4-6 are also reflective of this thicker wick layer. The heat pipe system with this increased wick layer fraction result in an increase in cell mass of 7.4%.

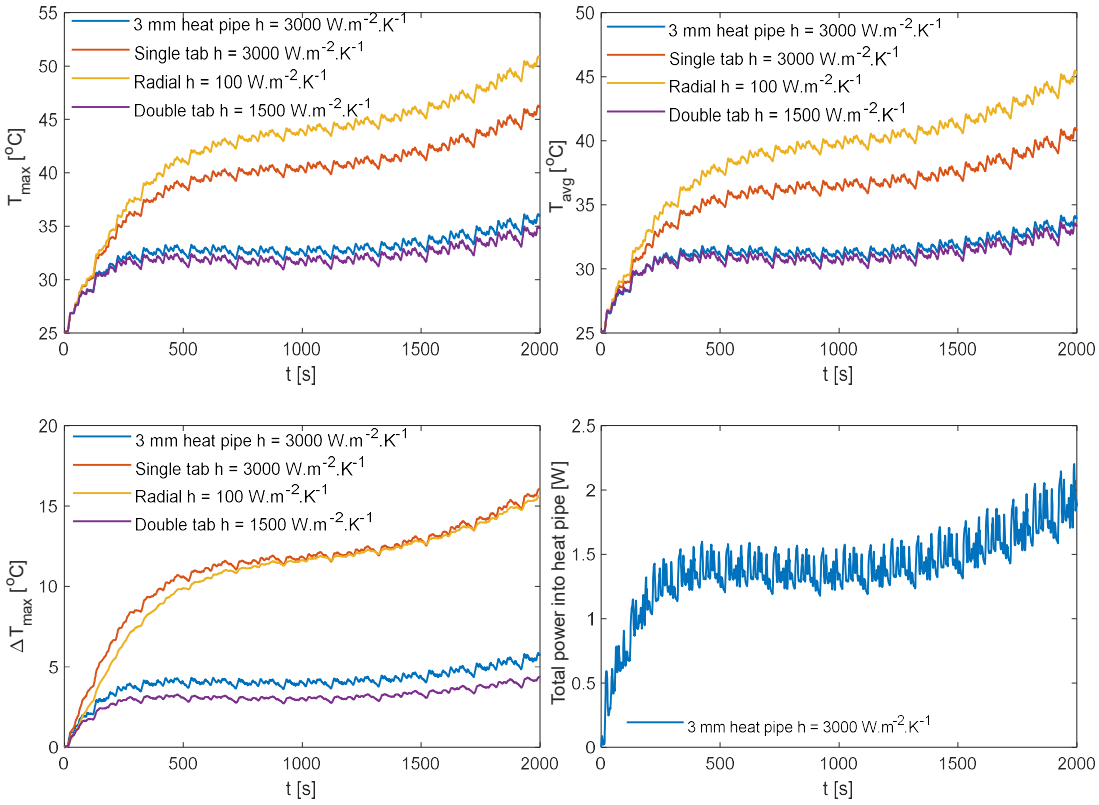

Figure 4-9: Transient thermal performance of the 18650 EV cell as a function of cooling strategy with (a) T_{max} evolution (b) ΔT_{max} evolution (c) T_{avg} evolution

For the EV performance cycle, similar observations are made. The lower thermal resistance values for double tab and heat pipe cooling dampen out the thermal oscillations relative to radial and single tab cooling, particularly during the deep discharge range where the heat generation rate spikes. Here, the transient heat pipe power load remains within the design limit of 3.6 W for the 3 mm heat pipe, and therefore does not require modification of the wick structure.

4.6 FURTHER WORK

Given the significant theoretical improvements in the thermal performance of the heat pipe system over singular tab cooling, further investigation should target the practical issues associated with incorporating the heat pipe and spreader discs into the cell internals. This should focus on identifying methods to avoid a potential short circuit given the electrical pathway created from the heat pipe and spreader discs, whilst avoiding additional resistances that can compromise the added benefit of utilising the axial conduction pathways within the cell. To further understand the effect of the complex internal cell gradients on cell ageing, manufacture of a test cell specimen should be carried out together with an

experimental analysis to quantify and compare the ageing rates of the heat pipe cooled method relative to that of conventional bottom tab cooling under identical cell electrical loading and external cooling conditions.

4.7 CONCLUSION

Relative to past applications of heat pipes for cooling cylindrical battery cells, the proposed heat pipe system discussed in this Chapter utilises the more efficient axial heat conduction pathways present within the cell to further increase the rate of heat transfer from the cell into the heat pipe, thus addressing Research Objective 2 of this thesis. This is achieved through connecting a 2 mm thick metallic (aluminium) heat spreader disc to both ends of the heat pipe (acting as the cell mandrel material) which directly contacts the top and bottom portions of the cell material. The thermal modelling study highlights that the formed heat-conduction network enables a dramatic reduction in internal cell temperature gradient, owing to the reduced thermal resistance for heat transfer through the inside of the cell. This internal thermal management approach requires an external heat transfer mechanism to exist at only the base of the cell, which can simplify the pack-level thermal management design strategy. The heat pipe system also has the potential to be incorporated directly within the internals of individual battery cells for simpler integration within existing battery pack designs employing single tab cooling.

The immediate penalty of incorporating the heat pipe and spreader discs into the cell is a decrease in energy density and an increase in cell mass. Relative to the reference 18650 cell, the addition of the 3 mm heat pipe and 2 mm spreader discs reduces the cell volumetric energy density by 5.8 % and increases the cell mass by 11.7 %. For the 32113 cell, the cell volumetric energy density is reduced by 6.0 % and the mass increased by 7.4% with the 6 mm heat pipe and 2 mm spreader discs.

As the heat pipe system increases the rate of heat transfer to the base of the cell, the degree of cooling applied at the base should be maximised to fully utilise the potential offered by the heat pipe system in minimising the cell temperature rise. This necessitates the use of either forced convection with a liquid heat transfer medium or evaporative heat transfer.

5 CHAPTER FIVE - A STUDY INTO DIFFERENT CELL-LEVEL COOLING STRATEGIES FOR POUCH TYPE LITHIUM-ION CELLS IN AUTOMOTIVE APPLICATIONS

5.1 INTRODUCTION

This Chapter seeks to address Research Objective 3 by analysing the cooling performance of both surface and tab cooling methods for pouch cells when subject to a wide range of electrical loading conditions representative of xEV usage.

To quantify the thermal performance of surface and tab cooling, whilst identifying heat generation limits within the cell to which a particular cooling approach may be acceptable, a thermal modelling investigation is conducted.

This Chapter is structured as follows. Section 5.2 describes the modelling approach adopted to conduct the pouch cell-level cooling analysis, where Section 5.3 outlines the duty cycles used as input into the thermal model that are reflective of PHEVs and performance EVs. In Section 5.4, the cooling study is contained which compares the thermal performance of surface and tab cooling for cell designs with opposite and same ended tab configurations. Recommendations for Further Work and Conclusions from this study are contained in Section 5.5 and Section 5.6 respectively.

5.2 POUCH CELL THERMAL MODELLING

Different to cylindrical cells, the tabs of pouch cells protrude from the cell body as two distinct fin like structures. Given that Joule heating is known to occur within the tab bodies as the cells are cycled [167], it is necessary to consider the effect of tab heat transfer as the heat rejection from the tabs into the cell body can affect the thermal condition of the cell . Specifically, the effect of tab heat rejection on the temperature gradient of a 14.6 Ah pouch cell has been reported by Kim et al. [168], where they observed that as a result of the tab heat rejection, a hot spot was created under the positive tab leading to a peak temperature gradient of circa 5 ℃ across the cell surface. A subset of their results is displayed visually in Figure 5-1.

Kim et al. concluded that the formation of the hot spot under the positive tab (made from aluminium current collectors) was attributed to the greater electrical resistivity of aluminium relative to the negative tab comprised of the copper current collectors. Their observations

are consistent with that of Bazinski et al. who report that due to the greater resistivity of aluminium (circa 37% higher for aluminium than copper) [169], greater Joule heating is observed for the positive tab when the tabs are of the same thickness. Typical values for the resistivity of aluminium and copper at 25℃ are reported as $2.65 \times 10^{-8}\ \Omega.m$ and $1.68 \times 10^{-8}\ \Omega.m$ respectively [170].

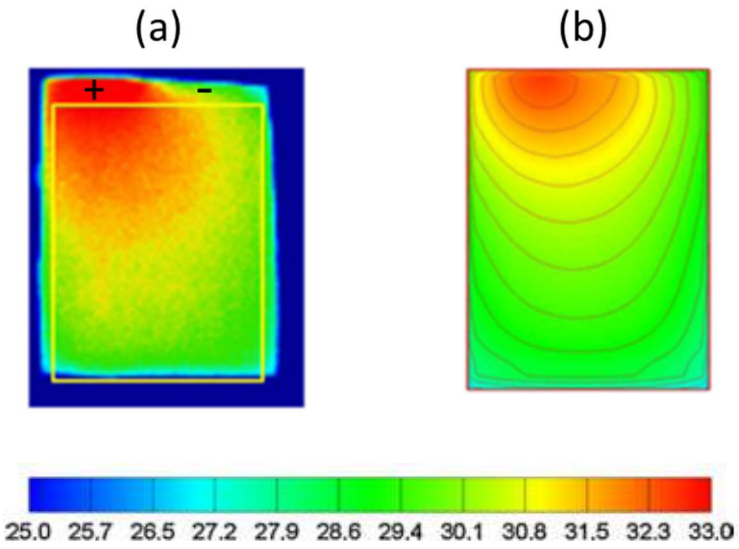

Figure 5-1: Kim et al. results (position of +ive and –ive tabs is added for clarity) for the cell surface temperature after 16 minutes during a 3C CC-CV charge with (a) experimental thermal imaging camera results of cell surface (b) simulated cell surface temperature [168]

To include the presence of the external cell tabs which is necessary to correctly capture the thermal gradient formation within pouch cells, it is no longer possible to use the previous 2-D model as implemented for the cylindrical cell study. This is since heat transfer between the tabs and cell cannot be captured alongside the perpendicular heat transfer occurring through the thickness of the cell without extension towards a 3-D thermal model. To develop a 3-D thermal model capable of satisfying these requirements to fulfil Research Objective 3, the use of the commercially available heat transfer modelling package COMSOL Multiphysics® 5.2a is employed for the cell-level modelling analysis.

The dimensions of a commercially available 53 Ah pouch cell with a graphite anode and nickel manganese cobalt oxide (NMC) cathode chemistry manufactured by XALT Energy [171] is used for the analysis to represent a pouch cell with an asymmetrical tab configuration (i.e. both tabs located on the same side of the cell). This cell is designed for use within energy storage systems for both hybrid and fully electric vehicles, and is also capable of providing the necessary power to drive high performance EV racing applications, having been

employed within Formula E in collaboration with Williams Advanced Engineering [172]. Therefore, the cell is well suited for this thermal study which considers EV, HEV and high performance EV usage. The dimensions of the cell are viewable in Figure 5-2 (a).

It is important to note, however, that the asymmetrical tab configuration of the cell is likely reflective of a design choice tailored towards ease of packing. With this arrangement, the tabs require an electrical connection to be present at only a single surface, which may decrease the packing complexity and improve volumetric energy density from the increased compactness. However, research by Samba et al. [173] demonstrates that such asymmetrical tab configurations are not optimised for improved cell uniformity (in terms of current distribution and thermal gradients). Specifically, the authors conclude that cell designs with symmetrical tabs (i.e. tabs that are positioned on opposite ends of the cell) allow for more uniform potential and current distribution across the cell, which in turn reduces the ohmic heat generation rate and enables for more uniform temperature distribution (when compared to an asymmetrical tab configuration). A symmetrical tab design is also utilised in the research by Hunt et al. [108], which demonstrated that cooling the tabs of pouch cells may enable reduced ageing rates relative to surface cooling under some circumstances. The authors recommended that future thermal management systems should seek to incorporate tab cooling strategies, although it is unsure whether these conclusions would remain if an asymmetrical tab configured cell was chosen in their analysis.

To further investigate the potential of tab cooling, a symmetrical tab arrangement is therefore also included in the thermal modelling study. The geometry of the symmetrical tab cell is shown in Figure 5-2 (b), which utilises the same tab and cell body dimensions as the asymmetrical tab case.

5.2.1 POUCH CELL THERMAL MODEL DEVELOPMENT

The body of the pouch cell is modelled as a homogenous bulk layer with an effective heat capacity, density and anisotropic thermal conductivity. As with the cylindrical cell thermal analysis, treating the cell as a homogenous structure in this manner has proven effective for the modelling of lithium-ion cells [141], whereby further examples of this approach applied to pouch cell thermal modelling can be viewed in [167], [174], [175].

In this analysis, the cell body is treated as simple rectangle where the tab structures are approximated as a fin structure with an extruded triangle cone base, which is in line with the modelling approach adopted in [79], [167], [141], [175]. With reference to Figure 5-2, the

dimensions of the cell and tab structures from the COMSOL thermal model are contained within Table 5-1.

The governing heat conduction equation is used to describe the heat transfer in the cell body and tab domains, which is represented in 3-D Cartesian coordinates via [141]:

$$\rho C_p \frac{\partial T}{\partial t} = \frac{\partial}{\partial x}\left(k_x \frac{\partial T}{\partial x}\right) + \frac{\partial}{\partial y}\left(k_y \frac{\partial T}{\partial y}\right) + \frac{\partial}{\partial z}\left(k_z \frac{\partial T}{\partial z}\right) + q''' \quad (56)$$

Where ρ is the effective cell density [kg.m^{-3}], T the local cell temperature [K], $C_p$the effective cell heat capacity [J.kg^{-1}.K^{-1}], t the time [s], q''' the volumetric heat generation rate [W.m^{-3}], x, y and z the cartesian coordinates [m] with respect to the coordinate axis shown in Figure 5-2, k_x the effective thermal conductivity in the x direction (i.e. perpendicular) [W.m^{-1}.K^{-1}], k_z the effective thermal conductivity in the z direction (i.e. axial) [W.m^{-1}.K^{-1}] and k_y the effective thermal conductivity in the y direction.

The heat generation rate within the cell body and tabs is assumed uniform throughout the material, consistent with the approach described in [141]. Newton's law of cooling is applied as the boundary condition for each exposed surface, which is given in Equation (5) in Chapter 3. For surfaces that are insulated, a value of zero is assigned for the heat transfer coefficient.

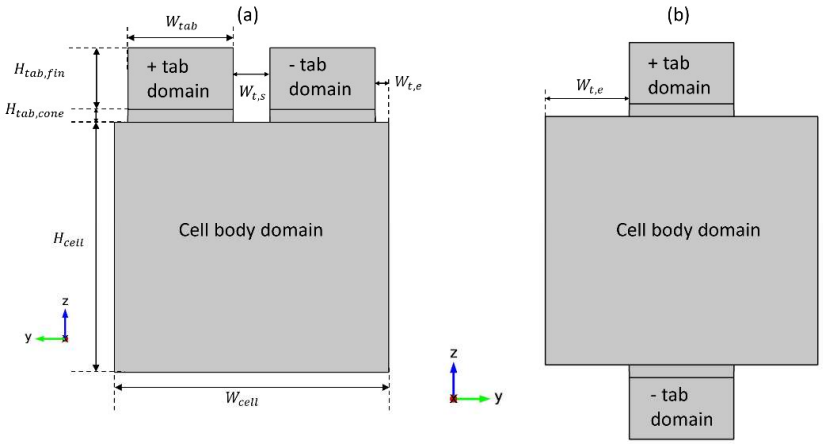

Figure 5-2: Pouch cell geometry schematics with (a) Same-sided tab layout (b) Opposite end tab layout

The heat generation in the battery tabs (base + fin) is characterised by Joule heating, which is described by the following source term [141]:

$$Q_t = I^2 R_t \tag{57}$$

Where Q_t is the heat generation rate within the tab structure (cone + fin) [W], I the battery cell current [A] and R_t the total resistance within the tab [Ω]. The resistance of the total tab domain is calculated from the summation of the resistance through the tab cone base ($R_{tab,cone}$) and tab fin section ($R_{tab,fin}$). The resistance of the tab cone with varying cross section is characterised via:

$$R_{tab,cone} = \rho_r \int_0^{H_{cone}} \frac{dx}{A(x)} \tag{58}$$

Where $R_{tab,cone}$ is the resistance through the tab base [Ω], ρ_r the electrical resistivity of the tab material [Ω.m], x the position along the height of the tab [m], H_{cone} the height of the tab cone and A the cross-sectional are of the tab base that varies with x [m^2].

The resistance of the tab fin structure is given by:

$$R_{tab,fin} = \frac{\rho_r H_{tab,fin}}{t_{tab} W_{tab}} \tag{59}$$

Where $R_{tab,fin}$ is the resistance of the tab fin section [Ω]. The total tab resistance is given by the sum of the fin and cone resistances:

$$R_t = R_{tab,cone} + R_{tab,fin} \tag{60}$$

Where R_t the total tab resistance used to calculate the tab heat generation rate in Equation (57). The calculated values of R_t for the negative and positive tab are 3.36x10^{-5} Ω and 5.30x10^{-5} Ω respectively. The calculation procedure can be viewed in Appendix A.7.

Table 5-1: Dimensions of the asymmetrical and symmetrical tab cells used in the COMSOL thermal model

Parameter	Definition	Value [mm]
H_{cell}	Height of the cell body	190.0
$H_{tab,fin}$	Height of the tab fin	47.0
$H_{tab,cone}$	Height of the tab cone	10.0
W_{tab}	Width of the tab	80.0
W_{cell}	Width of the cell body	208.0
t_{cell}	Thickness of the cell	11.8

$W_{t,s}$	Spacing between tabs	28.0
$W_{t,e}$	Distance between tab and cell edge	10 (asymmetrical cell), 64 (symmetrical cell)

Similar to the method discussed in Chapter Three, the heat generation within the cell material only considers the irreversible components of the heat generation as defined by Equation (30). For this analysis, a static value of 1.33 mΩ is specified for the cell R_η which is given in the cell manufacturer data sheet at 50% cell SOC [171].

5.3 DUTY CYCLES

The PHEV vehicle model described in Chapter Three Section 3.6 is used to generate the C-rate profiles for this PHEV vehicle study, which involves a 16 kWh PHEV vehicle comprising of 82 of the considered 53 Ah pouch cells. The outputted C-rate profiles from the PHEV model are viewable in Figure 5-3 (positive denotes discharge and negative charge), which also includes a race duty cycle for a performance EV derived under the same methodology as discussed in Chapter Four Section 4.5. Key metrics for the duty cycles are summarised in Table 5-2.

Table 5-2: Summary of the peak battery power, C-rates and average heat generation for the PHEV and performance EV driving scenarios using 53 Ah pouch cells

Drive cycle	Model output	PHEV
PHEV US06	Peak C-rate [hr^{-1}]	7.891
	Absolute C-rate average [hr^{-1}]	1.414
	Peak power [kW]	126.9
	Average cell heat generation [W]	14.18
PHEV WLTP Class 3	Peak C-rate [hr^{-1}]	3.888
	Absolute C-rate average [hr^{-1}]	0.659
	Peak power [kW]	62.51
	Average cell heat generation [W]	3.805
PHEV Artemis Motorway 150	Peak C-rate [hr^{-1}]	5.992
	Absolute C-rate average [hr^{-1}]	1.654
	Peak power [kW]	96.35
	Average cell heat generation [W]	15.34
PHEV Artemis Rural Road	Peak C-rate [hr^{-1}]	4.584
	Absolute C-rate average [hr^{-1}]	0.795
	Peak power [kW]	73.72
	Average cell heat generation [W]	5.073
PHEV Race cycle	Peak C-rate [hr^{-1}]	7.547
	Absolute C-rate average [hr^{-1}]	2.858
	Peak power [kW]	-
	Average cell heat generation [W]	49.18

Here, all cycles remain within the performance envelope of the cell which can accommodate peak C-rates of up to 8 C during discharge. For the PHEV case, the Artemis Motorway 150 cycle is the most aggressive electrical loading condition providing a time averaged heat generation rate of 15.34 W. As expected, the aggressive nature of the race duty cycle results in a much greater averaged heat generation rate of 49.18 W, which may be considered a potentially worst-case scenario for the design point of the automotive thermal management system using these cells. The heat generation profiles for the cell body considering the static overpotential resistance are shown in Figure 5-4.

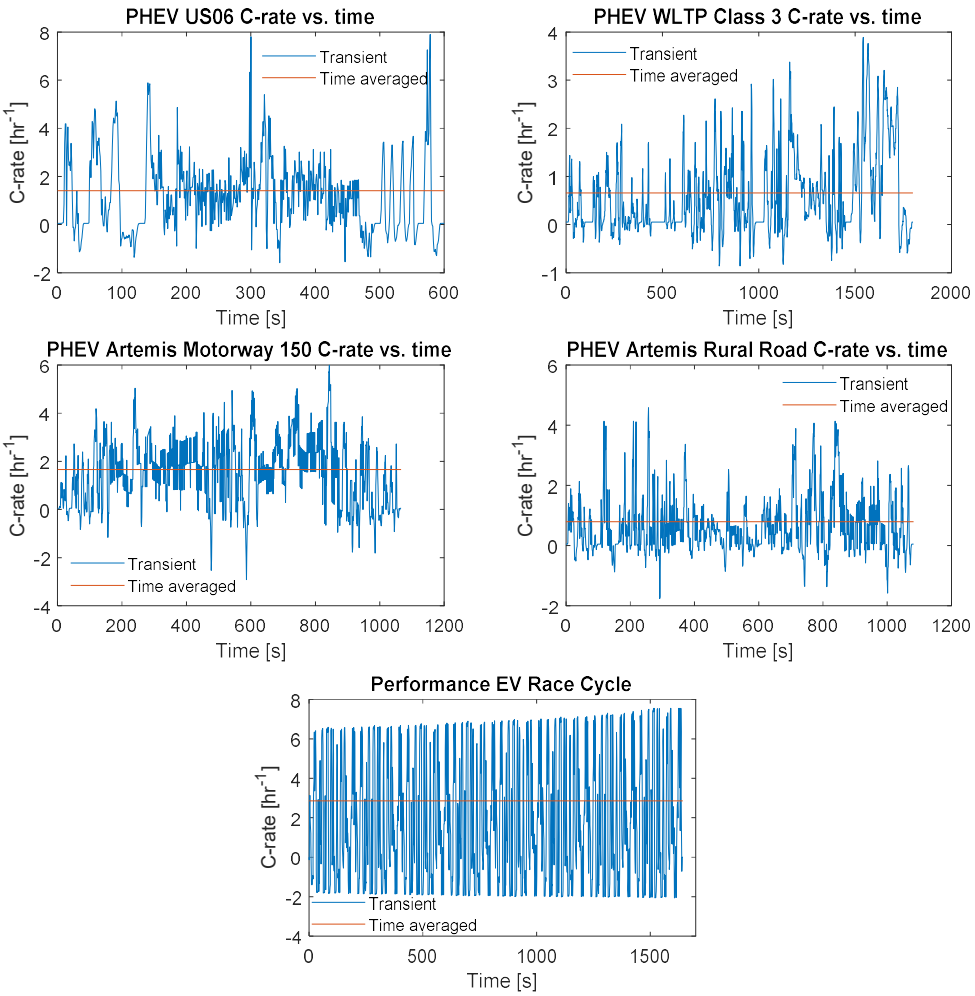

Figure 5-3: C-rate profiles of the analysed drive cycles using 53 Ah pouch cells (C-rate time average is taken over the absolute C-rate values)

5.4 COOLING STUDY ANALYSIS

In this section, the thermal performance of the considered pouch cells is simulated when subject to different exterior cooling boundary conditions. These include:

1. Single tab cooling
2. Double tab cooling
3. Single side cooling
4. Double side cooling

Schematics of the boundary surfaces subject to each cooling method are shown in Figure 5-5 for the cell with the asymmetrical tab layout. In the case of single tab cooling, the higher heat generating positive tab is subject to active cooling. All other surfaces of the cell not subject to active cooling are set as insulated boundary conditions.

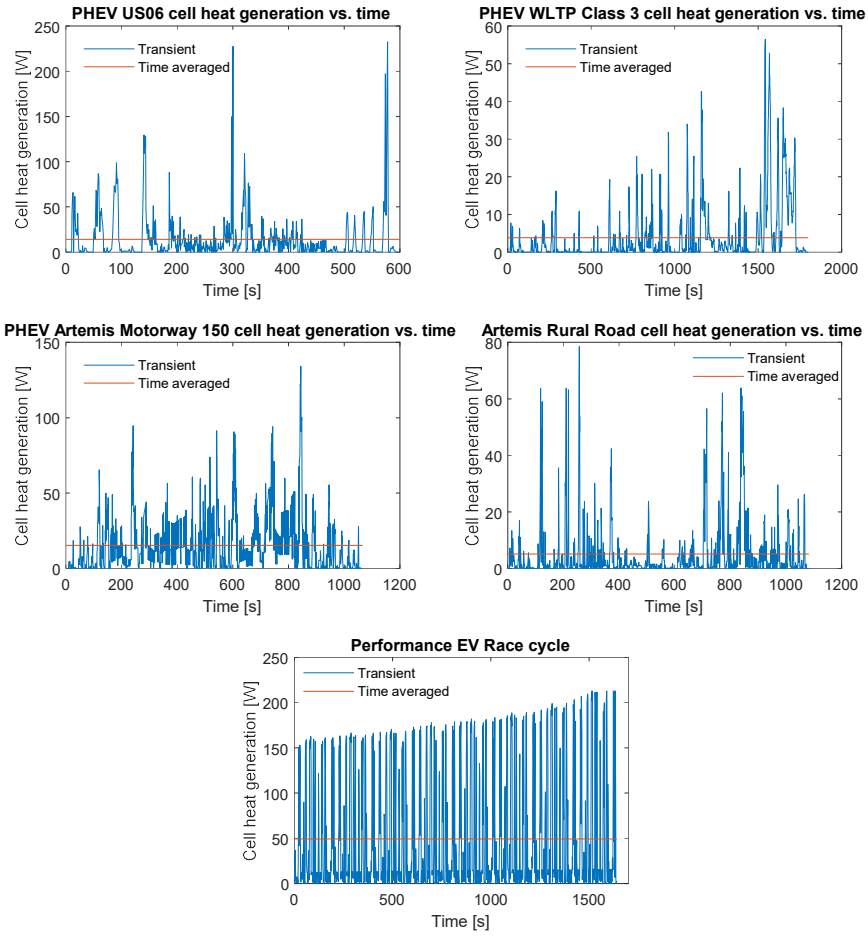

Figure 5-4: Pouch cell heat generation rate profiles for the simulation cooling study analysis

Static heat transfer coefficients are specified on the boundaries (as shown in Figure 5-5) to simulate both active air and liquid cooling. As with the analysis contained in Chapter Three, a value of h = 50 $W.m^{-1}.K^{-1}$ is used to represent active air cooling, and h = 750 $W.m^{-1}.K^{-1}$ used to represent liquid cooling e.g. obtainable with a 50-50 mixture of water glycol [78].

Since the heat transfer coefficient is treated as static in this analysis, this simplification ignores thermal gradients that may exist along the direction of the flow path due to the temperature change of the heat transfer medium, which may be large depending on the flowrate and heat transfer medium choice [73], [85]. Essentially, this method of thermal modelling may provide more favourable thermal performance for surface and tab cooling methods. More involved thermal models that account for change in heat transfer medium temperature along the flow path are analysed further in Chapter Six.

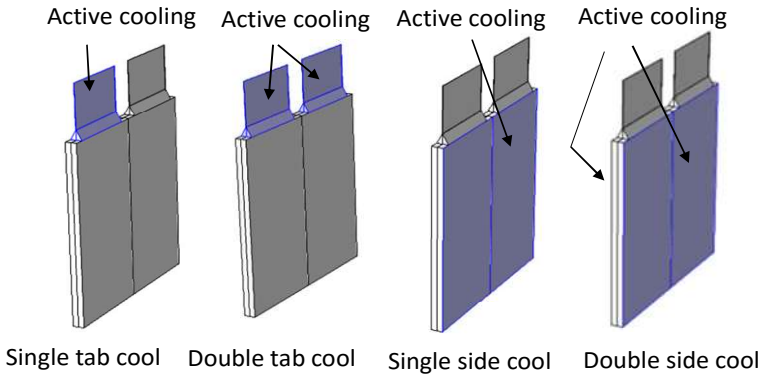

Figure 5-5: Locations of the applied active cooling boundary conditions in the asymmetric tab pouch cell thermal model

Values for the cell anisotropic thermal conductivity are taken as 0.28 $W.m^{-1}.K^{-1}$ for the perpendicular component [119] and 30 $W.m^{-1}.K^{-1}$ for the axial component, which is within the range of values reported in [122]. As with the cylindrical cell analysis, the chosen value for the perpendicular conductivity component includes the presence of contact resistances present within a real cell, which is important to avoid underestimating the maximum temperature and maximum temperature gradient [114].

A steady state-analysis is considered as an initial indication into the thermal performance of the cooling options. The time averaged heat generation rates across the WLTP Class 3, Artemis Motorway 150 and Race duty cycle are used to represent the realistic design points for the thermal management system for mild PHEV use, aggressive PHEV use and Performance EV racing respectively. Given the cell heat generation rate (which is a variable in this study), the average tab heat generation rate is calculated through multiplying the

averaged squared current across the drive cycle together with the tab resistance. The averaged squared cycle current is calculated by dividing the average cell body heat generation rate with the cell resistance (1.33 mΩ). In all simulations, the heat transfer medium temperature is set at 25 ℃.

A mesh independence study is conducted for both the same sided and opposite sided tab designed cells to ensure that the outputted thermal results are independent of the mesh size. An example of the mesh independence study result is contained in Figure 5-6 for the pouch cell with opposite side tabs subject to double tab liquid cooling under the WLTP Class 3 level of heat generation. To retain a level of computational efficiency whilst ensuring accuracy, the mesh with 309,280 elements is chosen given that T_{max} is unaffected with finer meshes.

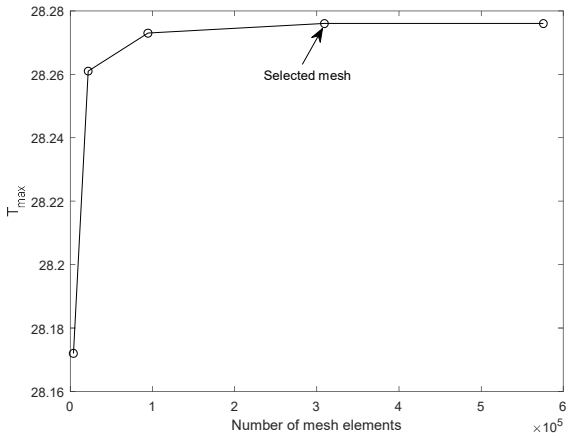

Figure 5-6: Mesh independence study for the opposite side tabs pouch cell under double tab liquid cooling at WLTP Class 3 levels of heat generation

5.4.1 TAB COOLING

The steady-state thermal results as a function of the cell body heat generation rate for each tab cooling strategy are presented in Figure 5-7. The averaged heat generation rate values from Table 5-2 that reflect the drive cycle scenarios are represented by the vertical arrows. Treadline equations are included which perfectly fit the data from the thermal model, given that the R^2 value is 1.

For the singular tab cooling methods, increasing the intensity of the cooling by transitioning from forced convection with air towards liquid results in a marked reduction in T_{avg}, while ΔT_{max} remains relatively unchanged. At the WLTP Class 3 level of heat generation, singular tab cooling with liquid or air is, however, incapable of limiting the maximum cell temperature

gradient to below 5 °C. As the calculated cell heat generation rate for a sustained 1 C discharge is 3.74 W (which may be reflective of a worst case EV use scenario), singular tab cooling methods are likely an inadequate thermal management choice for all xEVs, due to the poor temperature uniformity.

Cooling both tabs of the cell offers a marked improvement in both averaged temperature reduction and temperature uniformity. For the cell with the same sided tab design, double tab cooling with either air or liquid results in ΔT_{max} reaching circa 5 °C at the WLTP Class 3 heat generation rate. For air cooling, T_{avg} reaches 35.0 °C where T_{max} reaches 36.6°C (using the fitted treadline Equations in Table 5-5.). Therefore, it may be desirable to apply liquid cooling in the case of cooling both tabs for cells with same sided tab designs given the more acceptable T_{avg} of 29.3°C.

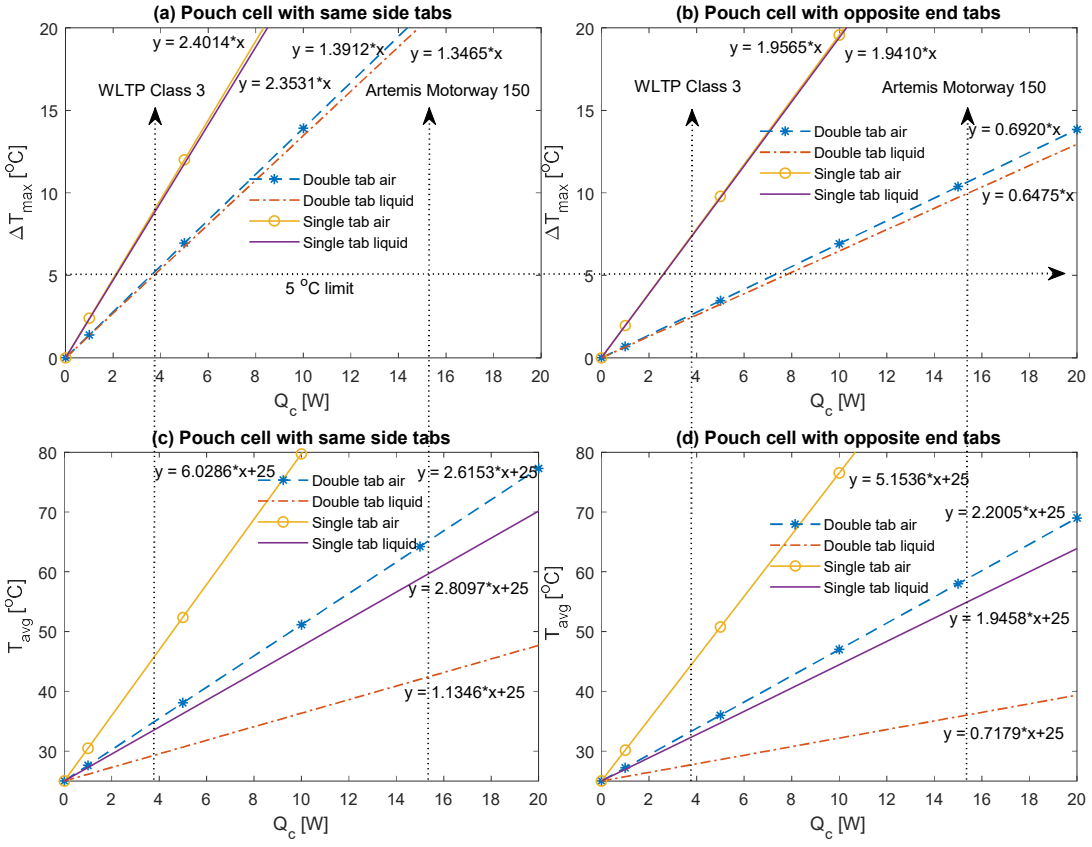

Figure 5-7: Pouch cell tab cooling steady-state thermal modelling results

In the case of opposite end tab designs, the reduced length of the heat transfer pathway between the cooled tab and cell hot spot improves the thermal performance. Relative to same sided tab cooling, the opposite side tab design under air cooling results in lower T_{avg} and T_{max} values of 33.4 °C and 33.9 °C respectively. Therefore, the potential of air cooled tab designs may be more acceptable with the opposite tab configured cell for PHEV

applications under mild cycles (WLTP Class 3). Ultimately, a double tab liquid cooled solution will enable for lower T_{max} values of 28.3 °C. The choice of the heat transfer medium may be governed by other factors such as overall complexity with integrating the strategy into the pack-level design, total pack heat removal rate requirements, cost, or concerns over leakage risk.

The thermal contours of the cell subject to singular and double liquid tab cooling for both cell tab designs are shown in Figure 5-8 under the PHEV WLTP Class 3 averaged heat generation rate. Here, the nature of the formed surface gradient can be seen, which illustrates the issues of tab cooling on cells with same sided tabs due to the poorer temperature uniformity across the cell.

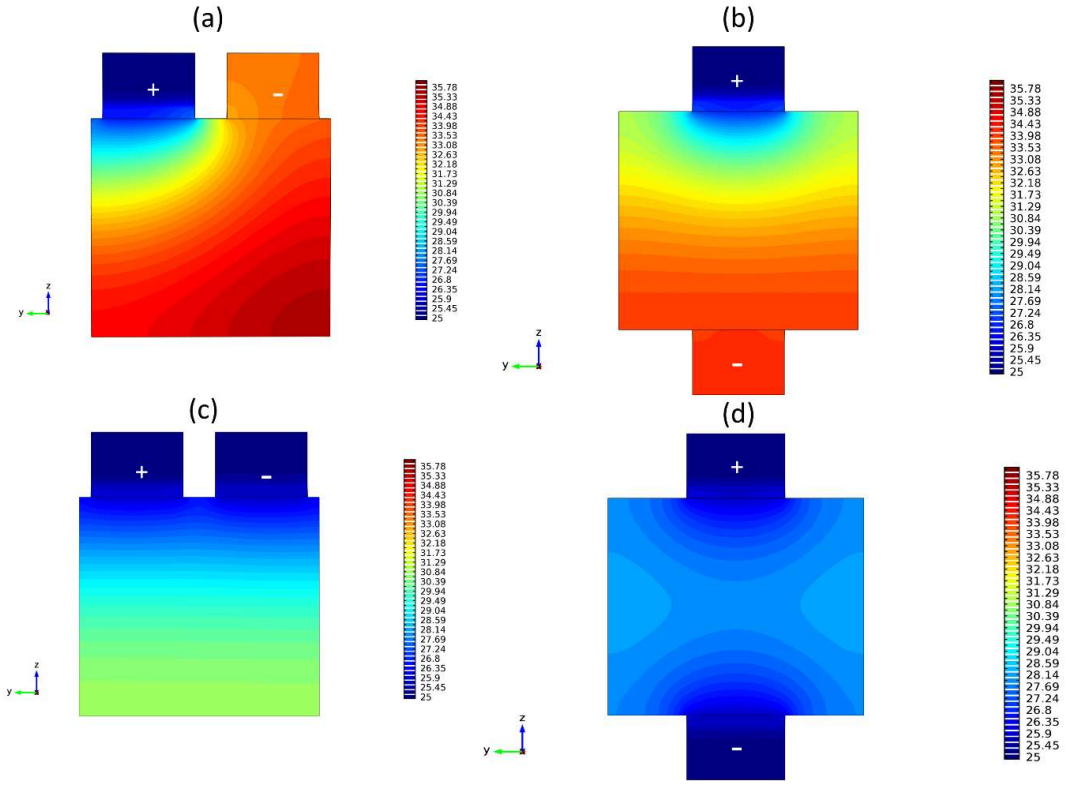

Figure 5-8: Thermal contours of active liquid tab cooling under the PHEV WLTP Class 3 average heat generation rate for (a) single tab liquid (same sided tab) (b) single tab liquid (opposite end tab) (c) double tab liquid (same sided tab) (d) double tab liquid opposite end tab)

For aggressive PHEV cycles (Artemis Motorway 150), the applicability of tab cooling becomes more uncertain. Even with the more thermally preferable opposite end tab configuration, ΔT_{max} reaches 9.9 °C and T_{avg} 36.0 °C when liquid cooled. In order to limit ΔT_{max} to 5 °C, the averaged drive cycle heat generation rate should not exceed 7.7 W for the double tab liquid cooled solution on the cell with opposite end tabs.

5.4.2 SURFACE COOLING

The steady-state thermal results as a function of the cell body heat generation rate for each surface cooled strategy are presented in Figure 5-9. For the WLTP Class 3 heat generation, single side cooling of the pouch cell with either air or liquid enables ΔT_{max} to remain comfortably below the 5 ℃ limit. With single side air cooling, T_{avg} and ΔT_{max} reach 28.3 ℃ and 2.0 ℃ respectively for the cell with the same sided tab configuration. Little difference is observed between the surface cooling performance when transitioning to the opposite end tab cell, where a marginal improvement is observed. Surface cooled methods may, therefore, enable the use of the potentially preferable same sided tab designed cells (in terms of simpler pack design and assembly) at minimal thermal penalty.

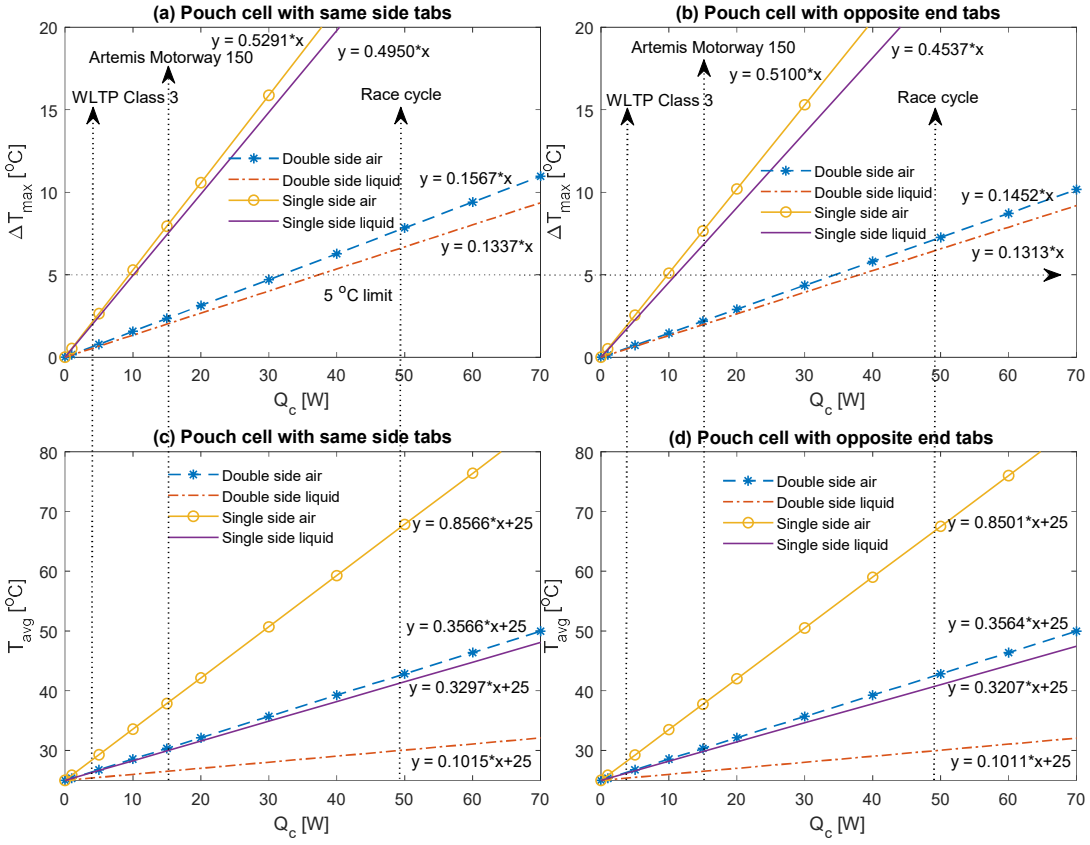

Figure 5-9: Pouch cell surface cooling steady-state thermal modelling results

Single side face cooling may also be preferable over double side cooling at the WLTP Class 3 level of heat generation given the adequate thermal performance. This is since a heat transfer mechanism is only required between every two cells along the stack, as opposed to between every cell within the stack. This strategy may simplify the duct arrangement in the case of indirect liquid cold plate cooling, as the heat transfer medium has less locations in which it must be routed and may require fewer seals from a lesser number of manifold

connections to reduce the leakage risk. The limitation of this strategy, however, is that the heat transfer pathway between the cell hot spot and cooled surface is doubled. This ultimately results in an increased perpendicular temperature gradient through the cell material and limits the level of internal heat generation the cell can be exposed to in order to remain below the 5 ℃ limit.

Such limitations of single side cooling become more apparent at the Artemis Motorway 150 heat generation rate. In the case of liquid cooling for the cell with same sided tabs, ΔT_{max} reaches 7.59 ℃ while T_{avg} remains relatively low at 30.1 ℃. These cooling methods are thus more constrained by their ability in limiting the rise in cell temperature gradient than in control over the averaged cell temperature rise. Double side cooling strategies are required in this instance to limit ΔT_{max} to below 5 ℃. The use of an air heat transfer medium may also potentially be applicable for double side cooling, although it is important to reiterate that these observations may change when accounting for the change in heat transfer medium temperature across the pouch cell face, which will be larger in the case of air cooling at the same flowrate due to the lower heat capacity relative to liquid with a water-glycol mixture (see Table 2-1 in Chapter Two).

In the case of the performance EV cycle, only double side cooling with liquid is able to limit T_{avg} to below 30 ℃. Using air as the heat transfer medium results in a large increase in T_{avg} with a value of 42.5 ℃, which is undesirable due to the implied accelerated temperature related ageing [29].

5.4.3 COMPARISON BETWEEN SURFACE AND TAB COOLING

A summary of the key thermal performance metrics for the case of double tab cooling, single side cooling and double side cooling as a function of the characteristic heat generation rate is shown in Table 5-3. Here, the tab cooling strategies are for the cell with opposite end tabs and the surface cooled strategies for the cell with same ended tabs.

Table 5-3: Pouch cell cooling steady-state thermal performance summary (same sided tab arrangement for surface cooling and opposite tab arrangement for tab cooling strategies)

	Double Tab liquid			Single side liquid			Double side air			Double side liquid		
Duty cycle	T_{max} [℃]	T_{avg} [℃]	ΔT_{max} [℃]	T_{max} [℃]	T_{avg} [℃]	ΔT_{max} [℃]	T_{max} [℃]	T_{avg} [℃]	ΔT_{max} [℃]	T_{max} [℃]	T_{avg} [℃]	ΔT_{max} [℃]
WLTP Class 3	28.28	27.73	2.46	27.00	26.25	1.88	26.57	26.36	0.60	25.57	25.39	0.51

Artemis 150	38.20	36.01	9.93	33.05	30.06	7.59	31.34	30.47	2.40	27.29	26.56	2.05
Race cycle	67.34	60.31	31.85	50.81	41.22	24.35	45.31	42.54	7.71	32.36	29.99	6.58

From Table 5-3, it is evident that double tab cooling strategies are incapable of controlling the cell thermals to within acceptable limits under the performance EV level of heat generation, with T_{max} exceeding 67 ℃ which is over the maximum temperature limit of the cell (65 ℃). Aside from accelerated degradation, this presents an increased risk of the cell entering thermal runaway if it were repeatably cycled and allowed to approach a quasi steady-state. Therefore, these strategies are likely more suited towards lower levels of heat generation e.g. WLTP Class 3 cycle, or cycles that have a time averaged heat generation rate below 7.7 W to limit ΔT_{max} to 5 ℃.

Cooling a single side of the pouch cell is limited in its ability to control ΔT_{max} due to the longer heat transfer pathway between the cell hot spot and coolant source. This, combined with the poor perpendicular thermal conductivity of the cell (0.28 $W.m^{-1}.K^{-1}$) results in large (>5 ℃) temperature gradients at the Artemis Motorway 150 heat generation rate. As with double tab cooling, single side cooling options are potentially limited to mild PHEV applications with lower heat generation rates. The benefit of single side cooling in these instances over tab cooling is through enabling the use of cell designs with same sided tabs, given that the thermal performance is relatively independent on the tab location. However, whilst tab cooling provides slightly higher values for the magnitude of ΔT_{max} and T_{avg}, the research by Hunt et al. [108] suggest that the overall ageing rate of tab cooling may be lower in some instances due to the more preferable axial direction of the temperature gradient, which allows the individual layers within the cell to operate more uniformly.

In the work of Hunt et al., they compared the capacity loss of 5 Ah NMC pouch cells with opposite end tab configurations under double tab cooling versus double side surface cooling. Peltier elements were used to apply a constant 20 ℃ boundary condition on the cooled tabs for the tab cooled case and on the front and back surfaces of the cell for the surface cooled case. After 1000 continuous cycles of 1 C discharge followed by 1 C charge, they observed that the tab cooled cell experienced 7.1% capacity loss, whereas the surface cooled cell experienced a 9.4% capacity loss. For more aggressive continuous cycling at 6 C followed by a 2 C charge, the difference in capacity loss after 1000 cycles between the two cooling strategies increased, where the tab cooled cell experienced a 6.2% capacity loss and the

surface cooled cell a 15.8% capacity loss. The authors also compared the theoretical 1-D thermal resistance for tab and surface cooling options based on the geometry and material properties of the cell given via [108]:

$$R = \frac{x_h}{A.k} \tag{61}$$

Where R is the thermal resistance [K.W^{-1}], A the heat transfer area perpendicular to the direction of heat flow [m^2], x_h the length of the heat transfer pathway [m] and k the thermal conductivity [W.m^{-1}.K^{-1}].

Values of the conduction thermal resistance calculated by Hunt et al. using Equation (61) and for the cell in this work are shown in Table 5-4. Here it is observed that based on the material properties and dimensions of the cells, the Hunt et al. cell is more favoured towards tab cooling than the larger format cell considered in this analysis. Therefore, it is not expected that the double tab liquid cooled cell under the Artemis Motorway 150 heat generation condition would provide a lower ageing rate than when cooled on both sides with liquid, given the vastly reduced ΔT_{max} and T_{avg}. Ultimately, further experimental work should seek to quantify the weighting between the values of T_{avg}, ΔT_{max} and *direction* of ΔT_{max} on the overall ageing rate of the cell, which to the authors knowledge is not well understood in the literature. Therefore, given these uncertainties, the common consensus for a 5 °C limit on ΔT_{max} is followed and assumed acceptable for both perpendicular and axial gradients.

Table 5-4: 1-dimensional conduction thermal resistance comparison between the Hunt et al. cell and the cell analysed in this work

	Double side surface cooling 1-D thermal resistance [K.W^{-1}]	Double tab cooling 1-D thermal resistance [K.W^{-1}]	Percentage decrease in resistance of surface cooling relative to tab cooling [%]
Hunt et al. cell	2.4	3.7	35.1
Cell in this work	0.53	1.3	59.2

A summary of the fitted trendline equations (in the form of a straight line) for each analysed cooling method from the thermal model for both the cell with opposite and same ended tabs are shown in Table 5-5. Here $m_{T_{max}}$, $m_{\Delta T_{max}}$ and m_{Tavg} (with units of K.W^{-1}) refer to the slope of the line for the results of T_{max}, ΔT_{max} and T_{avg} respectively. In the case of $m_{T_{max}}$ and m_{Tavg} the value for the 'y' axis intercept is 25 [°C], where the intercept is zero in the

case of ΔT_{max}. Lower values for the slope are indicative of improved thermal performance due to a lowered thermal resistance for heat transfer.

Table 5-5: Values for the slope of the fitted straight line equations for T_{max}, T_{avg} and ΔT_{max}

	Pouch cell with same sided tabs			Pouch cell with opposite end tabs		
	$m_{T_{max}}$ [K.W^{-1}]	$m_{T_{avg}}$ [K.W^{-1}]	$m_{\Delta T_{max}}$ [K.W^{-1}]	$m_{T_{max}}$ [K.W^{-1}]	$m_{T_{avg}}$ [K.W^{-1}]	$m_{\Delta T_{max}}$ [K.W^{-1}]
Single tab air	6.0286	5.4740	2.4014	5.6272	5.1536	1.9565
Single tab liquid	2.8097	2.2572	2.3531	2.4193	1.9458	1.9410
Double tab air	3.0523	2.6153	1.3912	2.3450	2.2005	0.6920
Double tab liquid	1.5665	1.1346	1.3465	0.8608	0.7179	0.6475
Single side air	1.0319	0.8566	0.5291	1.0155	0.8501	0.5100
Double side air	0.4130	0.3566	0.1567	0.4052	0.3564	0.1452
Single side liquid	0.5247	0.3297	0.4950	0.4834	0.3207	0.4537
Double side liquid	0.1496	0.1015	0.1337	0.1475	0.1011	0.1313

5.5 FURTHER WORK

Further study should expand on the steady-state analysis to analyse the full transient response of the cell when subject to tab and surface cooling methods, particularly under more intensive shorter electrical loading periods where quasi steady-state may not be reached. This analysis is discussed further in Chapter Six for the race cycle case.

A practical implementation of double side cooling should be developed to tackle the aggressive nature of the performance EV race cycle, given the simulated inadequate thermal performance of double tab cooling.

Further experimental work should also seek to quantify the weighting between the values of T_{avg}, ΔT_{max} and *direction* of ΔT_{max} on the overall ageing rate of the cell which will further identify the heat generation limits in which tab cooling may be applied above the common consensus for the 5 °C limit on ΔT_{max}.

5.6 CONCLUSION

To address Research Objective 3, the following conclusions are drawn on the cell-level thermal management options for the analysed pouch cells under different automotive duty cycles.

The steady-state thermal analysis suggests that singular tab cooling options are an inadequate thermal management choice for the considered large format lithium-ion pouch cell, which is reflective of a common format used in the automotive industry. This is due to the poor control over the maximum temperature gradient (ΔT_{max}) through the cell, where gradients in excess of 7 ℃ are predicted under heat generation rates reflective of 1C EV discharges and mild PHEV duty cycles (WLTP Class 3). This is for a cell design that contains opposite ended tab layouts, which is required in order to maximise the thermal performance of tab cooling. In the case where the tabs are located on the same side of the cell, larger gradients on the order of 9 ℃ are predicted.

Incorporating double tab cooling for the cell design with opposite ended tabs greatly improves the thermal condition of the cell. Relative to single tab cooling, steady-state values of ΔT_{max} are predicted to be near 3 times lower for a given heat generation rate. This extends the ability of tab cooling to limit ΔT_{max} to 5 ℃ under averaged heat generation rates up to 7.7 W when liquid cooled. This covers the mild PHEV WLTP Class 3 cycle (3.8 W). There is also the potential to incorporate air cooling at this level of heat generation given that the averaged cell operating temperature (T_{avg}) is limited to below 35 ℃ with an ambient heat transfer medium temperature of 25 ℃.

Cooling a single surface of the cell is more constrained in its ability to limit ΔT_{max} than in controlling T_{avg}. At the PHEV WLTP Class 3 level of heat generation, ΔT_{max} is limited to around 2℃. However, for the more aggressive PHEV Artemis Motorway 150 duty cycle (15.3W), ΔT_{max} exceeds 7 ℃. It is expected that single side cooling may be an alternative to double tab liquid cooling for milder PHEV duty cycles and commercial EV usage. However, based on results from the literature, the formed perpendicular gradient through the cell induced by surface cooling is expected to incur an increased ageing rate relative to a comparable magnitude axial temperature gradient formed through tab cooling. Further experimental work is required to quantify the weighting between the values of T_{avg}, ΔT_{max} and *direction* of ΔT_{max} on the overall ageing rate of the cell which is not currently well defined.

Cooling both large faces of the pouch cell results in the lowest rise in T_{avg} for all the analysed cooling choices. The shorter heat transfer pathway between the cell hot spot and cooling surface vastly improves the cell temperature uniformity relative to single surface cooling, where for a given steady-state heat generation rate ΔT_{max} is near 4 times lower. This strategy is the only method which enables ΔT_{max} to remain below 7 ℃ under the performance EV race cycle (49.2 W), where single side cooling and double tab cooling with liquid heat transfer mediums result in excessive values of circa 24 ℃ and 32 ℃ respectively. Based on these observations, it is recommended that a double side cooling strategy should be sought for such large format pouch cells under aggressive PHEV and performance EV driving scenarios.

The above conclusions address Research Objective 3, whilst providing Thermacore with practical and implementable guidelines into which cooling strategy may be preferable for a given characteristic heat generation rate. This information may be employed to design the initial architecture of the BTMS, and underpin the concept before detailed design commences. A summary of the advantages and disadvantages of each cooling solution is contained in Table 5-6.

Table 5-6: Advantages and disadvantages of tab and surface cooling solutions for the analysed large format pouch cells

Cooling method	Advantages	Disadvantages
Single tab	• Simpler to target cooling at only a single tab. • Formed temperature gradient is axial along the layers of the cell, which may reduce the ageing rate when compared to a perpendicular gradient of comparable magnitude.	• Poor control over the cell temperature uniformity – permits only low averaged cell heat generation rates of 2.6 W to limit ΔT_{max} to 5 °C, which is below the expected thermal design point for EVs and PHEVs subject to mild duty cycles (WLTP Class 3). • Requires a cell design with opposite ended tabs to maximise thermal performance which may add additional complexity and volume to the overall pack design. • Requires a high convection rate to counteract the limited heat transfer area available, which renders direct air cooling inadequate. • Integrating the tab cooling mechanism together with the required electrical connections may be complex.
Double tab	• Vastly improved temperature uniformity relative to single tab cooling - steady-state volumetric temperature gradient is predicted to be near 3 times lower for a given heat generation rate. • Formed temperature gradient is axial along the layers of the cell, which may reduce the ageing rate when compared to a perpendicular gradient of comparable magnitude. • The increased overall surface area and reduced heat transfer pathway extend the use of tab cooling towards higher heat generation conditions - ΔT_{max} is limited to 5 °C up to averaged heat generation rates of 7.7 W when	• Requires a cell design with opposite ended tabs to maximise thermal performance which may add additional complexity and extra volume to the overall pack design. • Integrating the tab cooling mechanism together with the required electrical connections may be complex • Results in high values of ΔT_{max} (circa 10 °C) at the more aggressive PHEV Artemis Motorway 150 heat generation rate. • Unable to control the thermals of the cell within safe limits at the performance EV averaged heat generation rate. Results in extreme values of ΔT_{max} greater than 30 °C and T_{avg} of 60 °C.

	liquid cooled which covers typical commercial EV use and mild PHEV duty cycles. • Potential to use air cooling - T_{avg} may be limited to below 35 ℃ at the WLTP Class 3 level of heat generation.	
Single side	• Thermal performance is relatively insensitive to the tab location - enables the use of same sided tab designed cells which may be preferable from a packing perspective to reduce the volume penalty of the design. • ΔT_{max} is limited to 5 ℃ up to averaged heat generation rates of 10.1 W when liquid cooled which covers typical commercial EV use and mild PHEV duty cycles. • The surface cooling mechanism does not require integration with the cell electrical connections which may simplify the pack design. • Cooling only a single surface of the cell requires a heat transfer mechanism to exist between every two cells along the stack, which may reduce the pack design complexity relative to cooling both surface of each cell. • Potential to use air cooling - T_{avg} may be limited to circa 28 ℃ at the WLTP Class 3 level of heat generation.	• Poor temperature uniformity under higher heat generation conditions - the long heat transfer pathway between the cell hot spot and coolant source results in large values of ΔT_{max} (7.6 ℃) under the PHEV Artemis Motorway 150 heat generation. • Formed temperature gradient is perpendicular between the layers within the cell, which may increase the ageing rate when compared to an axial gradient of comparable magnitude. .
Double side	• Vastly improved temperature uniformity relative to single side cooling - steady-state volumetric temperature gradient is predicted to be near 4 times lower for a given heat generation rate • Large available heat transfer area allows for low T_{avg} of 30 ℃ even under the aggressive performance EV race cycle when liquid cooled.	• Formed temperature gradient is perpendicular between the layers within the cell, which may increase the ageing rate when compared to an axial gradient of comparable magnitude. • Requires heat transfer mechanisms on both side of the cell which may add extra volume, weight and complexity to the design.

6 CHAPTER SIX- EXPERIMENTAL AND SIMULATION ANALYSIS OF A NOVEL COOLING MATERIAL FOR LARGE FORMAT AUTOMOTIVE LITHIUM-ION BATTERIES

6.1 INTRODUCTION

Based on the conclusions from Chapter Five, a double side cooling strategy is recommended for the large format pouch cell when subject to the performance EV duty cycle. To address this challenge, whilst satisfying Research Objective 4, a fin based BTMS design is adopted. To improve the thermal performance of the fin BTMS given the limitations of using conventional aluminium materials as discussed in Chapter Two, a new fin material with higher thermal conductance is sought.

In this Chapter, the thermal performance of a novel fin material developed by the sponsor company is assessed for use in a BTMS. The fin material under investigation is comprised of an annealed pyrolytic graphite (APG) core, which is encapsulated within an aluminium foil skin layer. The general manufacturing steps of the APG based fin involve first manufacturing Pyrolytic graphite (PG) using a chemical vapour deposition process (CVD) through the pyrolysis of natural gas. The PG is deposited on a suitable substrate within a vacuum, at a temperature between 1750-2250℃ [176]. The APG is then formed by annealing the PG at elevated temperatures of up to 3600 ℃ [177]. The formed APG is then cut to size and bonded to the skin layer using an adhesive, where the composite fin is further subject to compression within two heated blocks up to temperatures of 150 ℃ for bonding.

The skin layer provides mechanical support and protection for the APG core which is fragile in nature [177]. The formed composite sleeve is termed ‘k-core’ by the industrial partner. The annealing process enables the APG core insert to have a very high thermal conductivity along the XY plane of APG, where conductivity values as high as 1700 W.m^{-1}.K^{-1} are achievable at 25℃ depending on the manufacturing process [178]. However, heat conducted perpendicular to the APG layers is poor and of the order of 10 W.m^{-1}.K^{-1}. In applications that require a thick k-core insert, thermal vias of conductive metal can be inserted to channel the flow of heat into the APG, improving the effective thermal conductance of the finished part [57]. The k-core technology is identified as a promising material for use in a fin based BTMS due to its much higher thermal conductance relative to aluminium and lower density (2260 kg.m^{-3} for APG vs. 2700 kg.m^{-3} for aluminium [178]) that offers the potential for weight reduction and superior thermal performance.

The high thermal conductance and low density of APG k-core products offered by Thermacore have enabled its use in a variety of weight critical thermal management applications, such as in aerospace satellites and military aircraft [179]. The k-core sleeves discussed in this thesis are the first prototype samples developed for pouch cell thermal management.

This Chapter is structured as follows. Section 6.2 describes the design of the test rig used to experimentally measure the thermal performance of the fin material, together with a description of the fin material used. The assembly procedure of the test rig is discussed in Section 6.3. In Section 6.4, a baseline thermal model of the test rig is developed for validation purposes, which is later built upon to simulate the thermal performance of the proposed novel BTMS design. The experimental procedure, together with the drive cycle profiles used to electrically load the cells is discussed in Section 6.5. Justification for the assumptions assumed with the arrangement of the rest rig is discussed in Section 6.6. In Section 6.7, the experimental temperature results from the test rig for the highly conductive fins are compared against conventional copper and aluminium fins under a wide range of electrical loading conditions that cover standard EV, PHEV and high performance EV race conditions. The accuracy of the baseline thermal model against the results obtained from the test rig for all fin material types is contained within Section 6.8. In Section 6.9, the novel fin BTMS design for practical application is presented and its performance simulated using an extended thermal model. Here an optimisation study is conducted to analyse the effect of coolant flowrate, channel diameter and fin thickness of the thermal, power, weight and volume metrics of the BTMS design. Further work and Conclusions from this study are contained in Section 6.10 and Section 6.11 respectively.

6.2 EXPERIMENTAL RIG DESIGN AND MATERIALS

To gauge the cooling performance of the k-core fins when pressurised against the surfaces of real large format automotive pouch cells, an experimental test rig and testing procedure is developed. The test rig is designed to provide fin cooling on the front and back surfaces of three large format pouch batteries (53 Ah with a graphite anode and NMC cathode manufactured by XALT Energy [171] as discussed in Chapter Five). The cells contained within the rig are separated by layers of insulating material, which act as support structures for the cells and cooling fins, in addition to isolating the cells from one another to achieve independent samples. The test rig is arranged to provide an insulated boundary on the surface of the fin not in contact with the cell, to be more reflective of stack level cooling with

a fin twice as thick. One edge of each of the cooling fins is bent to provide 25 mm of contact length onto an external cold plate, which is used to dissipate the heat from the fin. A schematic of the fin cooled concept for a single cell is shown in Figure 6-1. To provide reference cooling comparisons to the k-core fin thermal performance, conventional copper and aluminium fins are also manufactured and tested.

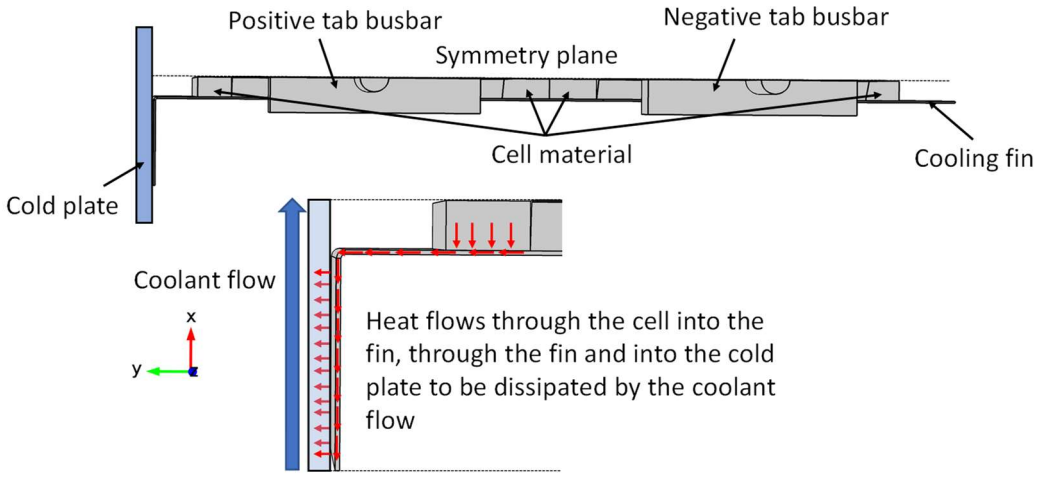

Figure 6-1: Schematic of the test rig fin cooled concept on the half-cell-level

Figure 6-2 (a)-(b) outlines the conceptual design of the test rig, which has been developed in collaboration with another researcher within the group. Here, two separate compartments are shown with each containing 3 cells to increase the number of samples for each experiment (note the partitioning insulation material is not shown in these images). The compartments are separated by a central cold plate (provided by the WMG Energy Innovation Centre) which acts to dissipate the heat conducted from the cells by the fins. The cells are supported by the tabs which are clamped into the busbar blocks. The assembled shell of the test rig highlighting the location of the cold plate is shown in Figure 6-2 (b)-(c).

In practise, it was found that utilising both compartments during the assembly procedure was overly complex and proved difficult to apply clamping pressure of the cold plate onto the bent fin edges. In addition, it was only possible to acquire 6 samples of the k-core fins, therefore, all testing was conducted on only a single compartment. Full descriptions on the assembly and testing procedure are contained in Section 6.3 and Section 6.5 respectively.

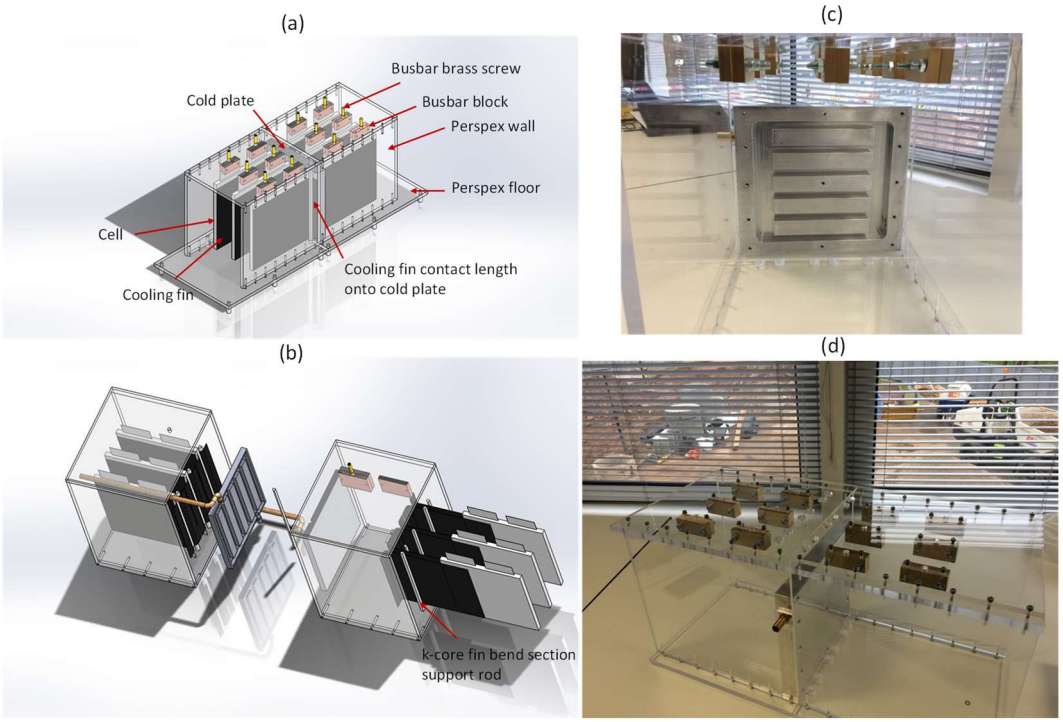

Figure 6-2: Conceptual design of the fin cooled test rig showing both compartments with (a) angle view (b) top view highlighting the location of the cold plate (c) assembled shell of the test rig highlighting the internal cold plate structure (d) angle view of the assembled test rig shell with both compartments

With reference to Figure 6-2 (b), the cold plate orientation shows the inlet water duct traversing across the top of the cells. During assembly, this was altered to pass outside of the compartment as shown in Figure 6-2 (c) which better matched the layout of the test rig chamber. In addition, the k-core bend section support rods were removed for simplicity due to the satisfactory rigidity of the formed sheets after bending (discussed further in Section 6.2.1). The external dimensions of the cold plate are shown in Table 6-1.

Table 6-1: External cold plate dimensions

Height [mm]	Length [mm]	Thickness [mm]
210	250	30

A list of the full test rig requirements, purpose of the requirements and Sections within this Chapter that demonstrate evidence of meeting these requirements is shown in Table 6-2.

Table 6-2: Test rig requirements, purpose and supporting evidence of meeting the requirements

Test rig Requirement	Purpose of the requirement	Evidence the requirement has been met
1) Enable fin cooling on the front and back surfaces of large format pouch cells, where	Enables for a comparison between the thermal performance of fin materials with different thermal	Discussed in Section 6.6.1.

	equal cooling on both the surfaces is achieved.	conductivity under double side pouch cell surface cooling.	
2)	Test rig must be capable providing fin cooling on multiple cells at once during the experiment.	Increase the number of fin cooled cell samples to increase the significance of the results.	Shown in Section 6.3.
3)	Fin cooled cells must be insulated from one another.	Achieve independent samples.	Discussed in 6.6.2.
4)	Minimise the formation of contact resistances between the cell surface and fin body, and between the fin contact length and external cold plate.	Improve the degree of cooling onto the cell.	Discussed in 6.6.3.
5)	Provide a means to electrically connect the cells to the cycler equipment.	Allow for the cell to be cycled.	Tabs clamped within brass buss bar blocks. Shown in Section 6.3.
6)	Provide support for the cells and fins.	Ensure that the cells or fins do not move during the experiment.	Insulating material and side pressure bag compresses the cell-fin stack. Shown in Section 6.3.

6.2.1 FIN MATERIALS AND THERMOCOUPLE PLACEMENT

The k-core, copper and aluminium fins for the experiment are sized based off the schematics of the 53 Ah cell manufactured by XALT Energy, which is shown in Figure 6-3 (a). The measured dimensions of the real cell are shown in Figure 6-3 (b), which displays additional detail of the cell structure particularly around the tab area.

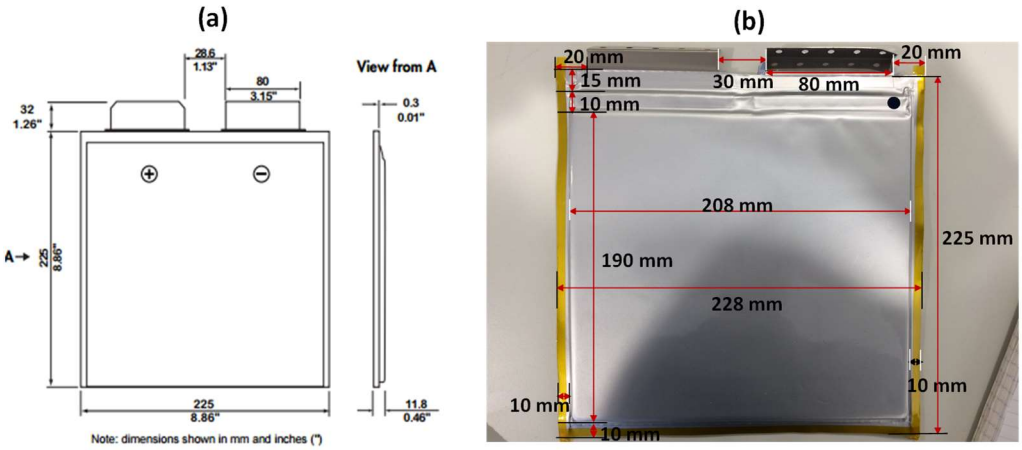

Figure 6-3: (a) Schematic of the cell given in the cell manufacturer sheet [171] *(b) Measured dimensions of the real cell*

The dimensions and weight of the fin samples are shown in Table 6-3, all of which have been manufactured with a thickness requirement of 0.5 mm, where for the k-core fin the internal APG layer is specified as 0.5 mm.

Figure 6-4 (a) reveals the APG core contained within the sleeve, together with the aluminium skin layer encapsulant. A side-by-side comparison between the k-core fin and reference aluminium fin is also shown in Figure 6-4 (b). Due to the fragility of the APG, the k-core fin requires a minimum bend radius of 7.5 mm (as specified by Thermacore) to form the contact length onto the cold plate. The bend radius for the k-core samples is achieved by welding an iron rod (15 mm in diameter) onto a flat metal plate such that the weld joint forms a flat surface. The k-core fin is carefully formed over the rod to achieve the flat 25 mm of contact following completion of the bend. For the baseline copper and aluminium sheets, a perpendicular bend is achieved with a hand operated sheet metal break, again enabling 25 mm of flat contact length. The 25 mm of contact length is chosen to maximise the contact surface area of the fin edge onto the cold plate, given constraints on the available surface area offered by the cold plate.

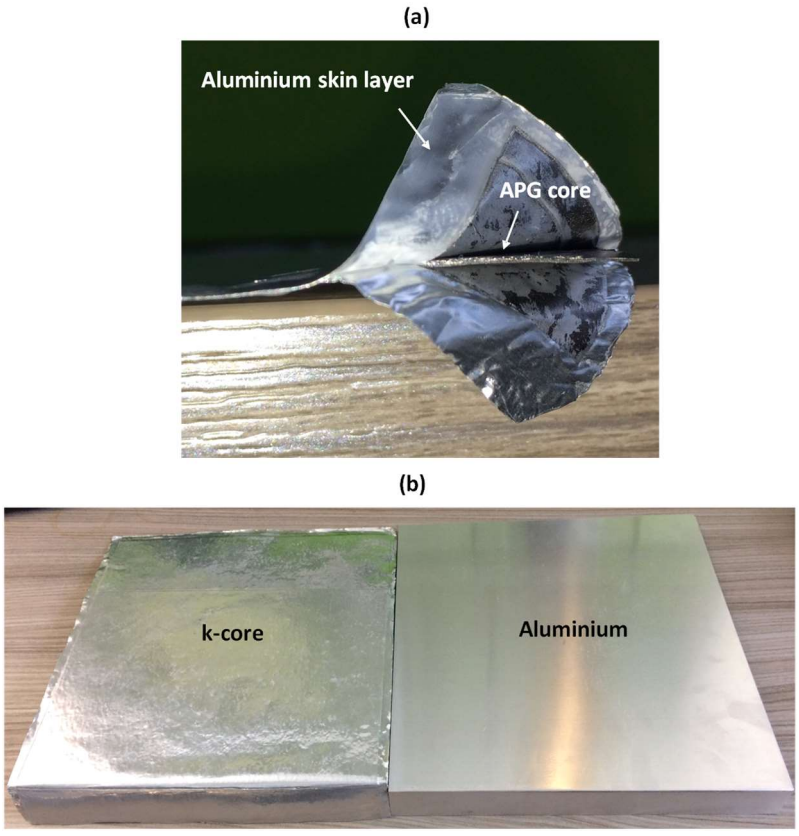

Figure 6-4: Fin materials used with (a) k-core fin with revealed APG core and skin layer (b) side-by-side comparison of k-core fin and aluminium fin

The laminate foil on the k-core fin gives a boundary of 5 mm around the APG core, which is neglected in the height and length dimensions shown for the fin body and contact length sections. For measuring and weighing, the average value over the 6 samples is taken. A micrometre with an accuracy of 0.01 mm is used to measure the thickness of the fin sheets, where 3 measurements are taken for each sample (two on the fin body and one on the bent contact edge). The average over all measurements and samples is taken to represent the fin thickness. The APG core thickness and aluminium skin is also measured separately, with values of 0.52±0.01 mm for the APG core and 0.08 ±0.01 mm for the skin layer.

To track the temperature evolution of the fin in contact with the cell during operation, T-type thermocouples are located across the fin surface. Direct thermocouple attachment onto the cell surface is not attempted due to the creation of air gaps which would hamper the heat transfer into the fin, in addition to safety concerns of the pin point thermocouples piercing the pouch cell when under stack compression. Figure 6-5 (a) highlights the 15 thermocouple (TC) arrangement adopted for the k-core fin, and Figure 6-5 (b) the arrangement adopted for the copper and aluminium reference case fins. With reference to Figure 6-6 (e), this thermocouple placement is only present on the front fins for each cell due to limitations in the number of measuring channels. On the back fins, 3 thermocouples are placed at locations 5,7, and 9 to check for parity between readings on both fins. This arrangement is shown in Figure 6-5. The placement of the thermocouples seek to provide measurements that approximate the maximum fin temperature at TC5 (furthest from the cooling source) and the maximum fin temperature gradient (TC5-TC9), of which are key thermal metrics to gauge the performance of the thermal management system.

Table 6-3: Measured fin properties of the experimental samples

Fin material	Fin body dimensions			Fin contact length dimensions			Total fin weight
	Height [mm]	*Length [mm]*	*Thickness [mm]*	*Height [mm]*	*Length [mm]*	*Thickness [mm]*	[g]
Copper	220±1	235±1	0.52±0.01	220±1	25±1	0.52±0.01	258±1
Aluminium	220±1	235±1	0.50±0.01	220±1	25±1	0.50±0.01	74±1
k-core (not including laminate aluminium boundary edges in length and height measurments)	210±1	220±1	0.68±0.01	210±1	25±1	0.68±0.01	74±1

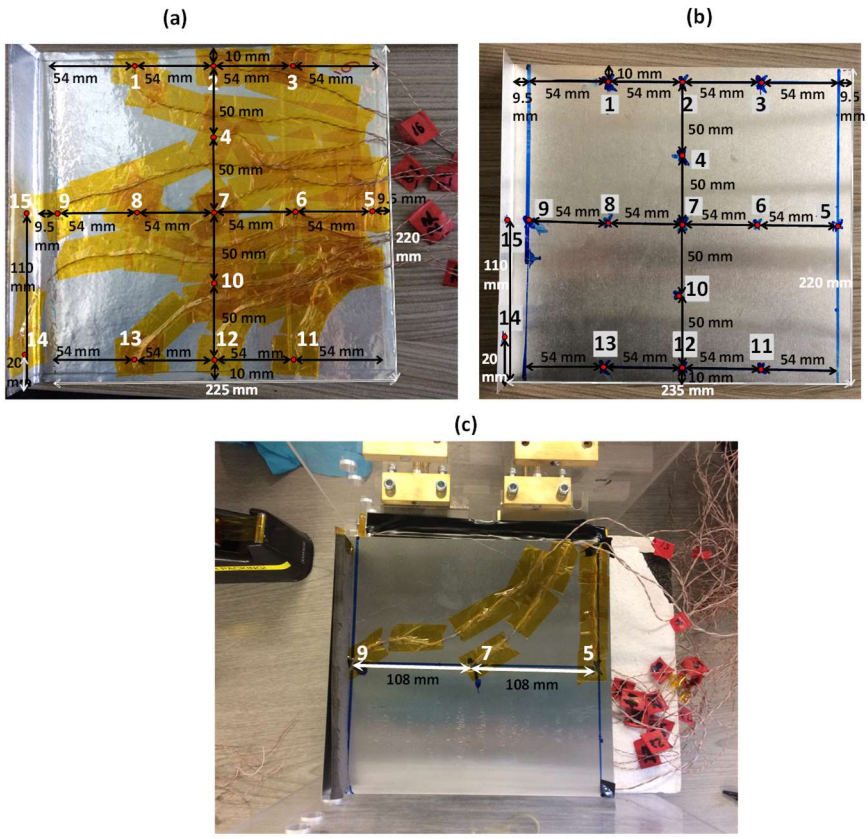

Figure 6-5: Thermocouple placement on (a) front k-core fin (b) front aluminium/copper fin (aluminium fin shown) (c) back fin (aluminium fin shown)

6.3 TEST RIG ASSEMBLY PROCEDURE

In this section, the assembly of the test rig is separated into 4 key stages (each discussed in turn). These systematic stages are:

- Stage 1 – Insertion of the first insulation layers and metallic cooling fin
- Stage 2 – Insertion of the first cell
- Stage 3 – Insertion of remaining cells, side air wedge bag and cold plate
- Stage 4 - Electrical and thermal interconnections

6.3.1 STAGE 1 – INSERTION OF THE FIRST INSULATION LAYERS AND METALLIC COOLING FIN

With reference to Figure 6-6 (a), the test rig shell consisting of multiple Perspex walls is first attached together with threaded screws. During the first stage of assembly, one of the outer walls is removed to enable top down access to the rig. The first layer of insulation material is added, which consists of four 5 mm thick polystyrene sheets placed in contact with the test rig outer wall. Four sheets are chosen to provide increased compactness.

Following the addition of the polystyrene sheets, a 20 mm thick slab of FOAMGLAS is added as the second distinct layer. The FOAMGLAS material is highly insulative in nature with a thermal conductivity of 0.046 W.m^{-1}.K^{-1} at 40 ℃ [180]. A further polystyrene sheet is placed in between the FOAMGLAS and subsequently stacked metallic cooling fin. This is to protect the fin from the abrasive nature of the FOAMGLAS which is comprised of sintered glass particles. In between the bent edges of the fins and FOAMGLAS, a compressible buffer foam layer is added (10 mm thick and 20 mm in width) to protect the thermocouples along the fin edge from the FOAMGLAS when the rig is pressurised.

Busbar blocks are attached to the roof of the test rig. The busbars are comprised of two brass blocks, where one block contains an M8 screw thread. In this block, the M8 brass screw is welded into the thread to ensure the creation of minimal resistance. The protruding length of the screw from the busbar is 5 cm in length.

Figure 6-6 (a) displays the completed Stage 1 arrangement following the addition of the metallic cooling fin (k-core fin shown in this instance). The cooling fin is slotted on top of the outer polystyrene sheet, with the bent fin edge supported by the strip of buffer foam.

6.3.2 STAGE 2 – INSERTION OF THE FIRST CELL

With reference to Figure 6-6 (b)-(d), following placement of the first fin (front fin) the first cell is added. The remaining fin (back fin) is placed in contact with the other surface of the cell followed by a 5 mm polystyrene sheet and subsequent 20 mm thick FOAMGLAS slab. The cell tabs are positioned within one busbar block, with the second block added on top and clamped to the other block using screws. The cell is positioned such that the aluminium positive tab of the cell is located near the cooling edge of the fin, with the negative copper tab located at the rear of the test rig furthest from the cooling source. This stacking arrangement is repeated for the remaining two cells.

6.3.3 STAGE 3 – INSERTION OF REMAINING CELLS, SIDE AIR WEDGE BAG AND COLD PLATE

With reference to Figure 6-6 (e)-(g), upon completion of stacking with the remaining cells, an air wedge bag is added in between the outer FOAMGLAS slab and test rig wall to apply side pressure on the stack. The side pressure compresses the stack to increase thermal contact between the cooling fin and cell surfaces. The air wedge bag is hand operated, where the applied pressure is controlled via the use of the pressure dial. The pressure is applied manually until the dial reads 0.2 bar, which is the maximum pressure allowed until the test

rig wall begins to bulge. This pressure is used for all experiments to ensure parity between tests.

On the side walls of the test rig, sections are machine cut to accommodate the inlet and outlet hoses of the cold plate. An additional cut is also made on one side to accommodate the air wedge bag pressure line. The cold plate is placed into the front face of the test rig as viewable in Figure 6-6 (f). A back Perspex panel is added to the rear of the rig to provide a rigid surface for pressure to be applied. Buffer foam is added onto the rear of the FOAMGLAS slabs in between the back Perspex panel to further distribute the pressure equally between the slabs. Four clamps (only two shown in Figure 6-6 (f)-(g)) are hand tightened to push the cold plate onto the front of the stack, in turn providing pressurised contact of the fin edge onto the cold plate to minimise thermal contact resistances.

6.3.4 STAGE 4 – ELECTRICAL AND THERMAL INTERCONNECTORS

With reference to Figure 6-6 (h)-(j), for testing, the rig is transferred to a climate chamber (VT 3050). The inlet and outlets of the external cold plate are connected to a LAUDA unit, where a flowrate of 10 $L.min^{-1}$ of a water-glycol mixture is pumped through at a regulated set-point temperature of 25 ℃. Greater flowrates are not chosen as to avoid over pressuring the connections at the cold plate inlets and outlets to reduce the risk of leakage. The assumption that the chosen cold plate flowrate is sufficient to provide uniform cooling on each of the bent fin edges is checked further in Section 6.6.

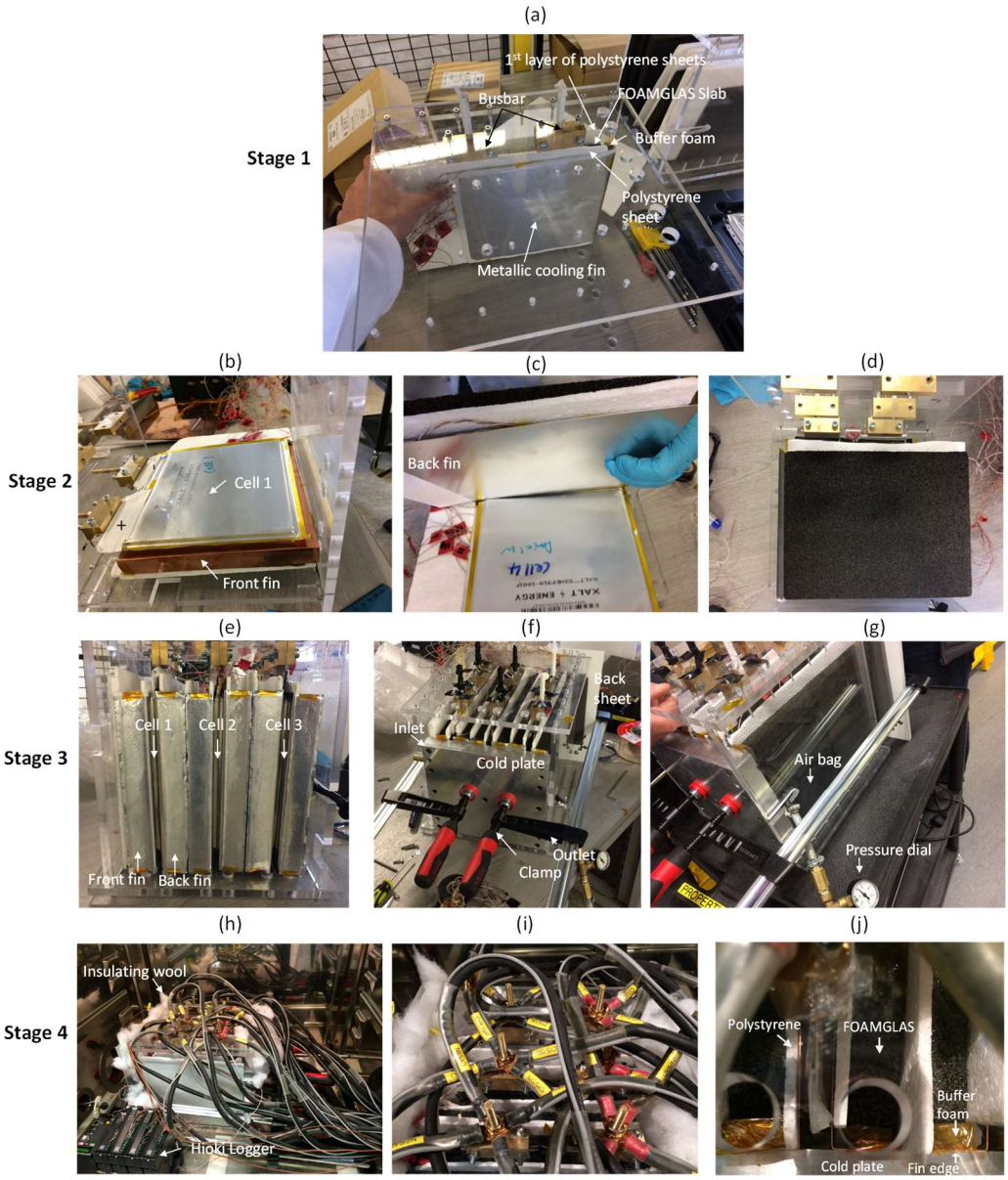

Figure 6-6: Images of the test rig during its different stages of assembly with (a) Stage 1 assembly with the first front fin insert (b) addition of the first cell (c) addition of the first back fin (d) addition of the partitioning insulation material (e) completed stacking arrangement (with k-core fins) (f) addition of the front cold plate (g) side view of the test rig showing the air wedge bag position (h) fully assembled test rig within the climate chamber with thermal and electrical interconnectors in place (i) top view of the load cable arrangement (j) exploded view of the contact between the fin edge and external cold plate

The electrical load cables on the cell are connected to the protruding screws from the cell busbars. A total of 4 cables per busbar is used to accommodate peak currents of up to 400 A. The load cables are tightened onto the screw via the use of a brass washer, brass nut and torque wrench until the applied force reading from the wrench reaches 45 N.m. The positioning of the load cables is shown in Figure 6-6 (i).

Figure 6-6 (h) displays the complete arrangement of the test rig within the climate chamber. Insulation (plastic wool) is added to the exposed portions of the test rig where large air gaps

exist to limit the effect of convective cooling from the climate chamber ambient. The data logger tracking the thermocouple temperature (Hioki 8423 Memory HiLOGGER with 8948 Voltage/Temp units) is also viewable. The data logger sampling rate is set to 1 s under continuous monitoring mode.

The four clamps are distributed symmetrically near the top and bottom portions of the cold plate to provide uniform pressure onto the fin edges. Figure 6-6 (j) displays an exploded view of the fin contact onto the cold plate.

Safety thermocouples (J-type) are feed through the insulating wool and placed on the rear of the cell edge not in contact with the cooling fin. The safety thermocouples are utilised by the cell cycler software to ensure that a temperature limit of 65 ℃ is not exceeded during testing. The climate chamber ambient is set to retain a constant temperature of 25 ℃ throughout testing.

6.4 TEST RIG THERMAL MODEL

In this section, a baseline thermal model of the test rig (that includes the cooling fin, a half cell, cell tabs and busbar) is developed to act as a tool for validation upon which to develop a more involved thermal model for further simulation studies. Given that the geometry of the aluminum and copper fins are similar (aside from the slight discrepancy in measured fin thickness of 0.02 mm between the two), one geometric model is developed using these geometries and a separate model is developed for the k-core material. The thermal model of the experiment is developed using COMSOL Multiphysics version 5.2a, which is also used to model the heat transfer physics. The assumptions used to model the cell are as discussed previously in Section 5.2.1 of Chapter Five and therefore will not be repeated here. In Summary, Equation (56) is used to model the heat transfer through the cell, tabs and cooling fin. The tab heat generation rate estimation is treated in the same manner. The estimation of the cell body heat generation rate is discussed in Section 6.4.4. Thermal contact resistances between the cell and cooling fin are not considered in the thermal model. The suitability of this assumption is discussed further in Section 6.6.3

6.4.1 COPPER AND ALUMINUM FIN COOLED GEOMETRY

As discussed within [73], to reduce the size of the thermal model and to improve computational time, symmetry planes are employed. This involves modelling half a cell to

utilise the symmetry plane along the central axis of the cell given that there exists a cooling fin on both the front and back of the cell.

The modelling of the cell body and tabs follows the same approach as outlined in Section 5.2.1 of Chapter Five. The determination of the tab cone and fin height is based off the dimensions in Figure 6-3 (b), where the concealed portion of the tab that shares an approximate thickens to the exposed portion is measured as 15 mm in height. In the geometric model, the fin portion of the tabs is taken as the addition of the exposed height and the concealed height, which gives a total height of 47 mm. The remaining folds of the tab prior to the fin portion are approximated as an extruded triangle (with a height of 10 mm). The cell is treated as a simple rectangle.

A schematic of the half-cell geometry with the cooling fin for copper and aluminum materials is displayed in Figure 6-7 (b). The bend radius portion of the fin is set as 1 mm to approximate that of a near perpendicular bend. A full list of values for the dimension parameters used in the copper and aluminum fin geometric models is included in Table 6-4.

The convection coefficients applied on the surfaces of the cell used in the thermal model are shown in Figure 6-7 (d). These are discussed further in Section 6.4.6.

6.4.2 K-CORE FIN COOLED GEOMETRY

The schematic of the half-cell geometry for the k-core fin is displayed in Figure 6-7 (a). To simplify the model, the APG core is only included, where the geometry of the skin aluminum laminate layer is ignored due to its very thin relative size. Due to the absence of the skin layer, the full length of the APG core is clamped onto the cold plate, therefore, there is an absence of a partition at the top of the fin as in the case of Figure 6-7 (c). The dimensional parameters used in the k-core fin geometric model are contained within Table 6-4.

Table 6-4: Dimensions of the cell and fin geometry used in the baseline thermal model

Parameter	Definition	Aluminum fin model	Copper fin model	k-core fin model
H_{cell} [mm]	Height of the cell body	190.0	190.0	190.0
$H_{tab,fin}$ [mm]	Height of the tab fin	47.0	47.0	47.0
$H_{tab,cone}$ [mm]	Height of the tab base	10.0	10.0	10.0
H_{Screw} [mm]	Height of the protruding screw	50.0	50.0	50.0
H_{bus} [mm]	Height of the busbar block	25.0	25.0	25.0
H_{offset} [mm]	Distance between the base of the fin and the base of the cell	15.0	15.0	15.0
H_{fin} [mm]	Height of the cooling fin	220.0	220.0	210.0

W_{bus} [mm]	Width of the busbar block	60.0	60.0	60.0
W_{offset} [mm]	Distance between the edge of the cell and the edge of the fin	15.0	15.0	10.0
W_{tab} [mm]	Width of the tab	80.0	80.0	80.0
W_{fin} [mm]	Width of the cooling fin	235.0	235.0	220.0
W_{cell} [mm]	Width of the cell body	208.0	208.0	208.0
t_{fin} [mm]	Thickness of the cooling fin	0.50	0.52	0.52
r_{bend} [mm]	Bend radius of the fin bend junction	1.0	1.0	7.5
t_{offset} [mm]	Distance between the outer fin bent edge and nearest cell edge	13.0	13.0	9.5
C_w [mm]	Contact length of the bent fin edge onto the cold plate	25.0	25.0	25.0.
t_{cell} [mm]	Thickness of the cell	11.8	11.8	11.8
t_{screw} [mm]	Radius of the screw	4.0	4.0	4.0
t_{tab} [mm]	Thickness of the tab fin portion	0.3	0.3	0.3
t_{bus} [mm]	Thickness of the busbar block	10.0	10.0	10.0

6.4.3 3-D THERMAL MODEL EQUATIONS

6.4.4 CELL HEAT GENERATION CALCULATION

Within the cell body, the internal heat generation rate is estimated through the use of a validated 1-D electrochemical model coupled with a 1-D thermal model based on the same 53 Ah cells used in this study [141]. The model has been developed by another researcher within the group and is used through collaboration to provide the heat generation profiles for this analysis.

The 1-D electrochemical model considers a single cell sandwich structure comprised of the negative current collector (copper), negative electrode (graphite), separator layer, positive electrode (NMC) and positive current collector layer (aluminium). A full list of the governing 1-D electrochemical equations (together with the solution procedure for the coupling of the models), boundary conditions and parameters used can be found in [141] and therefore will not be repeated here. In summary, the equations include the electrochemical reaction kinetics, ion transport and charge conservation in the electrolyte and solid particle phases and the material balance for lithium-ions in the electrolyte and solid phases. The 1-D electrochemical model coupled with the 1-D thermal model is used as a simplification in this research to reduce the computational cost of a full 3-D electrochemical model. The heat generation output of the 1-D models is instead used as an input into the 3-D thermal model to provide the full temperature distribution.

The cell heat generation rate that is solved for using the 1-D electrochemical and 1-D thermal model is given by the general energy balance for the battery system as presented by Bernardi et al. [135]:

$$q = q_{irr} + q_{rev} = I.(U_{OCV} - V) - I.T.\frac{\partial U_{OCV}}{\partial T} \quad (62)$$

Where q is the total battery heat generation rate [W], q_{rev} the reversible component of the heat generation [W], q_{irr} the irreversible component the heat generation [W], U_{OCV} the battery open circuit voltage [V] and V the battery cell potential [V].

6.4.5 THERMAL MODEL PARAMETERS FOR THE 3-D THERMAL MODEL

The battery thermal parameters used in the model are presented in Table 6-5.

Table 6-5: Battery thermal model parameters

C_p [J.kg^{-1}.K^{-1}]	ρ [kg.m^{-3}]	M [kg]	k_x [W.m^{-1}.K^{-1}]	k_y [W.m^{-1}.K^{-1}]	k_z [W.m^{-1}.K^{-1}]
1500	2390	1.15	0.28 [119]	30 [122]	30 [122]

Values for k_y and k_z are taken from the experimental range reported by Bazinski et al. [122] (which is consistent with other axial values reported for the thermal conductivity of lithium ion cells [88]), whereby the cross-plane thermal conductivity k_x is taken from experiments carried out by Vertiz et al. [119]. This value is representative of a pouch cell saturated in electrolyte and includes the presence of contact resistances between layers within its effective value. The effective cell density of the battery body is calculated from the volume of the battery and its weighed mass.

Given that the heat capacity of the cell has not been measured directly, and is a scope for further work, a static value of 1500 J.kg^{-1}.K^{-1} is assumed in all subsequent thermal modelling, which is within the range of values reported for the effective heat capacity of lithium-ion pouch type batteries [181]. The applicability of this value is further analysed through a sensitivity study on the values of the cell heat capacity which is contained in Section 6.8.

For the aluminum and copper fins, the material displays isotropic thermal conductivity. However, the k-core fin displays anisotropic thermal conductivity. With reference to the coordinate scale in Figure 6-7, the thermal parameters for the fin materials used in the different fin domains of the thermal model are included in Table 6-6. Values for the anisotropic thermal conductivity of the k-core fin are provided by the sponsor company.

Table 6-6: Thermal parameters for the fin materials employed in the thermal model

Fin body thermal parameters					
Fin material	C_p [J.kg^{-1}.K^{-1}]	ρ [kg.m^{-3}]	k_x [W.m^{-1}.K^{-1}]	k_y [W.m^{-1}.K^{-1}]	k_z [W.m^{-1}.K^{-1}]
Copper	385	8960	385	385	385
Aluminium	900	2700	220	220	220
k-core	702	2260	10	1100	1100
Fin bend radius thermal parameters					
Fin material	C_p [J.kg^{-1}.K^{-1}]	ρ [kg.m^{-3}]	k_x [W.m^{-1}.K^{-1}]	k_y [W.m^{-1}.K^{-1}]	k_z [W.m^{-1}.K^{-1}]
Copper	385	8960	385	385	385
Aluminium	900	2700	220	220	220
k-core	702	2260	1100	1100	1100
Fin bent edge thermal parameters					
Fin material	C_p [J.kg^{-1}.K^{-1}]	ρ [kg.m^{-3}]	k_x [W.m^{-1}.K^{-1}]	k_y [W.m^{-1}.K^{-1}]	k_z [W.m^{-1}.K^{-1}]
Copper	385	8960	385	385	385
Aluminium	900	2700	220	220	220
k-core	702	2260	1100	10	1100

For the bend radius portion of the fin, the thermal conductivity is not specified in curvilinear coordinates for the k-core fin. Therefore, it is assumed that in the bend radius the thermal conductivity is isotopic with the same value as in the in-plane thermal conductivity. As discussed within Section 6.10, validation of this assumption constitutes one area of further work from this research.

6.4.6 CONVECTION COEFFICIENTS

Aside from the insulation condition present along the cell central axis, exterior convective boundary conditions are specified on the exposed surfaces of the cell, fin and tabs. Their definition and values are shown in Table 6-7.

A value of 750 W.m^{-2}.K^{-1} is chosen for h_1, which is in the region achievable from liquid cooling using water-glycol [78]. For the exposed portion of the fin not clamped onto the cold plate with the aluminium and copper fins and also for the cell tab and edges of the fin, a value for h_2 of 10 W.m^{-2}.K^{-1} is chosen to represent natural convection with the ambient air [107]. Natural convection is specified on these surfaces given that they are protected by the test rig roof from the forced convection climate chamber air circulation effects. For the exposed tab busbars, a value of 25 W.m^{-2}.K^{-1} is given for h_4 to account for the climate chamber forced convection as described in [164]. To account for the edge cooling effect on the top, bottom and side edges of the pouch cell [182] a value of 20 W.m^{-2}.K^{-1} is specified for h_5.

Table 6-7: Heat transfer coefficient values used in the thermal model

h	Definition	Value [$W.m^{-2}.K^{-1}$]
h_1	Heat transfer coefficient along the clamped fin edge onto the cold plate	750
h_2	Heat transfer coefficient on the edges of the fin, exposed tabs and bend radius portion of the fin	10
h_3	Heat transfer coefficient on the exposed fin body not in contact with the cell surface	1.1
h_4	Heat transfer coefficient on the tab busbar blocks and protruding screw	25
h_5	Heat transfer coefficient on the edges of the cell body	20

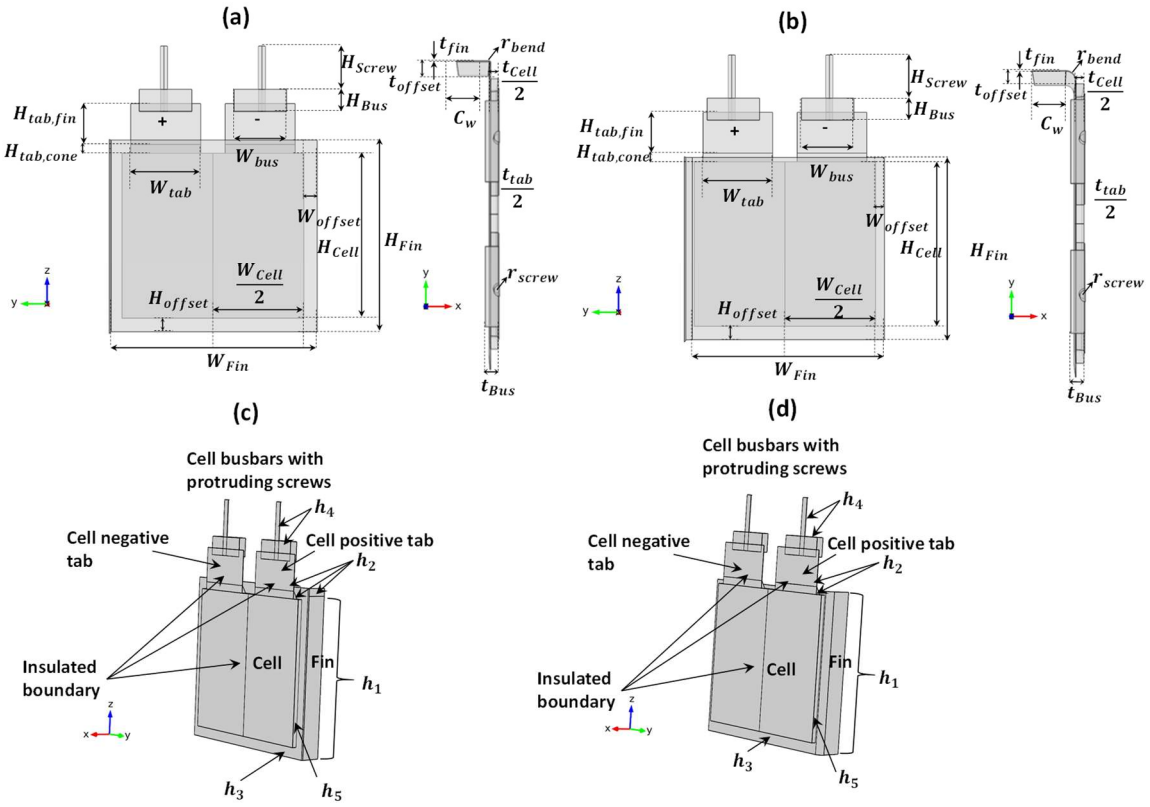

Figure 6-7: Geometry of the cell and fins used in the thermal models with (a) schematic of the aluminium and copper model geometry (b) schematic of the k-core model geometry (c) location of the applied convective coefficients for the aluminium and copper model (d) location of the applied convective coefficients for the k-core model

Within an ideal set up with perfect thermal insulation, the value for h_3 on the surfaces of the cooling fin not in contact with the cell body would be zero. However, to account for heat transfer between the fin and surrounding insulation slabs, a non-zero convection coefficient is present. A value for h_3 of 1.1 $W.m^{-1}.K^{1}$ is assumed to represent the non-ideal thermal insulation. The locations of the applied convective coefficients for the cell boundary conditions are viewable in Figure 6-7 (c)-(d).

6.4.7 MESH INDEPENDENCE TEST AND SOLVER CONFIGURATION

The time dependent solver within COMSOL is employed as the solution method for the thermal model. The relative tolerance for the solver is kept at the default value of 0.01, where the absolute tolerance for the temperature field is also kept at default with a value of 0.001. A strict time step of 1 s is set as the maximum time step for the solution to match the resolution of the input heat generation profile. The maximum number of iterations per time step is set as 50.

A mesh independence study is performed on the model to ensure that the chosen mesh size is independent of the outputted values. The mesh independence study is performed using the steady-state solver to reduce the computational time. In this case, average values for the half-cell heat generation rate, aluminium tab and copper tab are set as 22.88 W, 0.979 W and 0.621 W respectively. These values are based on the time averaged heat generation rate from the EV race duty cycle for a complete cell, which is shown in Figure 6-9.

The results of the mesh independence analysis are shown in Figure 6-8. Here, it is observed that increasing the mesh size past 6.62×10^5 elements does not affect the value for the maximum battery temperature, therefore this mesh size is chosen for validation of the test rig thermal model discussed in Section 6.8.

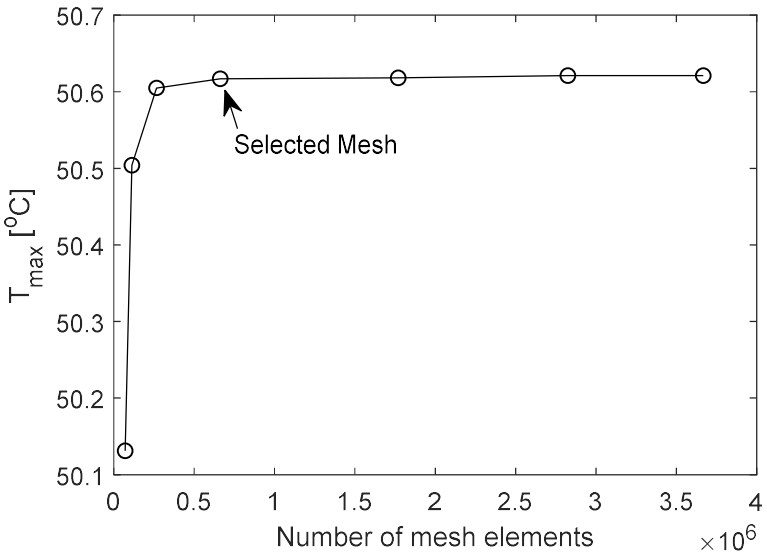

Figure 6-8: Mesh independence test for the test rig fin cooled pouch cell thermal model under the time averaged heat generation rate of the race duty cycle

6.5 EXPERIMENTAL PROCEDURE

To thermally test the performance of the fins, 6 of the unaged 53 Ah cells with a nominal voltage of 3.7 V are subject to 3 loops of a PHEV WLTP Class 3 duty cycle and a separate high-performance race duty cycle (as used in Chapter Five), which are viewable in Figure 6-9 (a)-(b) (negative current denotes discharge and positive current charge). The calculated full cell heat generation profiles are show in Figure 6-9 (c)-(d). Here, it is observed that the time averaged cell heat generation across the race duty cycle is 45.8 W, which is comparable to the simplified averaged heat generation using a static cell resistance of 1.33 mΩ (as discussed in the analysis in Chapter Five) giving 49.2 W.

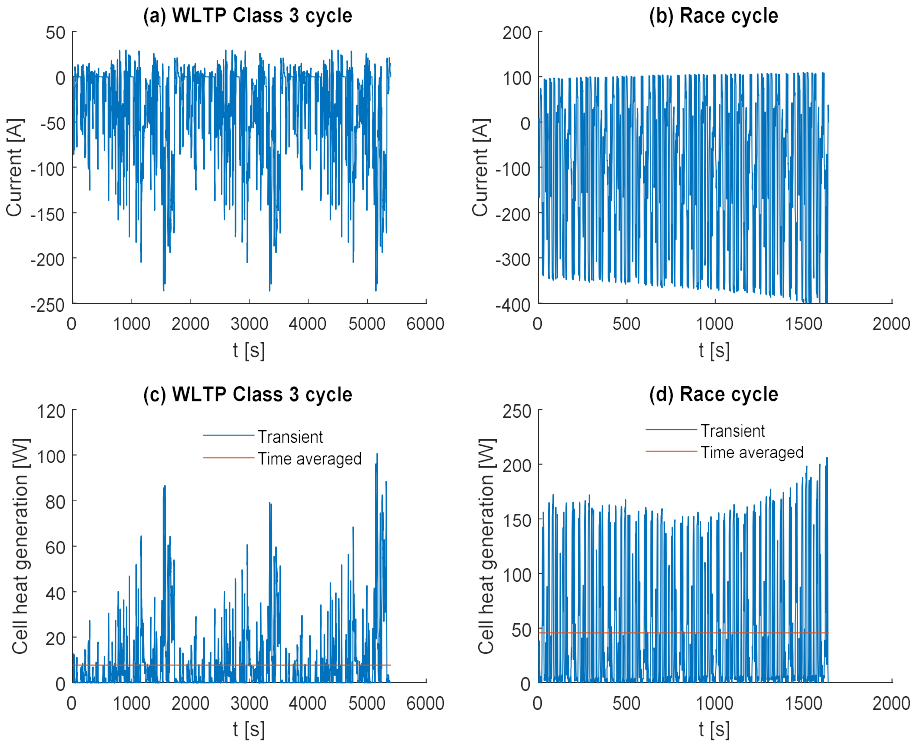

Figure 6-9: Drive cycle data used for the experiment and thermal modelling with (a) WLTP Class 3 current profile (b) Race cycle current profile (c) WLTP Class 3 full cell body heat generation rate (d) Race cycle full cell body heat generation rate

The starting cell SOC for the WLTP and race cycle is 100% and 95% respectively. Standard 1 C, 2 C and 3 C full discharges (from 100-0% SOC) are also analysed to provide further comparisons. The electrical loading conditions considered for the test are summarised in Table 6-8, which also highlights the order in which the testing is conducted as given by the cycle number.

For testing, the cells are initially charged fully to 100% SOC using a constant current constant voltage charging procedure (CC-CV). This involves charging the cell at 53 A constantly until the cell voltage limit of 4.2 V is reached, after which the charging voltage is held at 4.2 A and the current reduced until it reaches 2.65 A (cell nominal capacity/20) where the cell is considered fully charged.

A flowchart displaying the cycling procedure for the k-core and aluminium and copper fins is included in Figure 6-10. Here 'I' is the cell current (which is contained in the first true or false step). Safety header limits are also added in the software (not shown in the simplified flowchart). These included stop conditions for the test if:

- The cell voltage exceeds 4.3 V (to prevent overcharging)
- The cell voltage decreases below 2.6 V (to prevent overdischarging)
- The rate of temperature rises increases by 4 °C.s^{-1} or higher (to prevent thermal runaway)
- A maximum limit on the cell temperature of 65 °C.

The discrepancy in cycles between the k-core fin tests and copper/aluminium fin tests is twofold. Firstly, the k-core fins include a 5 C discharge cycle as the second cycle which results in large peak temperatures between 60-65 °C. This is deemed excessive. Due to safety concerns with the 5 C test using inferior cooling material, it is not executed for the lower conductive aluminium and copper fins. Instead, a 2 C discharge is used for the aluminium and copper fins as the second duty cycle. This is reflected in the cycle. no. displayed in Table 6-8.

Table 6-8: Cell electrical loading conditions used in the experiment

Cycle type	Cycle no.	Starting cell SOC [%]	Peak current (discharge) [A]	Peak current (charge) [A]
1C discharge	5	100	53.0	0
PHEV (16 kWh) WLTP Class 3 drive cycle (3 loops)	4	100	236.3	29.1
2C discharge (copper and aluminium fins only*)	2	100	106.3	0
3C discharge	1	100	159.0	0
Race cycle	3	95	400	109.1

* during the aluminium fin testing cell 6 is cooled by k-core fins to obtain one 2 C sample

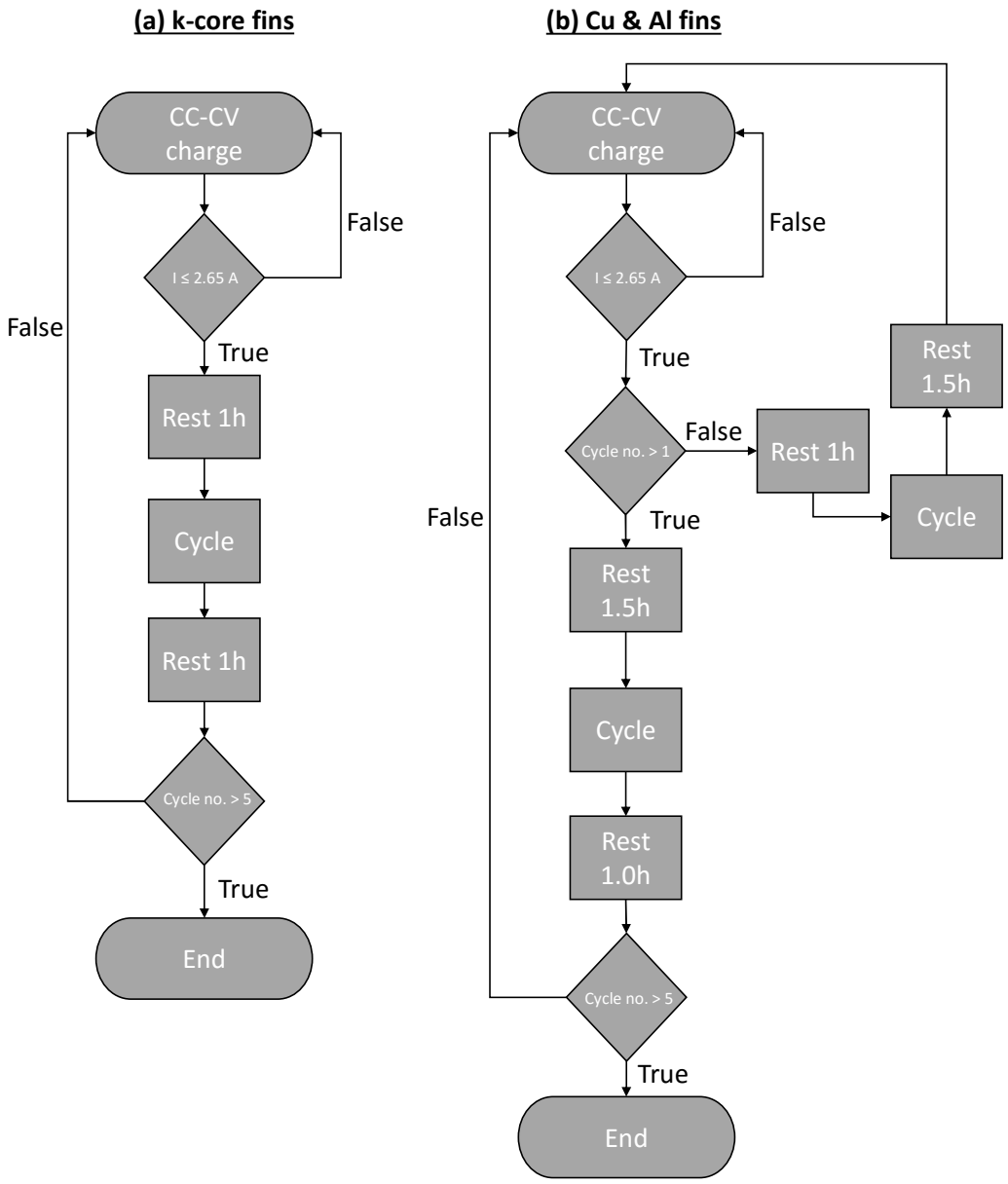

Figure 6-10: Flowchart for the experimental cycling procedure for (a) k-core fins (b) copper and aluminium fins

The second discrepancy is due to an increase in rest period. For the k-core fins, a 1 hour rest period is chosen following both charge and discharging. The justification for this rest time is based on an initial test with cells 1 & 3 on the first day of testing with the k-core fins. This initial test includes the most strenuous duty cycles (3 C, 5 C and race cycle) to maximise the thermal load on the cell. This tests the suitability of a 1 hour rest period in enabling the measured hot spot to reach thermal equilibrium with the climate chamber ambient prior to initiation of the next analysed cycle. The results of the initial resting period test are included in Figure 6-11. Here, the final 1 C discharge does not complete for cell 3 due to an error applied in the cycling code. This was rectified in subsequent testing.

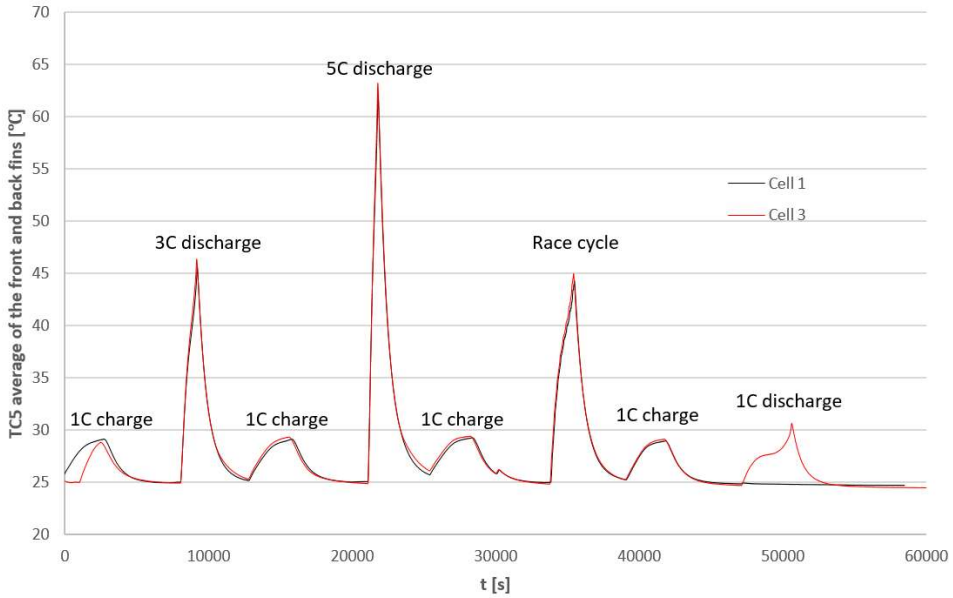

Figure 6-11: Initial resting period test for the k-core fin with cell 1 and cell 3

From Figure 6-11, the 1 hour resting period is sufficient to enable the measured fin hot spot at TC5 to reach thermal equilibrium with the ambient. This resting period is therefore used for the main k-core sheet testing. With reference to Figure 6-10 (b), the rest period following a charge step is increased from 1 h to 1.5 h for the copper and aluminium fin materials. This is performed to allow the measured hot spot additional time to reach thermal equilibrium with the climate chamber ambient for the lower conductive copper and aluminium fins. Rest periods greater than 1.5 h were not chosen to ensure that the full testing length does not exceed 22 hours, due to limitations in the availability of the testing equipment, which required each test to be completed within a 24 hour period

The outputted cycle profiles from the flowchart for the k-core fins and copper/aluminium fins are viewable in Figure 6-12 and Figure 6-13 respectively. In Figure 6-13 It is noted that for the first duty cycle, the preceding rest period following the first charge step is left at 1 hour. This results in the first cycle (the 3 C discharge) only receiving a 1 hour rest period following the initial charge. This was a result of an error in the coding and was not noticed until further post processing following the experiment. The effect of the rest period on the degree of cooling achieved is discussed further in Section 6.6.

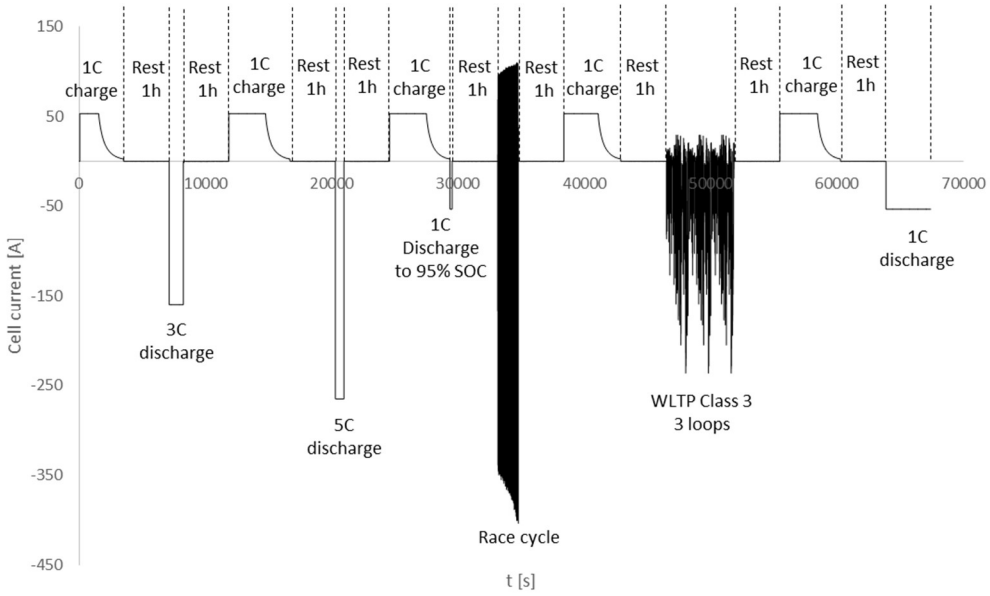

Figure 6-12: Full current testing profile used in the k-core fin experimental runs

Prior to initiation of the testing current profile into the cycler software, the thermal chamber door is closed and sealed where the climate chamber is left to reach its set point temperature of 25 ℃. The Hioki logger is left to track the temperature readings from the thermocouples continuously. The software then initiates the current profile into each of the 3 cells within the test rig, thus commencing the experiment.

To double the number of cell samples from 3 to 6, cells 1,2,3 are switched with cells 4,5,6 (i.e. cell 1->4, cell 2 ->5, cell 3->6) following completion of the first full testing run for that given fin material type. This results in two runs for each of the individual sheet material types. This requires the rig to be dissembled and then reassembled each day. Every two days, the thermocouples are detached from the given fin material and reattached to the next fin material to be analysed. Testing is first conducted with the k-core, copper and finally aluminium fins.

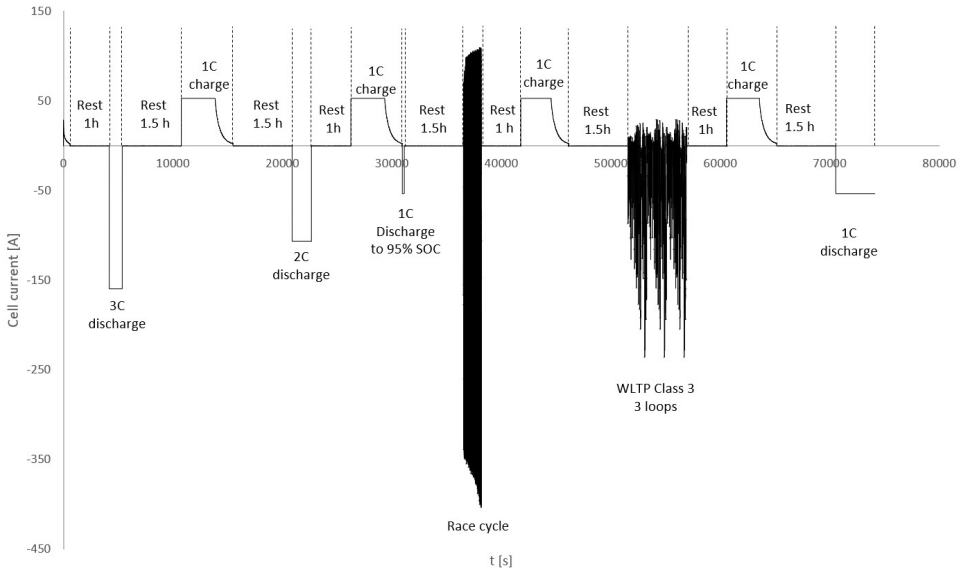

Figure 6-13: Full current testing profile used in the copper and aluminium fin experimental runs

Figure 6-14 displays a front view of the assembled rig (without external cooling plate in place) for each fin material type. Note these images do not display the hand pump with the added pressure dial. As shown in Figure 6-6 (g), this was added prior to transferal into the climate chamber for testing to achieve the 0.2 bar of applied stack pressure for each test.

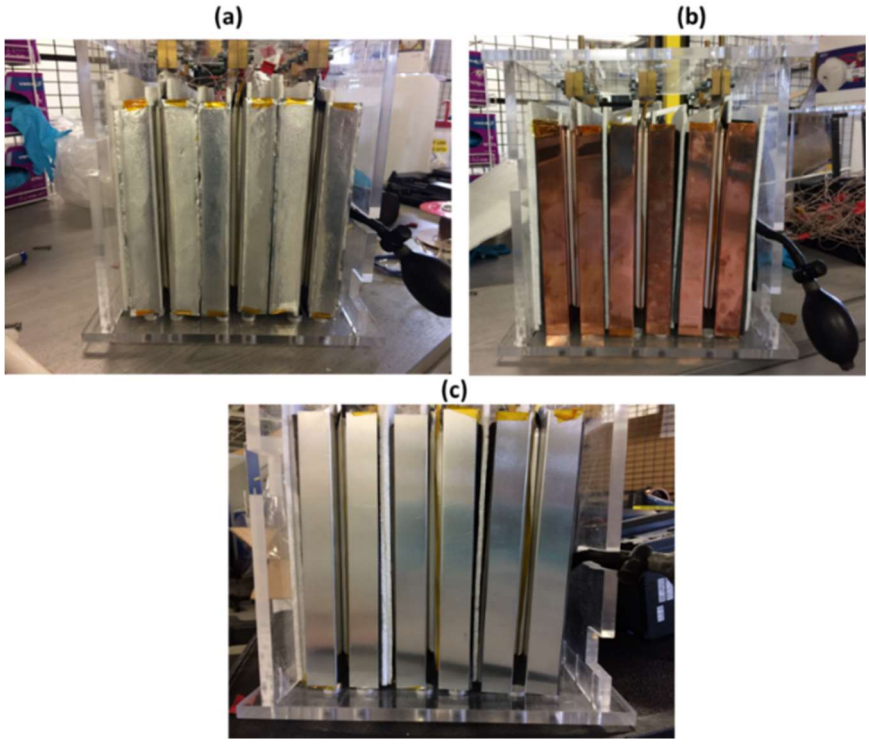

Figure 6-14: Front view of the assembled test rig for each of the fin material types with (a) k-core fins (b) copper fins (c) aluminium fins

6.6 JUSTIFICATION OF ASSUMPTIONS

In this section the assumptions assumed for the test rig are analysed prior to discussion of the full results set. The assumptions are summarised in Table 6-9 and discussed in turn.

Table 6-9: Summary of assumptions for the fin cooled experimental test rig

Assumption no.	Assumption
1	Test rig has been set-up correctly to achieve symmetry along its central axis. Therefore, differences between the readings from the front and back fins at the same TC locations should not show any significant statistical evidence to suggest that they are dissimilar
2	The test rig has been set up correctly to achieve independent isolated samples - The coolant flowrate of 10 $L.min^{-1}$ is therefore sufficient for the experiment. Heat transferred from a fin edge is dissipated quickly and does not impact the heat removal rate of adjacent fins (i.e. negligible neighbouring temperature effects between the cells from the cold plate)
3	The cooling contact of the fin body onto the cell surface is sufficient to minimise thermal contact resistances
4	The resting period of 1.5 hour prior to commencing an analysed cycle is sufficient to enable the copper and aluminium fin measured hot spot to reach thermal equilibrium with the test chamber environment

6.6.1 ASSUMPTION 1 - TEST RIG HAS BEEN SET-UP CORRECTLY TO ACHIEVE SYMMETRY ALONG ITS CENTRAL AXIS

A statistical analysis is conducted to investigate whether there are any significant differences between the temperature readings from the front and back fins that may suggest the symmetry condition is not achieved.

A full statistical analysis on the results for the 3 C discharge test cases has been conducted for the Applied Statistical Methods post module assignment contained in [183]. The 3 C discharge case is chosen given that it contains the most complete cell samples for each fin material, as the 3 C runs avoid issues with the cycler equipment (discussed further in in Section 6.7). In the analysis contained within [183], the fin material type A, B and C represent the aluminium, copper and k-core fin respectively. The results from the analysis will not be repeated in full here, however, a brief overview is presented for completeness.

A paired student t-test reveals that there are no significant differences between the thermocouple readings at locations TC5 and the difference between readings from TC5-TC9 of the front and back fins at the $\alpha = 0.05$ level i.e. there is a 5% risk that a differences exist. This is the case for all the tested fin materials, therefore, there is statistical evidence supporting that the rig has been assembled (for cells 1, 2, 3) and re-assembled (for cells 4, 5, 6) in a manner to achieve the desired symmetry condition. The results of the t-test analysis for the TC5 reading and TC5-TC9 values are contained in Appendix A.8.

6.6.2 ASSUMPTION 2 – THE TEST RIG HAS BEEN SET UP CORRECTLY TO ACHIEVE INDEPENDENT ISOLATED SAMPLES.

An exploratory data analysis also contained within [183] reveals that no outliers are observed in the data for either the maximum fin temperature or the maximum fin temperature gradient measurements. This is the case for all fin material types for the final temperature measurements at the end of the 3 C discharge condition. Generated box plots highlighting the results for the aluminium, copper and k-core fins are viewable in Appendix A.9.

As no outliers are observed from the boxplot for all the back fin samples, front fin samples, pooled data (from all front fin + back fin samples), batch A samples (pooled results from Cells 1,2 & 3) and batch B samples (pooled results from Cells 4,5,6), there is no immediate evidence to suggest that the data from the cell samples are dissimilar from one another. This supports the assumption that the test rig has been set-up correctly to achieve independent samples within each batch. Full transient profiles of the temperature measurements averaged over the front and back fins for each sample is contained within Appendix A.10 for each electrical loading condition. The strong agreement between each of the obtained samples also reaffirms this assumption

6.6.3 ASSUMPTION 4 - THE COOLING CONTACT OF THE FIN BODY ONTO THE CELL SURFACE IS SUFFICIENT TO MINIMISE THERMAL CONTACT RESISTANCES

As it is not possible to place thermocouples directly onto the cell surface, a thermocouple is placed on the edge of the cell for one of the aluminium fin runs to analyse whether there is a noticeable difference between that reading and the reading from thermocouples at location TC5. Figure 6-15 displays the location of the thermocouple on the edge of the cell.

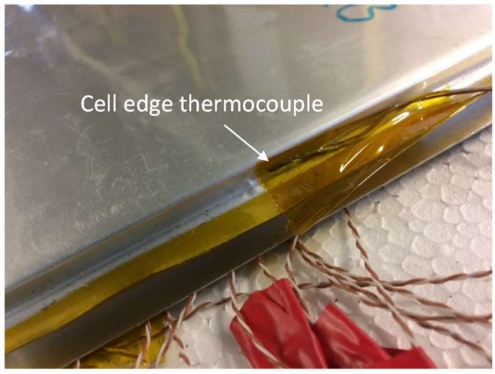

Figure 6-15: Placement of thermocouple onto cell edge near the location of TC5

The comparison between the thermocouple on the edge of the cell and the average value for TC5 from both the front and back fins is shown in Figure 6-16.

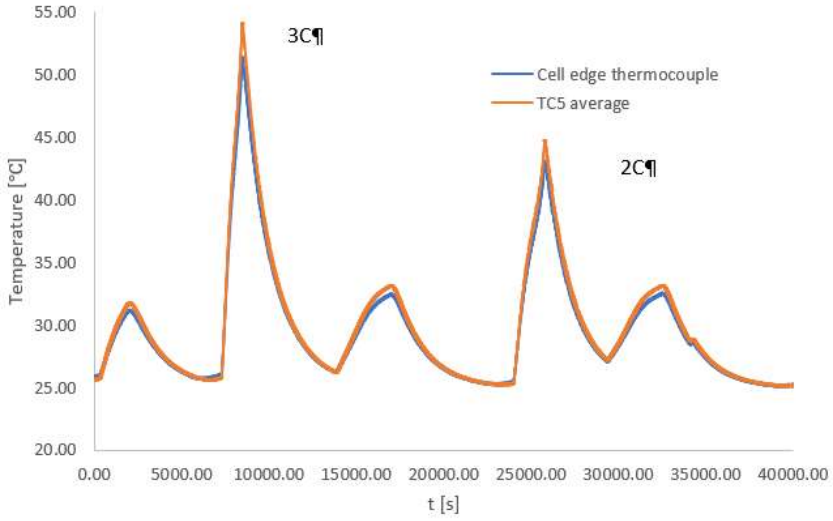

Figure 6-16: Comparison between the average value of TC5 from the front and back fins to the edge thermocouple for cell 1 with the aluminium fins

Figure 6-16 highlights that there is good agreement between the TC5 temperature readings and the edge thermocouple temperature reading. The maximum percentage difference between the two is 5.0%, whereby the edge thermocouple reading is slightly lower than that on the fin at TC5. This may be due to the additional cooling experienced on the cell edge given that it is exposed to the surrounding air channel at the rear of the test rig. This result points towards strong contact being present between the cooling fin and cell surface, as if the fin TC5 reading were lower than the edge thermocouple on the cell, this would imply a large contact resistance between the fin and cell surface. Given that this is not the case, the assumption that the thermal resistance between the cell and fin surface is negligible appears

to be justifiable. In addition, the transient thermal responses of the thermocouple readings from the individual cell samples during the race duty cycle contained within Appendix A.10 highlight that even very small temperature fluctuations are measurable. If poor contact were present, this information would not likely not be of sufficient resolution to capture such small transients.

6.6.4 ASSUMPTION 5 -THE RESTING PERIOD OF 1.5 HOUR PRIOR TO COMMENCING AN ANALYSED CYCLE IS SUFFICIENT TO ENABLE THE COPPER AND ALUMINIUM FIN MEASURED HOT SPOT TO REACH THERMAL EQUILIBRIUM WITH THE TEST CHAMBER ENVIRONMENT

An example of the full output temperature profile of the TC5 average between the front and back fins for the cell 4 sample during the copper fin test is resented in Figure 6-17. Here, it is observed that the hot spot fin temperature reaches 25 ℃ prior to the imitation of each analysed test run (even for the starting 3 C run where the resting period was 1 hour in error).

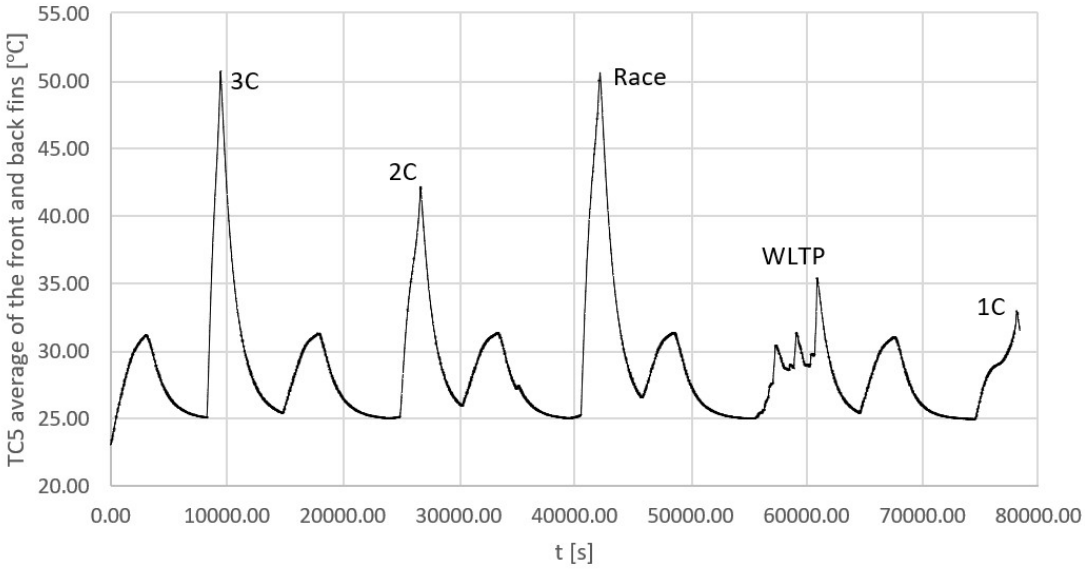

Figure 6-17: Full temperature profile at TC5 for cell 4 using the copper fins

The subsequent result for the aluminium fin cell 4 sample is shown in Figure 6-18. Here, it is observed that for the 1 hour resting period prior to the 3 C discharge, the TC5 reading average does not exactly reach 25 ℃, where instead the value is 25.5 ℃. For the remaining cycles where the rest period is extended to 1.5h, the hot spot has further time to cool, reaching values of 25.2℃. Ideally, a longer rest period is required to reach exactly 25.0 ℃. Therefore, this discrepancy of 0.5 ℃ for the starting point of the 3 C discharge between the aluminium and other more conductive fins may add a degree of variance between

comparison tests, although as the value is only on the order of 0.5 ℃ it is expected to be small.

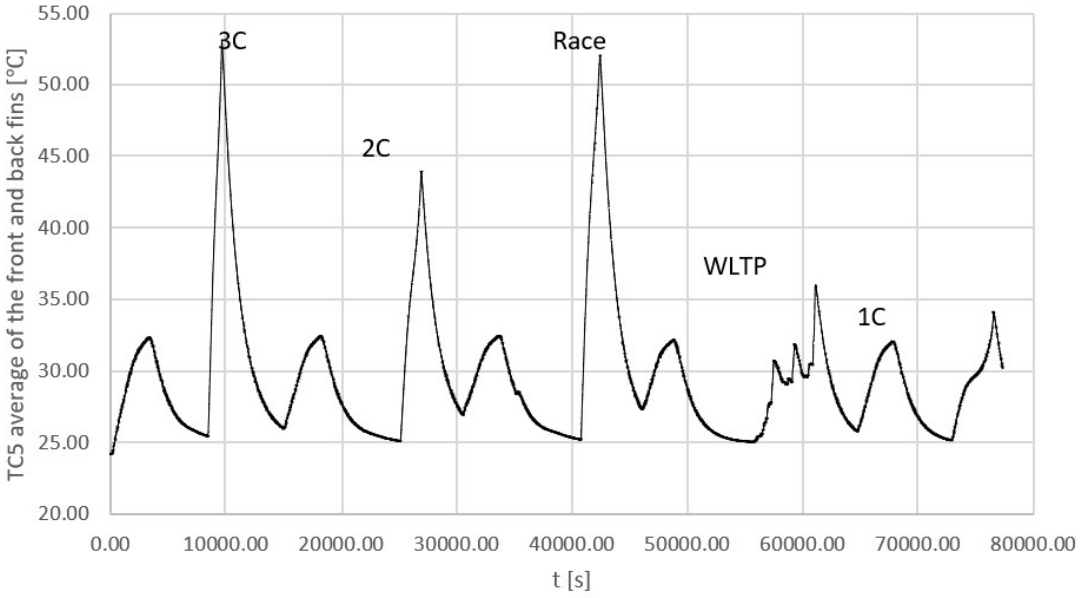

Figure 6-18: Full temperature profile at TC5 for cell 4 using the aluminium fins

6.7 EXPERIMENTAL RESULTS

The experimental temperature readings on the fin surface at locations TC5, and the difference between TC5 and TC9, for all analysed electrical loading conditions and fin materials are shown in Figure 6-19, where marker points are shown at increments of 500 s. Given that TC5 and TC9 have two thermocouple readings per cell (one on the front and one on the back fin), the average of the two readings is taken as the value for that given cell. The average value over all the individual cell samples is taken to represent the value for the given fin material type and thermocouple location. Comparison of the average curve to those of each individual cell sample is shown for every electrical loading condition and fin type in Appendix A.10 for completeness.

Due to issues with the cycler equipment failing to reinitiate testing between some cycle runs, the full set of 6 cell readings was not obtainable for all analysed electrical loading conditions. Table 6-10 displays the number of cell samples obtained for each fin material type and each duty cycle used to provide the average for the values in Figure 6-19.

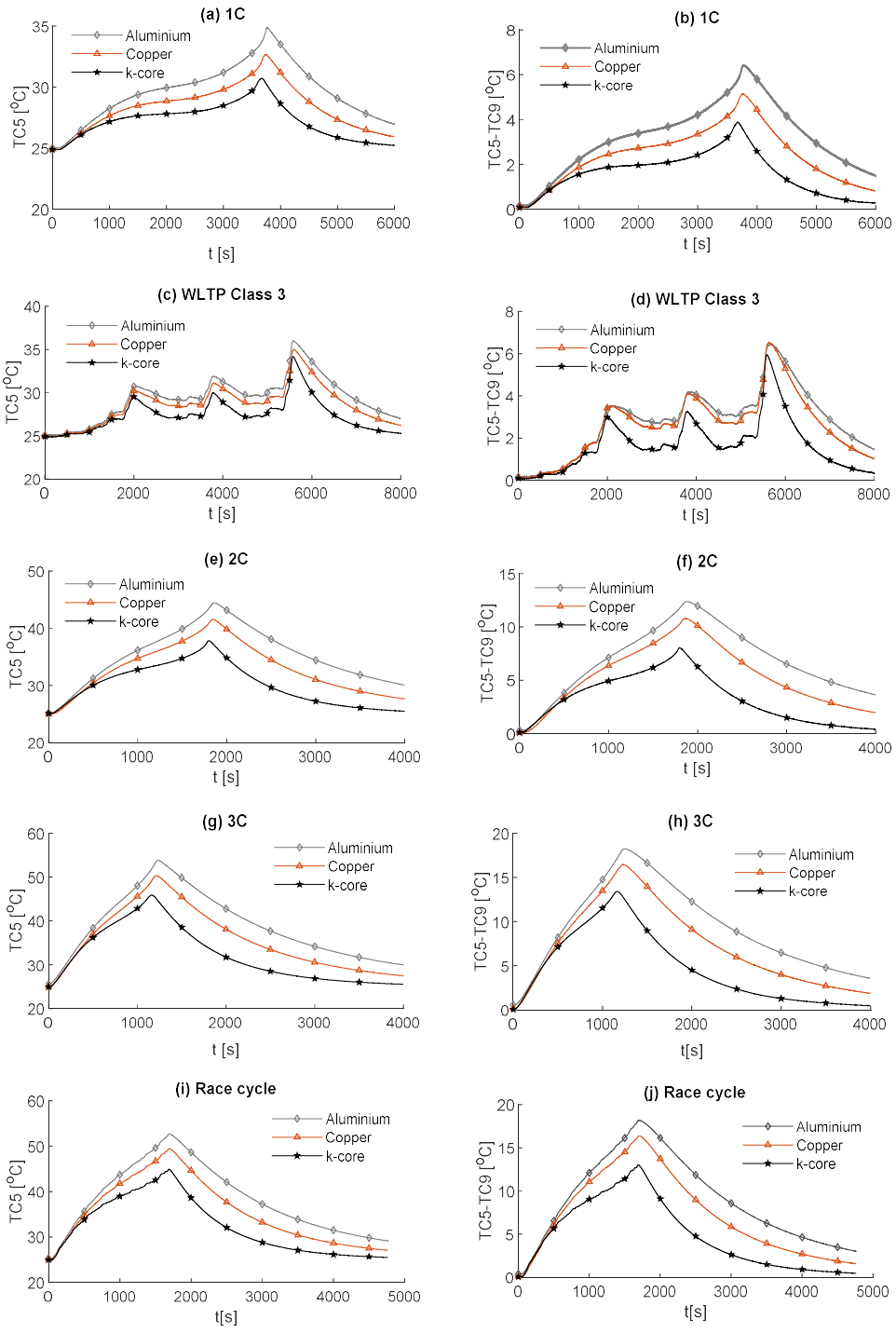

Figure 6-19: Experimental results obtained from the test rig for (a) 1 C discharge TC5 reading (b) 1 C discharge TC5-TC9 (c) WLTP Class 3 cycle TC5 reading (d) WLTP Class 3 cycle TC5-TC9 reading (e) 2 C discharge TC5 reading (f) 2 C discharge TC9-TC5 reading (g) 3 C TC5 reading (h) 3 C TC5-TC9 reading (i) Race cycle TC5 reading (j) Race cycle TC5-TC9 reading

Table 6-10: Number of experimental cell samples obtained for each analysed electrical loading condition and fin material type

Duty cycle	Fin material					
	Aluminium		Copper		k-core	
	No. cell samples	Cell number	No. cell samples	Cell number	No. cell samples	Cell number
Race	4	1*,2,3,4	5	1,3,4,5,6	5	1,3,4,5,6
3 C	5	1*,2,3,4,5	6	1,2,3,4,5,6	6	1,2,3,4,5,6
2 C	5	1*,2,3,4,5	6	1,2,3,4,5,6	1	6
WLTP Class 3	1	4	2	1,4	2	4,5
1 C	2	3,4	4	1,3,4,5	4	3,4,5,6,

* Cell 1 was damaged during disassembly prior to the aluminium fin tests, therefore it was replaced with a new cell termed Cell 1*

As the location of TC5 is furthest from the cooling source, it is the hottest measured location on the fin surface ($T_{max,f}$). Similarly, as TC9 is the closest location on the fin body to the cooling source, it is the coolest measured location. Therefore, TC5-TC9 gives the maximum measured fin surface temperature gradient ($\Delta T_{max,f}$). Given the compact packing of the test rig and the small thickness of the fins, it is assumed that the thermal resistance between the cell surface and the fin is negligible. Therefore, the fin temperature distribution is assumed to approximate the cell surface temperature distribution. Figure 6-19 highlights that for the 1 C discharge condition, all fin material types enable $T_{max,f}$ to remain below 35℃. However, the superior in plane thermal conductivity of the k-core fin enables a noticeable reduction in $\Delta T_{max,f}$ of 39.1% relative to the aluminium fin. The k-core fin is the only material that successfully limits the maximum value of $\Delta T_{max,f}$ to below 5 ℃.

Throughout the WLTP Class 3 cycle, the k-core fin provides an average value for $T_{max,s}$ of 27.4 ℃ and $\Delta T_{max,f}$ of 1.7 ℃. For the aluminium and copper fins, the average value for $T_{max,f}$ is 29.1 ℃ and 28.4 ℃ respectively, with a corresponding average value for $\Delta T_{max,f}$ of 2.6 ℃ and 2.4 ℃. The greatest increase in temperature during the cycle occurs for cell SOC levels below 10%, therefore, provided the deep discharge region is avoided during commercial use, the k-core fin may not be necessary for this level of fin thickness given that the aluminium fin offers satisfactory thermal control. The benefit of k-core for this electrical loading may be in the use of thinner fins, where the thickness may be altered to provide the same thermal control at a reduced volume and mass penalty (discussed further in Section 6.9).

For more aggressive electrical loading conditions, the improvement of the k-core fin over conventional aluminium in reducing $T_{max,f}$ and $\Delta T_{max,f}$ becomes more apparent. This is

observed in the race duty cycle, 3 C and 2 C discharge conditions where the k-core fin provides a reduction in $T_{max,f}$ of circa 15%. In particular, for the 3 C and race cycles, the k-core fin provides a value for $T_{max,f}$ of 46 ℃ and 45 ℃ respectively where the copper and aluminium fins both result in $T_{max,f}$ values near or exceeding 50 ℃. As recommended by Sato [184], this threshold should not be surpassed for a lithium-ion battery to avoid accelerated degradation and reduced cycle life. Thomas et al. [185] also report significant increases in power fade of lithium ion batteries when exposed to temperatures above 45 ℃, where they experimentally observed the power fade increasing from circa 22% at 45 ℃ to circa 33% at 55 ℃ after 20 weeks of soak time at the given temperature when stored at 60% SOC.

Table 6-11 summarises the experimental maximum values for $T_{max,f}$ and $\Delta T_{max,f}$ obtained during each electrical loading condition as a function of fin material type. Whilst the k-core fin provides an appreciable reduction in $T_{max,f}$ and $\Delta T_{max,f}$ relative to both aluminium and copper for the race duty cycle, the k-core fin still results in large values for $T_{max,f}$ of 44.9 ℃ and $\Delta T_{max,f}$ of 13.0 ℃. This points towards a limitation of cooling only 1 edge of the fin, particularly for this analysed pouch cell where the heat transfer pathway between the non-cooled edge of the fin and the cooled edge is relatively long compared to alternative cell designs. Single edge cooling, even with the k-core fin, may therefore be an inadequate thermal management choice when subject to long term track racing use due to both the excessive peak temperature and surface temperature gradients.

Table 6-11: Summary of the maximum values for recorded fin temperature and fin temperature gradient at the end of the tested electrical loading conditions

Fin material	**Test case**									
	Race		**3 C discharge**		**2 C discharge**		**WLTP Class 3**		**1 C discharge**	
	$T_{max,f}$ [℃]	$\Delta T_{max,f}$ [℃]	$T_{max,f}$ [℃]	$\Delta T_{max,f}$ [℃]	$T_{max,f}$ [℃]	$\Delta T_{max,f}$ [℃]	$T_{max,f}$ [℃]	$\Delta T_{max,f}$ [℃]	$T_{max,f}$ [℃]	$\Delta T_{max,f}$ [℃]
Aluminium	52.7	18.2	53.8	18.3	44.5	12.4	36.0	6.5	34.9	6.4
Copper	49.4	16.4	50.3	16.5	41.5	10.8	35.0	6.5	32.7	5.1
k-core	44.9	13.0	45.9	13.4	37.8	8.0	34.2	5.9	30.7	3.9
	Race		**3 C discharge**		**2 C discharge**		**WLTP Class 3**		**1 C discharge**	
	$T_{max,f}$ [℃]	$\Delta T_{max,f}$ [℃]	$T_{max,f}$ [℃]	$\Delta T_{max,f}$ [℃]	$T_{max,f}$ [℃]	$\Delta T_{max,f}$ [℃]	$T_{max,f}$ [℃]	$\Delta T_{max,f}$ [℃]	$T_{max,f}$ [℃]	$\Delta T_{max,f}$ [℃]

k-core fin % decrease relative to aluminium [%]	14.8	28.6	14.7	26.8	15.1	35.5	5.0	9.2	12.0	39.1
k-core fin % decrease relative to copper [%]	9.1	20.7	8.7	21.8	8.9	25.9	2.3	9.2	6.1	23.5

6.7.1 ERROR ANALYSIS

A statistical analysis highlighting the results of the standard deviation and standard error of the TC5 and TC9 measurements is shown in Table 6-12.

Table 6-12: The statistical data from the obtained samples at the end of each test case.

		Mean			Standard Deviation			Standard Error		
Test Case	**Fin Material**	**TC5 [°C]**	**TC9 [°C]**	**$\Delta T_{max,f}$ [°C]**	**TC5 [°C]**	**TC9 [°C]**	**$\Delta T_{max,f}$ [°C]**	**TC5 [°C]**	**TC9 [°C]**	**$\Delta T_{max,f}$ [°C]**
1 C	Aluminium	34.52	28.56	5.96	0.50	0.15	0.65	0.36	0.11	0.46
	Copper	32.74	27.57	5.16	0.23	0.25	0.41	0.12	0.13	0.20
	k-core	30.88	26.95	3.92	0.22	0.06	0.23	0.11	0.03	0.12
WLTP Class 3	Aluminium	-	-	-	-	-	-	-	-	-
	Copper	35.01	28.48	6.53	0.53	0.34	0.19	0.38	0.24	0.14
	k-core	34.19	28.24	5.94	0.22	0.33	0.11	0.16	0.23	0.08
2 C	Aluminium	44.54	32.13	12.41	0.69	0.61	1.03	0.31	0.27	0.46
	Copper	41.57	30.77	10.81	0.43	0.45	0.67	0.18	0.19	0.27
	k-core	-	-	-	-	-	-	-	-	-
3 C	Aluminium	53.88	35.59	18.30	1.12	0.89	1.60	0.50	0.40	0.72
	Copper	50.43	34.04	16.39	0.38	0.53	0.78	0.16	0.22	0.32
	k-core	46.19	32.63	13.56	0.48	0.18	0.39	0.20	0.07	0.16
Race cycle	Aluminium	52.69	34.52	18.18	0.92	0.78	1.41	0.46	0.39	0.70
	Copper	49.43	33.05.	16.37	0.70	0.69	0.77	0.31	0.31	0.34
	k-core	44.90	31.89	13.02	0.47	0.29	0.37	0.21	0.13	0.16

The results for the aluminium WLTP Class 3 and k-core fin 2 C condition are not applicable given that only a single sample is achieved for each of these conditions. Sources of experimental variation between the samples may be due to slight offsets in the cell position within the busbar blocks, which alters the alignment of the thermocouple locations relative to the cell location. An example of an offset in the position of the cell to the left is represented schematically in Figure 6-20. As shown, the offset results in the location of TC5 now being further from the cell body, which may result in a lower reading than the reference position where TC5 is positioned closer to the heat generation source. Similarly, as TC5 is now positioned to the left, TC9 is in turned positioned to overlay further across the cell and, therefore, is further from the cold plate. This effect may increase the reading of TC9 relative to the reference case without any offset. An example of an offset in the cell tab positioning to the left may have occurred for Cell 3 during the copper fin experiments, as this would explain why it consistently has one of the highest TC9 readings yet also the lowest TC5

reading when compared to the other samples (see Figures A.10.6–A.10.10 in Appendix A.10 that contain the temperature measurements for the individual cell samples).

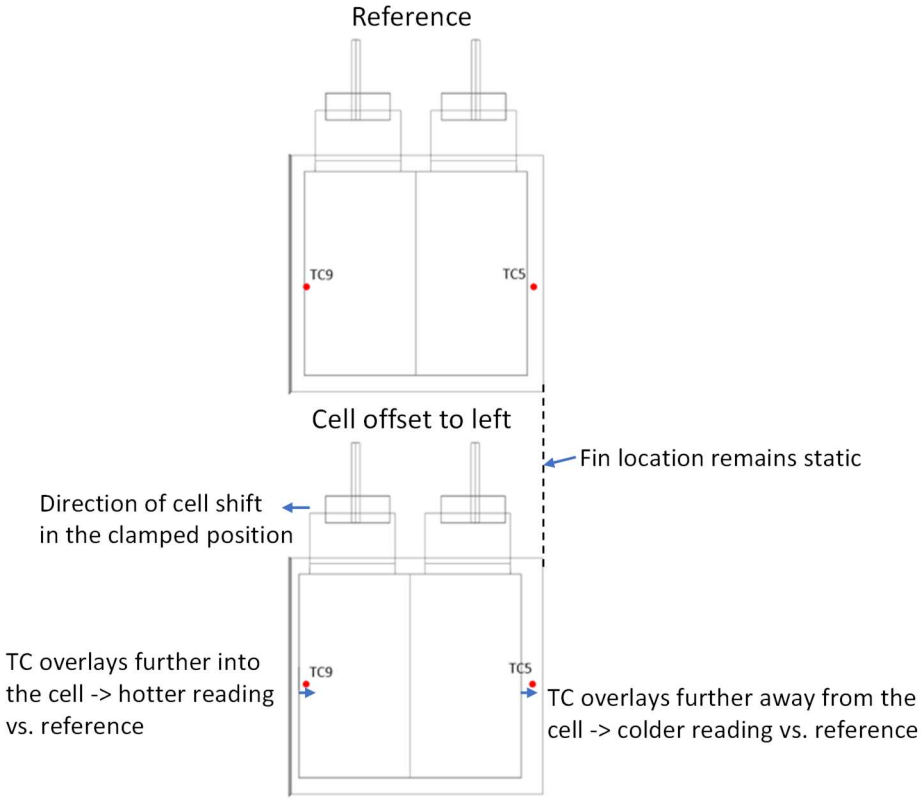

Figure 6-20: A potential cause of variation due to the fin body and cell being offset between samples.

6.8 VALIDATION OF THE BATTERY THERMAL MODEL

To enable an accurate extended simulation analysis into the performance of fin cooling, the accuracy of the single edge fin cooled thermal model is compared to the experimental results obtained from the test rig. A sensitivity study on the value for the cell heat capacity is first performed. The static value for the heat capacity values that are considered are 1300 $J.kg^{-1}.K^{-1}$ and 1500 $J.kg^{-1}.K^{-1}$, which are within the bounds reported by Bazinski et al. [181] at 25 ℃ and 55 ℃ respectively. The sensitivity analysis is compared against the experimental data for aluminum fin cooling under the race duty cycle, whereby the results are presented in Figure 6-21. Here, it is observed that a value for C_p of 1500 $J.kg^{-1}.K^{-1}$ provides the greatest agreement with the experimental temperature data at both TC5 and TC9 locations. This can be seen in the response of the cell temperature rise during the duration of the duty cycle in addition to the transient cooldown of the cell following termination of the current.

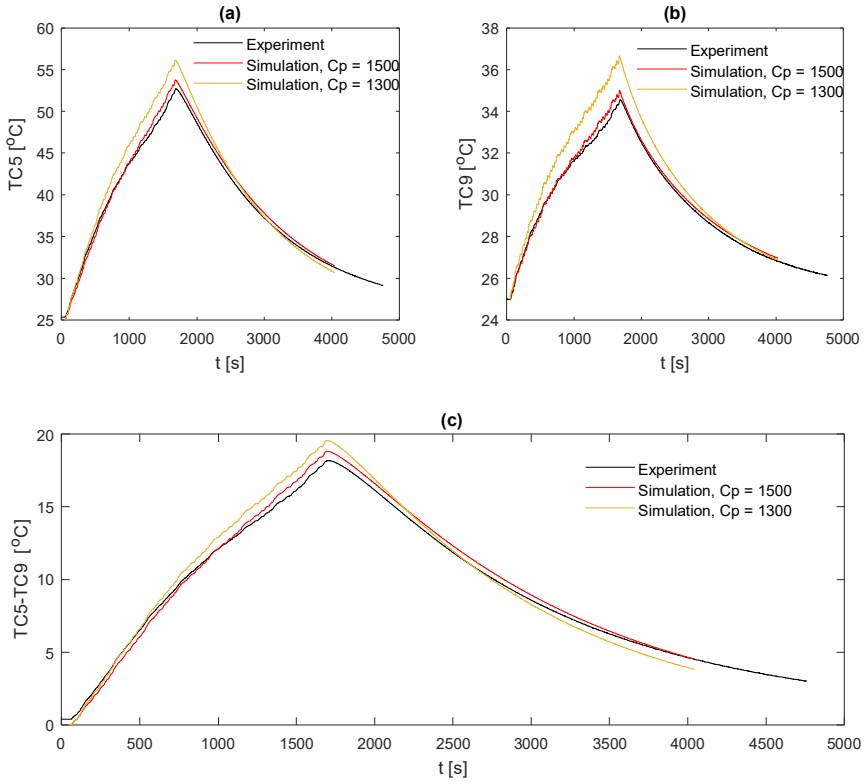

Figure 6-21: Heat capacity sensitivity study for the aluminium fin comparison to the experimental temperature measurements for (a) TC5 (b) TC9 (c) TC5-TC9

A static value of 1500 $J.kg^{-1}.K^{-1}$ for the cell heat capacity is therefore used for all subsequent thermal modelling for all fin material types.

Further validation of the thermal model is performed for both the WLTP Class 3 and race cycle, where a comparison between the full transient readings at measurement location TC5 is conducted. The results are contained in Figure 6-22.

Given that validation against only 1 temperature location on its own is inadequate due to the large temperature gradients observed across the fin surface, a full comparison between the 15 point thermocouple locations at the end of the race duty cycle is also performed to provide a full thermal map of the fin surface. The analysis is conducted for all fin material types and is viewable in Figure 6-23.

From Figure 6-22 (a), (c) and (e) for the WLTP Class 3 cycle, the mean absolute percentage error (MAPE) between the simulated and experimental TC5 reading across 8000 s for the aluminium, copper and k-core fins is 1.19%, 1.16% and 1.14% respectively. Similarly, the maximum percentage error (MPE) for the aluminium, copper and k-core fins is 4.8%, 6.1% and 8.4% respectively. The model under predicts the large temperature spike during the

deep discharge region of the cell where the final resting SOC is 5%. This may be due to inaccuracies in the heat generation calculation which underestimates the large increase in cell overpotential resistance during very low SOC levels.

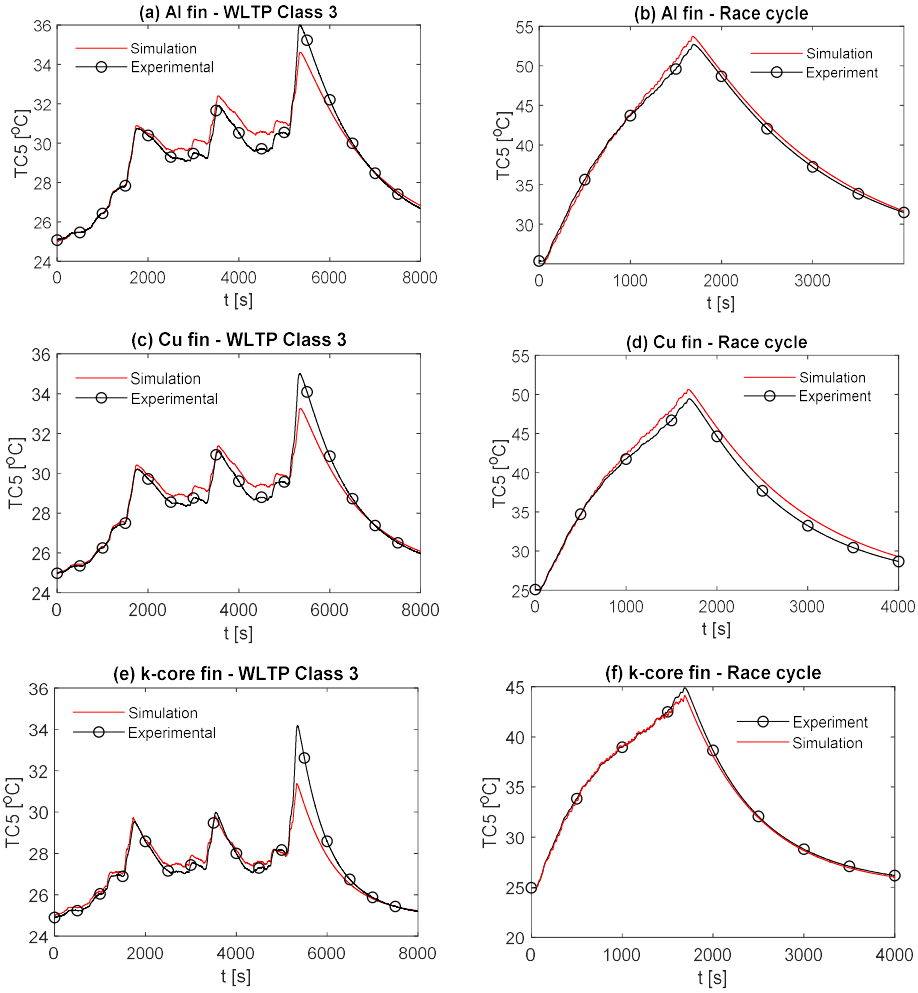

Figure 6-22: Full transient comparison between the thermal model and experimental data at the TC5 location for (a) Al fin – WLTP Class 3 (b) Al fin -Race cycle (c) Cu fin – WLTP Class 3 (d) Cu fin – Race cycle (e) k-core fin – WLTP Class 3 (f) k-core fin – Race cycle

In the case of the race duty cycle (Figure 6-22 (b), (d) and (f)), the MAPE values for the aluminium, copper and k-core fins across 4000 s is 1.3%, 2.4% and 0.6% respectively. The results for the MPE during the race cycle is lower than the case for the WLTP cycle, with values of 2.5%, 3.9% and 2.4% for the aluminium, copper and k-core fins respectively. The lower MPE may arise from the fact that the cell SOC does not go below 10% during the race cycle, therefore, additional rapid increase in cell overpotential resistance not captured fully by the model are avoided.

The thermal maps of the fin surface for the k-core, aluminium and copper fin are viewable in Figure 6-23. The position of the 15 thermocouple point measurements that coincide with the experimental locations in Figure 6-5 (a)-(b), together with the annotated values for the simulation at the end of the race cycle are shown. The accuracy of the thermal map is compared to the 15 point measurements across the front fins, where the average is taken across all the front fin samples to represent the experimental value. The results of the comparison are shown in Table 6-13.

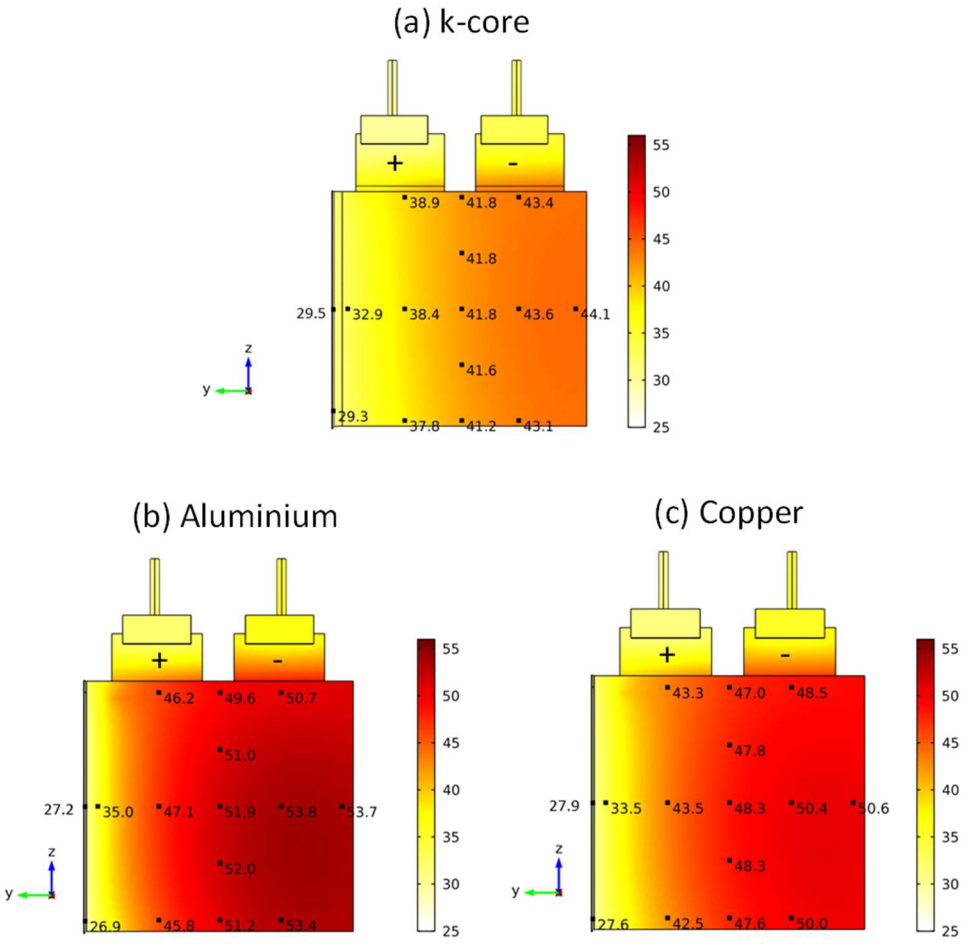

Figure 6-23: Simulated fin surface thermal map at the end of the race cycle for (a) k-core fin (b) aluminium fin (c) copper fin (colorbar units in °C)

Table 6-13 highlights that as with the transient TC5 comparison, there is excellent agreement between the model and test data across all fin materials. The strong agreement lends further accuracy to the assumption that the test rig has been set-up correctly such as to capture the cooling symmetry, in addition to achieving minimal thermal resistance between the cell surface and fin surface.

The largest error occurs for TC1 for the aluminium fin with a value of 9.0%. The remainder of the point comparisons outside TC1 provide errors below 5%, except for TC2 for the copper fin where the error is 5.6%.

Table 6-13: Comparison data between the simulated thermal maps and experimental thermocouple readings at the end of the race duty cycle

	Aluminium fin			Copper fin			k-core fin		
TC number	Simulation [°C]	Experiment [°C]	Error [%]	Simulation [°C]	Experiment [°C]	Error [%]	Simulation [°C]	Experiment [°C]	Error [%]
1	46.2	42.4	8.96	43.3	40.0	8.25	38.9	37.1	4.85
2	49.6	47.3	4.86	47.0	44.5	5.62	41.8	40.9	2.20
3	50.7	49.7	2.01	48.5	46.4	4.53	43.4	43.1	0.70
4	51.0	49.2	3.66	47.8	46.0	3.91	41.8	41.5	0.72
5	53.7	52.5	2.29	50.6	49.1	3.05	44.1	44.5	0.90
6	53.8	52.4	2.67	50.4	49.0	2.86	43.6	44.0	0.91
7	51.9	49.4	5.06	48.3	47.0	2.77	41.8	42.0	0.48
8	47.1	46.8	0.64	43.5	42.3	2.84	38.4	38.0	1.05
9	35.0	34.4	1.74	33.5	33.9	1.18	32.9	32.0	2.81
10	52.0	51.2	1.56	48.3	47.7	1.26	41.6	42.5	2.12
11	53.4	53.0	0.75	50.0	49.7	0.60	43.1	44.1	2.27
12	51.2	51.0	0.39	47.6	47.9	0.63	41.2	42.4	2.83
13	45.8	46.5	1.51	42.5	43.3	1.85	37.8	38.6	2.07
14	26.9	26.3	2.28	27.6	27.2	1.47	29.3	29.1	0.69
15	27.2	26.1	4.21	27.9	26.9	3.72	29.5	29.1	1.37

6.9 SIMULATION ANALYSIS

To further study the applicability of the k-core material to a future in-vehicle application, a more practical edge cooled concept for cooling the fins is proposed. A schematic of the fin cooling BTMS design is shown in Figure 6-24, which is developed in collaboration with Thermacore. This design enables increased packing of the cells as the edges of the fins no longer require bending. Instead, the edges are inserted within extruded metallic aluminium cooling elements which contain a central liquid channel to dissipate the heat transferred from the fin ends. The liquid is distributed along a top manifold (not shown) and flows down along the length of the metallic ducts, providing cooling along the whole length of the fin edge. The parallel nature of the design is expected to minimise the formation of any temperature gradients between cells within a module, provided that the distribution manifold enables equal distribution of coolant to each channel. To reduce the thermal resistance of the system from a shorter heat transfer pathway, a two edge fin cooled strategy is employed. Treatment of the end cells within the module is not considered in this analysis.

A schematic of the BTMS design on the module level highlighting the parallel cooling achieved along the fin edges is shown in Figure 6-25.

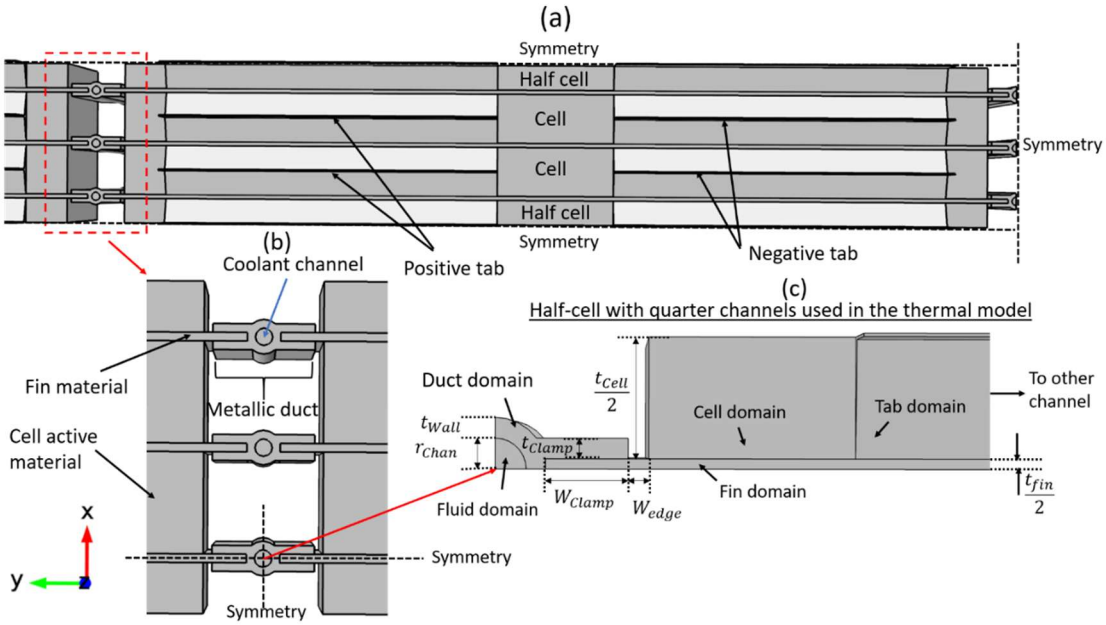

Figure 6-24: Schematic of the proposed edge cooled fin BTMS design with (a) top down view of cells and cooling system (b) exploded view of cooling channels and fins ends (c) geometry of the half-cell with quarter channels used in the thermal model (note right coolant channel, cell portion and tab not shown)

The symmetry planes present within the design are utilised by the thermal model to reduce the computational cost. This results in a thermal model with a half-cell and quarter coolant channel on each fin end, as shown in Figure 6-24 (c). Symmetry planes are employed along the length of the fin half thickness in the 'y' direction, along the corner coolant and duct faces in the 'x' and 'y' directions and along the mid-plane of the cell and tabs in the 'y' direction. On the exposed edges of the metallic ducts and cell tabs a static h value of 5 $W.m^{-2}.K^{-1}$ is applied. On the sides of the cell, the static h value of 20 $W.m^{-2}.K^{-1}$ is retained to capture the edge cooling effects of the pouch laminate folds. The heat generation profiles under the race duty cycle for the cell and tab structures used in the validated test rig thermal model are input as the source terms. The conjugate heat transfer package in COMSOL Multiphysics 5.2a is utilised to model the transient conjugate heat transfer between the liquid coolant streams, cell and fin bodies. Laminar flow is specified for the liquid domains given that the Reynolds number is below 2300 [186] in all instances. The governing equations used in the thermal model (together with Equation (56)) include the continuity, momentum conservation and energy conservation equations for the liquid domains under the assumption of incompressible flow which are given by [187]:

Continuity equation for the liquid:

$$\rho_w \nabla.(\vec{v}) = 0 \tag{63}$$

Momentum conservation equation for the liquid:

$$\rho_w \frac{\partial \vec{v}}{\partial t} + \rho_w(\vec{v}.\nabla)\vec{v} = \nabla.[-pI_m + \mu_w(\nabla\vec{v} + (\nabla\vec{v})^T)] + F \tag{64}$$

Conservation of energy equation for the liquid:

$$\rho_w C_{pw} \frac{\partial T_w}{\partial t} + \rho_w C_{pw}\vec{v}.\nabla T_w = \nabla.(k_w \nabla T_w) \tag{65}$$

Where ρ_w is the density of water [kg.m^{-3}], $\vec{v}$ the velocity vector [m.s^{-1}], p the pressure [Pa], I_m the identity matrix, μ_w the dynamic viscosity of water [kg.m^{-1}.s^{-1}], C_{pw} the heat capacity of water [J.kg^{-1}.K^{-1}] and F the body force [N.m^{-3}].

With reference to Figure 6-24 (c), W_{clamp} refers to the length of fin embedded in the aluminium cooling duct [m], W_{edge} the spacing between the embedded fin portion and cell edge [m], t_{Wall} the thickness of the duct wall [m] and r_{Chan} the radius of the cooling channel [m]. The fin body is positioned to directly overlay the cell material, whereby the fin and duct height are equal to H_{cell}. The dimensions of the fin and duct are given in Table 6-14.

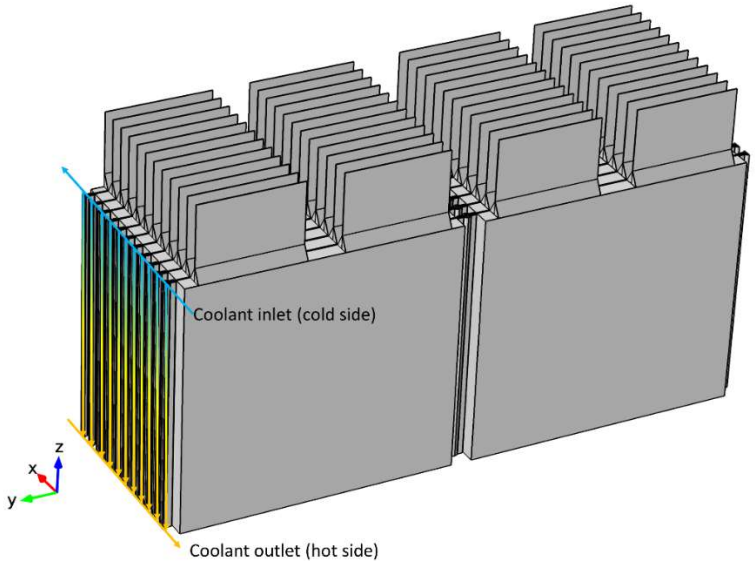

Figure 6-25: Schematic of the fin BTMS design on the module level

Table 6-14: Dimension of the duct and fin used in the proposed edge cooled thermal model

H_{fin} [mm]	W_{fin} [mm]	W_{edge} [mm]	W_{clamp} [mm]	t_{Wall} [mm]
190.0	218	1.0	4.0	1.0

The thickness of the fin and radius of the cooling channel are considered as design variables in this study. Again, the skin layer on the k-core fin is ignored in the thermal modelling, however, its presence is included in the volume and mass considerations. A mesh independence analysis is performed to ensure that the chosen mesh size provides the greatest accuracy at a reasonable computational cost. The results of the mesh independence study on the output value of T_{max} [°C] for the case of a 3 mm cooling channel diameter and 0.003 kg.s^{-1} of channel mass flowrate (where quarter of this value is specified in each channel in the thermal model) with a k-core fin thickness of 0.5 mm (i.e. 1.16 mm reflective sandwich thickness between cells on the module level considering the 0.08 mm thick skin layer) is shown in Figure 6-26.

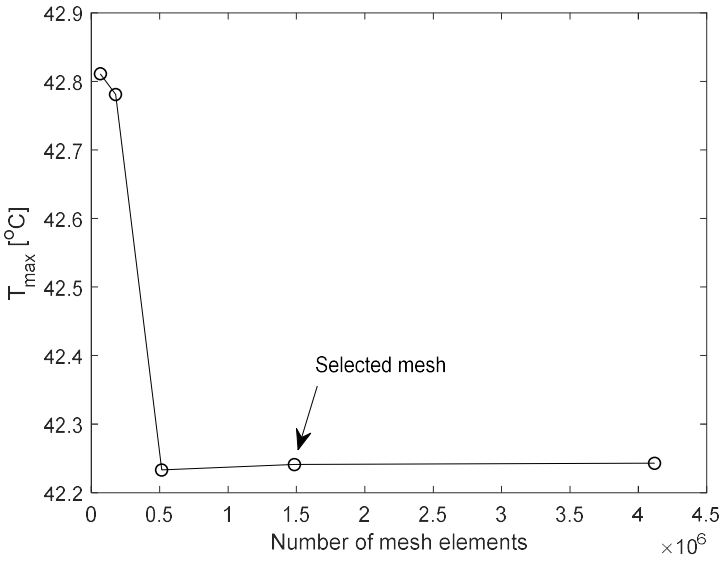

Figure 6-26: Example of the mesh independence study for 3 mm channel diameter and 0.003 kg.s^{-1} inlet mass flowrate

The mesh independence study is repeated each time the channel diameter and/or the fin thickness is varied. In all simulations, the race duty cycle (1642 s) with an additional zero current cool down period of 358 s is specified for the cell electrical loading. The relative tolerance for the solver is kept at the default value of 0.01, where the absolute tolerance for the temperature, pressure and velocity fields is also kept at default with a value of 5E-4. A

strict time step of 1 s is set as the maximum time step for the solution to match the resolution of the input heat generation profile. The maximum number of iterations per time step is set as 50.

6.9.1 EFFECT OF CHANNEL MASS FLOWRATE

The effect of channel mass flowrate on T_{max}, T_{avg}, ΔT_{max} and the average temperature increase of the exiting water coolant $\Delta T_{av,water}$ for the case of a 2 mm coolant channel diameter and 1.16 mm sandwich k-core fin thickness is shown in Figure 6-27. Here, it is observed that the low 0.001 kg.s^{-1} mass flowrate results in a large increase in $\Delta T_{av,water}$ of circa 10 ℃ at the end of the race duty cycle, leading to a peak in T_{max} of 46.1 ℃. Increasing the mass flowrate further to 0.0015 kg.s^{-1} results in a decrease in both T_{max} and T_{avg} of 1.8 ℃. However, further increases in the mass flowrate results in declining reductions in the cell thermals, where increasing the mass flowrate from 0.0025 kg.s^{-1} to 0.003 kg.s^{-1} decreases T_{max} by only 0.61℃. This may be caused by either the heat transfer rate being increasingly limited by conduction through the cell material, through the fin material or a combination of both as the convective heat transfer rate increases (discussed further in Section 6.9.3). Consideration of the choice of mass flowrate must be placed on the desired temperature control given the increased pressure drop from accommodating the larger mass flowrate. As shown in Table 6-15, the pressure drop increases by 2400.7 Pa from tripling the mass flowrate from 0.001 kg.s^{-1} to 0.003 kg.s^{-1}, which would incur more parasitic power losses for the system as shown by the values for ideal pump power P [W], which is given by [79]:

$$P = \Delta p . V_{chan} \tag{66}$$

Where Δp is the channel pressure drop [Pa] and V_{chan} the channel volumetric flowrate [m^3.s^{-1}]. Even for the large channel mass flowrate of 0.003 kg.s^{-1}, the ideal pump power is small with a value of 9.42 mW. For a battery pack comprising 288 cells, corresponding to an EV of circa 56 kW, the total pump power is 2.7 W. This is relatively insignificant relative to the typical cabin heating requirement for EVs which is on the order of 3 kW as stated by LaClair et al. [188].

Table 6-15: Effect of channel mass flowrate on channel pressure drop for 2 mm channel diameter

	Channel mass flowrate [kg.s^{-1}]				
	0.001	0.0015	0.002	0.0025	0.003
Channel pressure drop [Pa]	730.5	1248.7	1821.1	2436.7	3131.2

Ideal pump power per cell [mW]	0.731	1.88	3.65	6.11	9.42

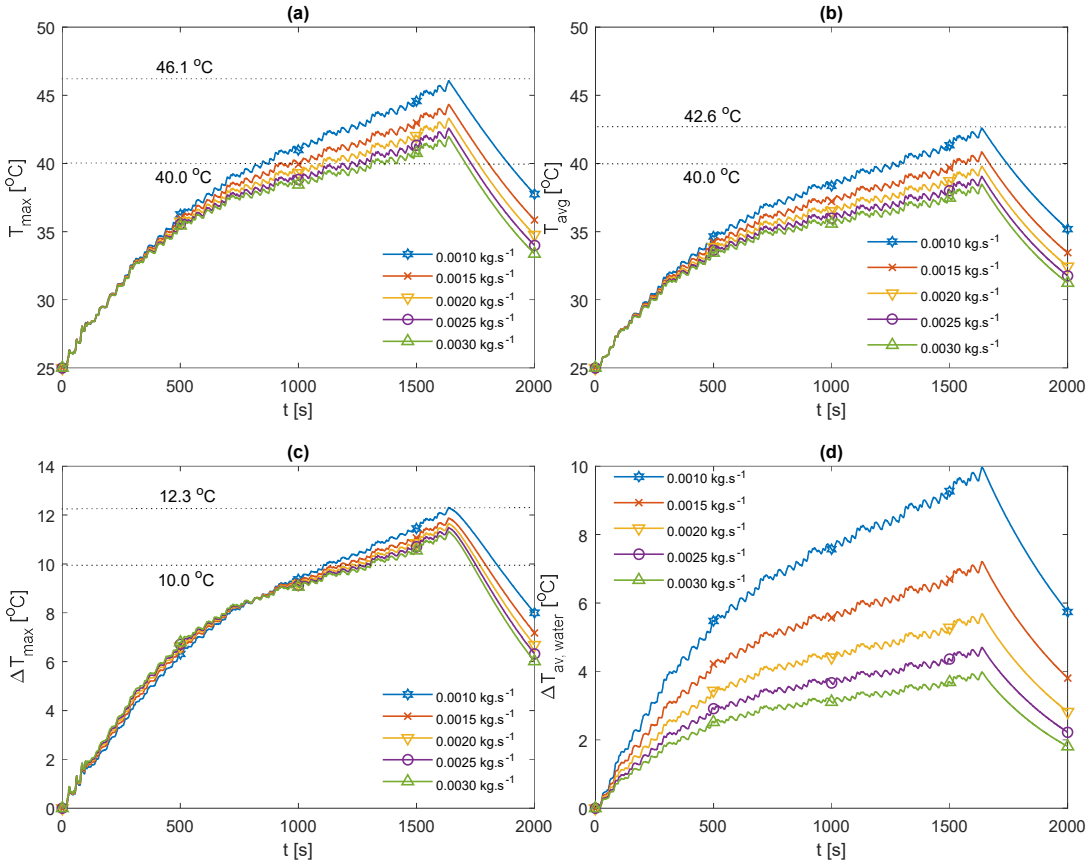

Figure 6-27: Effect of liquid flowrate on the k-core fin BTMS thermal performance with 2 mm channel diameter during the race duty cycle for (a) maximum cell temperature (b) volume averaged cell temperature (c) maximum cell temperature gradient (d) average exiting water coolant temperature

Interestingly, ΔT_{max} appears to be relatively insensitive to the value of the channel mass flowrate, where for the 0.001 kg.s^{-1} value ΔT_{max} peaks at 12.3 ℃ declining to 11.3 ℃ when the flowrate is increased by a factor of 3 to 0.003 kg.s^{-1}. Considering that the $\Delta T_{av,water}$ decrease is relatively large during this transition (from 10.0 ℃ to 4.0 ℃), it highlights the ability of the k-core fin BTMS ability to efficiently control the temperature gradient even under large fluctuations in $\Delta T_{av,water}$ (i.e. low liquid flowrate), where the effect of the axial temperature change of the water coolant is counteracted by conduction along the metallic cooling duct and k-core fin. This is visualised in Figure 6-28, which displays the thermal contours of the cell core and front view of the fin mid-plane as a function of increasing mass flowrate.

Also observed is that up until circa 800 s, higher mass flowrates give slightly larger temperature gradients for the cell, where past circa 800 s a transition is achieved where the

maximum temperature gradient is lower with increasing flowrate. This may be explained by the nature of the developing cell hot spot, where up until circa 300 s the hot spot formation is relatively unaffected between channel flowrate as the temperature field throughout the battery develops. Lower coolant flowrate in this region lead to lower heat transfer from the cell surface, which allows the cell to initially heat more uniformly. Past circa 300 s, the hot spot begins to display a deviation between coolant flowrates, where the rate of increase in the hot spot temperature is reduced as the flowrate increases. The continued reduction in the hot spot temperature rise when using larger coolant flowrates eventually results in an overall decrease in ΔT_{max}.

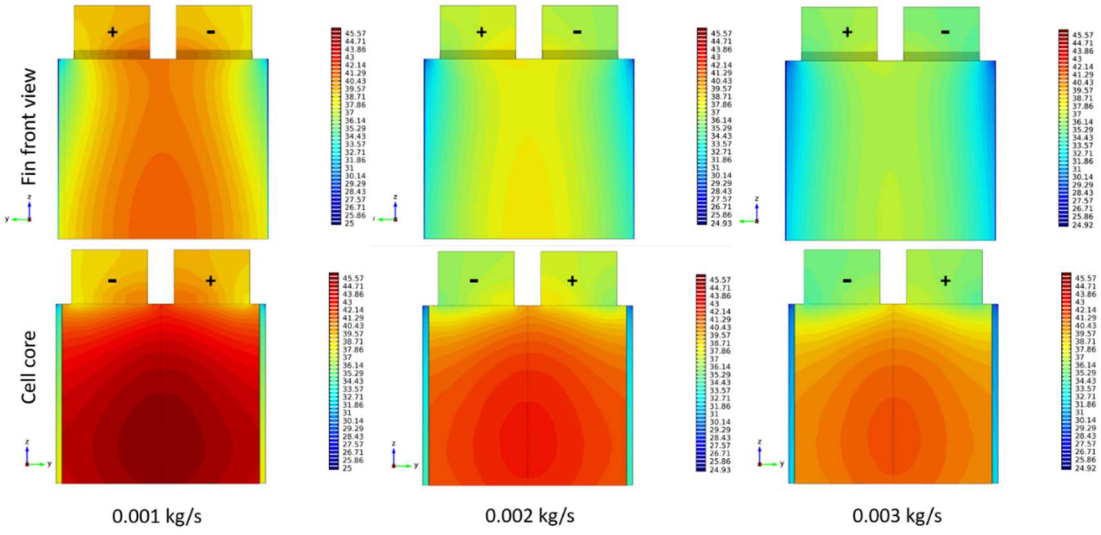

Figure 6-28: Thermal contours of the cell core and fin front view under increasing channel mass flowrate with 2 mm channel diameter (colour bar units in ℃)

6.9.2 EFFECT OF CHANNEL DIAMETER

The effect of the channel diameter on the battery maximum temperature is shown in Figure 6-29 for a set channel mass flowrate of 0.003 kg.s^{-1} and 1.16 mm sandwich thick fin. Increasing the size of the cooling channel offers an increase in heat transfer area around the cooling duct, however, the channel velocity is also reduced. Specifically, the inlet velocity decreases from 0.96 m.s^{-1} with the 2 mm diameter channel to 0.26 m.s^{-1} with the 4 mm diameter channel. Figure 6-29 demonstrates that the overall effect on T_{max} is a slight decrease as the channel diameter decreases, where the peak cell temperature at the end of the race cycle is 0.66 ℃ greater with the 4 mm channel diameter than the 2 mm channel diameter with 0.003 kg.s^{-1} channel mass flowrate.. However, as shown in Table 6-16, significant reductions in channel pressure drop are observed with larger channel diameters, where the pressure drop decreases from 3132.2 Pa with the 2 mm diameter channel to 163.0

Pa with the 4 mm diameter channel. Therefore, the 2 mm channel is relatively inefficient under this level of channel flowrate.

The choice between the 3 mm channel and 4 channel may be more involved. Increasing the size of the channel also results in an increase in overall size of the coolant system, together with additional mass. The mass of the BTMS increases by 1.97% upon transitioning from the 3 mm to 4 mm sized channel diameter by considering the additional fluid and duct volume. However, the 4 mm diameter channel has the ability to accept larger mass flowrates while remaining under laminar flow. The effect of doubling the channel flowrate to 0.006 kg.s^{-1} on T_{max} for the 4 mm system is also shown in Figure 6-29, where T_{max} reduces by 1.8 °C (relative to the 2 mm channel at 0.003 kg.s^{-1} mass flowrate) with a channel pressure drop of 430.6 Pa and ideal pump power of 2.59 mW. The flexibility of the 4 mm channel system in providing a wider cooling capacity range together with the lower pressure drop may potentially be worth the increase in volume and mass penalty.

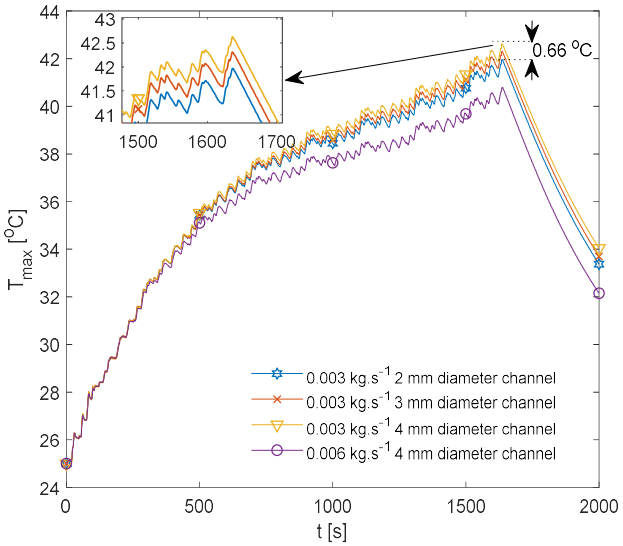

Figure 6-29: Effect of channel diameter on T_{max}

Table 6-16: Channel pressure drop as a function of cooling channel diameter for a channel flowrate of 0.003 kg.s^{-1}

	Channel diameter [mm]		
	2	3	4
Channel pressure drop [Pa]	3131.2	555.2	163.0
Ideal pump power per cell [mW]	9.42	1.67	0.490

6.9.3 EFFECT OF FIN THICKNESS

The effect of increasing the fin thickness on the battery thermal condition is shown in Figure 6-30 (a)-(c) for the 3 mm diameter channel with 0.003 kg.s^{-1} flowrate and Figure 6-30 (d)-(f) for the 4 mm diameter channel and 0.006 kg.s^{-1} flowrate. The skin layer thickness is set as a constant for each fin thickness with a value of 0.08 mm.

The thermal conductivity of the k-core fin is assumed to remain constant as its thickness is varied in this study. The effect of the fin thickness on the effective thermal conductivity of the k-core fins is a scope for further work. It is expected that this analysis is conservative, as thicker fins with greater APG core fraction are expected to increase the effective in-plane thermal conductivity, where in this study the thermal conductivity values used are those for the experimental sample with a thickness of 0.68 mm.

From Figure 6-30, it is observed that increasing the fin thickness offers an improvement in both the battery operating temperature and temperature uniformity. Transitioning from the 0.66 mm thick fin to the 1.16 mm fin reduces T_{max} by 2.39 ℃ for the 3 mm channel case at the end of the race cycle. However, the level of reduction in T_{max} upon further increasing the fin thickness decreases, where only a 1.13 ℃ reduction is observed from 1.16 mm to 1.66 mm and 0.70 ℃ from 1.66 mm to 2.16 mm. Similar levels of reduction are also observed for the 4 mm diameter channel case where the flowrate is doubled, which may imply that the overall heat transfer rate becomes increasingly limited by the poor heat transfer rate through the cell in the perpendicular direction as the fin thickness is increased, which is a limitation of the cell material properties and cell thickness.

Table 6-17 summarises the thermal performance metrics of the battery at the end of the race cycle for the analysed fin thicknesses, where the effect on the cell surface temperature gradient $\Delta T_{max,s}$ is also included.

Table 6-17: Tabulated thermal results at the end of the race duty cycle as a function of fin thickness and channel mass flowrate

	0.003 kg.s^{-1} channel flowrate				0.006 kg.s^{-1} channel flowrate			
Sandwich fin thickness	T_{max} [℃]	T_{avg} [℃]	ΔT_{max} [℃]	$\Delta T_{max,s}$ [℃]	T_{max} [℃]	T_{avg} [℃]	ΔT_{max} [℃]	$\Delta T_{max,s}$ [℃]
0.66	44.78	41.11	14.22	10.41	43.32	39.61	13.84	10.07
1.16	42.39	38.85	11.67	7.06	40.69	37.07	11.51	6.91
1.66	41.26	37.77	10.63	5.60	39.66	36.13	10.22	5.21
2.16	40.56	37.09	9.84	4.56	38.94	35.54	9.55	4.35

Overall, the 4 mm channel with double the flowrate offers a reduction on the order of circa 1.6 °C in both T_{max} and T_{avg} relative to the 3 mm channel for all the analysed fin material thicknesses. Therefore, the 4 mm channel system with 1.16 mm sandwich fin thickness offers similar control over T_{max} and T_{avg} as the 3 mm channel system with the 2.16 mm thick fin operating at half the mass flowrate. The thicker fin, however, enables a lower ΔT_{max} by 1.7 °C. The 4 mm channel system at 0.006 kg.s^{-1} also consumes circa 55% more ideal pump power then the 3 mm channel system operating at 0.003 kg.s^{-1}. However, the weight increase of the 3 mm system with the 2.16 mm fin is circa 62% greater. Increasing the thickness of the fin past 1.16 mm may potentially be undesirable given the poor improvement in thermal performance for the level of increased weight and reduced packing efficiency of the system, as shown in Figure 6-33 and Figure 6-34 respectively.

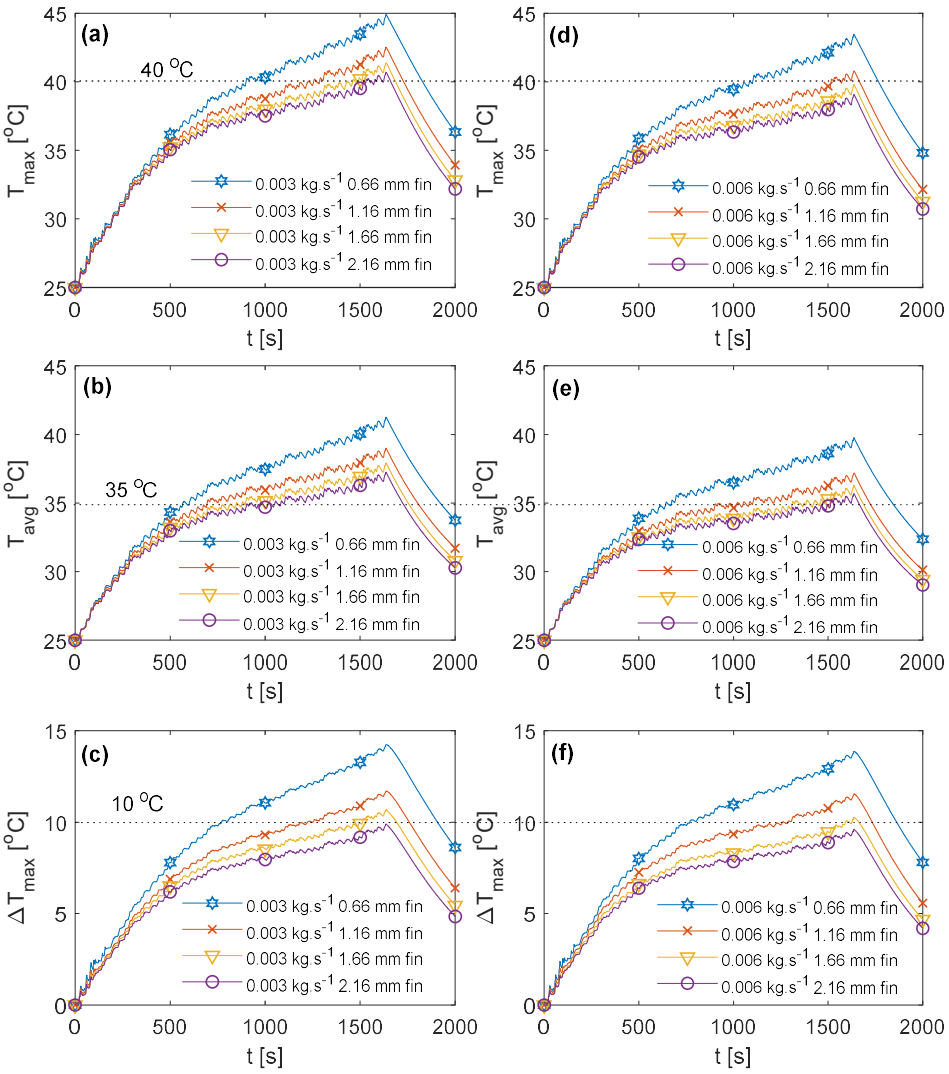

Figure 6-30: Thermal performance of the k-core fin BTMS under different fin thickness with (a)-(c) 0.003 kg.s^{-1} and 3 mm channel diameter (d)-(f) 0.006 kg.s^{-1} and 4 mm channel diameter

6.9.4 COMPARISON WITH CONVENTIONAL FIN MATERIALS

Comparisons between the thermal performance of the k-core fin BTMS to that using conventional copper and aluminium fin materials is shown in Figure 6-31. For the k-core fin, a 1 mm thick APG layer is specified giving a total thickness of 1.16 mm with the skin layer, where for the copper and aluminium fins the total thickness is 1 mm. A channel diameter of 4 mm and a channel mass flowrate of 0.006 kg.s^{-1} are considered. The case where no fin cooling on the cell is also shown, which further highlights the importance of active cooling under this electrical loading condition given that T_{max} approaches 70 °C. In addition, liquid double tab cooling with a static heat transfer coefficient of 750 W.m^{-2}.K^{-1} is also included for a cell with opposite end tabs to demonstrate that tab cooling is still ineffective for this level of heat generation when considering the transient thermal analysis. This is since T_{max} approaches 53 °C, with ΔT_{max} exceeding 22 °C.

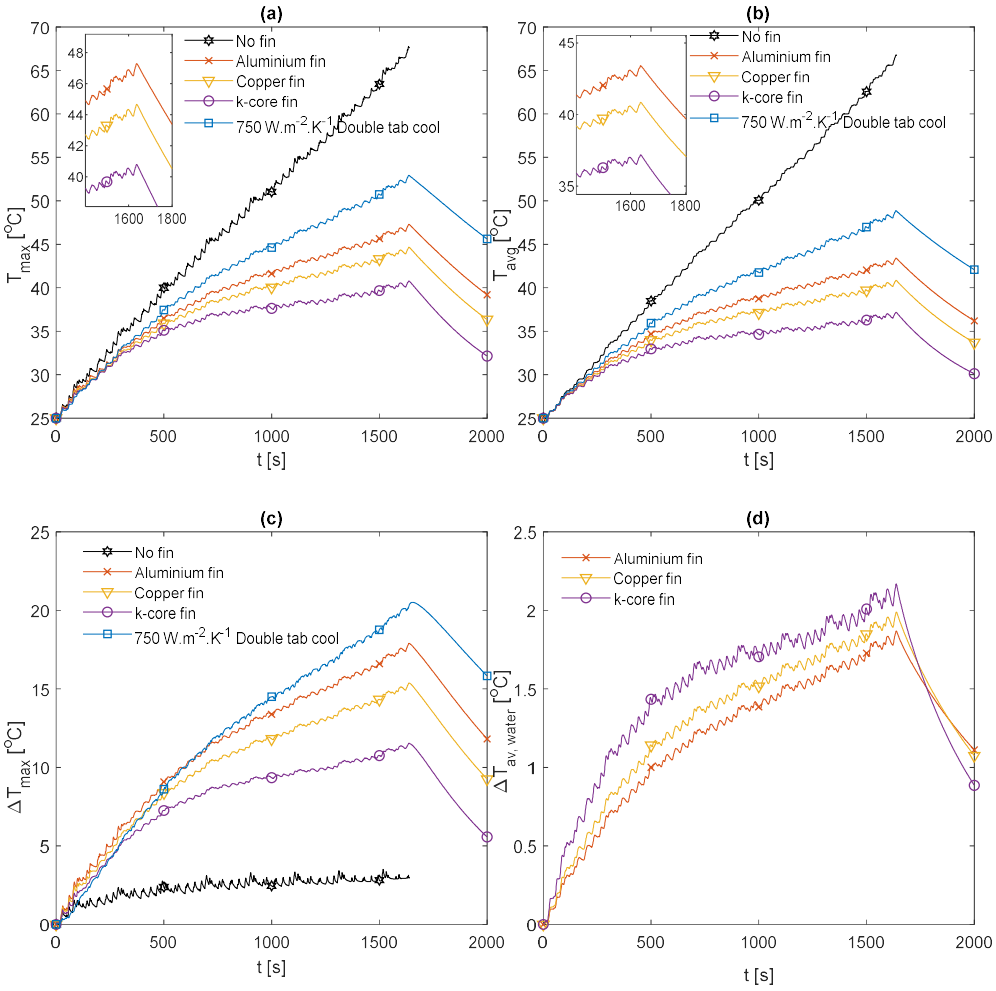

Figure 6-31: Effect of fin material choice on the BTMS thermal performance with 4 mm channel diameter and 0.006 kg.s^{-1} channel flow during the race duty cycle for (a) maximum cell temperature (b) volume averaged cell temperature (c) maximum cell temperature gradient (d) average exiting water coolant temperature

Relative to the aluminium fin, at the end of the duty cycle the k-core fin provides a decrease in T_{max} and T_{avg} of 6.52 ℃ and 6.25 ℃ respectively. Similar decreases in ΔT_{max}.of 6.37 ℃ are also achieved upon transitioning from the aluminium fin to the k-core fin. The decrease in cell surface temperature gradient is, however, more apparent with the k-core fin where a decrease of 8.3 ℃ is observed relative to aluminium. The superior ability of the k-core fin in improving the temperature uniformity of the cell is further demonstrated in Figure 6-32.

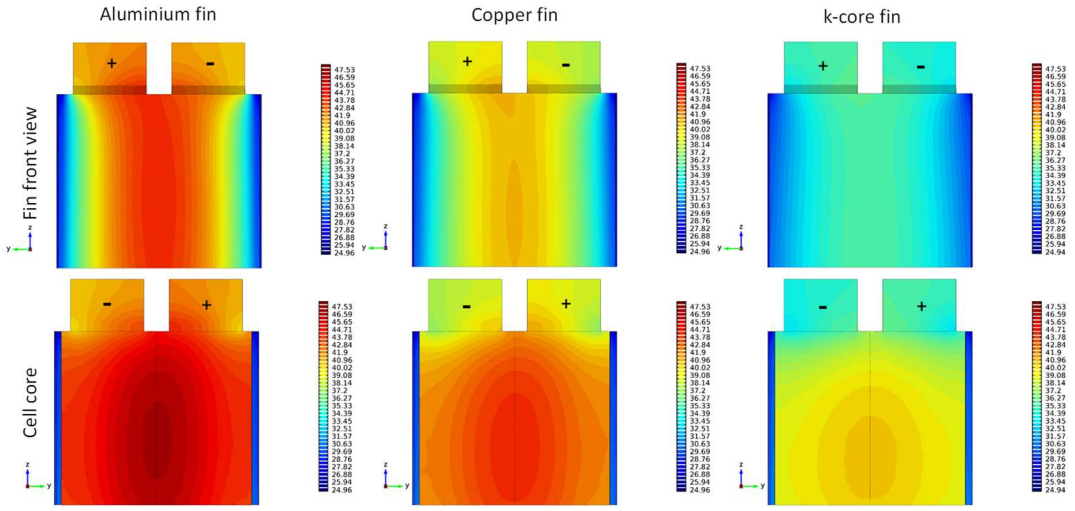

Figure 6-32: Thermal contours of the cell core and fin front view at the end of the race duty cycle with 0.006 kg.s^{-1}channel flow under different fin materials

The weight penalty of the fin BTMS as a function of fin material and fin thickness is shown in Figure 6-33. The k-core fin provides a slightly lower weight penalty than the aluminium fin at thickness of 1.16 and 1.00 mm respectively, with a value of 11.3%. This value is significantly lower than the fin BTMS design reported by Chen et al. [79] (which also considers a 1 mm thick fin between cells) which added 39% extra weight to the cell, further highlighting the efficiency of the proposed design as a lightweight solution under high performance EV conditions.

Figure 6-33 demonstrates that as the k-core fin thickness increases, the weight penalty is lowered relative to aluminium. This is due to the increased fraction of lighter APG relative to the aluminium skin layer. Investigating methods to reduce the skin layer thickness, or through using lighter encapsulant materials such as Kapton could further improve the weight efficiency of the k-core fin and is a scope for further work. The copper fin results in a large increase in mass added to the cell, with a value of 33.9% with the 1.00 mm thick fin, likely rendering it unsuitable for practical use.

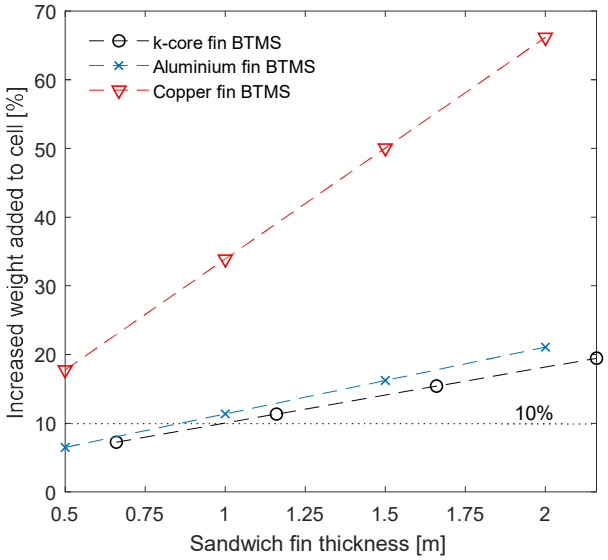

Figure 6-33: Effect of fin thickness on the BTMS weight as a function of fin material

A volume packing metric ($V_{m,p}$) can be defined, which considers the sandwich thickness of the fin in relation to the cell thickness.

$$V_{m,p} = \frac{Cell\ thickness}{Cell\ thickness + fin\ thickness} \tag{67}$$

Where $V_{m,p}$ is the volume packing metric. Values closer to unity for $V_{m,p}$ are conducive towards a more compact thermal management design. The volume packing metric as a function of sandwich fin thickness for the analysed cell is shown in Figure 6-34.

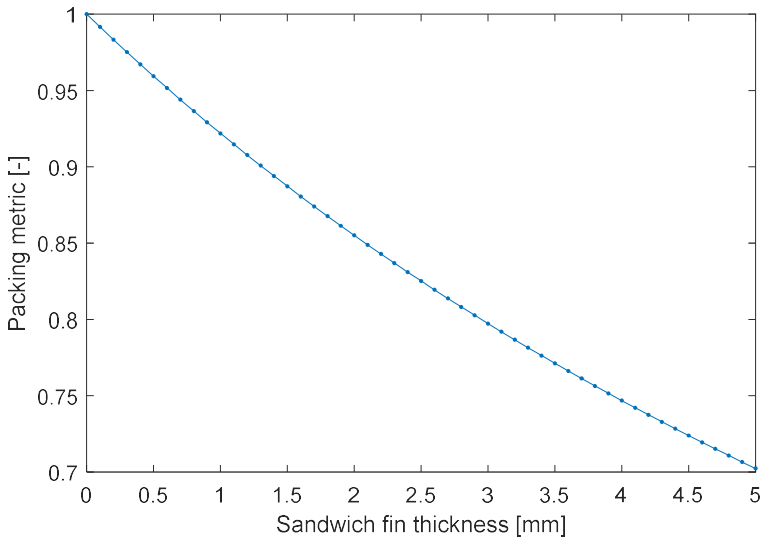

Figure 6-34: Volume packing metric as a function of the fin thickness

In this comparison, all fin materials provide a relatively high value for $V_{m,p}$ where the value for the k-core fin is reduced slightly from 0.922 to 0.910 due to the skin layer presence. A summary of the key thermal performance, weight and packing metrics from the comparison is included in Table 6-18.

Table 6-18: Tabulated thermal results at the end of the race duty cycle as a function of fin material

Fin material	T_{max} [°C]	T_{avg} [°C]	ΔT_{max} [°C]	$\Delta T_{max,s}$ [°C]	Increased weight added to cell [%]	Packing metric [-]
Aluminium (1.00 mm)	47.21	43.32	17.88	15.25	11.36	0.922
Copper (1.00 mm)	44.58	40.75	15.35	11.95	33.91	0.922
k-core (1.16 mm)	40.69	37.07	11.51	6.91	11.33	0.910

6.10 FURTHER WORK

Given the thermal improvement of the k-core fins over the reference case fins, further work should seek to analyse the effect of the reduced temperature gradient and peak temperature on the ageing rate of the cells. This would require long term testing of cells cooled with k-core fins and separate cells with aluminium fins under exact external cooling and electrical loading conditions.

The suitability of other encapsulating materials, such as Kapton, should be investigated to further lower the mass and volume penalty associated with the k-core fins. The thermal conductivity of k-core in curvilinear coordinates and also as a function of fin thickness is also another area for further research.

Heat capacity testing should also be carried out on the cells to compare the experimental value with the value used based on that reported in the literature. In addition, further characterisation of the cells and improved parameterisation of the cell model should be investigated to improve the accuracy of the predicted heat generation for values of stored energy less than 10% SOC.

6.11 CONCLUSION

K-core technology offered by Thermacore is identified as an attractive solution for a cooling material for pouch cells, given its light-weight properties and superior effective thermal conductivity when compared to conventional aluminium fins used in the current state of the art of BTMS. The heat removal ability of the k-core fin is demonstrated in both the experimental and simulation study to be superior to aluminium fins for the same weight

penalty. In addressing Research Objective 4, the thermal performance of the k-core fin in both the test rig configuration and simulated novel BTMS design is as follows.

The experimental results using the developed test rig reveal that single edge fin cooling pouch cells with k-core sheets can limit the maximum recorded fin surface temperature to 44.9℃, while the reference case aluminium fin reaches temperatures of 52.7 ℃ under an aggressive track racing cycle. This enables the cell cooled with k-core to operate within a far safer tolerance, given that the maximum temperature threshold for the cell is 65 ℃. However, whilst the k-core fin also provides greater temperature uniformity across the fin surface (13.0 ℃ measured gradient vs. 18.2 ℃ for aluminium), the thermals of the cell are still outside recommended limits present in the literature to limit cell ageing.

The extended simulation study on the presented novel two edge fin cooling solution highlights that the 1.16 mm thick k-core fin can limit the maximum volume averaged cell temperature rise and maximum cell surface temperature gradient to only 37.1 ℃ and 6.9 ℃ respectively, where the comparably sized aluminium fin results in surface temperature gradients exceeding 15 ℃.

A study on the effect of the fin thickness on the BTMS thermal performance suggests that k-core fins thicker than 1.16 mm may be undesirable due to the declining trade-off in thermal improvement from the incurred increase in system weight and reduced packing efficiency. With a fin thickness of 1.16 mm sandwiched between cells, the increased weight added to the cell is just 11.3% which is far less than the reported weight penalties from other fin cooled BTMS designs reported in the literature.

Due to the larger thermal head room offered by the k-core fin when two edge cooled, the thickness of the fin could be halved whilst still offering improved thermal performance over both aluminium and copper fins at even lower mass and volume penalties. The promising results of this work may act to accelerate the adoption of future lightweight, inherently safer fin cooling designs for automotive battery systems.

Figure 6-35 highlights the key areas of research conducted in Chapter Six that addresses Research Objective 4.

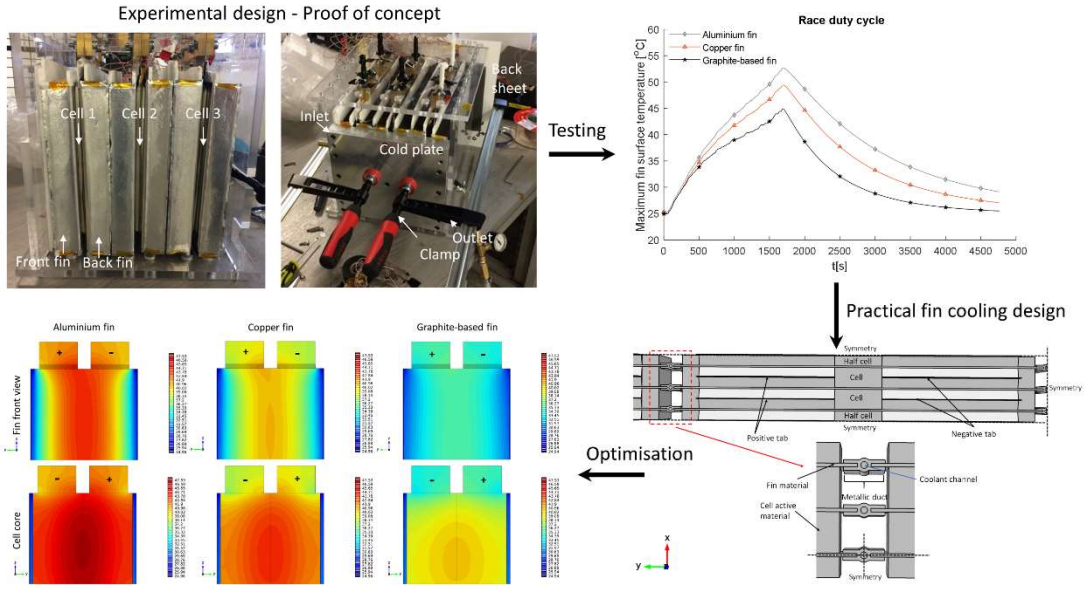

Figure 6-35: Graphical summary of the main areas of research conducted in Chapter Six

7 CHAPTER SEVEN- REFLECTIVE REVIEW AND FURTHER WORK

In this Chapter a reflective review on the research contained within the Portfolio is conducted. The innovation claims stemming from the research are presented, which demonstrates the impact of the research in terms of its contribution to academia and the industrial sponsor company Thermacore. A summary of the innovation claims and the contribution to academia and Thermacore are summarised in Table 7-1. Opportunities for Further Work are contained in Section 7.4.

7.1 INNOVATION CLAIM 1: NOVEL CELL-LEVEL THERMAL MANAGEMENT DESIGN CHARTS ARE CREATED FOR AUTOMOTIVE CYLINDRICAL CELLS

A 2-D validated transient bulk layer thermal model is created that captures the dominant thermal properties of cylindrical cells. The model is utilised to address Research Objective 1, which seeks to fill the research gap pertaining to a lack of understanding on the thermal performance of different cell-level thermal management strategies for cylindrical cells as a function of electrical loading conditions which reflect aggressive yet realistic use scenarios for a representative EV, PHEV and HEV. The 2-D capability and consideration of the cell anisotropic thermal conductivity enable for thermal comparisons between conventional outer surface cooling methods as a function of the cell heat generation rate. These include radial surface cooling, tab cooling and a combination of radial and tab cooling approaches.

Impact for Thermacore has been achieved through the development of steady-state thermal charts that provide clarity and useful initial design guidelines for developing the initial architecture of the BTMS as a function of the vehicle type and usage condition (e.g. EV or PHEV). Specifically, the research has demonstrated that cylindrical 18650 cells subject to steady-state heat generation rates greater than 1.1 W (reflective of performance EV applications) and cylindrical 32113 cells subject to HEV driving conditions require more involved thermal management consideration than is achievable with conventional exterior radial and single tab surface cooling. This highlights the limitations with the current approach to cylindrical cell thermal management (therefore emphasising the important contribution to academia) which defines the current state of the art for BTMS design. Applications that require internal core cooling are therefore defined, further advancing the academic understanding of cylindrical cell-level thermal management.

For 18650 cells subject to heat generation rates less than 1.1 W (which is expected to cover the majority of PHEV driving conditions), single tab cooling strategies employing liquid cooling are expected to provide adequate thermal performance and be preferable over radial liquid cooling due to the more favourable direction of the formed internal temperature gradients. The impact of this research to Thermacore is in the provision of knowledge to advise potential clients into suitable cell-level thermal management strategies based on their duty cycle requirements for common formats of cylindrical cells used in automotive applications.

The initial research is published in the 2016 Powertrains Modelling and Control Testing conference proceedings in [189] and later expanded for publication in the International Journal of Powertrains in [109] demonstrating the contribution of this research to academia.

7.2 INNOVATION CLAIM 2: A NOVEL INTERNAL COOLING APPROACH IS DEVELOPED FOR AUTOMOTIVE CYLYNDRICAL CELLS

The developed 2-D transient thermal model is expanded to include the presence of an internal heat pipe system that traverses the cell mandrel of cylindrical format battery cells. The novelty of the heat pipe system is in the addition of top and bottom metallic heat spreader discs connected to either end of the heat pipe. This enables the more efficient axial heat conduction pathways present within the cell to be utilised resulting in a dramatic reduction in the cell thermal resistance, where reductions of up to 67.8 ± 1.4% in the resistance value are achievable with the heat pipe system relative to conventional single tab cooling. This overcomes the issues relating to past research on internal heat pipe cooling [107] (and addresses Research Objective 2) which lacks the mechanism of axial cooling, resulting in the heat pipe providing minimal improvement over a solid copper rod due to the limiting heat transfer resistance in the perpendicular direction.

The superior thermal control offered by the internal heat pipe system extends the potential of simpler single sided tab cooling approaches to more aggressive electrical loading conditions (for example EV track racing conditions and HEV duty cycles) that as identified in the thermal design charts in Innovation Claim 1, are not acceptable thermally with either conventional radial or single tab cooling approaches.

Impact for Thermacore is provided through this theoretical research which acts as a foundation to further develop the advanced cooling solution for cylindrical format automotive cells. The research is published in the Journal of Power Sources contained within

[190] highlighting the contribution to academia through advancing the effectiveness of internal heat pipe cooling for cylindrical cells.

7.3 INNOVATION CLAIM 3: A NOVEL FIN MATERIAL AND FIN COOLED BTMS DESIGN IS DEVELOPED FOR LARGE FORMAT AUTOMOTIVE POUCH CELLS

In addressing Research Objective 3, the research from Chapter Five has identified that cooling the large surface faces of pouch cells is likely required for aggressive PHEV duty cycles and performance EV applications. This is because tab cooling large format pouch batteries suffers from inadequate available heat transfer area at the battery tabs which renders these strategies incapable of controlling the battery operating temperature rise to safe limits when exposed to aggressive PHEV and performance EV conditions.

Due to the issues pertaining to indirect liquid cold plates with their inherent leakage concerns, an extended surface/fin cooling approach is sought to target cooling on the large front and back surfaces of pouch cells. The attractive properties of the solid conduction k-core technology developed by Thermacore (e.g. lower density than aluminium and superior effective thermal conductivity) offer a promising solution as an advanced cooling material in a fin based BTMS.

To assess the suitability of k-core as a battery cooling material, an experimental test rig is developed in which k-core fins are manufactured to provide fin cooling on real large format 53 Ah pouch cells designed for high performance automotive applications. The thermal performance of the fins is compared against conventional aluminium and copper materials, in which the experimental testing demonstrates the superior thermal management performance offered by k-core for the same weight penalty as aluminium.

Based on the promising results from the experimental work, a novel conceptual fin cooled BTMS design is further developed and presented for use in a real vehicle. The two edge fin cooled solution offers parallel cooling between cells within a module, an inherent design choice that acts to minimise the development of module-level temperature gradients to reduce the negative performance impacts associated with unwanted temperature inhomogeneities [40].

The contribution to academia is demonstrated in the extensive thermal analysis of the advanced fin material, which quantifies the thermal improvement relative to conventional fin materials used in current generation BTMS. Relative to aluminium fins with comparable

weight and volume penalties, the k-core fin BTMS is simulated to offer a 55% reduction in cell surface temperature gradient and a decrease in the average battery volumetric temperature rise of 6.3 ℃. The larger thermal head room offered by the k-core fin offers the flexibility to halve the fin thickness and achieve improved thermal performance over both aluminium and copper fins at even lower mass and volume penalties, thus addressing Research Objective 4. The weight penalty of the proposed BTMS is significantly lighter than other fin based BTMS reported in the literature [79] (11% vs. 39% weight added to the cell), highlighting its potential in a future vehicle application.

The promising results of this work have demonstrated strong impact to Thermacore, leading to the acquisition of a patent on the fin BTMS design (US Provisional Application Number 62593706, details of which are included in the Personal Profile document of the Portfolio).

Evidence of the contribution of the research from Chapter Six to academia is shown in the 2017 IEEE Vehicle Power and Propulsion Conference Paper contained within [191], where the aluminium and copper fin test rig results are presented to further the understanding on potential applications for fin cooled BTMS in the literature. The k-core fin research, together with the novel edge cooled BTMS design, is under review in the Journal of Energy Conversion and Management. Further academic contributions from this portion of the research may act to accelerate the adoption of future lightweight, inherently safer fin cooling designs for automotive battery systems.

Table 7-1: Summary of the thesis Innovation claims

Innovation number	Innovation claim	Contribution to academia	Impact to Thermacore
1	1). Novel cell-level thermal management design charts are created for automotive cylindrical cells. Clarifies the usage cases that require non-conventional cooling methods.	Published in the International Journal of Powertrains [109].	Identifies the usage cases that are in particular need for more involved thermal management strategies. Guides the choice of target market to launch an advanced BTMS design that addresses these thermal limitations.
2	2). Novel internal cooling approach is developed for automotive cylindrical cells employing a heat pipe system.	Published in the Journal of Power Sources [190].	Quantifies the theoretical thermal performance improvement of an internal heat pipe system for core cooling cylindrical cells. Provides a foundation on which to further develop the design for use in a real application.
3	3). A novel fin material and fin cooled BTMS design is developed for large format automotive pouch cells.	Aluminium and copper fin results published in the 2017 IEEE Vehicle Power and Propulsion Conference Paper contained within [191]. K-core fin results and the novel fin cooled BTMS design are under review in the Journal of Energy Conversion and Management	Thermacore have filled a US Provisional patent application on the k-core fin BTMS design. The research may act to propel the deployment of k-core based BTMS for use in future electrified vehicles, thus extending the range of inherently safer fin cooled BTMS to more aggressive duty cycles.

7.4 FURTHER WORK

The conclusions from Chapter Three outline that liquid tab cooling may be a preferable strategy over liquid radial cooling for cylindrical cells suitable up to aggressive PHEV applications (where the time averaged heat generation rate does not exceed 1.1 W). This is since the direction of the temperature gradient is axial through the cell and predicted to remain below 5 ℃. However, to the authors knowledge, little experimental work has been reported within the literature on how a liquid tab cooled strategy would be implemented in a BTMS design. Further work should seek to conduct experiments to further investigate the potential of tab cooling, such as through contacting discrete coolant tubes across the base of cylindrical cells whilst varying the liquid flowrate to control the heat transfer rate. The method in which the cooling strategy is implemented at the tab together with the electrical connections would require careful consideration as to not introduce excessive thermal resistance between the tab base and coolant medium.

The theoretical benefit of incorporating the proposed heat pipe system in Chapter Four is demonstrated. However, practical implementation of the device inside the cell requires further investigation. The top spreader disc may require perforated holes throughout to enable passage of the current collector tabs, which also may require an electrically insulating laminate to ensure that an electrical connection is not created between the positive and negative tabs of the cell. Manufacture of test heat pipe devices with the spreader discs connected is recommended, where the assembly steps for wrapping the cell layers around the heat pipe should be explored. This avenue of research could be combined with the first further work recommendation of investigating the tab cooling mechanism, given that the heat pipe system acts to increase the thermal performance of a singular tab cooled stagey. Comparisons between the cell thermal performance with and without the heat pipe device under singular tab cooling could then be performed.

The results stemming from the simulation work on the novel fin cooled BTMS design presented in Chapter Six highlight its potential as an advanced BTMS design under aggressive performance EV duty cycles. Further work should seek to extend the research by manufacturing the solution on the module level. Here, further testing can seek to gauge the improved thermal conditions of the cell on the ageing rate under long term testing. The ageing rate of cells cooled with k-core fins could be compared to that using aluminium fins under the same fin thickness and external cooling flowrate through the side cooling ducts in contact with the fin edges. This may quantify the benefit of seeking more effective thermal

management based on differences in ageing rate. Further, electrically insulating Kapton encapsulated k-core fins should be assessed, given the potential for further weight reduction and therefore improved gravimetric energy density of the BTMS design.

A summary of opportunities for further work identified from the thesis research is contained in Table 7-2.

Table 7-2: Summary of opportunities for further work identified from the thesis

Further work no.	Extends on research conducted in Chapter no.	Description of research opportunities
1	Three	Experimentally investigate the thermal performance of a liquid tab cooled approach for cylindrical format cells.
2	Four	Investigate how the heat pipe system would be practically inserted within a real cylindrical cell. Avoiding the creation of an internal short circuit is imperative.
3	Six	A module level assembly of the fin cooled BTMS design should be manufactured and tested. This will further assess the real-world performance of the BTMS design on an experimental level. Long term ageing testing on cells cooled with k-core in comparison to those cooled with conventional aluminium may act to quantify the benefit of using greater thermally conductive fin materials in terms of differences in ageing rate. The use of Kapton encapsulated APG should also be explored for further weight reduction.

8 CHAPTER 8 - CONCLUSIONS

A critical review on battery thermal management systems (BTMS) for automotive applications (conducted in Chapter Two) has identified that a majority of cooling solutions within the current state of the art seek to target exterior cooling of battery cells in both cylindrical and pouch type formats. These strategies rely on the predominant heat transfer mode being perpendicular through the layers of the cell, which can lead to large thermal resistances stemming from the poor effective perpendicular thermal conductivity of lithium-ion cells. This limiting resistance (of which is particularly problematic for cylindrical cells) can cause excessive internal temperature gradients and hot spots to develop within the cell as it is cycled, which has been shown to accelerate irreversible capacity loss and power fade which reduces power delivery.

To mitigate thermal issues for cylindrical cells, a few studies have sought to employ internal cooling to lower the thermal resistance and improve the heat transfer rate. However, it is not properly defined within the literature as to what electrical loading conditions require such involved thermal management methods, given recommended limits on averaged battery operating temperature and internal temperature gradient magnitude. Therefore, it is unclear whether internal cooling is required for cells subject to realistic electric vehicle (EV), plug-in hybrid vehicle (PHEV), hybrid vehicle (HEV) or performance EV usage cases. This knowledge gap drives Research Objective 1, which seeks to analyse the cell-level thermal response of different variants of cylindrical cells as a function of the applied cooling strategy and electrical loading condition. Quantifying the thermal performance in this manner acts to identify usage cases that are in particular need for more involved internal core cooling approaches, thus guiding the direction of further research.

In addressing Research Objective 1, Chapter Three presents a validated transient 2-D thermal model capable of capturing the dominate thermal properties of cylindrical lithium ion cells, which is utilised to analyse the cell-level thermal performance when subject to different exterior cooling approaches. It is identified that for 18650 format batteries commonly employed in EV and PHEV use cases, conventional surface or tab cooling strategies are likely capable of limiting the internal temperature gradient rise to below $5℃$, which is widely reported in the literature as an acceptable limit. Therefore, it is predicted that internal core cooling is not necessarily required under these circumstances. However, the developed thermal charts contained in Chapter Three highlight the limited cooling ability offered by radial and single tab cooling as the internal heat generation rate increases. Specifically, for

32113 type cylindrical cells subject to HEV driving conditions, extreme internal temperature gradients in excess of 15 ℃ are predicted for both radial surface and single tab cooling. This is also the case for 18650 cells subject to performance EV conditions. Therefore, it is identified that these applications are candidates to benefit particularly from internal cooling. The thermal charts contained in Chapter Three act to further the understanding on the theoretical cooling performance of different tab and surface cooling configurations to guide the overall cell-level thermal management strategy of the BTMS design for different automotive usages cases.

In response to the identified need for internal cooling under HEV and performance EV applications, Research Objective 2 investigates methods to improve the cooling performance of heat pipes (of which is a core technology of the sponsor company) inserted within the core of cylindrical cells. This Objective is tackled in Chapter Four, which presents a novel internal cooling device employing a heat pipe connected to top and bottom heat spreader discs. The inclusion of the metallic discs act to extend the heat transfer potential of internal heat pipe cooling past that offered currently in the literature (thus demonstrating important contributions to academia), given that the more efficient axial heat conduction pathways within the cell are utilised. The device is simulated to offer a reduction in cell thermal resistance by up to 67.8% relative to single tab cooling without the addition, extending the use of a single tab cooling approach upwards to HEV and performance EV applications. With this reduced resistance, thermal gradients occurring inside common format cylindrical batteries are simulated to be reduced near the recommended threshold of 5 ℃ during even the most strenuous of use case, which is not possible with conventional radial or singular tab cooling strategies. The heat pipe device has the potential to be directly incorporated within the internals of individual battery cells used in conventional singular tab cooling arrangements. This offers a direct improvement to the thermal uniformity of batteries integrated within current heating, ventilation and air conditioning (HVAC) cooling systems. Impact to Thermacore is achieved through this theoretical research, which acts as a foundation upon which to develop further practical based work to integrate the heat pipe device within real cylindrical cells as an advanced cooling solution.

The second stream of related research focuses on thermal management methods and considerations for pouch cells, a format of lithium-ion battery which is witnessing increased use within automotive energy storage systems. Research Objective 3 seeks to clarify the cell-level thermal management strategy for pouch cells as a function of the electrical loading condition, of which is not clearly defined within the literature. This Objective is addressed by

the research contained within Chapter Five, where cell-level thermal models are developed to analyse the thermal performance of exterior tab and surface cooling options. Due to the limited surface area offered by tab cooling, it is predicted that surface cooling on both the front and back surfaces is required to limit the averaged cell temperature rise and internal gradient to more acceptable limits under aggressive PHEV and performance EV duty cycles. For commercial EV use and some mild PHEV cycles, liquid tab cooling for the analysed cell with opposite ended tab configurations is expected to be satisfactory, where the maximum temperature gradient can be limited to the 5 ℃ range provided the averaged cell body heat generation rate remains below 7.7 W.

Based on the recommendations from Chapter Five, a double sided surface cooling approach for pouch cells is sought to address the thermal management needs of performance EV applications. To reduce the inherent leakage concerns associated with conventional methods of attaching liquid cooled mini-channel cold plates to the pouch surfaces (of which is representative of the current state of the art for pouch cell based BTMS), a conduction-based fin cooling solution is investigated. To lower the thermal resistance penalty associated over the use of conventional aluminium fins, and extend the reach of fin cooling and the associated inherent safety benefits to more aggressive electrical loading conditions, Research Objective 4 is defined. This Objective seeks to quantify the thermal performance of a new, highly conductive fin material (for use in a fin based BTMS) employing advanced solid conduction technology offered by Thermacore. This Research Objective is addressed in Chapter Six, which experimentally investigates the thermal performance of the new fin against conventional copper and aluminium fin materials. Further, a novel practical implementation for the fin based BTMS is presented, where an extended simulation analysis demonstrates the improved thermal efficiency of the design relative to other fin based BTMS reported in the literature, offering important contributions to academia. Specifically, the new fin offers a reduction in the cell surface temperature gradient of up to 55% and maximum cell temperature reduction of circa 15% relative to conventional aluminium fins, enabling constraints on cell temperature rise and thermal gradient reduction to more readily be satisfied. As the fin is a conduction element with no moving parts, it can be substituted into existing aluminium fin based BTMS used within current HVAC cooling systems to directly improve the thermal performance at no additional weight penalty.

The novel cooling approaches presented within this thesis offer impact to both Thermacore and the scientific community, through advancing the development of next generation BTMS that provide improved thermal efficiency relative to the current BTMS state of the art.

9 REFERENCES

[1] A. Mahmoudzadeh Andwari, A. Pesiridis, S. Rajoo, R. Martinez-Botas, and V. Esfahanian, "A review of Battery Electric Vehicle technology and readiness levels," *Renew. Sustain. Energy Rev.*, vol. 78, no. May, pp. 414–430, 2017.

[2] F. Karimi and R. Khalilpour, "Evolution of carbon capture and storage research: Trends of international collaborations and knowledge maps," *Int. J. Greenh. Gas Control*, vol. 37, pp. 362–376, 2015.

[3] F. Cao, Q. Liu, T. Yang, T. Zhu, J. Bai, and L. Zhao, "Full-year simulation of solar chimney power plants in Northwest China," *Renew. Energy*, vol. 119, pp. 421–428, 2018.

[4] C. Chancham, J. Waewsak, and Y. Gagnon, "Offshore wind resource assessment and wind power plant optimization in the Gulf of Thailand," *Energy*, vol. 139, pp. 706–731, 2017.

[5] Y. H. Bae, K. O. Kim, and B. H. Choi, "Lake Sihwa tidal power plant project," *Ocean Eng.*, vol. 37, no. 5–6, pp. 454–463, 2010.

[6] EU Commision, "Road transport: Reducing CO2 emissions from vehicles," *European Commision*, 2015. [Online]. Available: http://ec.europa.eu/clima/policies/transport/vehicles/index_en.htm. [Accessed: 14-Jan-2016].

[7] International Energy Agency (IEA), "Technology roadmap: Electric and plug-in hybrid electric vehicles," *Int. Energy Agency, Tech. Rep*, no. June, p. 52, 2011.

[8] International Energy Agency, "Global EV Outlook 2017: Two million and counting," 2017.

[9] Goldman Sachs Global Investment Research, "Electric Vehicle Boom : ICE-ing The Combustion Engine," 2017.

[10] C. C. Chan, "The state of the art of electric, hybrid, and fuel cell vehicles," *Proc. IEEE*, vol. 95, no. 4, pp. 704–718, 2007.

[11] B. Nykvist and M. Nilsson, "Rapidly falling costs of battery packs for electric vehicles," *Nat. Clim. Chang.*, vol. 5, no. 4, pp. 329–332, Apr. 2015.

[12] C. Linse and R. Kuhn, "Design of high-voltage battery packs for electric vehicles," in *Advances in Battery Technologies for Electric Vehicles*, Elsevier Ltd., 2015, pp. 245–263.

[13] A. Dinger *et al.*, "Focus Batteries for Electric Cars," p. 18, 2010.

[14] C. Cluzel and C. Douglas, "Cost and performance of EV batteries," 2012.

[15] J. F. Miller, "Analysis of current and projected battery manufacturing costs for electric, hybrid, and plug-in hybrid electric vehicles," *World Electr. Veh. J.*, vol. 4, no. 1, pp. 347–350, 2011.

[16] Automotive Council UK; Advanced Propulsion Center UK, “Electrical Energy Storage Roadmap,” 2018.

[17] USABC, “USABC Goals for Advanced Batteries for PHEVs for FY 2018 to 2020 Commercialization,” 2014. [Online]. Available: http://www.uscar.org/guest/article_view.php?articles_id=85. [Accessed: 09-Sep-2018].

[18] USABC, “US Advanced Battery Consortium LLC: USABC Goals for Advanced Batteries for Evs - CY 2020 Commercialization,” 2014. [Online]. Available: http://www.uscar.org/guest/article_view.php?articles_id=85.

[19] R. Spotnitz, “Simulation of capacity fade in lithium-ion batteries,” *J. Power Sources*, vol. 113, no. August 2002, pp. 72–80, 2003.

[20] X. Luo, J. Wang, M. Dooner, and J. Clarke, “Overview of current development in electrical energy storage technologies and the application potential in power system operation,” *Appl. Energy*, vol. 137, pp. 511–536, 2015.

[21] H. D. Yoo, E. Markevich, G. Salitra, D. Sharon, and D. Aurbach, “On the challenge of developing advanced technologies for electrochemical energy storage and conversion,” *Mater. Today*, vol. 17, no. 3, pp. 110–121, 2014.

[22] G. E. Blomgren, “The Development and Future of Lithium Ion Batteries,” *J. Electrochem. Soc.*, vol. 164, no. 1, pp. A5019–A5025, 2017.

[23] P. Tan *et al.*, “Advances and challenges in lithium-air batteries,” *Appl. Energy*, vol. 204, pp. 780–806, 2017.

[24] U. R. Farooqui, A. L. Ahmad, and N. A. Hamid, “Challenges and potential advantages of membranes in lithium air batteries: A review,” *Renew. Sustain. Energy Rev.*, vol. 77, no. December 2016, pp. 1114–1129, 2017.

[25] H. Zhao *et al.*, “A review on anode for lithium-sulfur batteries: Progress and prospects,” *Chem. Eng. J.*, vol. 347, no. April, pp. 343–365, 2018.

[26] G. Li, Z. Chen, and J. Lu, “Lithium-Sulfur Batteries for Commercial Applications,” *Chem*, vol. 4, no. 1, pp. 3–7, 2018.

[27] X. Zhang, H. Xie, C. S. Kim, K. Zaghib, A. Mauger, and C. M. Julien, “Advances in lithium—sulfur batteries,” *Mater. Sci. Eng. R Reports*, vol. 121, pp. 1–29, 2017.

[28] G. E. Blomgren, “The Development and Future of Lithium Ion Batteries,” *J. Electrochem. Soc.*, vol. 164, no. 1, pp. A5019–A5025, 2017.

[29] T. M. Bandhauer, S. Garimella, and T. F. Fuller, “A Critical Review of Thermal Issues in Lithium-Ion Batteries,” *J. Electrochem. Soc.*, vol. 158, p. R1, 2011.

[30] A. Tourani, P. White, and P. Ivey, “Analysis of electric and thermal behaviour of lithium-ion cells in realistic driving cycles,” *J. Power Sources*, vol. 268, pp. 301–314, 2014.

[31] G. K. A. Pesaran , S.Santhanagopalan, “Addressing the Impact of Temperature

Extremes on Large Format Li-Ion Batteries for Vehicle Applications," in *30TH INTERNATIONAL BATTERY SEMINAR*, 2013.

[32] Y. Ji, Y. Zhang, and C.-Y. Wang, "Li-Ion Cell Operation at Low Temperatures," *J. Electrochem. Soc.*, vol. 160, no. 4, pp. A636–A649, 2013.

[33] A. H. Zimmerman and M. V Quinzio, "Lithium Plating in Lithium-Ion Cells," *Lithium*, no. November, 2010.

[34] V. Agubra and J. Fergus, "Lithium Ion Battery Anode Aging Mechanisms," *Materials (Basel).*, vol. 6, no. 4, pp. 1310–1325, 2013.

[35] T. Waldmann, M. Wilka, M. Kasper, M. Fleischhammer, and M. Wohlfahrt-Mehrens, "Temperature dependent ageing mechanisms in Lithium-ion batteries – A Post-Mortem study," *J. Power Sources*, vol. 262, pp. 129–135, 2014.

[36] V. Zinth *et al.*, "Lithium plating in lithium-ion batteries at sub-ambient temperatures investigated by in situ neutron diffraction," *J. Power Sources*, vol. 271, pp. 152–159, 2014.

[37] A. Kvasha *et al.*, "A comparative study of thermal runaway of commercial lithium ion cells," *Energy*, vol. 159, pp. 547–557, 2018.

[38] J. Vetter *et al.*, "Ageing mechanisms in lithium-ion batteries," *J. Power Sources*, vol. 147, no. 1–2, pp. 269–281, 2005.

[39] Q. Wang, B. Jiang, B. Li, and Y. Yan, "A critical review of thermal management models and solutions of lithium-ion batteries for the development of pure electric vehicles," *Renew. Sustain. Energy Rev.*, vol. 64, pp. 106–128, 2016.

[40] N. Yang, X. Zhang, B. Shang, and G. Li, "Unbalanced discharging and aging due to temperature differences among the cells in a lithium-ion battery pack with parallel combination," *J. Power Sources*, vol. 306, pp. 733–741, 2016.

[41] M. Fleckenstein, O. Bohlen, M. a. Roscher, and B. Bäker, "Current density and state of charge inhomogeneities in Li-ion battery cells with LiFePO4 as cathode material due to temperature gradients," *J. Power Sources*, vol. 196, no. 10, pp. 4769–4778, 2011.

[42] Y. Troxler *et al.*, "The effect of thermal gradients on the performance of lithium-ion batteries," *J. Power Sources*, vol. 247, pp. 1018–1025, 2014.

[43] M. Fleckenstein, O. Bohlen, and B. Bäker, "Aging effect of temperature gradients in Li-ion cells experimental and simulative investigations and the consequences on thermal battery management," *World Electr. Veh. J.*, vol. 5, no. 2, pp. 322–333, 2012.

[44] A. Greco, D. Cao, X. Jiang, and H. Yang, "A theoretical and computational study of lithium-ion battery thermal management for electric vehicles using heat pipes," *J. Power Sources*, vol. 257, pp. 344–355, 2014.

[45] Y. Ye, L. H. Saw, Y. Shi, and A. a. O. Tay, "Numerical analyses on optimizing a heat pipe thermal management system for lithium-ion batteries during fast charging,"

Appl. Therm. Eng., vol. 86, pp. 281–291, 2015.

[46] A. Pesaran, “Battery thermal models for hybrid vehicle simulations,” *J. Power Sources*, vol. 110, pp. 377–382, 2002.

[47] T.-H. Tran, S. Harmand, and B. Sahut, “Experimental investigation on heat pipe cooling for Hybrid Electric Vehicle and Electric Vehicle lithium-ion battery,” *J. Power Sources*, vol. 265, pp. 262–272, 2014.

[48] R. Zhao, J. Gu, and J. Liu, “An experimental study of heat pipe thermal management system with wet cooling method for lithium ion batteries,” *J. Power Sources*, vol. 273, pp. 1089–1097, 2015.

[49] Q. Wang, P. Ping, X. Zhao, G. Chu, J. Sun, and C. Chen, “Thermal runaway caused fire and explosion of lithium ion battery,” *J. Power Sources*, vol. 208, pp. 210–224, 2012.

[50] E. Hosseinzadeh, A. Barai, J. Marco, and P. Jennings, “A Comparative Study on Different Cooling Strategies for Lithium-Ion Battery Cells,” *Eur. Batter. Hybrid Fuel Cell Electr. Veh. Congr. (EEVC 2017)*, pp. 1–9, 2017.

[51] Z. Rao and S. Wang, “A review of power battery thermal energy management,” *Renew. Sustain. Energy Rev.*, vol. 15, no. 9, pp. 4554–4571, 2011.

[52] A. Pesaran, “Battery Thermal Management in EVs and HEVs : Issues and Solutions,” *Adv. Automot. Batter. Conf.*, p. 10, 2001.

[53] C. Huber and R. Kuhn, “13 - Thermal management of batteries for electric vehicles,” in *Advances in Battery Technologies for Electric Vehicles*, B. S. G. Tillmetz, Ed. Woodhead Publishing, 2015, pp. 327–358.

[54] S. Park and D. Jung, “Battery cell arrangement and heat transfer fluid effects on the parasitic power consumption and the cell temperature distribution in a hybrid electric vehicle,” *J. Power Sources*, vol. 227, pp. 191–198, 2013.

[55] AAVID Thermacore, “About Us.” pp. 1–30, 2017.

[56] D. Reay, R. McGlen, and P. Kew, *Heat pipes: Theory, design and applications*. Butterworth-Heinemann, 2013.

[57] Thermacore, “k-Core ® : A New Dimension in Conductive Heat Transfer,” 2013. [Online]. Available: https://www.thermacore.com/documents/k-Core_Product_Brochure.pdf. [Accessed: 15-May-2018].

[58] C. Morris, “Charged EVs _ Nissan announces price for replacement LEAF battery,” 2014. [Online]. Available: https://chargedevs.com/newswire/nissan-announces-price-for-replacement-leaf-battery/.

[59] U.S. Climate Data, “Climate Phoenix - Arizona,” 2019. [Online]. Available: https://www.usclimatedata.com/climate/arizona/united-states/3172. [Accessed: 07-Mar-2019].

[60] J. LeSage, “Nissan’s Andy Palmer discusses Leaf battery degradation crisis [w/video].” 2012.

[61] A. Turpen, “New data from Canada shows cold weather range loss in Nissan LEAF and Chevrolet Volt - Torque News,” 2013. [Online]. Available: http://www.torquenews.com/1080/new-data-canada-shows-cold-weather-range-loss-nissan-leaf-and-chevrolet-volt.

[62] Nissan, “2013 LEAF Owners Manual,” 2013.

[63] A. Pesaran, A. Vlahinos, and T. Stuart, “Cooling and preheating of batteries in hybrid electric vehicles,” *6th ASME-JSME Therm. Eng. …*, pp. 1–7, 2003.

[64] K. G. Gallagher and P. a. Nelson, “Manufacturing Costs of Batteries for Electric Vehicles,” in *Lithium-Ion Batteries Advances and Applications*, Elsevier, 2014, pp. 97–126.

[65] G. Xia, L. Cao, and G. Bi, “A review on battery thermal management in electric vehicle application,” *J. Power Sources*, vol. 367, pp. 90–105, 2017.

[66] M. Anderman, “The Tesla Battery Report Outline,” 2014.

[67] M. Zolot, A. a. Pesaran, and M. Mihalic, “Thermal Evaluation of Toyota Prius Battery Pack,” *SAE Int.*, no. 2002-01–1962, 2002.

[68] H. Sun, X. Wang, B. Tossan, and R. Dixon, “Three-dimensional thermal modeling of a lithium-ion battery pack,” *J. Power Sources*, vol. 206, pp. 349–356, 2012.

[69] U.S. Environmental Protection Agency, “Dynamometer Drive Schedules, Testing and Measuring Emissions,” *.Http://Www.Epa.Gov/Nvfel/Testing/Dynamometer.Htm*. [Online]. Available: http://www.epa.gov/nvfel/testing/dynamometer.htm.

[70] H. Sun and R. Dixon, “Development of cooling strategy for an air cooled lithium-ion battery pack,” *J. Power Sources*, vol. 272, pp. 404–414, 2014.

[71] H. Park, “A design of air flow configuration for cooling lithium ion battery in hybrid electric vehicles,” *J. Power Sources*, vol. 239, pp. 30–36, 2013.

[72] L. Fan, J. M. Khodadadi, and a. a. Pesaran, “A parametric study on thermal management of an air-cooled lithium-ion battery module for plug-in hybrid electric vehicles,” *J. Power Sources*, vol. 238, pp. 301–312, 2013.

[73] S. K. Mohammadian and Y. Zhang, “Thermal management optimization of an air-cooled Li-ion battery module using pin- fi n heat sinks for hybrid electric vehicles,” *J. Power Sources*, vol. 273, pp. 431–439, 2015.

[74] M. R. Giuliano, A. K. Prasad, and S. G. Advani, “Experimental study of an air-cooled thermal management system for high capacity lithium-titanate batteries,” *J. Power Sources*, vol. 216, pp. 345–352, 2012.

[75] R. Mahamud and C. Park, “Reciprocating air flow for Li-ion battery thermal management to improve temperature uniformity,” *J. Power Sources*, vol. 196, no. 13, pp. 5685–5696, 2011.

[76] Y. Deng *et al.*, “Effects of different coolants and cooling strategies on the cooling performance of the power lithium ion battery system: A review,” *Appl. Therm. Eng.*,

vol. 142, no. June, pp. 10–29, 2018.

[77] R. Zhao, S. Zhang, J. Liu, and J. Gu, “A review of thermal performance improving methods of lithium ion battery: Electrode modification and thermal management system,” *J. Power Sources*, vol. 299, pp. 557–577, 2015.

[78] G. H. Kim and A. Pesaran, “Battery Thermal Management System Design Modeling,” *22nd Int. Batter. Hybrid Fuel Cell Electr. Veh. Conf. Exhib. EVS22*, vol. 1, no. November, pp. 126–133, 2006.

[79] D. Chen, J. Jiang, G. Kim, C. Yang, and A. Pesaran, “Comparison of different cooling methods for lithium ion battery cells,” *Appl. Therm. Eng.*, vol. 94, pp. 846–854, 2016.

[80] C. Hendricks, N. Williard, S. Mathew, and M. Pecht, “A failure modes, mechanisms, and effects analysis (FMMEA) of lithium-ion batteries,” *J. Power Sources*, vol. 297, pp. 113–120, 2015.

[81] T. Dillard, “Look Inside A Tesla Model S Battery Pack.” 2015.

[82] Tesla Motors, “Patent US8647763 - Battery coolant jacket - Google Patents.”

[83] Chevrolet, “2016 CHEVROLET VOLT BATTERY SYSTEM,” 2016.

[84] Chevrolet, “Cooling fins help keep Chevrolet volt battery at ideal temperature,” 2011. [Online]. Available: http://media.gm.com/media/us/en/chevrolet/news.detail.html/content/Pages/news/us/en/2011/Feb/0214_battery.html.

[85] Y. Huo, Z. Rao, X. Liu, and J. Zhao, “Investigation of power battery thermal management by using mini-channel cold plate,” *Energy Convers. Manag.*, vol. 89, pp. 387–395, 2015.

[86] J. Zhao, Z. Rao, and Y. Li, “Thermal performance of mini-channel liquid cooled cylinder based battery thermal management for cylindrical lithium-ion power battery,” *Energy Convers. Manag.*, vol. 103, pp. 157–165, 2015.

[87] K. Shah *et al.*, “Modeling of steady-state convective cooling of cylindrical Li-ion cells,” *J. Power Sources*, vol. 258, pp. 374–381, 2014.

[88] S. J. Drake, D. a. Wetz, J. K. Ostanek, S. P. Miller, J. M. Heinzel, and a. Jain, “Measurement of anisotropic thermophysical properties of cylindrical Li-ion cells,” *J. Power Sources*, vol. 252, pp. 298–304, 2014.

[89] S. Basu, K. S. Hariharan, S. M. Kolake, T. Song, D. K. Sohn, and T. Yeo, “Coupled electrochemical thermal modelling of a novel Li-ion battery pack thermal management system,” *Appl. Energy*, vol. 181, pp. 1–13, 2016.

[90] R. Mastrullo, a W. Mauro, A. Rosato, and G. P. Vanoli, “Comparison of R744 and R134a heat transfer coefficients during flow boiling in a horizontal circular smooth tube,” in *International Conference on Renewable Energies and Power Quality*, 2009, vol. 52, no. 19–20, pp. 4184–4194.

[91] Munro & Associates, “BMW i3 Teardown and Benchmarking Study,” 2015.

[92] I. Munro & Associates, “BMWi3 Battery Pack,” 2015. [Online]. Available: https://www.youtube.com/watch?v=YZ9UpLkVJlo.

[93] R. Katkar, Satish; Laurain, Paul; Miccormick, “BATTERY SYSTEM AND METHOD FOR COOLING THE BATTERY SYSTEM - LG CHEM, LTD,” 2014.

[94] R. W. Van Gils, D. Danilov, P. H. L. Notten, M. F. M. Speetjens, and H. Nijmeijer, “Battery thermal management by boiling heat-transfer,” *Energy Convers. Manag.*, vol. 79, pp. 9–17, 2014.

[95] S. Al Hallaj and J. R. Selman, “A Novel Thermal Management System for Electric Vehicle Batteries Using Phase-Change Material,” *J. Electrochem. Soc.*, vol. 147, no. 9, p. 3231, 2000.

[96] W. Q. Li, Z. G. Qu, Y. L. He, and Y. B. Tao, “Experimental study of a passive thermal management system for high-powered lithium ion batteries using porous metal foam saturated with phase change materials,” *J. Power Sources*, vol. 255, pp. 9–15, 2014.

[97] R. Sabbah, R. Kizilel, J. R. Selman, and S. Al-Hallaj, “Active (air-cooled) vs. passive (phase change material) thermal management of high power lithium-ion packs: Limitation of temperature rise and uniformity of temperature distribution,” *J. Power Sources*, vol. 182, pp. 630–638, 2008.

[98] Z. Ling, F. Wang, X. Fang, X. Gao, and Z. Zhang, “A hybrid thermal management system for lithium ion batteries combining phase change materials with forced-air cooling,” *Appl. Energy*, vol. 148, pp. 403–409, 2015.

[99] R. K. Sharma, P. Ganesan, V. V. Tyagi, H. S. C. Metselaar, and S. C. Sandaran, “Developments in organic solid–liquid phase change materials and their applications in thermal energy storage,” *Energy Convers. Manag.*, vol. 95, pp. 193–228, 2015.

[100] Y. B. Tao and Y. L. He, “A review of phase change material and performance enhancement method for latent heat storage system,” *Renew. Sustain. Energy Rev.*, vol. 93, no. December 2016, pp. 245–259, 2018.

[101] S. a. Khateeb, M. M. Farid, J. R. Selman, and S. Al-Hallaj, “Design and simulation of a lithium-ion battery with a phase change material thermal management system for an electric scooter,” *J. Power Sources*, vol. 128, pp. 292–307, 2004.

[102] M. S. Wu, K. H. Liu, Y. Y. Wang, and C. C. Wan, “Heat dissipation design for lithium-ion batteries,” *J. Power Sources*, vol. 109, pp. 160–166, 2002.

[103] T. H. Tran, S. Harmand, B. Desmet, and S. Filangi, “Experimental investigation on the feasibility of heat pipe cooling for HEV/EV lithium-ion battery,” *Appl. Therm. Eng.*, vol. 63, no. 2, pp. 551–558, 2014.

[104] Z. Rao, S. Wang, M. Wu, Z. Lin, and F. Li, “Experimental investigation on thermal management of electric vehicle battery with heat pipe,” *Energy Convers. Manag.*, vol. 65, pp. 92–97, 2013.

[105] L. Song and J. W. Evans, “Electrochemical-Thermal Model of Lithium Polymer Batteries,” *J. Electrochem. Soc.*, vol. 147, no. 6, p. 2086, 2000.

[106] M. Sievers, U. Sievers, and S. S. Mao, “Thermal modelling of new Li-ion cell design modifications,” *Forsch. im Ingenieurwes.*, vol. 74, no. 4, pp. 215–231, 2010.

[107] K. Shah, C. McKee, D. Chalise, and a. Jain, “Experimental and numerical investigation of core cooling of Li-ion cells using heat pipes,” *Energy*, vol. 113, pp. 852–860, 2016.

[108] I. A. Hunt, Y. Zhao, Y. Patel, and J. Offer, “Surface Cooling Causes Accelerated Degradation Compared to Tab Cooling for Lithium-Ion Pouch Cells,” *J. Electrochem. Soc.*, vol. 163, no. 9, pp. A1846–A1852, 2016.

[109] D. Worwood, R. Algoo, R. J. McGlen, J. Marco, and D. Greenwood, “A study into different cell-level cooling strategies for cylindrical lithium-ion cells in automotive applications,” *Int. J. Powertrains*, vol. 7, no. 1–3, 2018.

[110] D. Worwood *et al.*, “A new approach to the internal thermal management of cylindrical battery cells for automotive applications,” *J. Power Sources*, vol. 346, pp. 151–166, 2017.

[111] D. Worwood *et al.*, “Thermal analysis of a lithium-ion pouch cell under aggressive automotive duty cycles with minimal cooling,” in *IET Conference Publications*, 2016, no. CP691.

[112] O. Capron, A. Samba, N. Omar, P. Van Den Bossche, and J. Van Mierlo, “Thermal behaviour investigation of a large and high power lithium iron phosphate cylindrical cell,” *Energies*, vol. 8, no. 9, pp. 10017–10042, 2015.

[113] S. C. Chen, C. C. Wan, and Y. Y. Wang, “Thermal analysis of lithium-ion batteries,” *J. Power Sources*, vol. 140, no. May 2004, pp. 111–124, 2005.

[114] Y. Ye, L. H. Saw, Y. Shi, K. Somasundaram, and A. a O. Tay, “Effect of thermal contact resistances on fast charging of large format lithium ion batteries,” *Electrochim. Acta*, vol. 134, pp. 327–337, 2014.

[115] V. Vishwakarma *et al.*, “Heat transfer enhancement in a lithium-ion cell through improved material-level thermal transport,” *J. Power Sources*, vol. 300, pp. 123–131, 2015.

[116] H. Maleki, “Thermal Properties of Lithium-Ion Battery and Components,” *J. Electrochem. Soc.*, vol. 146, no. 3, p. 947, 1999.

[117] E. Barsoukov, J. H. Jang, and H. Lee, “Thermal impedance spectroscopy for Li-ion batteries using heat-pulse response analysis,” *J. Power Sources*, vol. 109, pp. 313–320, 2002.

[118] R. Ponnappan and T. S. Ravigururajan, “Contact thermal resistance of Li-ion cell electrode stack,” *J. Power Sources*, vol. 129, no. 1 SPEC. ISS., pp. 7–13, 2004.

[119] G. Vertiz *et al.*, “Thermal characterization of large size lithium-ion pouch cell based on 1d electro-thermal model,” *J. Power Sources*, vol. 272, pp. 476–484, 2014.

[120] ASTM, “Standard Test Method for Steady-State Heat Flux Measurements and Thermal Transmission Properties by Means of the Guarded-Hat-Plate Apparatus,” 1997.

[121] Y. Ye, Y. Shi, and A. A. O. Tay, “Electro-thermal cycle life model for lithium iron phosphate battery,” *J. Power Sources*, vol. 217, pp. 509–518, 2012.

[122] S. J. Bazinski, X. Wang, B. P. Sangeorzan, and L. Guessous, “Measuring and assessing the effective in-plane thermal conductivity of lithium iron phosphate pouch cells,” *Energy*, vol. 114, pp. 1085–1092, 2016.

[123] T. Bergman, A. Lavine, F. Incropera, and D. Dewitt, *Fundamentals of Heat and Mass transfer*. Chicago: John Wiley & Sons, 2011.

[124] K. Shah *et al.*, “An experimentally validated transient thermal model for cylindrical Li-ion cells,” *Journal of Power Sources*, vol. 271. pp. 262–268, 2014.

[125] T. D. Hatchard *et al.*, “Importance of Heat Transfer by Radiation in Li - Ion Batteries during Thermal Abuse,” *Electrochem. Solid-State Lett.*, vol. 3, no. 7, pp. 305–308, 2000.

[126] S. Patankar, “Numerical heat transfer and fluid flow,” *Series in coputational methods in mechanics and thermal sciences*. pp. 1–197, 1980.

[127] R. Schneider, “Explicit and Implicit Finite-Difference Methods for the Diffusion Equation in Two Dimensions,” 2003.

[128] M. N. Ozisik, “Finite Difference Methods in Heat Transfer.” pp. 1–412, 1994.

[129] Y. Jaluria, *Computational Heat Transfer*, 2nd ed. London: Taylor & Francis, 2004.

[130] M. Xiao and S. Y. Choe, “Theoretical and experimental analysis of heat generations of a pouch type LiMn2O4/carbon high power Li-polymer battery,” *J. Power Sources*, vol. 241, pp. 46–55, 2013.

[131] K. Onda, H. Kameyama, T. Hanamoto, and K. Ito, “Experimental Study on Heat Generation Behavior of Small Lithium-Ion Secondary Batteries,” *J. Electrochem. Soc.*, vol. 150, p. A285, 2003.

[132] E. Schuster, C. Ziebert, A. Melcher, M. Rohde, and H. J. Seifert, “Thermal behavior and electrochemical heat generation in a commercial 40 Ah lithium ion pouch cell,” *J. Power Sources*, vol. 286, pp. 580–589, 2015.

[133] M. Abdul-Quadir, Yasir; Laurila, Tomi; Karppinen, Juha; Jalkanen, Kirsi; Vuorilehto, Kai; Skogstrom, Lasse; Paulstro-Krockel, “Experimental investigation of an adsorptive thermal energy storage,” *Int. J. energy Res.*, vol. 31, no. August 2007, pp. 135–147, 2007.

[134] W. Waag, S. Käbitz, and D. U. Sauer, “Experimental investigation of the lithium-ion battery impedance characteristic at various conditions and aging states and its influence on the application,” *Appl. Energy*, vol. 102, pp. 885–897, 2013.

[135] D. Bernardi, “A General Energy Balance for Battery Systems,” *J. Electrochem. Soc.*,

vol. 132, no. 1, p. 5, 1985.

[136] V. V. Viswanathan *et al.*, "Effect of entropy change of lithium intercalation in cathodes and anodes on Li-ion battery thermal management," *J. Power Sources*, vol. 195, no. 11, pp. 3720–3729, 2010.

[137] G. Piłatowicz, A. Marongiu, J. Drillkens, P. Sinhuber, and D. U. Sauer, "A critical overview of definitions and determination techniques of the internal resistance using lithium-ion, lead-acid, nickel metal-hydride batteries and electrochemical double-layer capacitors as examples," *J. Power Sources*, vol. 296, pp. 365–376, 2015.

[138] H.-G. Schweiger *et al.*, "Comparison of Several Methods for Determining the Internal Resistance of Lithium Ion Cells," *Sensors*, vol. 10, no. 6, pp. 5604–5625, 2010.

[139] K. Onda, T. Ohshima, M. Nakayama, K. Fukuda, and T. Araki, "Thermal behavior of small lithium-ion battery during rapid charge and discharge cycles," *J. Power Sources*, vol. 158, no. 1, pp. 535–542, 2006.

[140] M. J. Brand *et al.*, "Effects of vibrations and shocks on lithium-ion cells," *J. Power Sources*, vol. 288, pp. 62–69, 2015.

[141] E. Hosseinzadeh, R. Genieser, D. Worwood, A. Barai, J. Marco, and P. Jennings, "A systematic approach for electrochemical-thermal modelling of a large format lithium-ion battery for electric vehicle application," *J. Power Sources*, vol. 382, no. November 2017, pp. 77–94, 2018.

[142] S. B. Peterson, J. Apt, and J. F. Whitacre, "Lithium-ion battery cell degradation resulting from realistic vehicle and vehicle-to-grid utilization," *J. Power Sources*, vol. 195, no. 8, pp. 2385–2392, 2010.

[143] K. Young, C. Wang, L. Y. Wang, and K. Strunz, "Electric Vehicle Battery Technologies," in *Electric Vehicle Integration into Modern Power Networks*, R. Garcia-Valle and J. A. P. Lopes, Eds. Springer, 2013, pp. 15–56.

[144] N. Shidore and T. Bohn, "PHEV 'All electric range'and fuel economy in charge sustaining mode for low SOC operation of the JCS VL41M Li-ion battery using Battery HIL," *Proc. 23rd Int. Electr. …*, no. Cd, 2007.

[145] U. Eberle and R. von Helmolt, *Fuel Cell Electric Vehicles, Battery Electric Vehicles, and their Impact on Energy Storage Technologies: An Overview*. Elsevier B.V, 2010.

[146] TESLA, "2012 TESLA MODEL S 85kW SPECIFICATIONS," pp. 1–5, 2012.

[147] D. Sherman and M. Bramley, "Drag Queens: Five slippery cars enter a wind tunnel; one slinks out a winner.," *Car Driv.*, pp. 86–92, 2014.

[148] M. Nikowitz, *Advanced Hybrid and Electric Vehicles: System Optimization and Vehicle Integration*. Springer International Publishing, 2016.

[149] M. Tutuianu *et al.*, "Development of a World-wide Worldwide harmonized Light duty driving Test Cycle," *Tech. Rep.*, vol. 3, no. January, pp. 7–10, 2014.

[150] T. Barlow, S. Latham, I. Mccrae, and P. Boulter, "A reference book of driving cycles

for use in the measurement of road vehicle emissions," p. 280, 2009.

[151] Q. Kellner, E. Hosseinzadeh, G. Chouchelamane, W. D. Widanage, and J. Marco, "Battery cycle life test development for high-performance electric vehicle applications," *J. Energy Storage*, vol. 15, pp. 228–244, 2018.

[152] Green Car Congress, "A123 Systems supplying Li-ion batteries for new BMW ActiveHybrid 3 and ActiveHybrid 5 models," 2012. [Online]. Available: http://www.greencarcongress.com/2012/01/a123bmw-20120106.html. [Accessed: 16-Aug-2018].

[153] A123 Systems, "Nanophosphate High Power Lithium Ion Cell ANR32113M1Ultra-B," *MD100113-01 data sheet*, 2011.

[154] FastTech, "A123 AHR32113Ultra-B 3.6V 4400-4500mAh Rechargeable LiFePO Battery," 2015. [Online]. Available: https://www.fasttech.com/product/1683801-a123-ahr32113ultra-b-3-6v-4400-4500mah. [Accessed: 12-Aug-2015].

[155] M. Fleckenstein, S. Fischer, O. Bohlen, and B. Bäker, "Thermal Impedance Spectroscopy - A method for the thermal characterization of high power battery cells," *J. Power Sources*, vol. 223, pp. 259–267, 2013.

[156] Z. Rao, Z. Qian, Y. Kuang, and Y. Li, "Thermal performance of liquid cooling based thermal management system for cylindrical lithium-ion battery module with variable contact surface," *Appl. Therm. Eng.*, vol. 123, pp. 1514–1522, 2017.

[157] J. Whitelaw, "Convective Heat Transfer," 2011. [Online]. Available: http://www.thermopedia.com/content/660/. [Accessed: 14-Nov-2016].

[158] A. Fly and R. H. Thring, "A comparison of evaporative and liquid cooling methods for fuel cell vehicles," *Int. J. Hydrogen Energy*, vol. 41, no. 32, pp. 14217–14229, 2016.

[159] C. Kang *et al.*, "Three-dimensional carbon nanotubes for high capacity lithium-ion batteries," *J. Power Sources*, vol. 299, pp. 465–471, 2015.

[160] B. Rashidian, M. Amidpour, and M. R. J. Nasr, "Modeling the Transient Response of the Thermosyphon Heat Pipes," *Proc. World Congr. Eng.*, vol. II, 2008.

[161] International Association of Classification Societies, "Requirements concerning pipes and pressure vessels," 2016.

[162] F. X. Alvarez, J. Alvarez-Quintana, D. Jou, and J. R. Viejo, "Analytical expression for thermal conductivity of superlattices," *J. Appl. Phys.*, vol. 107, no. 8, pp. 462–467, 2010.

[163] J. C. Maxwell, *A Treatise on Electricity and Magnetism*. Cambridge University Press, 2010.

[164] S. Chacko and Y. M. Chung, "Thermal modelling of Li-ion polymer battery for electric vehicle drive cycles," *J. Power Sources*, vol. 213, pp. 296–303, 2012.

[165] Q. Kellner, E. Hosseinzadeh, G. Chouchelamane, W. D. Widanage, and J. Marco, "Battery cycle life test development for high-performance electric vehicle

applications," *J. Energy Storage*, vol. 15, pp. 228–244, 2018.

[166] Q. Kellner, W. Dhammika Widanage, and J. Marco, "Battery power requirements in high-performance electric vehicles," in *2016 IEEE Transportation Electrification Conference and Expo, ITEC 2016*, 2016.

[167] B. Wu, Z. Li, and J. Zhang, "Thermal Design for the Pouch-Type Large-Format Lithium-Ion Batteries: I. Thermo-Electrical Modeling and Origins of Temperature Non-Uniformity," *J. Electrochem. Soc.*, vol. 162, no. 1, pp. A181–A191, 2014.

[168] U. S. Kim, J. Yi, C. B. Shin, T. Han, and S. Park, "Modelling the thermal behaviour of a lithium-ion battery during charge," *J. Power Sources*, vol. 196, no. 11, pp. 5115–5121, 2011.

[169] S. J. Bazinski and X. Wang, "Thermal Effect of Cooling the Cathode Grid Tabs of a Lithium-Ion Pouch Cell," *J. Electrochem. Soc.*, vol. 161, no. 14, pp. A2168–A2174, 2014.

[170] P. S. Neelakanta, *Handbook of Electromagnetic Materials: Monolithic and Composite Versions and Their Applications*. Taylor & Francis, 1995.

[171] XALT Energy, "XALT 53 Ah High Energy (HE) Superior Lithium Ion Cell MODEL F910-1001." pp. 1–2, 2016.

[172] XALT Energy, "A Powerful Solution for Specialty Applications," 2017. [Online]. Available: https://www.xaltenergy.com/project/a-powerful-solution-for-specialty-applications/. [Accessed: 11-Oct-2018].

[173] A. Samba, N. Omar, H. Gualous, O. Capron, P. Van Den Bossche, and J. Van Mierlo, "Electrochimica Acta Impact of Tab Location on Large Format Lithium-Ion Pouch Cell Based on Fully Coupled Tree-Dimensional Electrochemical-Thermal Modeling," *Electrochim. Acta*, vol. 147, pp. 319–329, 2014.

[174] U. S. Kim, C. B. Shin, and C. S. Kim, "Modeling for the scale-up of a lithium-ion polymer battery," *J. Power Sources*, vol. 189, pp. 841–846, 2009.

[175] D. Worwood *et al.*, "Thermal analysis of a lithium-ion pouch cell under aggressive automotive duty cycles with minimal cooling," in *IET Hybrid and Electric Vehicles Conference (HEVC 2016)*, 2016.

[176] B. W. Gonser, *Modern Materials: Advances in Development and Applications*. Elsevier, 2013.

[177] S. Zhang, M. Vinson, P. Beshenich, and M. Montesano, "Evaluation and finite element modeling for new type of thermal material annealed pyrolytic graphite (APG)," *Thermochim. Acta*, vol. 442, pp. 6–9, 2006.

[178] Thermacore, "Introduction to Aluminum and Magnesium Annealed Pyrolytic Graphite (k-Core)," 2012.

[179] Thermacore, "Conduction Heat Transfer Expertise from k Technology," 2018. .

[180] Pittsburgh Corning, "FOAMGLAS® ONE," 2013. .

[181] S. J. Bazinski and X. Wang, “Experimental study on the influence of temperature and state-of-charge on the thermophysical properties of an LFP pouch cell,” *J. Power Sources*, vol. 293, pp. 283–291, 2015.

[182] U. S. Kim, C. B. Shin, and C. S. Kim, “Effect of electrode configuration on the thermal behavior of a lithium-polymer battery,” *J. Power Sources*, vol. 180, pp. 909–916, 2008.

[183] D. Worwood, “Applied Statistical Methods Post Module Assigmenet,” 2017.

[184] N. Sato, “Thermal behavior analysis of lithium-ion batteries for electric and hybrid vehicles,” *J. Power Sources*, vol. 99, pp. 70–77, 2001.

[185] E. V Thomas, H. L. Case, D. H. Doughty, R. G. Jungst, G. Nagasubramanian, and E. P. Roth, “Accelerated power degradation of Li-ion cells,” *J. Power Sources*, vol. 124, pp. 254–260, 2003.

[186] Z. Qian, Y. Li, and Z. Rao, “Thermal performance of lithium-ion battery thermal management system by using mini-channel cooling,” *Energy Convers. Manag.*, vol. 126, pp. 622–631, 2016.

[187] Y. Sun and W. J. Jasper, “Numerical modeling of heat and moisture transfer in a wearable convective cooling system for human comfort,” *Build. Environ.*, vol. 93, no. P2, pp. 50–62, 2015.

[188] T. J. LaClair, Z. Gao, O. Abdelaziz, M. Wang, E. Wolfe, and T. Craig, “Thermal Storage System for Electric Vehicle Cabin Heating - Component and System Analysis,” in *SAE Technical Paper*, 2016.

[189] D. Worwood, “A study into different cell-level cooling strategies for cylindrical lithium-ion cells in automotive applications,” 2016, pp. 7–9.

[190] D. Worwood *et al.*, “A new approach to the internal thermal management of cylindrical battery cells for automotive applications,” *J. Power Sources*, vol. 346, pp. 151–166, 2017.

[191] D. Worwood *et al.*, “Thermal Analysis of Fin Cooling Large Format Automotive Lithium-Ion Pouch Cells,” *2017 IEEE Veh. Power Propuls. Conf.*, pp. 1–6, Dec. 2017.

[192] M. Fetcenko, J. Koch, and M. Zelinsky, *Nickel–metal hydride and nickel–zinc batteries for hybrid electric vehicles and battery electric vehicles*, no. M. Elsevier Ltd., 2015.

[193] T. Waldmann, G. Geramifard, and M. Wohlfahrt-Mehrens, “Influence of current collecting tab design on thermal and electrochemical performance of cylindrical Lithium-ion cells during high current discharge,” *J. Energy Storage*, 2015.

[194] D. Xia, “Lithium Ion Rechargeable Batteries,” in *Electrochemical Technologies for Energy Storage and Conversion*, Wiley-VCH Verlag GmbH & Co. KGaA, 2011, pp. 69–109.

[195] J. B. Siegel, a. G. Stefanopoulou, P. Hagans, Y. Ding, and D. Gorsich, “Expansion of Lithium Ion Pouch Cell Batteries: Observations from Neutron Imaging,” *J.*

Electrochem. Soc., vol. 160, no. 8, pp. A1031–A1038, 2013.

[196] L. Saw, K. Somasundaram, Y. Ye, and A. Tay, "Electro-thermal analysis of Lithium Iron Phosphate battery for electric vehicles," *J. Power Sources*, vol. 249, pp. 231–238, 2014.

[197] B. W. Ninham and P. L. Nostro, *Molecular Forces and Self Assembly: In Colloid, Nano Sciences and Biology*. Cambridge University Press, 2010.

[198] Johnson Matthey, "Our Guide to Batteries," pp. 1–24, 2012.

[199] I. Buchmann, *Batteries in a Portable World*, 3rd ed. Richmond: Cadex Ekectronics Inc., 2011.

[200] Q. Wang *et al.*, "Experimental investigation on EV battery cooling and heating by heat pipes," pp. 1–7, 2014.

[201] P. Zhou, "Electric vehicle thermal management system," *US Patent 7,789,176*, vol. 2, no. 12. 2010.

[202] J. Voelcker, "Boeing 787 Batteries Same As Those In Electric Cars? Umm, NO," 2013. [Online]. Available: https://www.greencarreports.com/news/1081753_boeing-787-batteries-same-as-those-in-electric-cars-umm-no. [Accessed: 11-Nov-2015].

[203] P. Kurzweil, "Advances in Battery Technologies for Electric Vehicles," in *Advances in Battery Technologies for Electric Vehicles*, V. Scrosati, Bruno;Garche, Jurgen; Tillmetz, Ed. Woodhead Publishing, 2015, pp. 127–172.

[204] A123 Systems, "High Power Lithium Iron Phosphate 32113 Cylindrical Cells _ A123 Systems Products," 2015. [Online]. Available: http://www.a123systems.com/32113-lithium-iron-phosphate-high-power-batteries.htm.

[205] E. Johnson, "2014 McLaren P1 Official Photos and Info – News – Car and Driver," 2013. [Online]. Available: http://www.caranddriver.com/news/2014-mclaren-p1-official-photos-and-info-news.

[206] F. Rabenstein, M. Klüting, D. F. Kessler, J. Kretschmer, C.-O. Griebel, and E. Hockgeiger, "The Full-Hybrid Powertrain of the new BMW ActiveHybrid 5," 2011.

[207] A123 Systems, "A123 Systems Congratulates BMW on Launch of ActiveHybrid 5 and ActiveHybrid 3," 2015. [Online]. Available: http://www.a123systems.com/412cf8e8-b73d-40f9-9532-6a486937a6d6/media-room-2012-press-releases-detail.htm. [Accessed: 15-Jul-2015].

[208] J. Voelcker, "Nissan Leaf New Battery Cost_ $5,500 For Replacement With Heat-Resistant Chemistry," 2014. [Online]. Available: http://www.greencarreports.com/news/1092983_nissan-leaf-battery-cost-5500-for-replacement-with-heat-resistant-chemistry. [Accessed: 16-Jul-2015].

[209] L. Bingley, "Renault Zoe electric car review," 2013. [Online]. Available: http://www.greenmotor.co.uk/2013/03/renault-zoe-electric-car-review.html. [Accessed: 16-Jul-2015].

[210] Renault, “Renault Zoe Simply Revolutionary,” 2015.

[211] G. C. Congress, “First look at all-new Voltec propulsion system for 2G Volt; ‘the only thing in common is a shipping cap,’” 2014. [Online]. Available: http://www.greencarcongress.com/2014/10/20141029-voltec.html.

[212] B. Lofton, “Chevy Volt Battery System,” 2015. [Online]. Available: https://www.evhangar.com/system/battery-systems/sys-batt-chevy-volt/. [Accessed: 23-Nov-2015].

[213] Nextgreencar, “Volvo V60 to be first diesel plug-in hybrid,” 2011. [Online]. Available: http://www.nextgreencar.com/news/4413/Volvo-V60-to-be-first-diesel-plugin-hybrid/.

[214] H. Hornick, Will; Kuusisto, “Automotive iQ Interview IQPC.” [Online]. Available: http://www.automotive-iq.com/PDFS/Kuusisto_Volvo_BMS1.pdf.

[215] J. P. Lee, Peater K.;Chung, Youngwoo; OK, Tj;Hwang, KJ;Kim, Jaekyung;Jin, Matt;Park, “Global EV boom – revving up for the next upturn,” no. August, 2014.

[216] J. Meiners, “2016 Audi A3 e-tron Sportback Plug-In Hybrid,” 2014. [Online]. Available: http://www.caranddriver.com/reviews/2016-audi-a3-e-tron-sportback-plug-in-hybrid-first-drive-review.

[217] S. Shelton, “Audi says it will have a 300-mile range electric SUV in 2018,” 2015. [Online]. Available: http://gm-volt.com/2015/03/12/audi-says-it-will-have-a-300-mile-range-electric-suv-in-2018/.

[218] “Hyundai Sonata Plug-in Hybrid Review,” 2018. [Online]. Available: http://www.plugincars.com/hyundai-sonata-plug-hybrid. [Accessed: 09-Aug-2018].

[219] Green Car Congress, “First Drive: 2016 Hyundai Sonata PHEV and HEV,” 2015. [Online]. Available: http://www.greencarcongress.com/2015/05/20150526-sonata.html. [Accessed: 09-Aug-2018].

[220] Plugincars, “The BMW ActiveE _ PluginCars,” 2013. [Online]. Available: http://www.plugincars.com/bmw-activee. [Accessed: 15-Jul-2015].

[221] BWM, “BMW Technology Guide: Active Cruise Control.” 2013.

[222] BWM and B. M. W. Activee, “2. Technische Daten BMW ActiveE.,” 2011. [Online]. Available: http://www.langer.de/net/download/Technische Daten BMW ActiveE(1).pdf. [Accessed: 15-Jul-2015].

[223] O. Weber, “The Powerhouse,” 2014.

[224] A. Lennon, “Georgia Tech Clean Energy Series 2014 Panamera S E-Hybrid.” pp. 1–16, 2014.

[225] Porche, “World premiere of the Porsche Cayenne S E-Hybrid,” 2014. [Online]. Available: http://newsroom.porsche.com/en/products/world-premiere-of-the-porsche-cayenne-s-e-hybrid-10757.html. [Accessed: 16-Jul-2015].

[226] Mercedes-Benz, “S 500 PLUG-IN HYBRID,” 2014.

[227] Green Car Congress, “More details on the Mercedes-Benz S500 PLUG-IN HYBRID; new warranty for battery and PEEM,” 2014. [Online]. Available: http://www.greencarcongress.com/2014/09/20140915-s500phev.html. [Accessed: 14-Mar-2019].

[228] U. Kohler, “Sicherheitsmaßnahmen Si h h it ß h aus Sicht Si ht der d Hersteller t ll von Lithium-Ionen-Batterien,” 2012.

[229] M. Motors, “I-MIEV Technology.” 2015.

[230] Mitsubishi, “Charging your plug-in hybrid electric vehicle _ Mitsubishi Motors UK,” 2015. [Online]. Available: http://www.mitsubishi-cars.co.uk/outlander/charging.aspx.

[231] Mitsubishi, “MITSUBISHI OUTLANDER PHEV,” 2015. [Online]. Available: http://mitsubishi-motors.ie/car/outlander-phev/. [Accessed: 16-Jul-2015].

[232] Samsung, “Automotive(Electric Vehicle) Prismatic Battery Cells _ Samsung SDI,” 2014. [Online]. Available: http://www.samsungsdi.com/automotive-battery/battery-cells.

[233] G. Brooks, “ITALY: Hybrid technology secrets of LaFerrari revealed,” 2013. [Online]. Available: http://www.just-auto.com/news/hybrid-technology-secrets-of-laferrari-revealed_id132673.aspx. [Accessed: 16-Jul-2015].

[234] Porsche, “2015 Porsche 918 Spyder.” 2015.

[235] BMW GROUP, “The BMW i8 – New Take on The Ultimate Driving MachineTM powertrain, lightweight design and driving experience.,” 2013. [Online]. Available: https://www.press.bmwgroup.com/usa/pressDetail.html?title=the-bmw-i8-–-new-take-on-the-ultimate-driving-machinetm-powertrain-lightweight-design-and-driving&outputChannelId=9&id=T0144543EN_US&left_menu_item=node__6728. [Accessed: 16-Jul-2015].

[236] H. Kume, “BMW Increases Current Capacity of ‘X5’ PHEV’s Battery - HOME - Solar Power Plant Business,” 2015. [Online]. Available: http://techon.nikkeibp.co.jp/atclen/news_en/15mk/091500039/?ST=msbe. [Accessed: 14-Mar-2019].

[237] F. Renard, “2020 cathode materials cost competition for large scale applications and promising LFP best-in-class performer in term of price per kWh,” 2014.

[238] X. Energy, “XALT Energy _ Lithium Ion Battery Energy Solutions _ Total System Solutions,” 2015. [Online]. Available: http://www.xaltenergy.com/index.php/solutions.html. [Accessed: 23-Nov-2015].

[239] I. P. Tuersley, “Exploratory Data Analysis.” WMG, Applied statistical methods lecture notes, pp. 1–7, 2017.

A APPENDIX

A.1 BATTERY DESIGN

Lithium-ion batteries exist in many formats, the most common being cylindrical, pouch and prismatic. Each format has its advantages and disadvantages, which is one reason different formats exist. The main battery formats that currently prevail in the automotive industry are discussed in brief.

A.1.1 CYLINDRICAL CELLS

In the cylindrical format, the anode electrode is deposited on a copper current collector foil which is cut to size. Similarly, the cathode electrode is deposited on an aluminium foil. The two electrodes are then sandwiched together, separated by a separator layer which is inserted in between each electrode. The sandwich structure is passed through a winding process which forms a 'jelly roll'. The jelly roll is then inserted into a metallic housing, usually comprising of nickel plated steel. The top cap is added which contains the positive terminal, connecting the positive current collector layer to the terminal via a positive tab. The number of positive tab weld connections can reduce the overall current path, lowering the overall internal resistance at a cost of greater manufacturing complexity and cost [192], [193]. This manufacturing technique is therefore often adopted for power cells where greater current handling capabilities are required.

Prior to crimping and sealing, an electrolyte solution is injected into the cell to cover the separator layers. A cross section of a cylindrical battery cell can be viewed in Figure A. 1**.**

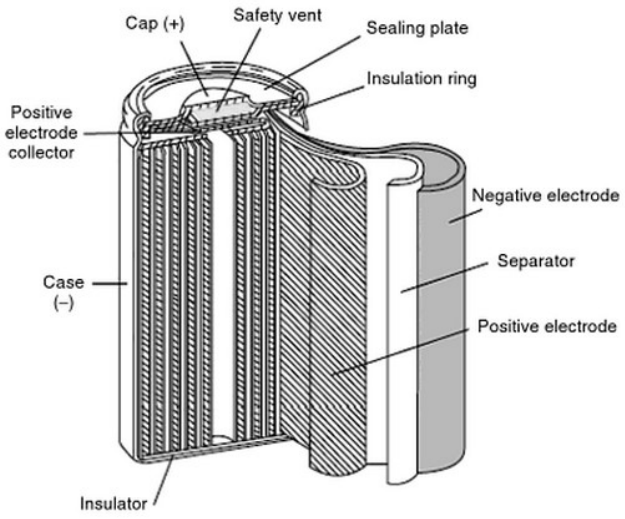

Figure A. 1: Cylindrical battery cell design [194]

Relative to other cell formats, cylindrical cells benefit from superior mechanical stability due to the presence of the steel metallic housing and cylindrical format which can endure high pressures without deformation. This avoids swelling issues, such as those present in pouch type formats [195], [196]. Safety features can also be easily incorporated, such as vents to purge excessive gas build-up created from abusive conditions, avoiding a potential thermal runaway. Due to their popular use in other power applications, the cylindrical format benefits from economies of scale, and is generally currently cheaper to manufacture than other formats that have yet reached such levels of manufacturing maturity [66].

However, the cylindrical format suffers from poor packing capabilities. In a hexagonal arrangement, the maximum theoretical packing density 0.91 [197]. In addition, the poor-through plane thermal conductivity is amplified in this design, particularly with large diameter cells. This phenomenon can lead to excessive hot spot formation near the core region when cooled radially, which is further highlighted in Chapter 3.

A.1.2 POUCH CELLS

Pouch cells utilise electrode stacking to form a sandwich structure, typically comprising of rectangular layers. The current collector layers are cut in a manner that forms protruding tabs for ease of current removal. The separator layer is inserted in a z-fold manner between the electrode layers, providing the necessary electrical insulation. A heat-sealable laminate foil is then applied to encase the stack, which following injection of the electrolyte, is sealed under vacuum to ensure dense packing of the individual layers. The cell is then charged to generate waste gas, which is then removed as part of the final manufacturing step during final sealing.

Due to the light-weight laminate-foil encasing, pouch cells have the potential to provide superior specific energy density, and together with their rectangular format, can achieve one of the highest packing densities (between 90-95 %) [198]. However, the poor mechanical properties of the cells can lead to issues with swelling from internal gas generation, which may require additional space allocation within the module to accommodate the expansion. In addition, as pouch-cells are a developing technology, non-standardised formats exist which increases their manufacturing cost due to low economies of scale. However, their design offers the potential to surpass the energy density of the cylindrical format once the technology readiness level increases [66]. A schematic of a pouch cell design can be viewed in Figure A. 2.

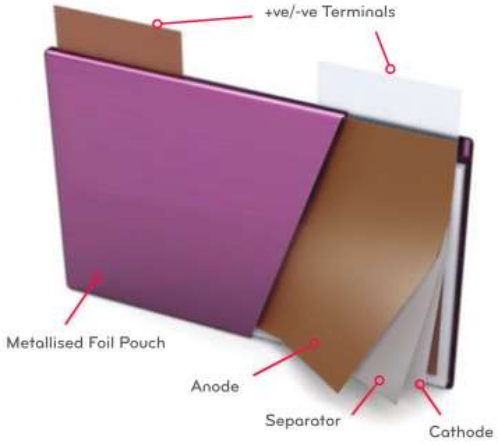

Figure A. 2: Pouch cell battery design [198]

A.1.3 PRISMATIC CELLS

Similar to cylindrical cells, prismatic cells use a wrapping approach which forms an oblong jelly roll. The oblong shape enables the formation of thinner cells, which is one reason for their adoption in electrical items such as mobile phones and laptops with ultra-thin designs. The prismatic format, however, offers poorer mechanical integrity than compared to the cylindrical format and therefore requires the use of a thicker encapsulating metallic container which decreases the specific energy density and adds to manufacturing costs [199]. As with the pouch cells, their large format limits the shape of the battery packaging which can be difficult to integrate into volume restrictions with certain designs of hybrid vehicles. A schematic of a prismatic cell design can be viewed in Figure A. 3

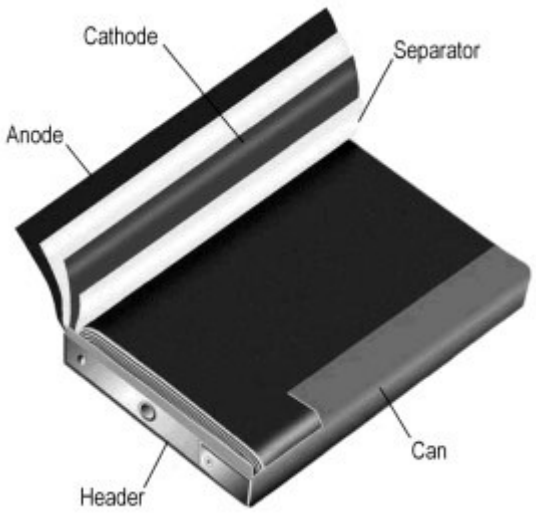

Figure A. 3: Prismatic battery cell design [199]

A.2 AUTOMOTIVE BATTERY PACKS

The term 'battery pack' not only encompasses the battery material, but includes other components required for operation of the battery. In general, a battery pack consists of all the battery modules (which contain the battery cells), the battery management system (BMS), BTMS, switch box and pack housing material. This is summarised in as presented by Linse and Kuhn [12].

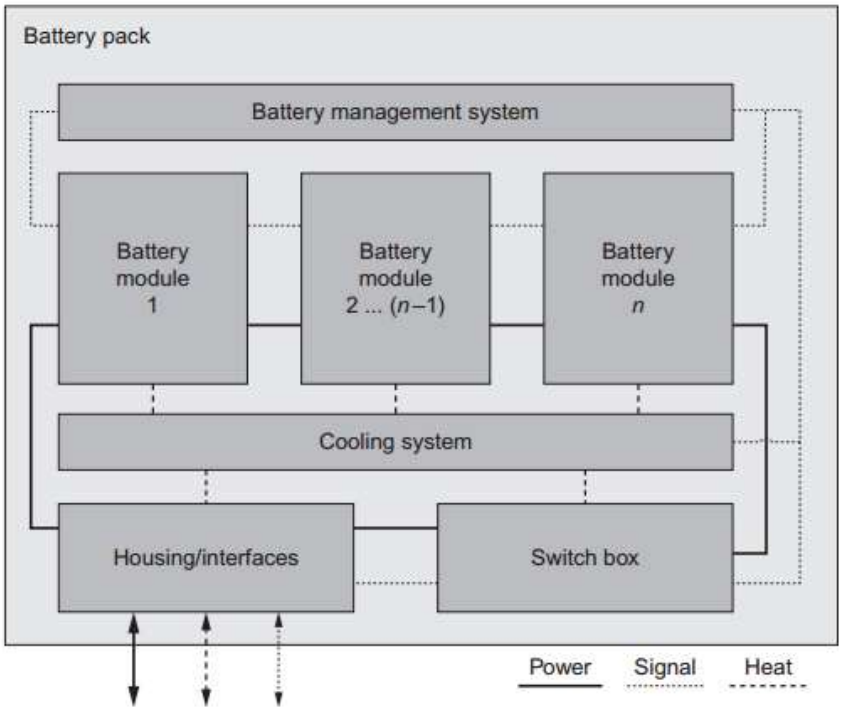

Figure A. 4: Typical components of a vehicle battery pack [12]

The BMS and switch box comprise the main power electronics of the pack. The BMS acts to monitor each battery module through sensors that measure individual cell terminal voltage, cell temperature and pack current. The BMS uses these measurements to manage the conditions within the pack and achieves this through sending signals to other components - e.g. the cooling system to alter the cooling duty based on the temperature of the cells. The BMS can also send signals to the switch box (which contains the fuses and disconnect switches) to deactivate the battery during unfavourable operating conditions (e.g. deep discharge or overcharge) to prevent damage to the battery [12]. The battery housing material structure provides mechanical integrity to the whole pack and may also act as an insulating material to protect the pack to a degree from extremities in ambient temperature when the BTMS is not in operation. The housing also supplies interfaces into and out of the

pack, such as inlet and outlet thermal interfaces for the BTMS heat transfer medium which may be connected to the vehicle air conditioning (AC) system.

Each battery module contains the battery cells, which can be connected together in both series and parallel combinations via the cell interconnect system. Neighbouring modules can also be connected electrically via the interconnect system. The cell supervision circuit acts to monitor the cell temperatures and terminal voltages, relaying the information to the BMS. Each module generally also contains its own module housing depending on the size and arrangement of the modules in the pack, to further improve the overall mechanical integrity of the pack.

Figure A. 5 displays the contents of a battery module as presented by Linse and Khun.

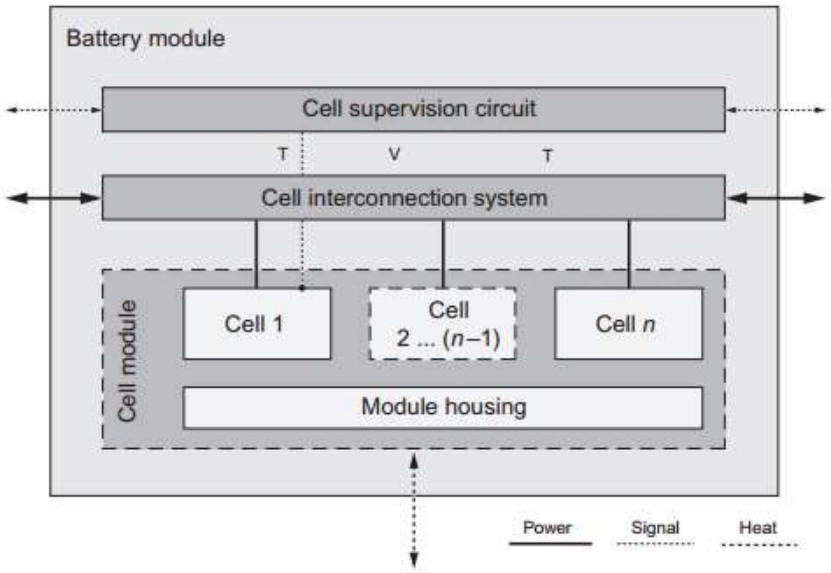

Figure A. 5: Typical components of vehicle battery module [12]

A.3 CHAPTER 2 LITERATURE REVIEW SUMMARY

Table A 1: Cooling performance summary of BTMS designs present in the literature

BTMS Type	Representative cell heat generation	Cooling properties	Cooling performance	Reference
• **Passive air cooling** • 12Ah cylindrical cells (44 mm diameter, 110m length) • Two annular aluminium fins 80 mm diameter, 5 mm thick attached to cell	• EV - 0.83 C discharge	• Natural convection • Air temperature at 15^{o}C	• Near uniform surface temperature • Measured surface temperature ~46^{o}C • Large modelled temperature in cell core from poor cell radial thermal conductivity, ~20^{o}C temp difference between surface and cell core • All values at end of 0.83 C discharge	Wu et al. [102]
• **Passive air-heat pipe cooling** • Cell type as above • Two copper heat pipes inserted into annular aluminium fins	EV – 0.83 C discharge	• Natural convection • Air temperature at 15^{o}C	• Uniform surface temperature • Measured surface temperature ~38^{o}C • ~20^{o}C temp rise between surface and cell core • All values at end of 0.83 C discharge	
• **Forced air cooling across attached**	EV – 0.83 C discharge	• Air temperature at 15^{o}C • Air flowrate not reported	• 3.5^{o}C temperature variation across surface	

aluminium fin onto cell surface • Cell type as above			• Maximum measured surface temperature ~26°C • ~20°C temp rise between surface and cell core • All values at end of 0.83 C discharge	
• **Forced air-heat pipe cooling** • Cell type as above • Two copper heat pipes inserted into annular aluminium fins • Fin array attached to heat pipe condenser ends • Active air blown over heat pipe condenser end only	EV – 0.83 C discharge	• Air temperature at 15°C • Air flowrate not reported	• Uniform surface temperature • Measured surface temperature 30°C • ~20°C temp rise between surface and cell core • Greater maximum surface temperature than active cooling without heat pipe due to thermal resistance incurred through conducting heat to the heat pipe condenser end. • All values at end of 0.83 C discharge	
• **Passive air cooling with finned copper heat sink** • Flat induction heater simulating heat flux from side of resin matrix module comprising 14 cylindrical 7 Ah cells	HEV - 100W module heat generation	• Natural convection • Air temperature at 20°C	• 46°C maximum heat sink temperature (measured) • Simulated peak cell temperature 57.3°C • Simulated maximum temperature difference between cells in module 1.6°C	Tran et al.[103]

(38 mm diameter, 142 mm length) • Heater attached to copper fined heat sink			• All values at steady state	
• **Passive air cooling with finned copper heat pipe heat sink** • Cell arrangement as above • Flat heat pipe attached to copper fin heat sink with thermal grease	HEV - 100W module heat generation	• Natural convection • Air temperature at 15^{o}C	• 38^{o}C maximum heat pipe temperature (measured) • Simulated peak cell temperature 49.5^{o}C • Simulated maximum temperature difference between cells in module 1.1^{o}C • All values at steady state	
• **Forced air cooling with finned copper heat sink** • Cell arrangement as above • Heater attached to copper fined heat sink	HEV - 100W module heat generation	• Forced convection of air at: 1. 0.2 m/s 2. 0.5 m/s 3. 1.5 m/s • Air temperature at 20^{o}C	• Maximum heat sink temperature (measured): 1. 37.0^{o}C (at 0.2 m/s) 2. 29.0^{o}C (at 0.5 m/s) 3. 24.0^{o}C (at 1/5 m/s) • Simulated peak cell temperature: 1. 48.5^{o}C (at 0.2 m/s) 2. 40.4^{o}C (at 0.5 m/s) 3. 35.4^{o}C (at 1.5 m/s) • Simulated maximum temperature difference between cells in module: 1. 0.9^{o}C (at 0.2 m/s) 2. 0.9^{o}C (at 0.5 m/s)	

			3. 0.9°C (at 1.5 m/s) • All values at steady state	
• **Forced air cooling with finned copper heat pipe heat sink** • Cell arrangement as above • Flat heat pipe attached to copper fin heat sink with thermal grease	HEV - 100W module heat generation	• Forced convection of air at: 4. 0.2 m/s 5. 0.5 m/s 6. 1.5 m/s • Air temperature at 20°C	• Maximum heat pipe temperature (measured): 1. 33.5°C 2. 29.0°C 3. 35.0°C • Simulated peak cell temperature: 1. 44.8°C 2. 40.5°C 3. 36.4°C • Simulated maximum temperature difference between cells in module: 1. 0.9°C 2. 0.9°C 3. 0.9°C • Poor performance of heat pipe at air speeds >0.2 m/s due to absence of phase change from poor design • All values at steady state	
• **Forced liquid-heat pipe cooling** • cylindrical heat pipes (5 mm diameter, 18 mm length) distributed	Input heater power: 1. 30 W 2. 50 W	• Heat pipe condenser ends submerged in water bath • 25°C water bath temperature • Condenser placed vertically above evaporator	• Maximum surface temperature of heater: 1. 36°C (at 30 W) 2. 42°C (at 50 W) • Maximum temperature difference across surface: 1. 4.9°C (at 30 W)	Rao et al.[104]

across resistive heater • Resistive heater acting to simulate 8 AH $LiFePO_4$ prismatic power battery • Flat evaporator ends of heat pipe connected to heater surface with silica gel •			2. 8.0°C (AT 50 W) • Temperature uniformity across surface worsened with varying heat pipe orientation away from vertical • All values at steady state •	
• Stack of 4 pouch cells (3 Ah) • Air cooled	• 3-C discharge • Volumetric cell heat generation not reported. Chemistry not reported, cannot estimate heat generation	• Natural convection • Air temperature at 25°C	• Measured maximum temperature of battery in stack = 48.8°C • Measured maximum temperature variation across stack = 6.8°C • Measured maximum temperature variation across centre battery surface = 2.1°C • All values at end of discharge	Zhao et al.[48]
• Stack of 4 pouch cells (3Ah) with flat ultra-thin aluminium heat pipes	• As above	• Natural convection • Air temperature at 25°C	• Measured maximum temperature of battery in stack = 41.1°C	

sandwiched between cells • Air/Heat pipe cooled			• Measured maximum temperature variation across stack = 2.9°C • Measured maximum temperature variation across centre battery surface = 0.8°C • All values at end of discharge
• Stack of 4 pouch cells (3Ah) with flat ultra-thin aluminium heat pipes sandwiched between cells • Air/Heat pipe cooled	• As above	• Forced convection over condenser ends. Flowrate of air not stated. Fan speed set at 1500 rpm • Air temperature at 25°C	• Measured maximum temperature of battery in stack = 31.8°C • Measured maximum temperature variation across stack = 2.2°C • Measured maximum temperature variation across centre battery surface = 0.7°C • No decrease in performance observed between horizontal and vertical orientations of heat pipe. • All values at end of discharge
• Stack of 4 pouch cells (3Ah) with flat ultra-thin aluminium heat pipes	• As above	• Condenser ends submerged in water bath • Water temperature at 25°C	• Measured maximum temperature of battery in stack = 38.2°C • Maximum temperature variation across stack = 6.2

sandwiched between cells • Liquid/Heat pipe cooled			• Maximum temperature variation across centre battery surface = 1.5^{o}C • Poor performance attributed to bubbles present at condenser ends • All values at end of discharge	
• Stack of 4 pouch cells (3Ah) with flat ultra-thin aluminium heat pipes sandwiched between cells • Liquid/Heat pipe cooled	• As above	• Spray cooling condenser ends with 0.7 ml water per spray. • Spray frequency = 1/min • Water temperature at approximately 19^{o}C	• Measured maximum temperature of battery in stack = 21.5^{o}C • Maximum temperature variation across stack = 1.2^{o}C • Maximum temperature variation across centre battery surface = 0.5^{o}C • All values at end of discharge	
• L shaped heat pipe inserted between two test batteries • Test batteries contain atonal 324 with two cartridge heaters to simulate battery heat generation • 5 mm aluminium plate along battery surface	• Input cartridge heater power: 1. 10 W ($0.432x10^{5}W/m^{3}$) 2. 30 W ($1.294x10^{5}W/m^{3}$)	• Condenser ends of heat pipe inserted into glycol-water (2:3 ratio) cooling channel • Evaporator vertically above condenser • 20^{o}C liquid temperature • 0.1158 m^{3}/hr flow • 35^{o}C ambient air temperature	• Measured maximum temperature of battery surface (not heat pipe side): 1. 39.2^{o}C (at 10 W) 2. 60.1 (at 30 W) • Temperature variation across surface not reported • All values at steady state	Wang et al.[200]

• Flattened evaporator section of heat pipe connected to aluminium plates • Liquid/heat pipe cooled				
• Flat 'heat pipe cold plate' inserted between prismatic cells (10 Ah) • Flat heat pipe attached to battery surfaces with thermal grease (1 mm thick, 3 $W.m^{-1}.K^{-1}$) • 4 condenser ends extending from heat pipe cold plate • Liquid/Heat pipe cooled • Heat pipes connected together with copper heat spreaders via soldering	• Measured average heat generation during charging at: 1. 3 C ($0.766x10^5 W/m^3$) 2. 5 C ($1.861x10^5 W/m^3$) 3. 8 C ($3.993x10^5 W/m^3$)	• Condenser ends submerged in liquid cooling channel • 8 Coper fins attached to condenser ends • 0.120 m^3/hr water flowrate • Water temperature at 25°C	• Maximum battery temperature along central plane (simulated): 1. 28.2°C (at $0.766x10^5 W/m^3$) 2. 33.2°C (at $1.861x10^5 W/m^3$) 3. 41.6°C ($3.993x10^5 W/m^3$) • Maximum battery cooling surface temperature (simulated): 1. 26.5°C (at $0.766x10^5 W/m^3$) 2. 29.1°C (at $1.861x10^5 W/m^3$) 3. 33.4°C ($3.993x10^5 W/m^3$) • Measured temperature difference across heat pipe cold plate surface (simulated): 3. 1.2°C (at $3.993x10^5 W/m^3$)	Ye at al.[45]

			• All values at end of discharge	
• As Above • Air/Heat pipe cooled	• As above	• Condenser ends submerged in air cooling channel • 29 Coper fins attached to condenser ends • 38.88 m^3/hr water flowrate • Air temperature at 25°C	• Maximum battery temperature along central plane (simulated): 4. 30.1°C (at 0.766x10^5W/m^3) 5. 37.5°C (at 1.861x10^5W/m^3) 6. 49.2°C (3.993x10^5W/m^3) • Temperature difference across cooling surface not reported • Large cooling channel temperature rise of air ~0.9°C per heat pipe plate at 5C charge • All values at end of discharge	
• Simulated HEV pack (1.94 kWh) • 3 modules in pack, each module containing 88 26650 cylindrical 2.3 Ah $LiFeP0_4$ cells • Staggered arrangement • Air cooling	• Calculated heat gen using I^2R relation for discharge: 1. 8.4 C (0.869x10^5W/m^3) 2. 10.9 C (1.449x10^5W/m^3) 3. 12.9 C (2.031x10^5W/m^3)	• Air blow through staggered cells in series fashion • 25°C inlet air temperature • Flowrate not reported for 1., and 2., heat gen. For 3. (12.9C) 16.20x10^2 m^3/hr	• Simulated peak pack temperature = 60°C for all heat generation rates • Simulated maximum cell-to-cell temperature difference within pack = 3°C • Parasitic fan power requirement for whole pack:	Park and Jung [54]

			1. 29 W (at $0.869x10^5 W/m^3$) 2. 260 W (at $1.449x10^5 W/m^3$) 3. 908 W (at $2.031x10^5 W/m^3$) • All values at steady state	
• Simulated HEV pack (1.94 kWh) • 3 modules in pack, each module containing 88 26650 cylindrical 2.3 Ah $LiFeP0_4$ cells • Staggered arrangement • Liquid cooling	• As above	• Direct contact of liquid.(mineral oil) • Passed through staggered cells in series fashion • 25°C inlet liquid temperature • Flowrate not reported for 1, and 2., heat gen. For 3. (12.9C) 19.76 m^3/hr mineral oil, $28.80x10^2$ m^3/hr air in secondary air/liquid heat exchanger	• Simulated peak pack temperature = 60°C for all heat generation rates • Simulated maximum cell-to-cell temperature difference within pack = 0.97°C • Parasitic fan power requirement for whole pack: 2. 28 W (at $1.441x10^5 W/m^3$) 3. 445 W (at $2.021x10^5 W/m^3$) • All values at steady state	
• Stack of 8 15 Ah prismatic LMO cells (0.456 kWh pack) • Each cell within stack cooled on one side • Air cooling	• Averaged cell heat generation rates = $0.280x10^5 W/m^3$	• Parallel distribution of heat transfer medium through cooling channels formed between cells • 20.4 m^3/hr total flowrate • 27°C inlet air temperature	• Simulated peak pack temperature = 33.87°C • Simulated maximum cell-to-cell temperature difference within pack = 2.80°C	Fan et al.[72]

			• Values after 600 s of heat generation • Using cooling on both sides of the cells reduced peak temperature to 33.41°C but worsened the temperature difference to 3.28°C • All values after 600s heat generation	
• Stack of 8 15 Ah prismatic $LiFePO_4$ cells (0.456 kWh pack) • 0.5 mm thick pin-fin aluminium heat sink placed along surface of each cell • Air cooled	• Discharge rates: 1. 2.8 C 2. 5 C • Cell volumetric heat generation not reported. Assuming I^2R relation and 7 mΩ internal resistance then: 1. $0.557x10^5 W/m^3$ 2. $1.775x10^5 W/m^3$	• Parallel flow of air through cooling channels in module stack • 10.17 m^3/hr total flowrate • 25°C inlet air temperature	• Maximum simulated pack temperature: 1. 46.9°C (at 2.8C) 2. 96.9°C (at 5C) • Maximum temperature difference across pack: 1. 1.6°C (at 2.8 C) 2. 5.6°C (at 5 C) • All values after 600s heat generation	Zhang et al.[73]

• Stack of 5 50 Ah pouch LTO cells • 4 cooling channels present within stack. Ends of stack insulated • Cell surfaces in cooling channel lined with 1.27 mm thick flat aluminium plate • Porous aluminium foam (20 pores per inch, 8% dense) inserted into cooling channel • Air cooled	• Measured averaged heat generation rate: $0.464 \times 10^5 W/m^3$ (4 C charge-discharge cycling for 90 min)	• Air flow injected into each cooling channel in parallel fashion • Total air flowrate 1. 11.52 m^3/hr 2. 15.84 m^3/hr • 22°C inlet air temperature	• Measured (thermochromics liquid crystal thermography) pack peak temperature: 1. 37.0°C (at 11.52 m^3/hr air flow) 2. 35. 0°C (at 15.84 m^3/hr air flow) • Parasitic fan power: 1. 11.04 W (at 11.52 m^3/hr air flow) 2. 22.76 W (at 15.84 m^3/hr air flow) • Maximum temperature variation across pack or cell surface not reported	Giuliano et al.[74]
• 0.109 Kwh sub-module • 8 LMO cylindrical cells in series (3.6 Ah, 42.4 mm diameter, 97.7 mm length) • Reciprocating flow series arrangement	• 7 C discharge. Volumetric cell heat generation not reported. Assuming only I^2R for heat generation term and an internal resistance of 8 mΩ then 0.368×10^5 W/m^3	• Series distribution of air over 8 cells • Flow reversal every 1200s • 20°C inlet air temperature • 14.95 m^3/hr total flowrate	• Simulated peak time averaged cell temperature = 29.4°C • Simulated time averaged maximum temperature variation between cells = 3.4°C	Mahamud and Park [75]

• Air cooled			• Simulated values at quasi steady state	
• Single 7 Ah $LiFePO_4$ pouch cell • 2 mm flat aluminium cold plate in contact with each side of the cell • 6 cooling channels carved along the axis of the aluminium plate to provide a pathway for in-direct liquid cooling • Liquid cooled (indirect)	• 5 C discharge. Volumetric cell heat generation not reported. Assuming only I^2R for heat generation term and an internal resistance of 15 mΩ then $1.901x10^5$ W/m^3	• Water flowing through cooling channels. Flow inlet begins at tab side of pouch cell • 25°C inlet water flowrate • 0.011 m^3/hr total flowrate	• Simulated peak cell temperature = 30.5°C • Simulated maximum temperature difference in battery = 4.8°C • Values at end of 5 C discharge	Huo et al.[85]
• 0.111 kWh HEV module • 20 18650 cells (1.5 Ah) • In-line arrangement • PCM/natural convection air cooled	• 6.67 C discharge. Nominal heat volumetric cell heat generation not reported.	• PCM inserted in the interstitial spaces between cells • Graphite/PCM-composite • Melting temperature range 52-55°C • Ambient air temperature: 1. 25°C 2. 45°C	• Simulated maximum volume averaged cell temperature: 1. 42.7°C (at 25°C ambient) 2. 54. 6°C (at 45°C ambient) • Simulated maximum pack temperature variation: 1. 0.07°C (at 25°C ambient)	Sabbah et al. [97]

			2. 0.40 (at 45°C ambient) • Values calculated at end of 6.67 C discharge
• As above	• 2 C discharge. Nominal heat volumetric cell heat generation not reported.	• As above	• Simulated maximum volume averaged cell temperature: 1. 33.7°C (at 25°C ambient) 2. 52.5°C (at 45°C ambient) • Simulated maximum pack temperature variation: 1. 0.03°C (at 25°C ambient) 2. 0.14 (at 45°C ambient) • Values calculated at end of 2 C discharge
• As above • Air cooled	• 6.67 C discharge. Nominal heat volumetric cell heat generation not reported.	• Air blown through interstitial spaces between cells • Parallel cooling • Cooling channel Reynolds number: 1. 13 2. 631	• Simulated maximum volume averaged cell temperature: 1. 46.0°C (at 25°C ambient, Re=13) 2. 42.9°C (at 25°C ambient, Re=631)

		3. 67 4. 670 • Ambient air temperature: 1. 25°C 2. 45°C	3. 64.8°C (at 45°C ambient, Re=67) 4. 61.7°C (at 45°C ambient, Re =670) • Simulated maximum pack temperature variation 1. 0.8°C (at 25°C ambient, Re=13) 2. 4.2°C (at 25°C ambient, Re=631) 3. 3.0°C (at 45°C ambient, Re=136) 4. 4.8°C (at 45°C ambient, Re=1347) • Values calculated at end of 6.67 C discharge
• As above • Air cooled	• 2 C discharge. Nominal heat volumetric cell heat generation not reported.	• As above • Cooling channel Reynolds number: 1. 13 2. 126 3. 67 4. 670 • Ambient air temperature: 1. 25°C	• Simulated maximum volume averaged cell temperature: 1. 34.7°C (at 25°C ambient, Re=13) 2. 33.1°C (at 25°C ambient, Re=126) 3. 53.8°C (at 45°C ambient, Re=67)

		2. 45°C C	4. 50.9°C (at 45°C ambient, Re =670) • Simulated maximum pack temperature variation 1. 0.58°C (at 25°C ambient, Re=13) 2. 1.84°C (at 25°C ambient, Re=126) 3. 1.62°C (at 45°C ambient, Re=67) 4. 2.06°C (at 45°C ambient, Re=670) • Values calculated at end of 2 C discharge

A.4 REVIEW OF XEV MODELS

Table A 2: Battery and thermal management choices for a sample of LDV vehicles within the xEV market sector

Cell geometry	Company	Model	Vehicle type	Thermal management method used	Cap (kWh)	Power (kW)	C rate	Cap (Ah)	Volt (V)	Number of cells	Cathode Chemistry	Battery supplier	Reference
Cylindrical	Tesla	Roadster	EV	Active liquid cooling	55.0	185	3.4	2.2	3.6	6945	LCO	Panasonic	[201], [202]
		Model S	EV	Active liquid cooling	85.0	310	3.6	3.1	3.6	7104	NCA	Panasonic	[146], [201], [203]
	McLaren	P1	PHEV	Active liquid cooling	4.7	130	27.7	4.4	3.3	324	$LiFePO_4$	Unknown	[204], [205]
	BMW	Active hybrid 5	HEV	Direct liquid refrigerant cooling	1.35	40	29.6	4.4	3.3	96	$LiFePO_4$	A123	[204], [206], [207]
Pouch	Nissan	Leaf	EV	Passive air cooled	24.0	80	3.3	33	3.7	194	LMO-NCA	AESC	[66], [203], [208]
	Renault	Zoe	EV	Active air cooling	26.0	65	2.9	36	3.7	192	NMC-LMO	LG Chem	[66], [203],

	Chevrolet	Volt	PHEV	Active liquid cooled	16.6	111	6.7	15	3.7	288	NMC-LMO	LG Chem	[209], [210] [83], [145], [148], [211], [212]
	Volvo	V60	PHEV	Active liquid cooling	11.2	50	4.5	15	3.7	200	NMC-LMO	LG Chem	[213]–[215]
	Audi	A3 e-tron sportback	PHEV	Active liquid cooling	8.8	75	8.5	28.0	3.3	96	$LiFePO_4$	LG Chem	[216], [217]
	Hyundai	Sonata	PHEV	Unknown	9.8	50	5.1	Unknown	Unknown	Unknown	Unknown	LG Chem	[218], [219]
	Hyundai	Sonata	HEV	Unknown	1.6	34	21.5	Unknown	Unknown	Unknown	Unknown	LG Chem	[219]
Prismatic	BMW	i-3	EV	Refrigerant gas cooling, electric heating.	22.0	125	5.7	60	3.8	96	NMC	Samsung	[91], [148], [203]
	BWM	ActiveE	EV	Active liquid cooling and liquid heating	32.0	125	3.9	40	3.7	192	NMC	Samsung	[220]–[222]

Porsche	Panemera S E-Hybrid	PHEV	Active liquid cooling	9.4	70	7.4	24.5	3.7	104	NMC-LMO	Samsung	[215], [223], [224]
Porsche	Cayenne S E-Hybrid	PHEV	Active liquid cooling	10.8	70	6.5	28	3.7	104	NMC-LMO	Samsung	[215], [225]
Mercedes	S 500	PHEV	Active liquid cooling	8.7	85	9.8	22.0	3.3	120	$LiFePO_4$	Johnson Controls-Saft	[226]–[228]
Mitsubishi	i-MiEV	EV	Active air cooling	16.5	60	3.8	50	3.7	88	NMC-LMO	Li Energy Japan	[66], [203], [229]
Mitsubishi	Outlander	PHEV	Active air cooling	12	120	10.0	40.0	3.7	80	NMC-LMO	Li Energy Japan	[66], [230], [231]
Ferrari	LaFerrari	MHEV	Active liquid cooling	2.3	120	52.2	5.9	3.3	120	NMC	Samsung	[232], [233]
Porsche	918 Spyder	PHEV	Active liquid cooling	6.8	230	33.8	5.9	3.7	312	NMC	Samsung	[234]
BMW	i-8	PHEV	Refrigerant gas cooling, electric heating.	7.1	96	13.5	20.0	3.7	96	NMC	Samsung	[148], [232],

													[235], [236]

A.5 BATTERY CHEMISTRIES

Table A 3: Properties of common lithium-ion battery chemistries (pulse length is 10 s, cont. denotes continuous) [198][199][66][237][238]

Cathode chemistry with exception of $LI_4Ti_5O_{12}$	**Cell specific energy density [Wh.kg^{-1}]**	**Cell energy density, [Wh.l^{-1}]**	**Cycle life (durability), 100% DoD**	**Estimated price [US$/Wh]**	**Power C-rate [hr^{-1}]**	**Onset of thermal runaway (safety) [^{o}C]**	**Nominal cell voltage [V]**	**Upper and lower operating temperature limits [^{o}C]**
$LiCoO_2$	170-185	450-490	500	0.31-0.46	1 C cont.	150	3.6	-20 to 60
$LiFeP0_4$ (EV/PHEV)	90-125	130-300	2000	0.3-0.6	5 C cont. 10 C pulse	270	3.2	-20 to 60
$LiFeP0_4$ (HEV)	80-108	200-240	>1000	0.4-1.0	30 C cont. 50 C pulse	270	3.2	-20 to 60
$LiMn_2O_4$	90-110	280	>1000	0.45-0.55	3-5 C cont.	255	3.8	-20 to 50
$LiNi_xCo_yMn_xO_Z$ (EV/PHEV)	155-190	330-400	1500	0.5-0.9	1 C cont. 5 C pulse	215	3.7	-20 to 60
$LiNi_xCo_yMn_xO_Z$ (HEV)	150	270-290	1500	0.5-0.9	20 C cont. 40 C pulse	215	3.7	-20 to 60
$LI_4Ti_5O_{12}$	65-100	118-200	12,000	1-1.7	10 C cont. 20 C pulse	Not susceptible	2.5	-50 to 75
$LiNi_{0.8}Co_{0.15}Al_{x0.05}O_2$	233	630	500	0.23-0.61	1 C cont. 5 C pulse	150	3.6	-20 to 60

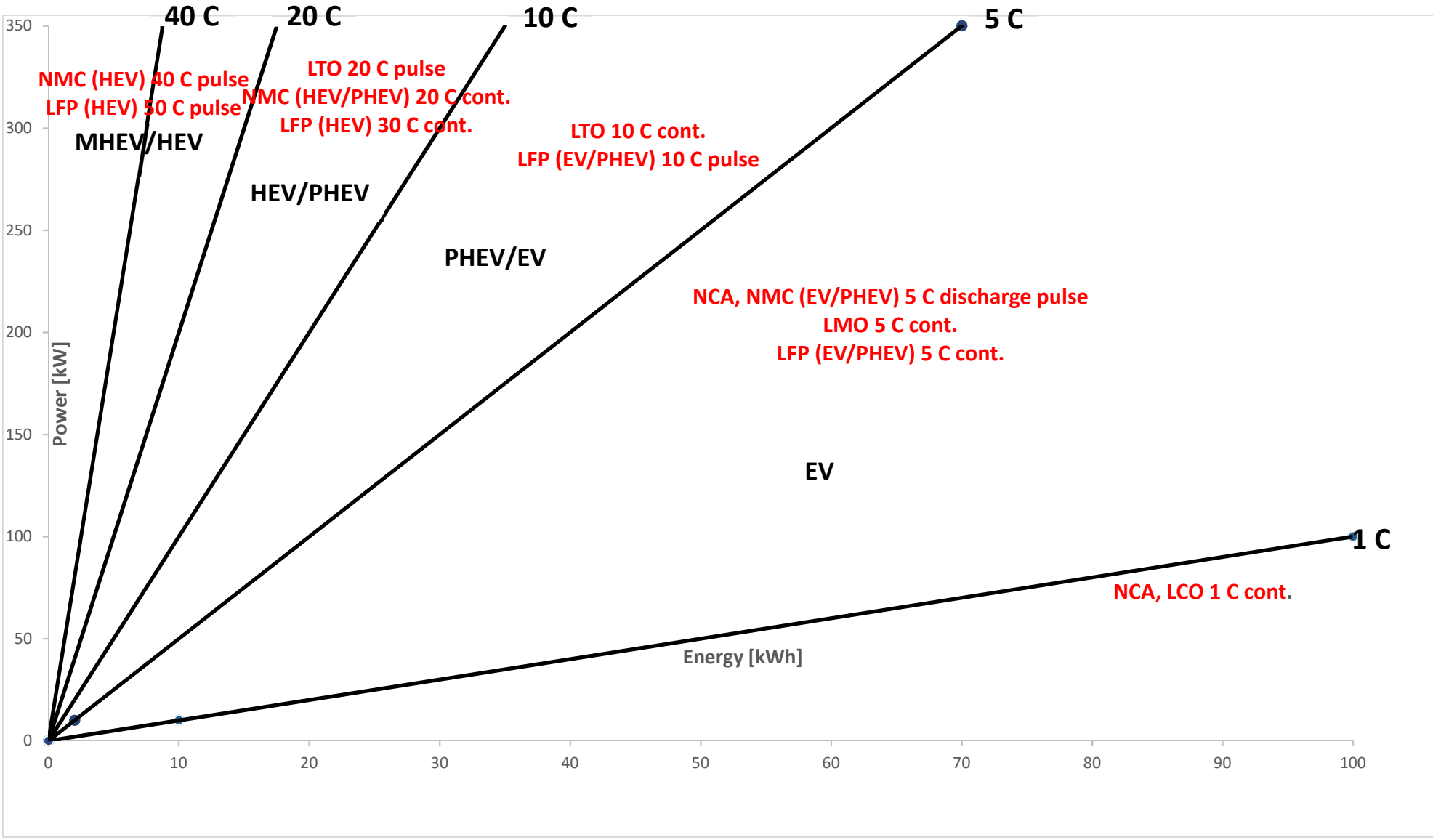

Figure A. 6: Appropriate chemistry choices for xEVs

A.6 HEAT PIPE EFFECTIVE DENSITY AND HEAT CAPACITY

Parameters used in the calculation of the heat pipe effective thermal and physical properties.

Table A 4: Density and heat capacity of water (liquid and vapour) [56]

Temperature [°C]	ρ_l [kg.m^{-3}]	ρ_v [kg.m^{-3}]	Cp_w [J.kg^{-1}.K^{-1}]	Cp_v [J.kg^{-1}.K^{-1}]
25	997	0.0275	4180	1830
40	992	0.05	4179	1890
60	983	0.13	4185	1910

Table A 5: Calculated heat pipe effective heat capacity and density for heat pipes designed to achieve a power capability if 3.60 W for the 18650 cell and 4.32 for the 32113 cell)

Cell type	Heat pipe size [mm]	Cp_{hp} [J.kg^{-1}.K^{-1}]	ρ_{hp} [kg.m^{-3}]	f_w [-]	f_{wi} [-]	f_v [-]
18650 cell	3 mm heat pipe	1594	5773	0.360	0.529	0.111
	4 mm heat pipe	1593	3791	0.278	0.270	0.452
	5 mm heat pipe	1624	2854	0.226	0.173	0.601
	6 mm heat pipe	1651	2280	0.190	0.120	0.690
	7 mm heat pipe	1674	1895	0.164	0.088	0.748
	8 mm heat pipe	1693	1619	0.144	0.068	0.788
32113 Cell	3 mm heat pipe	-	-	-	-	-
	4 mm heat pipe	1765	5503	0.278	0.626	0.096
	5 mm heat pipe	1718	3793	0.226	0.368	0.406
	6 mm heat pipe	1716	2931	0.190	0.255	0.555
	7 mm heat pipe	1722	2373	0.164	0.187	0.649
	8 mm heat pipe	1730	1984	0.144	0.143	0.713

A.7 CALCULATION OF POUCH CELL TAB RESISTANCE

The equation for resistance through a wire of varying cross-sectional area is used to calculate the electrical resistance through the pouch cell tab cone. This is represented by:

$$R_{tab,cone} = \rho_r \int_0^{H_{cone}} \frac{dx}{A(x)} \tag{68}$$

Where x is the position along the height of the tab in the x direction [m], $A(x)$ the tab cross-sectional area [m^2] that varies with x, $R_{tab,cone}$ the resistance of the tab cone [Ω] and ρ_r the electrical resistivity of the tab material [Ω.m]. A schematic of the tab cone structure is shown in Figure A. 7.

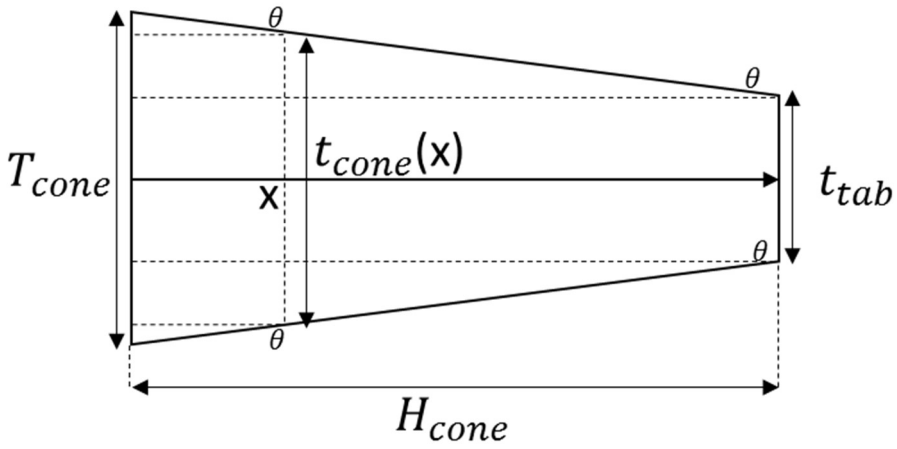

Figure A. 7: Schematic of the tab cone

Here the tab cross-sectional area $A(x)$ is represented by:

$$A(x) = (T_{cone} - 2xtan\theta)W_{tab} \tag{69}$$

Where T_{cone} is the thickness of the cone base (equal to the cell thickness) [m], W_{tab} the width of the tab [m], t_{tab} the thickness of the tab fin section [m] and H_{cone} the height of the tab [m]. The angle θ is calculated via:

$$\theta = \tan^{-1}\left(\frac{\frac{T_{cone} - t_{tab}}{2}}{H_{cone}}\right) = \tan^{-1}\left(\frac{\frac{0.0118 - 0.0003}{2}}{0.01}\right) = 0.5218\, rad$$

Equation (68) is solved for each tab material:

$$R_{tab,cone} = \rho_r \int_0^{H_{cone}} \frac{dx}{(T_{tab} - 2xtan\theta)W_{tab}} = \frac{\rho}{W_{tab}(-2tan\theta)} ln\left(\frac{-2tan\theta H_{cone} + T_{tab}}{T_{tab}}\right)$$

$$R_{cone} = 39.91383\rho$$

The electrical resistivity values for copper and aluminium are taken as:

$$\rho_{Al} = 2.65 \times 10^{-8}\ \Omega.m$$

$$\rho_{cu} = 1.68 \times 10^{-8}\ \Omega.m$$

The total resistance through the tab is given by the summation of the cone and tab fin resistance components. The resistance through the fin portion of the tab is given by:

$$R_{tab,fin} = \frac{\rho L}{A} = \frac{\rho L}{t_{tab} W_{tab}} \quad (70)$$

Where $R_{tab,fin}$ is that tab fin resistance [Ω] and L is the length of the tab fin [m]. $R_{tab,fin}$ is calculated as:

$$R_{tab,fin} = 1958.33\rho_r$$

Hence the total tab resistance is given by:

$$R_t = R_{tab,fin} + R_{tab,cone} = 1998.25\rho_r$$

Inputting the electrical resistivity values for the copper tab gives:

$$R_{t,cu} = 3.357 \times 10^{-5}\ \Omega$$

For the aluminium tab:

$$R_{t,Al} = 5.295 \times 10^{-5}\ \Omega$$

A.8 STUDENT T-TEST FOR THE POUCH CELL EXPERIMENT

The raw data obtained from the thermocouple sensors on the front and backs fins for the aluminium, copper and k-core fins at the end of the 3C discharge is contained within Table A 6, Table A 7 and Table A 8 respectively. The notation adopted for the thermocouple readings is as follows: TCB refers to the thermocouple location of the back fin and TCF the thermocouple location on the front fin. The locations of the thermocouple numbers on the front and back fin are shown in Figure 6-5

Table A 6: Thermocouple results for the aluminium fin at the end of the 3C discharge

Cell number	TCF5 [℃]	TCB5 [℃]	TCF9 [℃]	TCB9 [℃]
1	53.95	54.30	35.05	35.39
2	53.74	54.63	34.49	34.44
3	55.71	55.23	35.82	35.99
4	52.77	53.44	36.85	37.13
5	52.52	52.99	35.94	36.14

Table A 7: Thermocouple results for the copper fin at the end of the 3C discharge

Cell number	TCF5 [℃]	TCB5 [℃]	TCF9 [℃]	TCB9 [℃]
1	49.68	50.62	34.52	32.80
2	49.93	49.94	34.90	34.96
3	50.35	50.09	35.44	34.56
4	50.26	51.27	36.23	32.29
5	50.75	50.87	33.61	33.25
6	50.73	50.74	33.66	33.10

Table A 8: Thermocouple results for the k-core fin at the end of the 3C discharge

Cell number	TCF5 [℃]	TCB5 [℃]	TCF9 [℃]	TCB9 [℃]
1	45.10	45.73	32.53	32.35
2	45.65	46.39	32.61	32.72
3	46.37	46.38	32.67	32.34
4	44.96	46.25	32.89	32.45
5	46.47	47.03	32.69	32.84
6	46.93	46.65	33.30	32.57
6*	45.85	45.58	32.45	32.82

The results of the paired student t-test for the maximum fin temperature (TC5) and maximum fin temperature gradient (TC5-TC9) are contained within Table A 9 and Table A 10 respectively.

Table A 9: Paired t-test for maximum fin temperature (TC5) populations between front fins and back fins as a function of fin material type

Paired t-test for aluminium front fins - aluminium back fins				
	N (number of samples)	Mean [℃]	StDev [℃]	Standard Error (SE) Mean [℃]
Material A front fins	5	53.738	1.26	0.564
Material A back fins	5	54.118	0.903	0.404
Difference	5	-0.38	0.523	0.234
T-Test of mean difference = 0 (vs ≠ 0)				
T-Value	-1.63			
P-Value	0.179			
95% confidence interval (CI) for mean difference [℃]	(-1.029, 0.269)			
Paired t-test for copper front fins - copper back fins				
	N	Mean [℃]	StDev [℃]	SE Mean [℃]
Material A front fins	6	50.283	0.427	0.174
Material A back fins	6	50.588	0.497	0.203
Difference	6	-0.305	0.534	0.218
T-Test of mean difference = 0 (vs ≠ 0)				
T-Value	-1.40			
P-Value	0.221			
95% CI for mean difference [℃]	(-0.866, 0.256)			
Paired t-test for k-core front fins – k-core back fins				
	N	Mean [℃]	StDev [℃]	SE Mean [℃]
Material C front fins	7	45.904	0.73	0.276
Material C back fins	7	46.287	0.502	0.19
Difference	7	-0.383	0.584	0.221
T-Test of mean difference = 0 (vs ≠ 0)				
T-Value	-1.73			
P-Value	0.134			
95% CI for mean difference [℃]	(-0.923, 0.157)			

Table A 10: Paired t-test for maximum fin temperature gradient (TC5-TC9) populations between front fins and back fins as a function of fin material type

Paired t-test for aluminium front fins - aluminium back fins				
	N	Mean [℃]	StDev [℃]	SE Mean [℃]
Material A front fins	5	18.108	1.749	0.782
Material A back fins	5	18.3	1.65	0.738
Difference	5	-0.192	0.58	0.26
T-Test of mean difference = 0 (vs ≠ 0)				

T-Value	-0.74			
P-Value	0.500			
95% CI for mean difference [℃]	(-0.913, 0.529)			
Paired t-test for copper front fins - copper back fins				
	N	Mean [℃]	StDev [℃]	SE Mean [℃]
Material B front fins	6	15.557	1.263	0.516
Material B back fins	6	17.095	1.521	0.621
Difference	6	-1.538	1.914	0.781
T-Test of mean difference = 0 (vs ≠ 0)				
T-Value	-1.97			
P-Value	0.106			
95% CI for mean difference [℃]	(-3.547, 0.471)			
Paired t-test for k-core front fins – k-core back fins				
	N	Mean [℃]	StDev [℃]	SE Mean [℃]
Material C front fins	7	13.17	0.646	0.244
Material C back fins	7	13.703	0.499	0.189
Difference	7	-0.533	0.702	0.265
T-Test of mean difference = 0 (vs ≠ 0)				
T-Value	-2.01			
P-Value	0.091			
95% CI for mean difference [℃]	(-1.182, 0.116)			

The results from both tables support the assumption that the test rig had been set-up correctly, such as to create symmetry planes along the central axis of the cell. This is since the null hypothesis can be accepted given that the P-values are larger than 0.05 in all cases.

A.9 EXPLORATORY DATA ANALYSIS

An exploratory data analysis as described in [239] is first conducted to gauge the quality of the data in order to identify whether any observable skews, deficiencies in sample size or outliers within the data are apparent. The results for both the front and back fins are pooled and are viewable in Table A 11 which have been rounded to 1 decimal place. The data is pooled to increase the sample size. The data in Table A 11 is presented such that the maximum fin surface temperature is aligned with the corresponding fin temperature gradient across that fin.

Table A 11: Pooled temperature data from the front and back fin readings for each fin material type at the end of the 3C discharge

	Fin material type					
	Aluminium (A)		Copper (B)		k-core (C)	
	Maximum fin surface temperature [℃]	Maximum fin surface gradient [℃]	Maximum fin surface temperature [℃]	Maximum fin surface gradient [℃]	Maximum fin surface temperature [℃]	Maximum fin surface gradient [℃]
	52.5	15.9	49.7	15.2	45.1	12.6
	52.8	16.3	49.9	15.0	45.7	13.0
	53.0	16.6	50.4	14.9	46.4	13.7
	53.4	16.9	50.3	14.0	45.0	12.1
	53.7	18.9	50.8	17.1	46.5	13.8
	54.0	18.9	50.7	17.1	46.9	13.6
	54.3	19.2	50.6	17.8	45.9	13.4
	54.6	19.3	49.9	15.0	45.7	13.4
	55.2	19.9	50.1	15.5	46.4	13.7
	55.7	20.2	51.3	19.0	46.4	14.0
	--	-	50.9	17.6	46.3	13.8
		-	50.7	17.6	47.0	14.2
	-	-	-	-	46.7	14.1
	-	-	-	-	45.6	12.8
Mean	53.9	18.2	50.4	16.3	46.1	13.4
Median	53.8	18.9	50.5	16.3	46.3	13.7
Sample standard deviation (sx)	1.05	1.61	0.470	1.56	0.634	0.620
Range	3.2	4.3	1.6	5.0	2.0	2.1
Maximum	55.7	20.2	51.3	19.0	47.0	14.2
Minimum	52.5	15.9	49.7	14.0	45.0	12.1
Count	10	10	12	12	14	14

The boxplot results for each material type for both the maximum fin surface temperature and maximum fin surface temperature gradient are included in Figure A. 8. From the

boxplots it is observed that no outliers are observed for either variables (fin position, batch, pooled data, fin material type) with the mean being very similar to the average for all boxplots

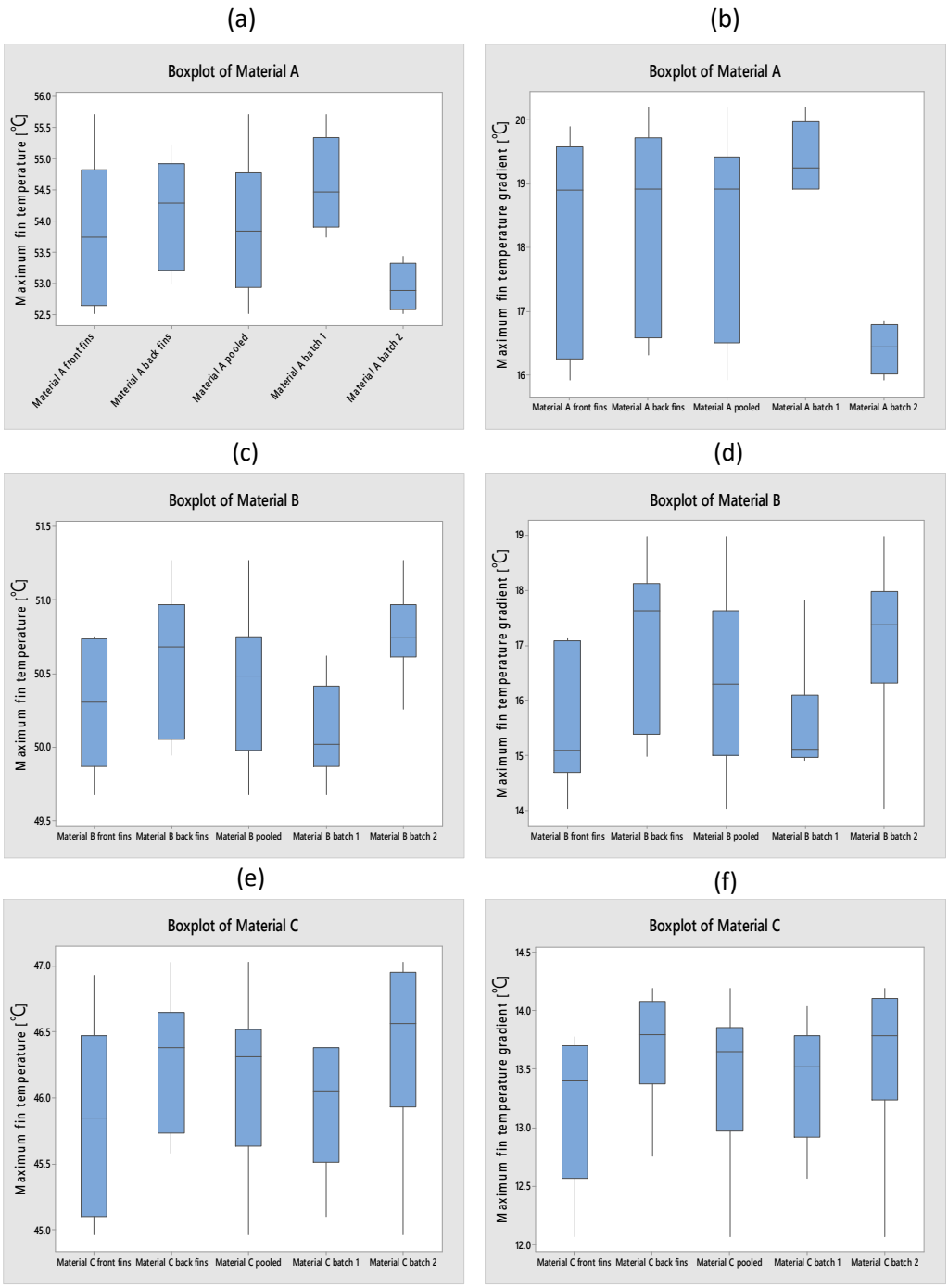

Figure A. 8: Box plots for (a) Aluminium fin TC5 data (b) Aluminium fin TC5-TC9 data (c) Copper fin TC5 data (d) Copper fin TC5-TC9 data (e) k-core fin TC5 data (f) k-core fin TC5-TC9 data [183]

A.10 INDIVIDUAL POUCH CELL SAMPLE RESULTS

A.10.1 K-CORE FIN RACE CYCLE

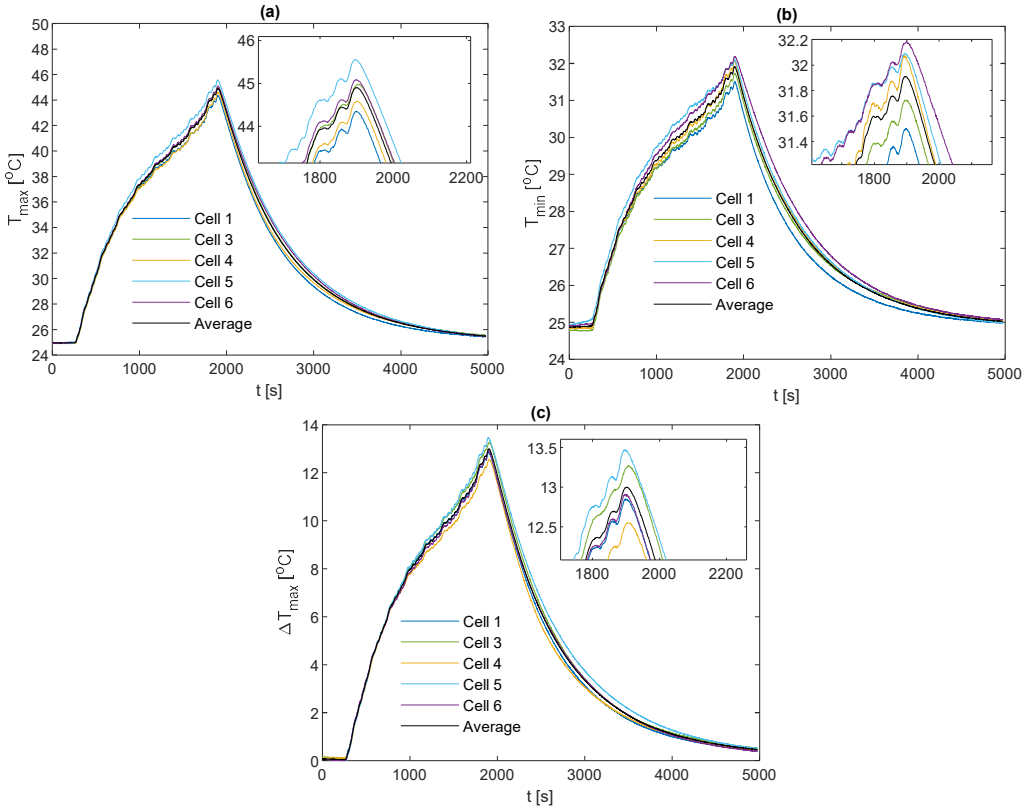

Figure A. 9: k-core fin race duty cycle results for all the tested cell samples with (a) TC5 measurements (b) TC9 measurements (c) maximum fin temperature gradient (TC5-TC9)

Table A 12: Values of TC5, TC9 and TC5-TC9 at the end of the race duty cycle for each sample under k-core fin cooling

Cell	TC5 [°C]	TC9 [°C]	TC5-TC9 [°C]
1	44.35	31.49	12.86
3	44.95	31.67	13.28
4	44.58	32.03	12.55
5	45.55	32.07	13.48
6	45.09	32.18	12.91

Table A 13: Mean, Standard Deviation and Standard Error for the sample values at the end of the race duty cycle under k-core fin cooling

Parameter	Mean [°C]	Standard deviation [°C]	Standard Error [°C]
TC5	44.90	0.465	0.208
TC9	31.89	0.293	0.131
TC5-TC9	13.02	0.367	0.164

A.10.2 K-CORE FIN 3 C DISCHARGE

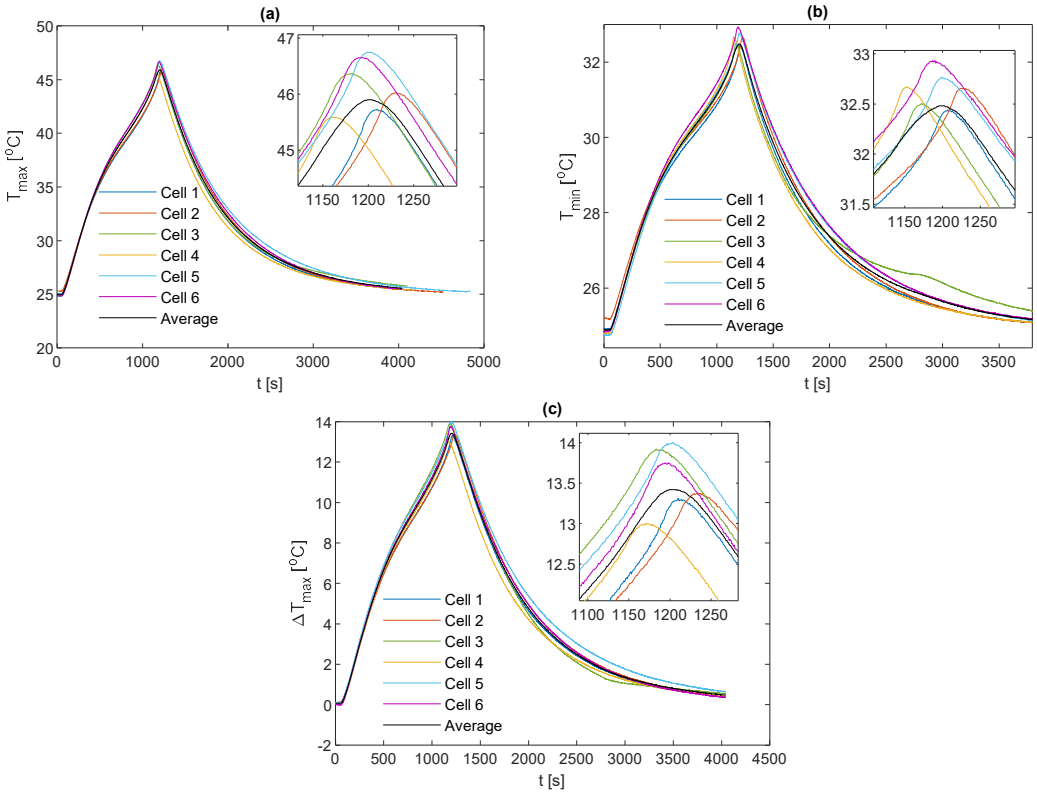

Figure A. 10: k-core fin 3 C results for all the tested cell samples with (a) TC5 measurements (b) TC9 measurements (c) maximum fin temperature gradient (TC5-TC9)

Table A 14: Values of TC5, TC9 and TC5-TC9 at the end of the 3 C discharge for each sample under k-core fin cooling

Cell	TC5 [°C]	TC9 [°C]	TC5-TC9 [°C]
1	45.73	32.42	13.31
2	46.02	32.65	13.37
3	46.37	32.45	13.92
4	45.59	32.59	13.00
5	46.75	32.75	14.00
6	46.65	32.90	13.75

Table A 15: Mean, Standard Deviation and Standard Error for the sample values at the end of the 3 C discharge under k-core fin cooling

Parameter	Mean [°C]	Standard deviation [°C]	Standard Error [°C]
TC5	46.19	0.481	0.196
TC9	32.63	0.182	0.074
TC5-TC9	13.56	0.393	0.160

A.10.3 K-CORE FIN 2 C DISCHARGE

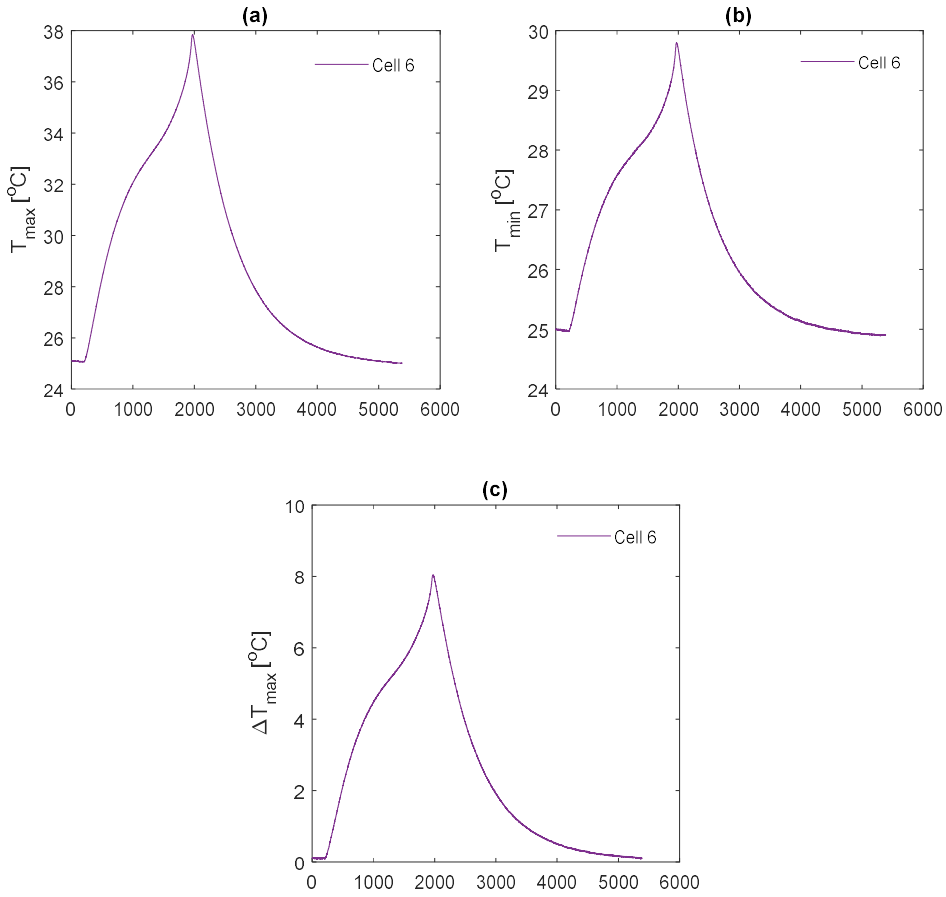

Figure A. 11: k-core fin 2 C results for all the tested cell samples with (a) TC5 measurements (b) TC9 measurements (c) maximum fin temperature gradient (TC5-TC9)

A.10.4 K-CORE FIN WLTP CLASS 3

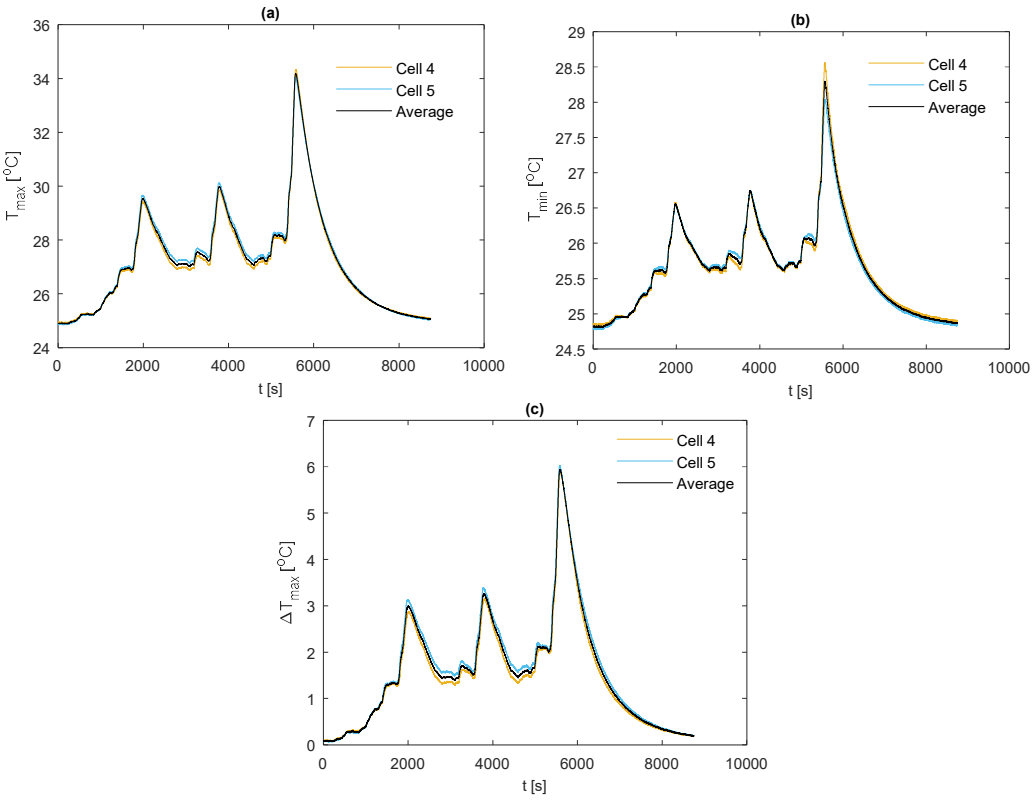

Figure A. 12: k-core fin WLTP Class 3 duty cycle results for cell samples 4 and 5 (a) TC5 measurements (b) TC9 measurements (c) maximum fin temperature gradient (TC5-TC9)

Table A 16: Values of TC5, TC9 and TC5-TC9 at the end of the WLTP Class 3 cycle for each sample under k-core fin cooling

Cell	TC5 [°C]	TC9 [°C]	TC5-TC9 [°C]
4	34.34	28.47	5.88
5	34.03	28.01	6.03

Table A 17: Mean, Standard Deviation and Standard Error for the sample values at the end of the WLTP Class 3 cycle under k-core fin cooling

Parameter	Mean [°C]	Standard deviation [°C]	Standard Error [°C]
TC5	34.19	0.219	0.155
TC9	28.24	0.325	0.230
TC5-TC9	5.95	0.106	0.075

A.10.5 K-CORE FIN 1 C DISCHARGE

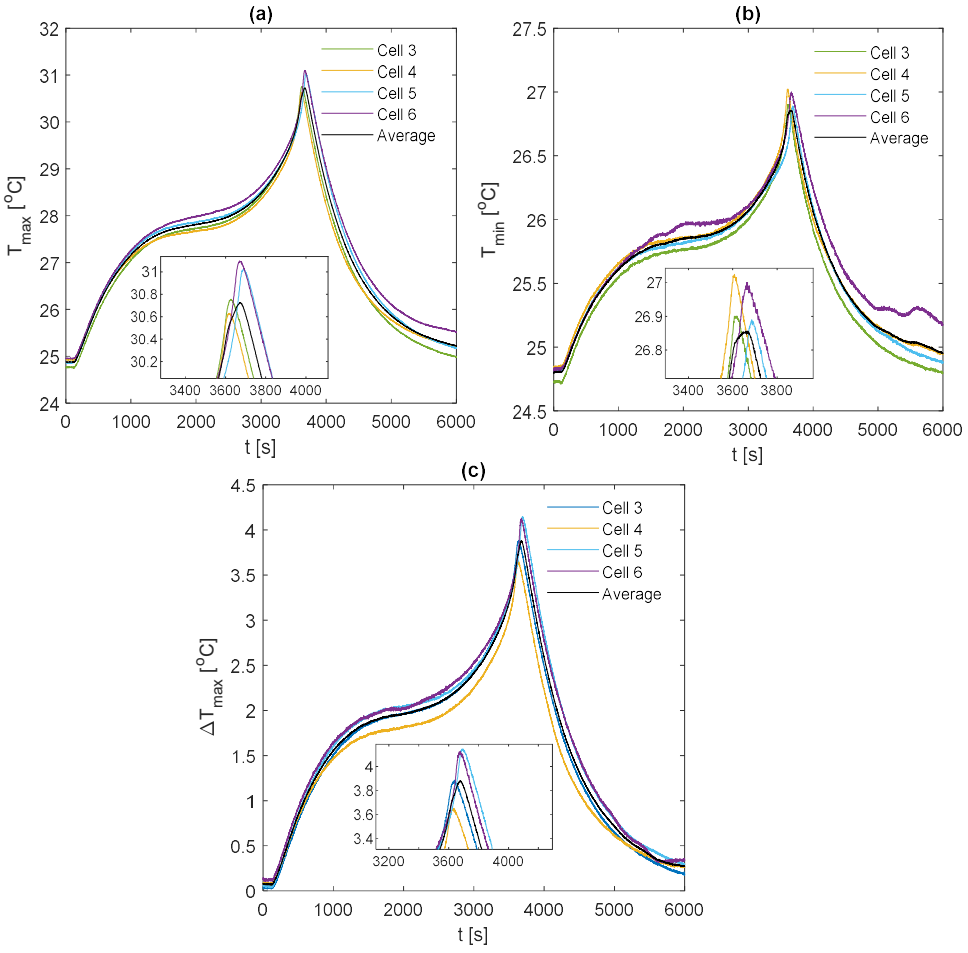

Figure A. 13: k-core fin 1 C discharge results for cell samples 3- 6 (a) TC5 measurements (b) TC9 measurements (c) maximum fin temperature gradient (TC5-TC9)

Table A 18: Values of TC5, TC9 and TC5-TC9 at the end of the 1 C discharge for each sample under k-core fin cooling

Cell	TC5 [°C]	TC9 [°C]	TC5-TC9 [°C]
3	30.75	26.88	3.88
4	30.63	26.98	3.65
5	31.02	26.88	4.15
6	31.10	26.98	4.13

Table A 19: Mean, Standard Deviation and Standard Error for the sample values at the end of the 1 C discharge under k-core fin cooling

Parameter	Mean [°C]	Standard deviation [°C]	Standard Error [°C]
TC5	30.88	0.222	0.111
TC9	26.95	0.059	0.030
TC5-TC9	3.92	0.234	0.117

A.10.6 COPPER FIN RACE CYCLE

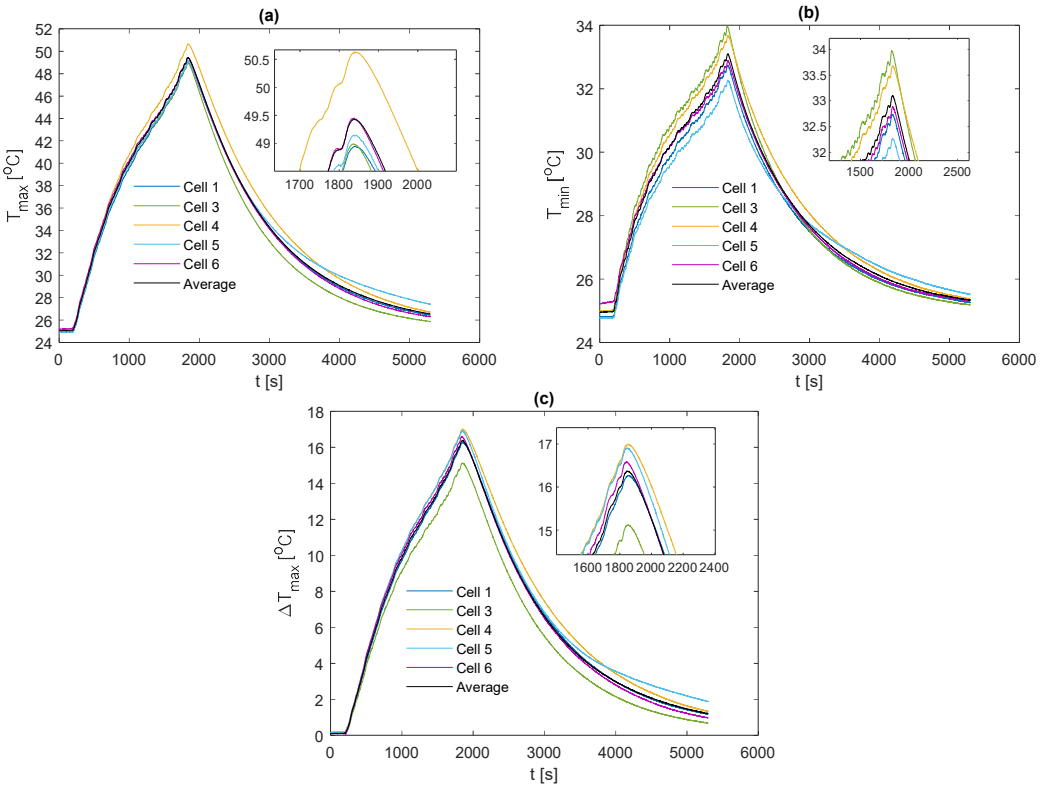

Figure A. 14: Copper fin race duty cycle results for all the tested cell samples with (a) TC5 measurements (b) TC9 measurements (c) maximum fin temperature gradient (TC5-TC9)

Table A 20: Values of TC5, TC9 and TC5-TC9 at the end of the race duty cycle for each sample under copper fin cooling

Cell	TC5 [°C]	TC9 [°C]	TC5-TC9 [°C]
1	48.95	32.68	16.27
3	48.98	33.88	15.10
4	50.63	33.64	16.99
5	49.15	32.24	16.91
6	49.42	32.83	16.59

Table A 21: Mean, Standard Deviation and Standard Error for the sample values at the end of the race duty cycle under copper fin cooling

Parameter	Mean [°C]	Standard deviation [°C]	Standard Error [°C]
TC5	49.43	0.698	0.312
TC9	33.05	0.685	0.306
TC5-TC9	16.37	0.766	0.343

A.10.7 COPPER FIN 3 C DISCHARGE

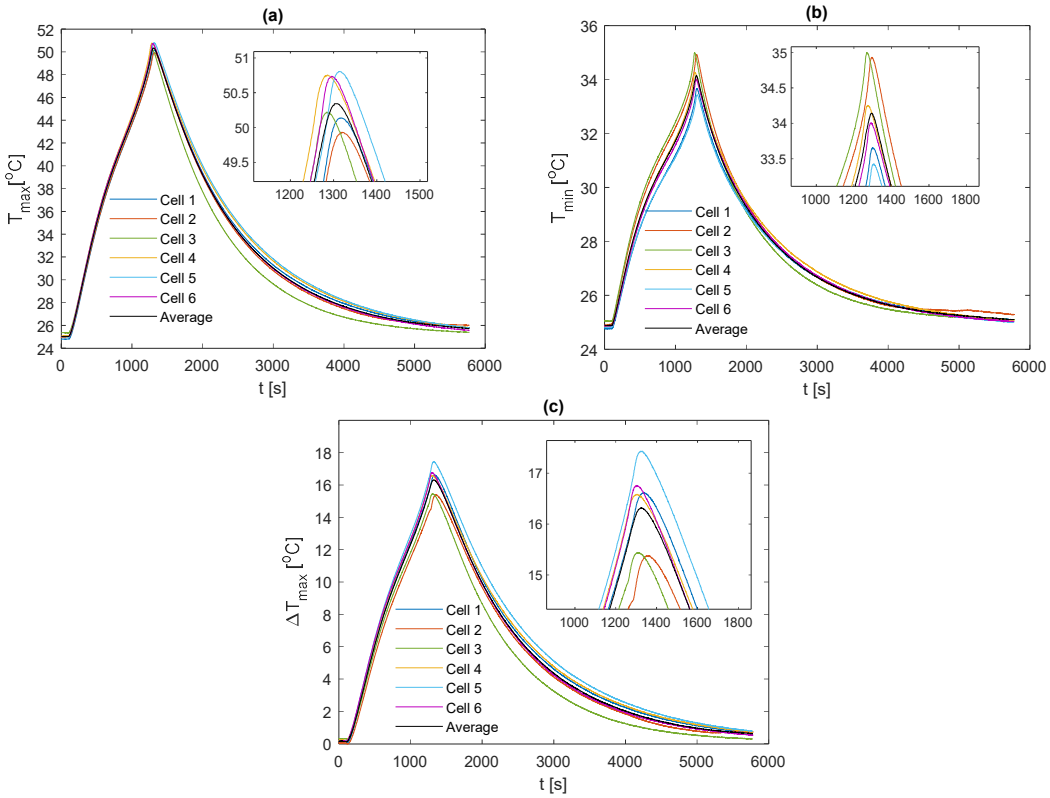

Figure A. 15: Copper fin 3 C discharge results for all the tested cell samples with (a) TC5 measurements (b) TC9 measurements (c) maximum fin temperature gradient (TC5-TC9)

Table A 22: Values of TC5, TC9 and TC5-TC9 at the end of the 3 C discharge for each sample under copper fin cooling

Cell	TC5 [°C]	TC9 [°C]	TC5-TC9 [°C]
1	50.13	33.51	16.62
2	49.92	34.54	15.38
3	50.22	34.67	15.55
4	50.76	34.17	16.59
5	50.80	33.37	17.43
6	50.73	33.95	16.78

Table A 23: Mean, Standard Deviation and Standard Error for the sample values at the end of the 3 C discharge under copper fin cooling

Parameter	Mean [°C]	Standard deviation [°C]	Standard Error [°C]
TC5	50.43	0.382	0.156
TC9	34.04	0.529	0.216
TC5-TC9	16.39	0.781	0.319

A.10.8 COPPER FIN 2 C DISCHARGE

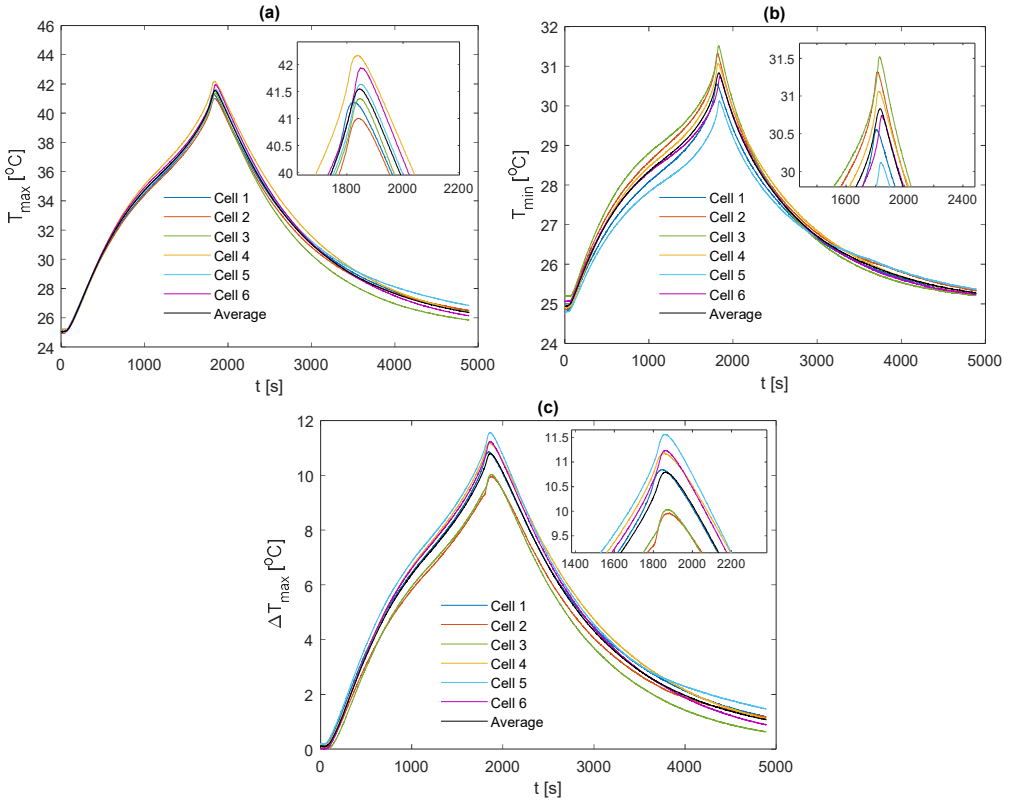

Figure A. 16: Copper fin 2 C discharge results for all the tested cell samples with (a) TC5 measurements (b) TC9 measurements (c) maximum fin temperature gradient (TC5-TC9)

Table A 24: Values of TC5, TC9 and TC5-TC9 at the end of the 2 C discharge for each sample under copper fin cooling

Cell	TC5 [°C]	TC9 [°C]	TC5-TC9 [°C]
1	41.31	30.46	10.85
2	41.01	31.05	9.96
3	41.37	31.33	10.04
4	42.17	30.98	11.19
5	41.63	30.07	11.56
6	41.94	30.70	11.24

Table A 25: Mean, Standard Deviation and Standard Error for the sample values at the end of the 2 C discharge under copper fin cooling

Parameter	Mean [°C]	Standard deviation [°C]	Standard Error [°C]
TC5	41.57	0.429	0.175
TC9	30.77	0.453	0.185
TC5-TC9	10.81	0.665	0.271

A.10.9 COPPER FIN WLTP CLASS 3

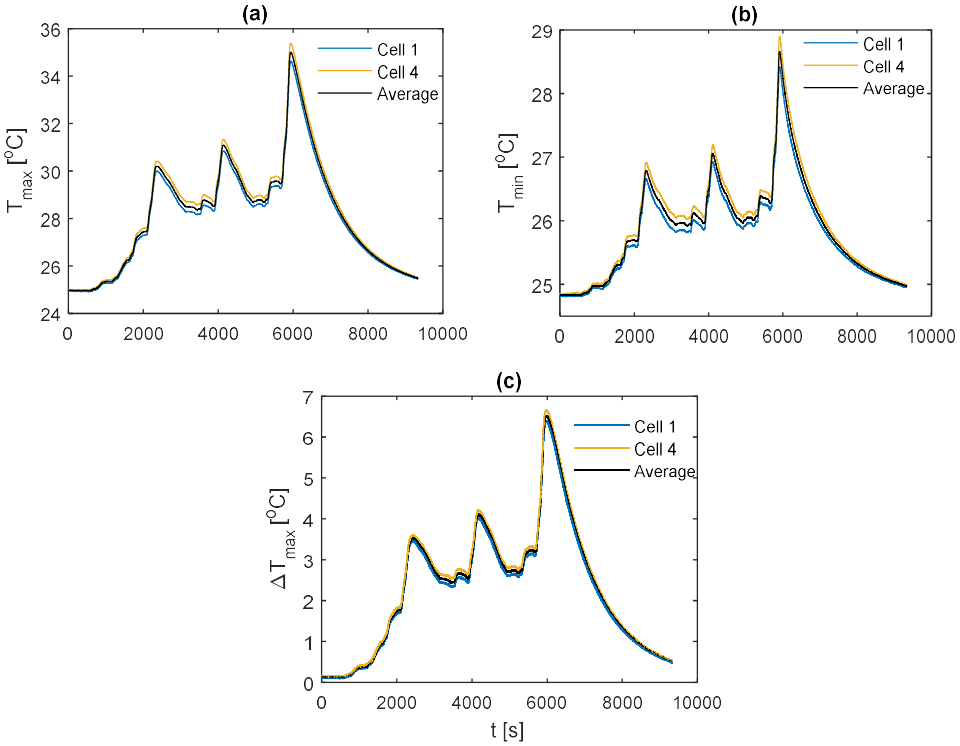

Figure A. 17: Copper fin WLTP Class 3 duty cycle results for cell samples 4 and 5 (a) TC5 measurements (b) TC9 measurements (c) maximum fin temperature gradient (TC5-TC9)

Table A 26: Values of TC5, TC9 and TC5-TC9 at the end of the WLTP Class 3 cycle for each sample under copper fin cooling

Cell	TC5 [°C]	TC9 [°C]	TC5-TC9 [°C]
1	34.63	28.24	6.39
4	35.38	28.72	6.66

Table A 27: Mean, Standard Deviation and Standard Error for the sample values at the end of the WLTP Class 3 cycle under copper fin cooling

Parameter	Mean [°C]	Standard deviation [°C]	Standard Error [°C]
TC5	35.01	0.530	0.375
TC9	28.48	0.339	0.240
TC5-TC9	6.53	0.191	0.135

A.10.10 COPPER FIN 1 C DISCHARGE

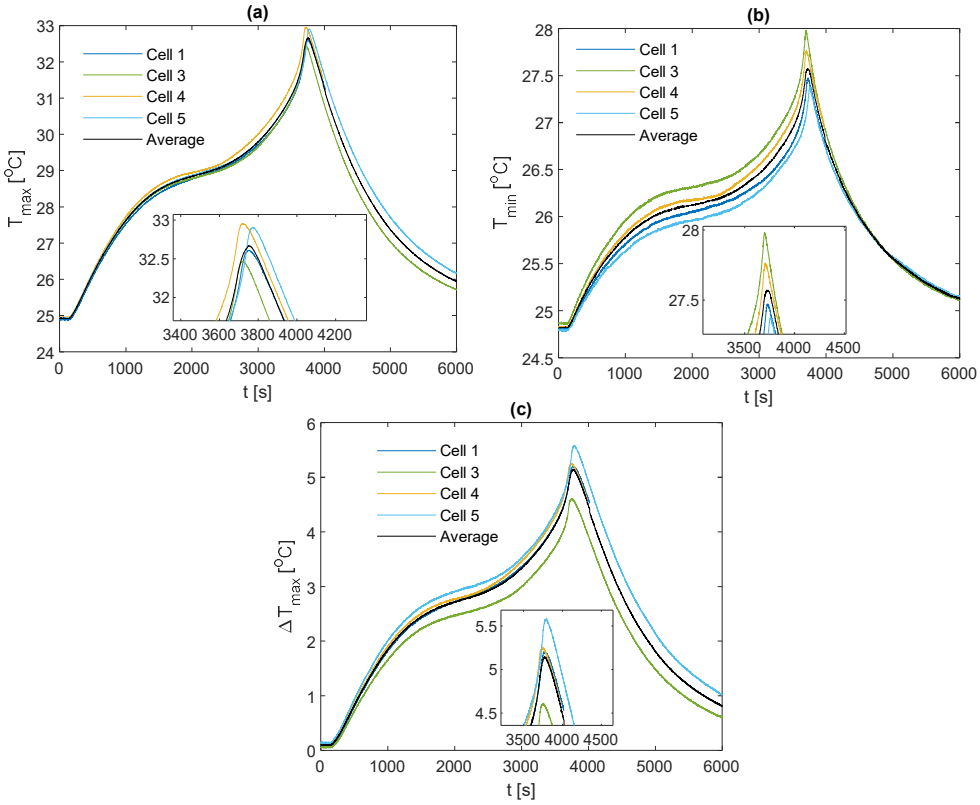

Figure A. 18: Copper fin 1 C discharge results for cell samples 3- 6 (a) TC5 measurements (b) TC9 measurements (c) maximum fin temperature gradient (TC5-TC9)

Table A 28: Values of TC5, TC9 and TC5-TC9 at the end of the 1 C discharge for each sample under copper fin cooling

Cell	TC5 [°C]	TC9 [°C]	TC5-TC9 [°C]
1	32.61	27.40	5.21
3	32.47	27.87	4.61
4	32.95	27.70	5.25
5	32.91	27.33	5.58

Table A 29: Mean, Standard Deviation and Standard Error for the sample values at the end of the 1 C discharge under copper fin cooling

Parameter	Mean [°C]	Standard deviation [°C]	Standard Error [°C]
TC5	32.74	0.233	0.116
TC9	27.57	0.252	0.126
TC5-TC9	5.16	0.406	0.203

A.10.11 ALUMINIUM FIN RACE CYCLE

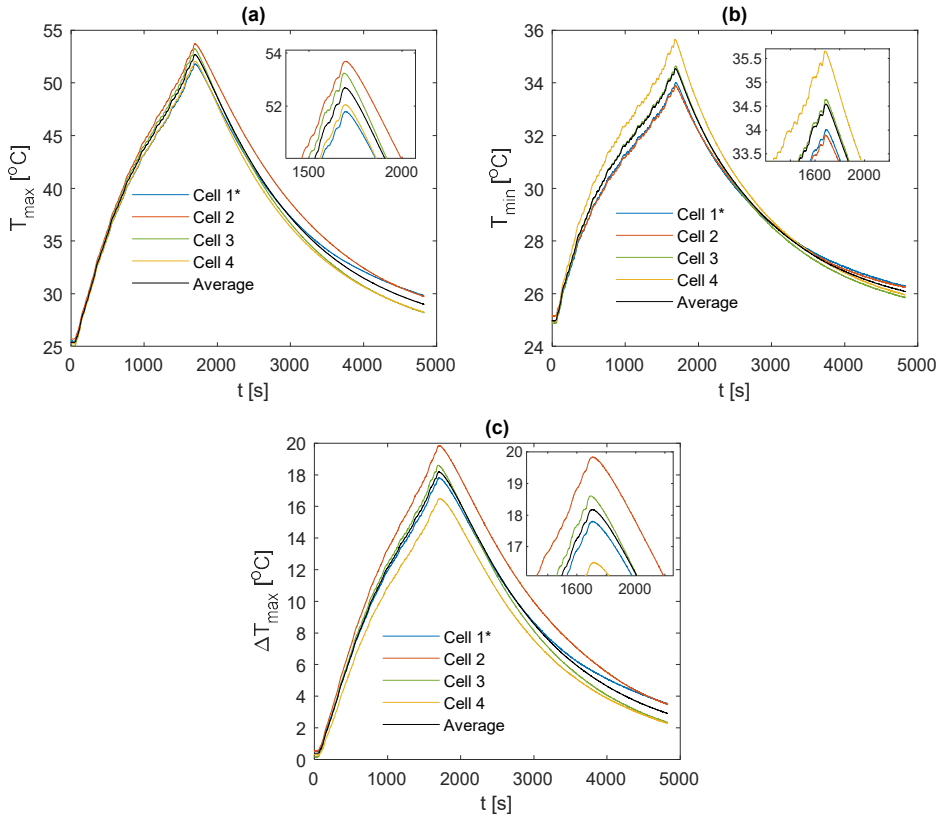

Figure A. 19: Aluminium fin race duty cycle results for all the tested cell samples with (a) TC5 measurements (b) TC9 measurements (c) maximum fin temperature gradient (TC5-TC9)

Table A 30: Values of TC5, TC9 and TC5-TC9 at the end of the race cycle for each sample under aluminium fin cooling

Cell	TC5 [°C]	TC9 [°C]	TC5-TC9 [°C]
1*	51.79	34.00	17.79
2	53.69	33.85	19.84
3	53.24	34.65	18.59
4	52.05	35.56	16.49

Table A 31: Mean, Standard Deviation and Standard Error for the sample values at the end of the race cycle under aluminium fin cooling

Parameter	Mean [°C]	Standard deviation [°C]	Standard Error [°C]
TC5	52.69	0.917	0.458
TC9	34.52	0.778	0.389
TC5-TC9	18.18	1.406	0.703

A.10.12 ALUMINIUM FIN 3 C DISCHARGE

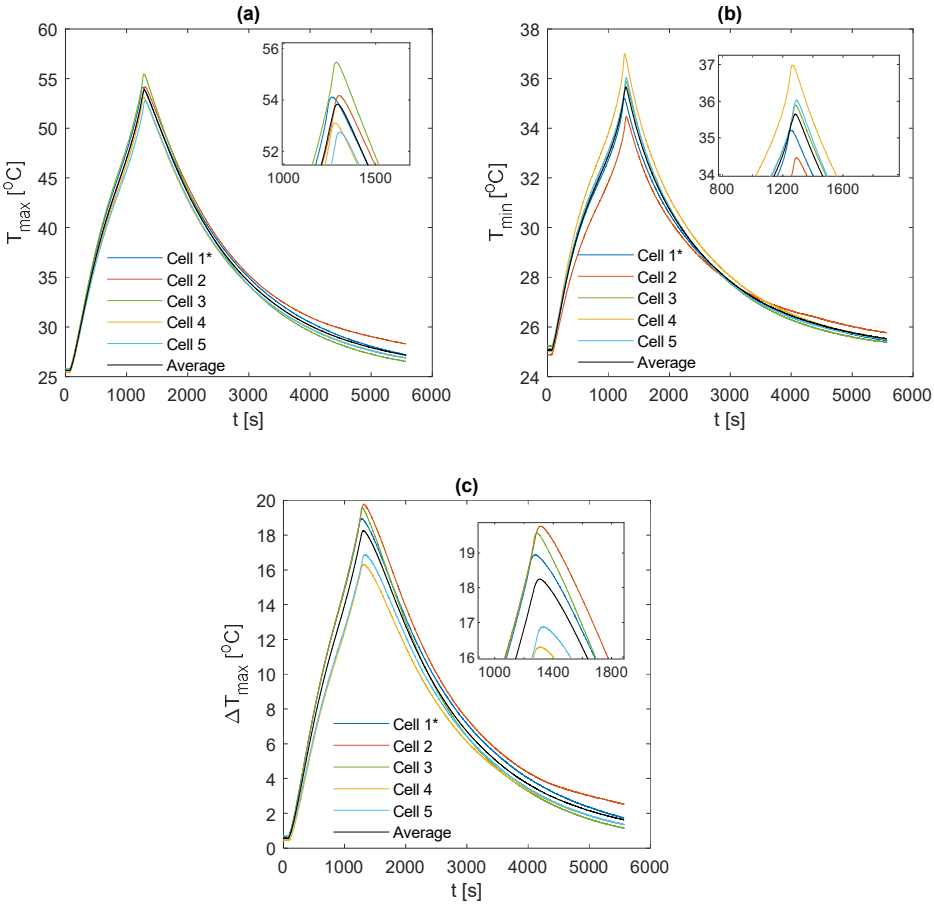

Figure A. 20: Aluminium fin 3 C discharge results for all the tested cell samples with (a) TC5 measurements (b) TC9 measurements (c) maximum fin temperature gradient (TC5-TC9)

Table A 32: Values of TC5, TC9 and TC5-TC9 at the end of the 3 C discharge for each sample under aluminium fin cooling

Cell	TC5 [°C]	TC9 [°C]	TC5-TC9 [°C]
1*	54.12	35.16	18.96
2	54.17	34.40	19.77
3	55.47	35.89	19.58
4	53.09	36.79	16.30
5	52.57	35.69	16.88

Table A 33: Mean, Standard Deviation and Standard Error for the sample values at the end of the 3 C discharge under aluminium fin cooling

Parameter	Mean [°C]	Standard deviation [°C]	Standard Error [°C]
TC5	53.88	1.119	0.500
TC9	35.59	0.886	0.396
TC5-TC9	18.30	1.601	0.716

A.10.13 ALUMINIUM FIN 2 C DISCHARGE

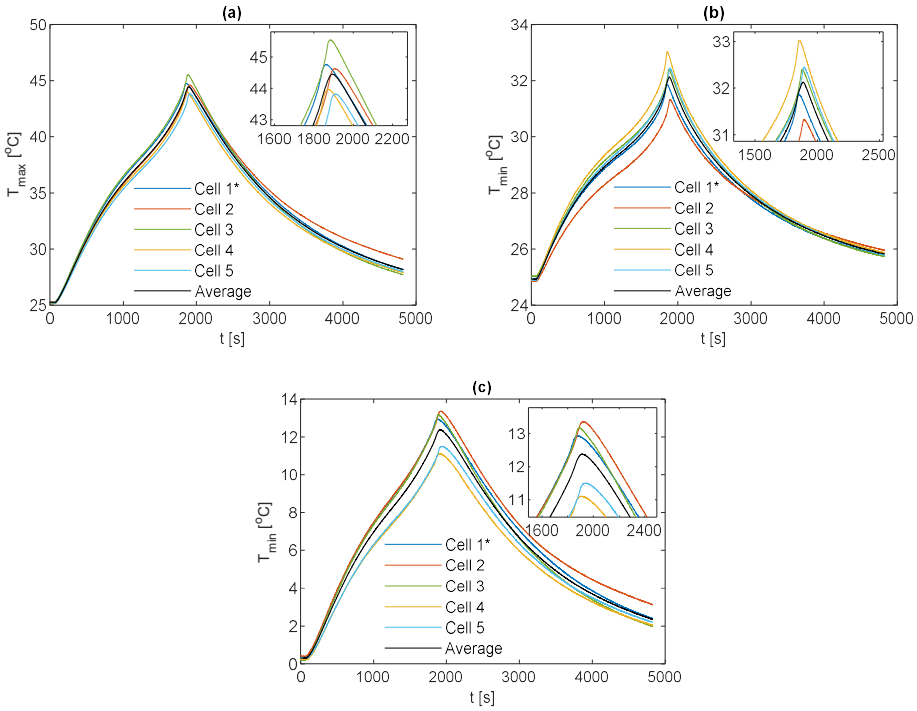

Figure A. 21: Aluminium fin 2 C discharge results for all the tested cell samples with (a) TC5 measurements (b) TC9 measurements (c) maximum fin temperature gradient (TC5-TC9)

Table A 34: Values of TC5, TC9 and TC5-TC9 at the end of the 2 C discharge for each sample under aluminium fin cooling

Cell	TC5 [°C]	TC9 [°C]	TC5-TC9 [°C]
1*	44.75	31.82	12.93
2	44.63	31.27	13.36
3	45.54	32.37	13.17
4	43.97	32.86	11.11
5	43.83	32.33	11.5

Table A 35: Mean, Standard Deviation and Standard Error for the sample values at the end of the 2 C discharge under aluminium fin cooling

Parameter	Mean [°C]	Standard deviation [°C]	Standard Error [°C]
TC5	44.54	0.686	0.307
TC9	32.13	0.605	0.271
TC5-TC9	12.41	1.033	0.462

A.10.14 ALUMINIUM FIN WLTP CLASS 3

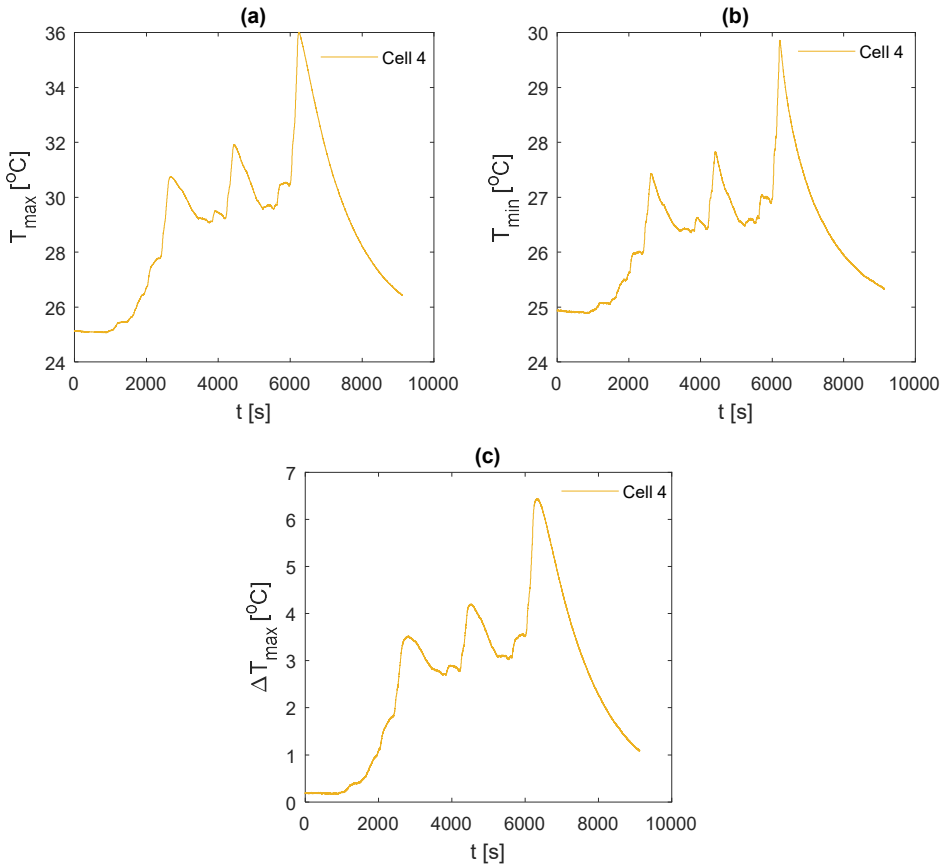

Figure A. 22: Aluminium fin WLTP Class 3 cycle results for all the tested cell samples with (a) TC5 measurements (b) TC9 measurements (c) maximum fin temperature gradient (TC5-TC9)

A.10.15 ALUMINIUM FIN 1 C DISCHARGE

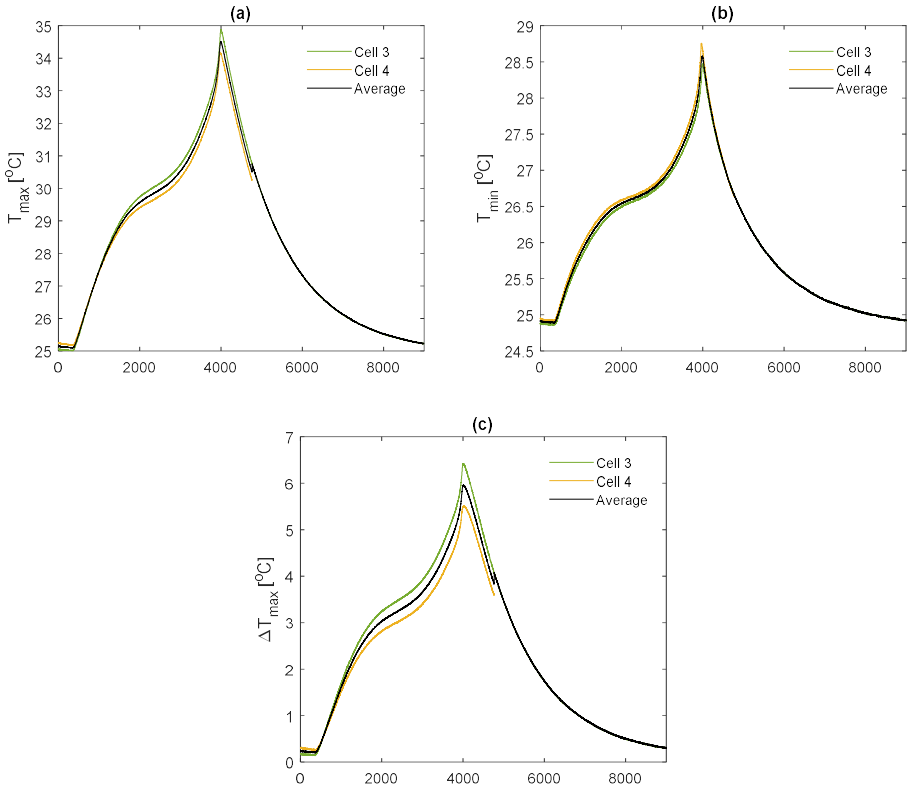

Figure A. 23: Aluminium fin 1 C discharge results for all the tested cell samples with (a) TC5 measurements (b) TC9 measurements (c) maximum fin temperature gradient (TC5-TC9)

Table A 36: Values of TC5, TC9 and TC5-TC9 at the end of the 1 C discharge for each sample under aluminium fin cooling

Cell	TC5 [°C]	TC9 [°C]	TC5-TC9 [°C]
3	34.87	28.45	6.42
4	34.16	28.66	5.5

Table A 37: Mean, Standard Deviation and Standard Error for the sample values at the end of the 2 C discharge under aluminium fin cooling

Parameter	Mean [°C]	Standard deviation [°C]	Standard Error [°C]
TC5	34.52	0.502	0.355
TC9	28.56	0.148	0.105
TC5-TC9	5.96	0.651	0.460